Converters for Optimizing Power Distribution in Fuel Cell Vehicles (Konverter zur Optimierung der Leistungsverteilung in Brennstoffzellen-Fahrzeugen)

Wensong Shen

October 27, 2022

Contents

Nomenclature

List of Notations

AC- alternative current
DC- direct current
DC/DC- direct current to direct current
D-duty cycle
f_s- switch operating frequency
N- number of phases
t_e- turn on conduction time of switch
T_P- switch operating period
T_s- system sampling time
ϕ- phase difference of PWMs

List of Abbreviations, Acronyms

ADC- Analog to Digital Converter
AFC- Alkaline Fuel Cell
BEV- Battery electric vehicle
BMS- Battery Management system
CAN BUS- Controller Area Network BUS
CCM- Continuous Conduction Mode
DAC- Digital to Analog Converter
D/A- Digital to Analog
DG- Distributed Generation
DMFC- Direct Methanol Fuel Cell
DRA- Digital Redesign Approach

e.g.- for example
etc.- and so on
EMI- Elector Magnetic Interference
ESR- Equivalent Series Resistance
E-switch- Electronic Switch
FCPM- Fuel Cell Power Module FCEV- Fuel cell Electric Vehicle
FFT- Fast Fourier Transform
HRS- Hydrogen Refueling Station
HF-High Frequency
IEA- International Energy Agency
i.e.- in other words
LOHC- Liquid Organic Hydrogen Carrier
M- Voltage Gain
MCU- Micro Controller Unit
MCFC- Molten Carbonate Fuel Cell
MOSFET- Metal-Oxide-Semiconductor Field-effect Transistor
MPPT- Maximum PowerPoint Tracking
NTC- Negative Temperature Coefficient
PAFC- Phosphoric Acid Fuel Cell PCU- Power Control Unit
PEMFC- Proton Exchange Membrane Fuel Cell
PFM- Pulse Frequency Modulation
PWM- Pulse Width Modulation
PTC- Positive Temperature Coefficient
PI- Proportional Integral
PRDCL- Parallel Resonant DC-Link
RMS- Root Mean Square
SWARM- Small 4 Wheel fuel cell passenger vehicle Applications in Regional and Municipal Transportation transport
SOFC- Solid Oxide Fuel Cell
SOA- Safe Operating Area
SoC- State of Charge
RC- Resonant Converter
QRC- Resonant Converter
USB- Universal Serial Bus
ZCT- Zero Current Transition
ZCS- Current Switching
ZTC- Zero Temperature coefficient
ZVS- Zero Voltage Switching
ZVT- Zero Voltage Transition

List of Figures

List of Tables

Introduction

Motivation

In order to increase the travel range of electrical vehicles, the use of fuel cells is currently being considered. For this application, the fuel cell system must be operated as gently as possible so that an acceptable lifetime is achieved. The combination of energy storage (battery, double-layer capacitors) and fuel cell enables gentle operation and also increases the efficiency of the powertrain. In this structure, the electric power distribution must be controlled by power electronic converters. In this work, different power electronic converters applied to fuel cell electric vehicles will be theoretically analyzed, simulated, and practically constructed to verify their feasibility. In order to optimize the powertrain of a fuel cell vehicle, and to test the operation of a converter in a fuel cell electric vehicle powertrain, it is necessary to reproduce the load on the powertrain under real driving conditions. Before implementing a fuel cell electric vehicle, a test bench for the powertrain of fuel cell electric vehicle will be built.

Thesis outline

In this work, the powertrains of fuel cell electric vehicles are introduced, different converters for improvement of fuel cell vehicle powertrain are proposed, analytically studied, digitally simulated and validated through practical experiments, and a test bench to verify powertrain systems is implemented. The dissertation consists of 6 chapters and organized as follows:

Chapter1

The first chapter introduces the current development of hydrogen energy in the world. Thanks to the excellent properties of hydrogen energy, it will play an important role in the future energy structure. One efficient way to utilize hydrogen is the fuel cell, and one of the end-use applications for fuel cells is the transportation industry, therefore, the basic principles and structures of fuel cells and fuel cell electric vehicles are also introduced in detail. It also explains the necessity of converters in fuel cell electric vehicles.

Chapter2

A novel concept of fuel cell electric vehicle powertrain is described in this chapter. When the output characteristics of the fuel cell stack and the DC bus bar of the powertrain satisfy certain conditions, the DC/DC converter in powertrain can be replaced by an electronic switch. The electronic switch only operates to buffering connect or disconnect the fuel cell to the DC bus bar.

This chapter focuses on the hardware and software control design of the electronic switch, and a prototype was built to verify the theoretical analysis and design. The results of this concept testing of powertrain are provided in chapter 5.

Chapter3

In Chapter 3, DC/DC converters of FCEV power rain are studied. Depending on the operating characteristics of the fuel cell stack in the powertrain, converters should provide both low ripple current and fast response to extend the life of the fuel cell. Among the numerous converters, multiphase converter are chosen for their obvious advantages.

This chapter concentrates on the theoretical analysis of multiphase buck converters. For the ease of understanding, the analysis expands from single-phase to multiphase buck converter. The calculation of ripple currents of the input and output, which relate to the number of phases, the derivation of the small-signal model and the multiphase current sharing are presented. Similarly, a 12kW laboratory prototype was built, and the control strategy in a fuel cell electric vehicle powertrain was verified using a single-phase buck converter.

Chapter4

To further optimize the efficiency and electromagnetic interference of the multiphase converters, soft-switching technology is considered for integration

into converter. Therefore, two types of soft-switching multiphase buck converters (multiphase ZVT-PWM buck converter and multiphase buck converter with parallel resonant DC-Link circuit) are studied in this chapter. The soft-switching process is analyzed mainly from the state change of the auxiliary circuit, and the conditions of the control timing of the auxiliary and power circuits are proposed. Finally, the characteristics of the two soft-switching multiphase buck converters are analyzed by comparing the measurement results of the prototypes.

Chapter5

This chapter describes the practical construction of a fuel cell electric vehicle test bench and the implementation of a small fuel cell electric vehicle, A detailed demonstration of the powertrains construction, including fuel cell power module, hydrogen and oxygen supply system, thermal management system, high-voltage battery pack (battery management system). The "passive hybrid system" described in Chapter 1 was verified on the completed experimental test bench.

Chapter6

The dissertation ends with Chapter 6, that consists of a conclusion, the contributions of the author, and possible work in the future.

Thesis objectives

In this dissertation. All laboratory prototypes as well as the test bench, small fuel cell electric vehicles were realized at the Jade University of Allied Sciences, in the Power Electronic laboratory, number L122a. In the process of research, the following technical equipment was used:

- Fuel cell power module, HyPM-HD-8, provided by HYDROGENICS company.
- Lithium iron phosphate battery pack.
- 70 MPa hydrogen storage tank, provided by ILJIN Composites and YOUNGDO company.
- Elano e-mobile, provided by H_2O e-mobile GmbH.

- Used software: LabVIEW, MATLAB 2021, MATLAB Simulink, LT-Spice.

Chapter 1.

From Hydrogen Energy to Fuel Cell Electric Vehicle

1.1 Hydrogen energy

With the increasing pressure to cope with climate change and the acceleration of energy low-carbon transformation, hydrogen energy has attracted worldwide attention for its advantages of cleanliness, flexibility, efficiency, and rich application scenarios [1–3]. Countries and regions such as Europe, the United States, Japan, South Korea and China have made substantial progress in the development of the hydrogen energy industry through strategic guidance, route planning, industrial support policies, and continuous investment [4].

Regarding the strategic layout of hydrogen energy, Europe regards hydrogen energy as an important guarantee for energy transition and low-carbon development. The United States attaches importance to the establishment of technological advantages in the hydrogen energy industry and the research and development of forward-looking technologies. Japan and South Korea are committed to building a hydrogen energy society and hydrogen economy, and in China, the use of hydrogen energy is mainly focused on the development of fuel cell buses and trucks [5]. In terms of technological development, hydrogen production by electrolysis of renewable energy, hydrogen storage in salt caverns, hydrogen transmission through pipelines, and the use of hydrogen to replace natural gas for heating will become key development directions.

Nowadays, hydrogen is used as an important industrial raw material, but in the energy transition, hydrogen is more important as an energy carrier,

with the characteristics of clean, efficient, renewable, transportable, and scenario applications. As an energy carrier, hydrogen can be used by combining with electricity in an innovative overall energy system. All primary resources such as fossil fuels, renewable energy sources (solar, wind, hydro, geothermic, biomass)and nuclear power could be used for hydrogen production and can be termed as one of the advantages of using hydrogen as an energy carrier [6–9]. In general, hydrogen as an energy carrier has the following advantages:

- **Diversified, clean, environmentally friendly and efficient secondary energy sources**
  Hydrogen is a secondary energy source that can be produced in a variety of ways, with less resource constraints. Using fuel cells, hydrogen energy is directly converted into electricity and water through electrochemical reactions, and does not emit pollutants. Compared to fossil fuels such as gasoline, diesel, natural gas, etc. Its conversion efficiency is not limited by the Carnot cycle, and the power generation efficiency is high, hence is a highly efficient energy source with zero pollution.

- **Ideal energy interconnection medium**
  Hydrogen energy is the medium to realize the transformation of various energy sources such as electricity, heat, and liquid fuels. The current energy system is mainly composed of power grids, heating networks, oil and gas pipeline networks. With fuel cell technology, hydrogen energy can be converted between different energy networks, and renewable energy and fossil fuels can be converted into electricity and heat at the same time. The reverse reaction produces hydrogen fuel to replace fossil fuels or energy storage, so as to realize the collaborative optimization between different energy networks, therefore, hydrogen energy is considered to be the best way to solve the energy resource crisis and environmental crisis.

- **Energy storage media that can be applied on a large scale**
  As the penetration rate of renewable energy continues to increase, seasonal and even annual peak shaving demand in grid will also increase day by day. The role of energy storage in the future energy system will continue to appear, but electrochemical energy storage and other energy storage methods are difficult to meet long-term, large-capacity energy storage requirements. Hydrogen energy can realize long-term and large-scale storage of electric or thermal energy more economically. It can be an important way to solve the problems of abandoning wind energy, solar energy, and guarantee the safe and stable operation of a high proportion of renewable energy systems in the future [10].

- **Rich application scenarios**
  There are abundant application modes of hydrogen energy, which can help major terminal applications such as industry, construction, and transportation to achieve low-carbon, including as a fuel cell vehicle in the transportation field, as an energy storage medium to support the integration and power generation of large-scale renewable energy. Distributed generation (DG) or co-generation provides electricity and heat for buildings, and directly provides clean energy or raw materials for industrial fields.

In the report *Energy Outlook 2020 Edition* (Published by BP p.l.c.) [11], the demand for hydrogen energy is predicted as follows: "The use of hydrogen as an energy carrier increases significantly in Rapid and Net Zero as the world transitions to a lower-carbon energy system". Figure 1.1 shows the estimated hydrogen energy usage in 2035 and 2050, divided and compared according to different industries (left) and regions (right). It is worth noting that the report pointed out that the demand for hydrogen energy is closely related to the situation of carbon reduction, and the situation of carbon reduction is mainly determined by the town government's policies, technology, and social preferences.

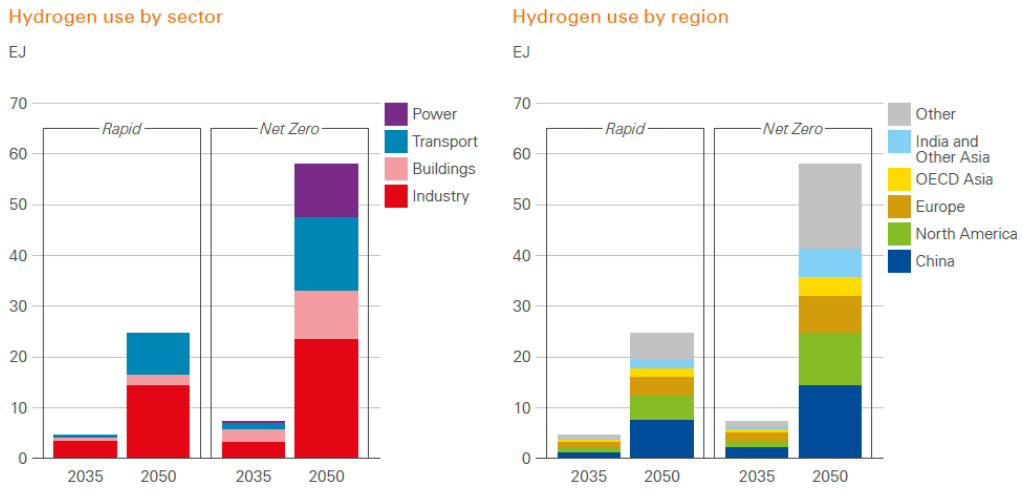

Figure 1.1: Hydrogen plays an increasing role as the world is transiting to a low-carbon energy system [11]

As with most technologies, the initial development and deployment phases of fuel cell technology is heavily dependent on government policies and incentives. From 2019 to 2020, many countries and regions have successively

introduced practical hydrogen energy strategies and hydrogen energy development road maps. Some countries and regions have made specific deployments for the application of hydrogen energy technology, mainly focusing on the application of hydrogen energy in the field of transportation, and have proposed hydrogen energy development goals in industry, construction, power generation, etc. (see Table 1.1).

As a new energy carrier, hydrogen still needs technical improvement of production, transportation, storage and end-applications [12]. The following Figure 1.2 illustrates the key information about the hydrogen energy supply chain, and the purple arrow shows the route of "From hydrogen to fuel cell electric vehicle (FCEV) ".

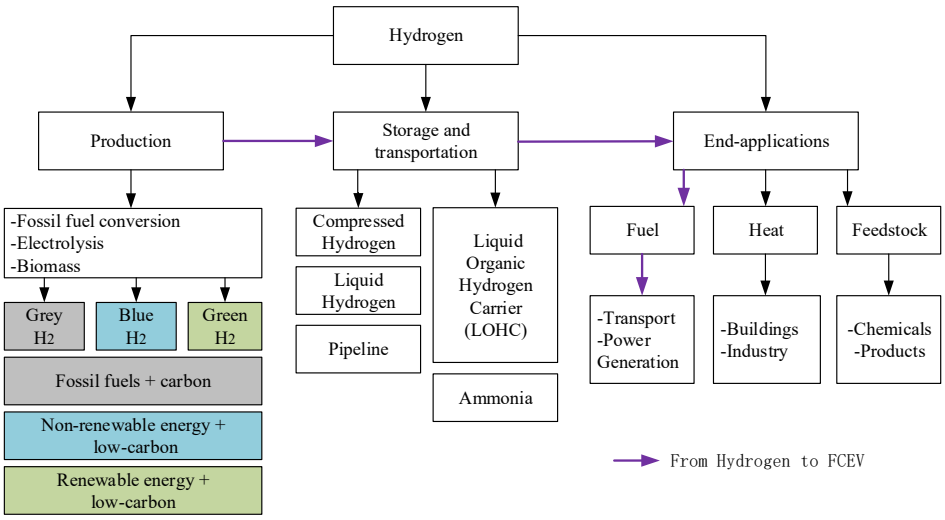

Figure 1.2: From hydrogen to fuel cell electric vehicle [original]

However, there are still obstacles to the large-scale and widespread use of hydrogen energy. Firstly, the cost of hydrogen production is still high compared to ordinary fossil fuels. Secondly, hydrogen, as the least dense gas, depends on high pressure conditions for storage and transportation at room temperature. Finally, the explosion limit of hydrogen is 4.0% to 75.6%, and it is difficult to guarantee the safety performance of hydrogen in a sealed environment, etc [13]. These unfavorable factors restrict the use and development of hydrogen energy, so it is necessary to solve these problems in order to realize the commercial use of hydrogen energy as soon as possible. Next, one of the important end-application for the use of hydrogen, the fuel cell electric vehicle, will be described in detail.

Table 1.1: Hydrogen energy development policies in different countries and regions

COUNTRY	POLICY	YEAR	DEPARTMENT
Germany	The National Hydrogen Strategy[a]	2020	Federal Ministry of Transport and Digital Infrastructure
European Union	A Hydrogen Strategy for A Climate-neutral Europe [b]	2020	European Commission
United States	Hydrogen Program Plan [c]	2020	U.S. Department of Energy
Japan	Strategy for Developing Hydrogen and Fuel-Cell Technologies [d]	2019	Ministry of Economy, TradE and Industry
South Korea	Korea Hydrogen Economy Roadmap[e]	2019	The Korean Governments
People's Republic Of China	New Energy Automobile Industry Development Plan (2021-2035) [f]	2020	The State Council of PR China

[a]https://www.bmwi.de
[b]https://ec.europa.eu
[c]https://www.hydrogen.energy.gov
[d]https://www.meti.go.jp
[e]https://www.iea.org
[f]http://www.gov.cn/zhengce/content

1.2 Fuelcells and Fuel cell electric vehicle

1.2.1 Fuel cells

In the first section, an important conversion path of hydrogen energy is mentioned, the conversion of hydrogen energy into electric energy through fuel cells. In 1839, William Grove [1] of the United Kingdom first discovered the power generation phenomenon of the reverse reaction of the hydrolysis process, the concept of fuel cells. From then on more than 100 years later, the Francis T. Bacon [2] brought fuel cells out of the laboratory and used them in people's production activities. In the 1960s, fuel cells were successfully applied to space vehicles and gradually developed to ground applications. Following thermal power generation and nuclear power generation, fuel cell power generation technology has attracted attention from all over the world for its high efficiency, low emissions, light weight, no pollution, and fuel diversification.

Commonly used ordinary batteries include alkaline dry batteries, lead-acid batteries, nickel-hydrogen batteries and lithium-ion batteries. Compared to ordinary batteries, fuel cells are both similar and quite different. They have similar power generation principles, and both have electrolytes, electrodes, positive and negative connection terminals in structure. The difference between the two is that the fuel cell is not a device that stores electrical energy, but is actually a power generation device. The chemical fuel is not stored inside the battery, but is supplied from the outside. In a fuel cell, the reactant fuel and oxidant can be continuously supplied to the electrode. As long as the electrode is separated in the electrolyte, the reaction product can be continuously discharged from the battery, at the same time, the corresponding continuous output of electrical energy and heat energy. It facilitates the replenishment of fuel, so that the battery can work for a long time or even without interruption. The reason why people call it a fuel cell is just because it is similar in structure to a battery: its external characteristics are like a battery, and as the load increases, its output voltage drops [14].

In fuel cells, power and energy are decoupled and can be independently tuned, that is for a fixed fuel cell stack more hydrogen allows higher energy capacity without changing the fuel cell size or power. Like batteries, fuel cells have advantages over combustion engines: they have no moving parts, are quiet, and require no oil changes and minimal maintenance. Fuel cells are also easily scalable, as individual cells can be stacked together to provide a wide range of power. They can range in size from less than a watt for portable

[1] William Robert Grove (1811 -1896)
[2] Francis Thomas Bacon (1904-1992)

power, to many megawatts for large-scale stationary power.

The fuel cell is actually a chemical reactor, which directly converts the chemical energy of the fuel and the oxidant into electrical energy. It does not have the prime mover on the traditional power generation device to drive the power generation device, and there is no direct combustion process. Fuel and oxidizer are continuously input from the outside, and it can continuously output electrical energy. Fuel cells can be more efficient than internal combustion engines, because the electrochemical reactions in a fuel cell generate electricity directly—while combustion has to convert the energy in the fuel first into mechanical energy and then into electrical energy. Fuel cell efficiencies of over 60% have been demonstrated, and over 80% efficiency is possible when fuel cells are used in combined heat and power applications [15].

A fuel cell uses the chemical energy of fuels such as natural or synthetic gas and hydrogen to produce electricity and thermal energy, and its by-products are generally harmless water and carbon dioxide. The operation of the fuel cell does not only rely on the battery itself, but also requires subsystems such as fuel and oxidant supply and reaction product discharge, in order to form a complete fuel cell system with the battery stack. Fuel cells can use a variety of fuels, including hydrogen, carbon, carbon monoxide, and lighter hydrocarbons. The oxidant usually uses pure oxygen or air. Its basic principle is equivalent to the reverse reaction of electrolysis, that is, the synthesis reaction of water. The fuel and oxidant are ionized into ions on the cathode and anode of the battery with the help of the catalyst. Since the ions can migrate between the electrodes through the electrolyte between the two electrodes, a voltage is formed between the cathode and anode electrodes. When the electrodes are included in a loop with an external load, it can supply power (generation). If fuel cells use hydrogen fuel directly, water is the only byproduct emitted, there is no carbon dioxide and no pollutants such as NO_x [16].

According to the type of electrolyte used, fuel cells can be divided into the following categories [17] :

- Alkaline Fuel Cell, AFC
- Proton Exchange Membrane Fuel Cell, PEMFC
- Phosphoric Acid Fuel Cell, PAFC
- Molten Carbonate Fuel Cell, MCFC
- Solid Oxide Fuel Cell, SOFC
- Direct Methanol Fuel Cell, DMFC

Figure 1.3 is a diagram of the operating principle of all fuel cells. The structure and performance of presented fuel cells are summarized in Table 1.2 [18].

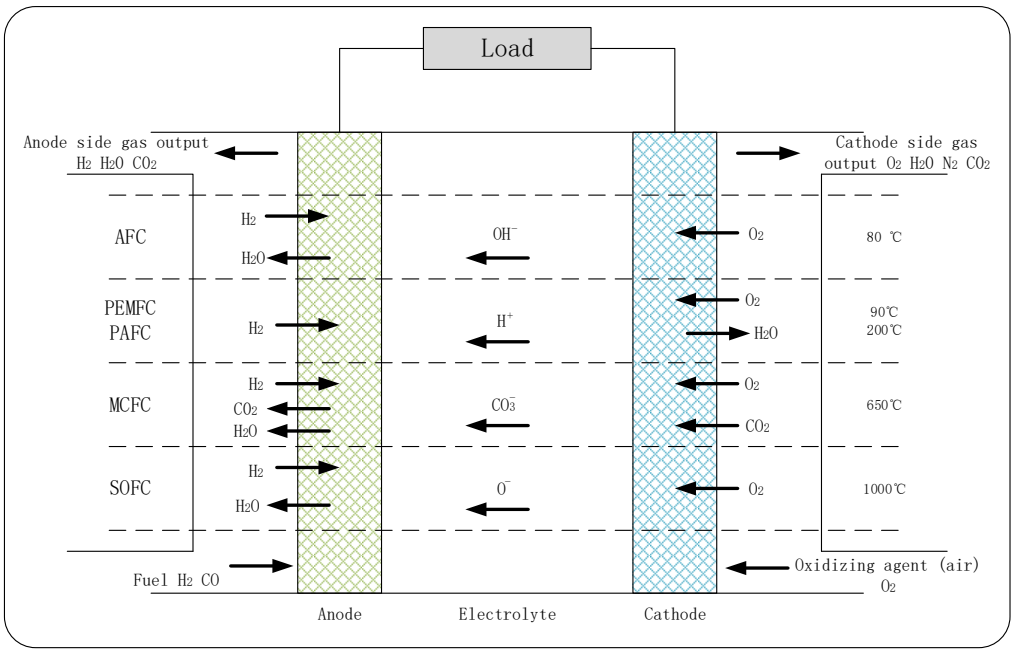

Figure 1.3: Schematic representation of fuel cells [original]

Among them, the DMFC, which is still in the development stage, uses perfluorosulfonic acid membrane as the electrolyte, and the working temperature is from room temperature to 200°C, which is used for micro mobile power [19].

Table 1.2: Structure and performance of different fuel cell types

TYPE	**AFC**	**PEMFC**	**PAFC**	**MCFC**	**SOFC**
Electrolyte	$NaOH$	Ion Exchange Membrane	phosphoric acid	Alkali Carbonates	Zirconia
Fuel	H_2	H_2	H_2 *and* CO	H_2 *and* CO	H_2 *and* CO
Oxidant	O_2	Air	Air	Air	Air
Cell Hardware	Polymer	Carbon or Metal based	Graphite based	Stainless Steel	Ceramic
Catalyst	Platinum	Platinum	Platinum	Nickel	Perovskites
Operation T	$60-90°C$	$20-100°C$	$150-200°C$	$600-700°C$	$650-1000°C$
System Output		$<250kW$	$50kW-1MW$	$<1MW$	$5kW-3MW$
Efficiency	60-65%	50-60%	36-42%	45-60%	60%
Applications	Aerospace	Backup portable power, small DG_1 and transportation	DG	Electric utility and Large DG	Auxiliary power, Electric utility and Large DG

The PEMFC is especially suitable for use in vehicles because of the low operating temperature (between 20°C and 100°C), the high power density and the fast start-up. The PEMFC consists of the thin, proton-conducting polymer membrane, between two catalytically active electrodes (Anode and Cathode) and gas diffusion layers is embedded. Hydrogen is supplied to the anode and atmospheric oxygen to the cathode. Hydrogen is oxidized to protons on the anode side, releasing two electrons, which diffuse through the membrane. At the cathode, oxygen is reduced with the electrons that were conducted from the anode to the cathode via an external circuit with an electrical consumer and reacts with the protons to from water [21]. The principle of fuel cell is presented in Figure 1.4. The chemistry of PEMFC is expressed by the equations 1.1 and 1.2.

At the anode:

$$H_2 = 2H^+ + 2e \tag{1.1}$$

At the cathode:

$$\frac{1}{2}\, O_2 + 2H^+ + 2e = H_2O \tag{1.2}$$

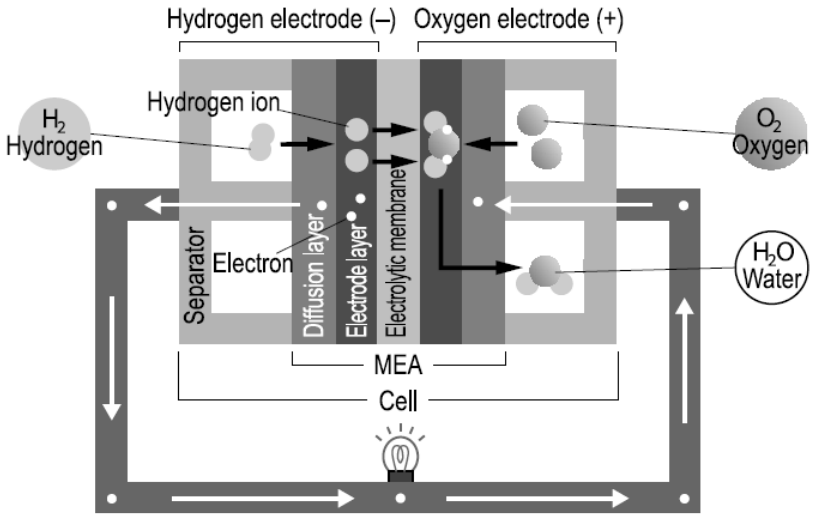

Figure 1.4: Schematic of the PEMFC fuel cell operation principle [22]

The theoretical open circuit voltage of the PEMFC is 1.23V, corresponding to the difference between the electrode potentials of oxygen and hydrogen. In

practical applications, the voltage of the fuel cell is affected by various factors that will produce voltage loss. The three main fuel cell loss mechanisms: activation, ohmic and concentration, all influence fuel cell performance in terms of voltage drop or load regulation as illustrated in Figure 1.5, showing measured polarization and power density curves with load current density variation for a PEMFC. It can be seen that, similar to solar cells, there is a maximum power point for an individual fuel cell, which also opens up the possibility of certain control algorithms, such as Maximum PowerPoint Tracking (MPPT) [23].

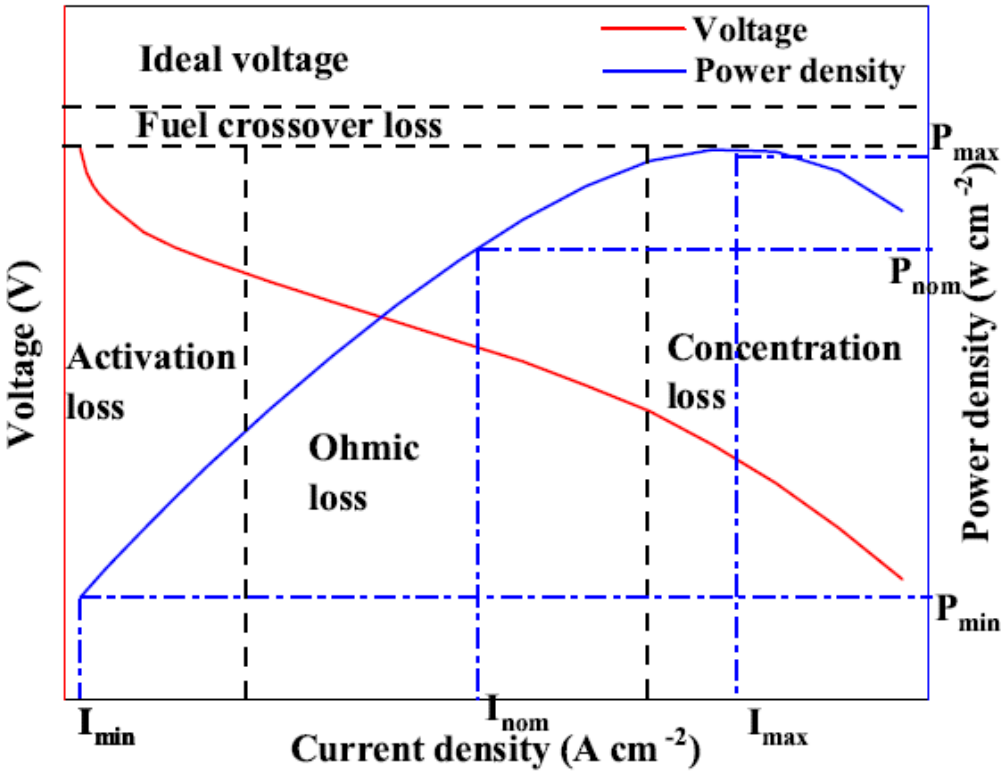

Figure 1.5: Polarization curve and corresponding power curve of PEMFC [14]

Normally, the rated operating voltage of an individual PEMFC is set between 0.4—0.9V and current values range is from 0.5—1.0A/cm^2 after losses. In practical applications, in order to reduce the currents required to deliver high power, hundreds of individual fuel cells are often connected in series (fuel cell stack), as shown in Figure 1.6.

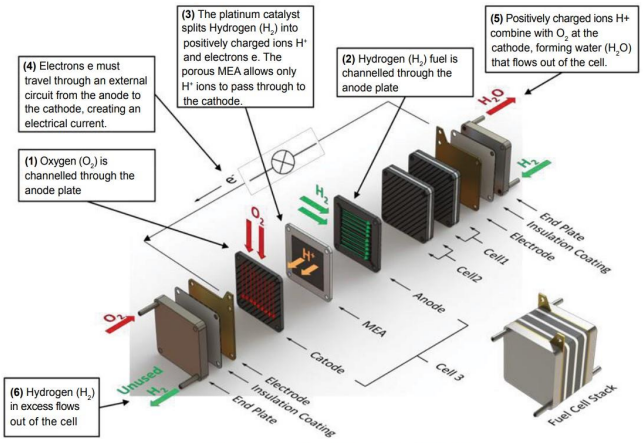

Figure 1.6: Schematics of a fuel cell stack operation and components [24]

Therefore, the output characteristics of the fuel cell stack are similar to the individual fuel cell. For example, Figure 1.7 illustrates the output characteristic curve of a PEMFC stack (NEDSTACK FCS 7-XXL), which is produced by company "Nedstack Fuel Cell Technology BV", with rated power 6.8kW @ 230A and 29.5V.

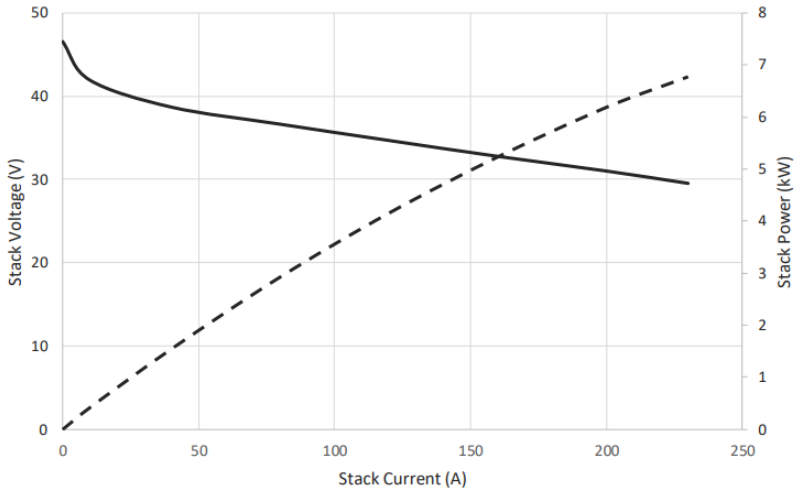

Current (A)	0	40	80	120	160	200	230
Stack Voltage (V)	46.6	38.7	36.6	34.7	32.7	31.0	29.5
Stack Power (kW)	0.0	1.5	2.9	4.2	5.2	6.2	6.8

Figure 1.7: The output characteristic curve of a PEMFC stack (NEDSTACK FCS 7-XXL) [25]

1.2.2 Fuel cell vehicles

In terminal applications, the transportation industry is an important development area for hydrogen energy and fuel cells [26, 27]. According to the statistics from the International Energy Agency (IEA), as of 2020, there are 34,800 fuel cell electric vehicles and 540 hydrogen refueling stations (HRS) in the world. Their distribution is shown in the Figure 1.8 below,

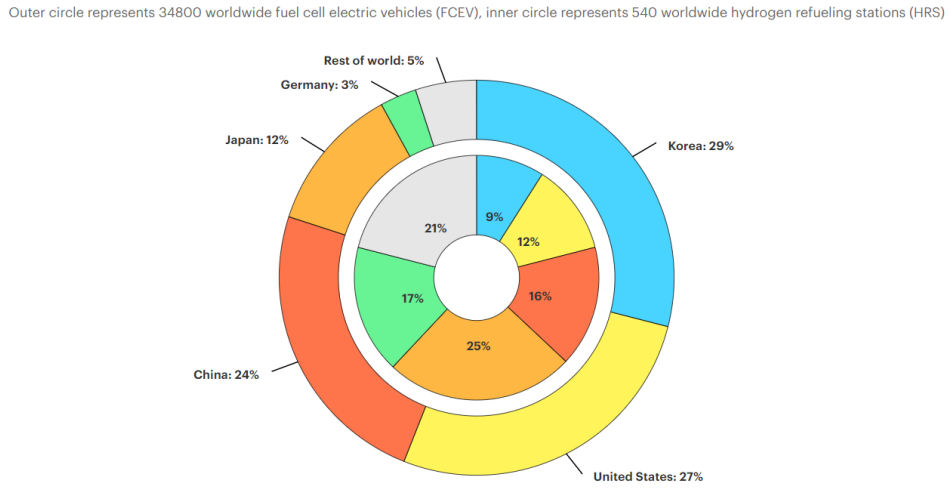

Figure 1.8: Fuel cell vehicles and hydrogen refueling station stock by region, 2020 [28]

Figure 1.9 shows the mode and distribution by region of fuel cell electric vehicles. Almost all fuel cell buses (93% of 5,648) and trucks (99% of 3,175) held by China. The mode of fuel cell electric vehicles in other regions is light-duty passenger vehicle, among them, 38% in South Korea, 35% in the United States, 15% in Japan and 4% in Germany. In 2020, a total of 9006 hydrogen fuel cell vehicles were globally sold, a year-by-year decrease of 9.1%. Among them, sales in the United States and China were slashed to 937 units (a decrease of 55% year-by-year) and 1,177 units (a decrease of 57% year-by-year). Thanks to strong government subsidies, South Korea's annual sales of hydrogen vehicles reached 5823 units (+39% year-by-year), contributing 65% of global sales that year. The sales of hydrogen vehicles in Japan and Germany were relatively moderate, with 761 and 308 respectively sold.

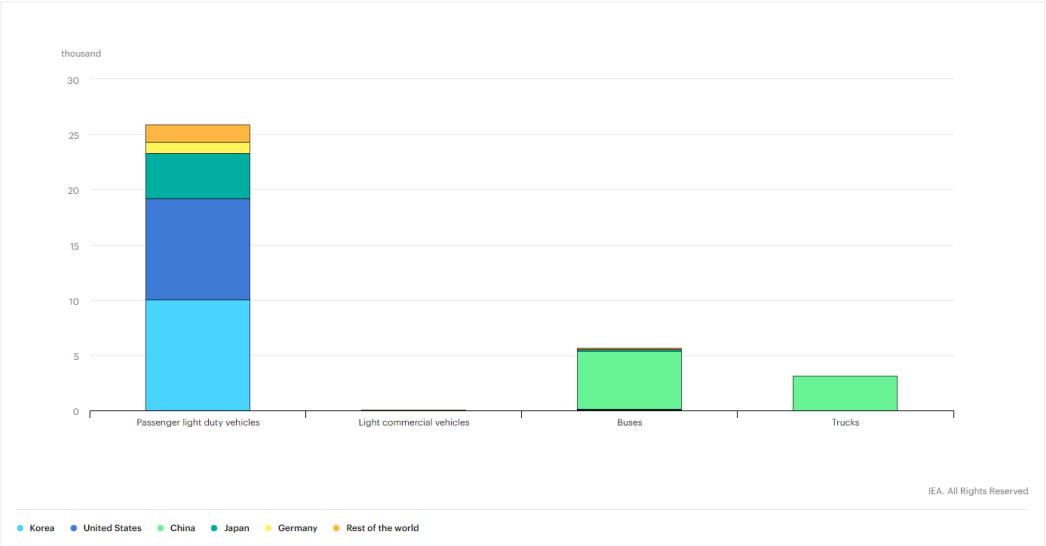

Figure 1.9: Fuel cell electric vehicles stock by region and by mode, 2020 [28]

Overall, compared to 2019, the number of fuel cell electric vehicles worldwide has increased by 38%, and the number of hydrogen refueling stations has increased by 108(25%). Various countries and regions have also increased their investment and policy support for the research of fuel cell electric vehicles, such as the European Union's project-Small 4 Wheel fuel cell passenger vehicle Applications in Regional and Municipal transportation transport (SWARM).

The SWARM project is establishing a large demonstration fleet of small passenger vehicles, at the same time building on and expanding existing European hydrogen refueling infrastructure. Three regions will be participating in this effort: the British Midlands and Wales (Birmingham, Coventry, and Abergavenny) , Brussels and the Wallonia region (Liège), and North Western Germany (Wilhelmshaven) and the Cologne area (Frenchmen).

The vehicles employed are three different types of low-cost, high fuel-efficiency, light-weight passenger cars specifically designed for cities and regional transport (Figure 1.10). The organizations Riversimple (Llandrindod Wells, Wales, UK), MicroCab (Coventry, UK) and Jade University (Wilhelmshaven, Germany) will contribute a sum of approx. 20 vehicles. These will be built during the project phase alongside the implementation of the hydrogen supply infrastructure. Europe-wide certification will be sought for both, vehicles and hydrogen installations in order to allow their use throughout Europe, thus increasing the commercial possibilities and continuing the project without further funding [30].

Figure 1.10: Vehicles rebuilt in the SWARM project: MicroCab, Elano e-mobile and Riversimple (From left to right) [29]

At Jade University Elano e-mobiles will be rebuilt. These small vehicles took already part in the German program "Electro-Mobility Regions" within the region North-West (Bremen-Oldenburg), where a fleet of 15 battery-electric vehicles is established. Based on these vehicles, in context of the project SWARM, battery-fuel cell hybrids called elano-FC will be developed.

One of the tasks of the Jade University is the integration of the fuel cell system into the electric powertrain of the Elano e-mobiles and the optimization of the powertrain for these vehicles. To check the different concepts and control variations, a test bench is constructed on which the powertrain can be loaded with real driving cycles. The research leading to these results has received funding from the European Union's Seventh Framework Programme (FP7/2007-2013) for the Fuel Cells and Hydrogen Joint Technology Initiative under grant agreement no 303485 [31–34].

1.2.3 Powertrain of fuel cell electric vehicles

The energy direct flow of a typical battery electric vehicle is shown in Figure 1.11. The battery pack obtains energy from the grid and stores it, and then converts it into mechanical energy by the electric motor through a power control unit (PCU), and during driving, the battery pack can recover the braking energy to extend the range. When the integration of the fuel cell system is completed, the energy flow of the fuel cell electric vehicle is shown in Figure 1.12. At this time, there are three ways to flow energy:

- The energy flow direct of a fuel cell electric vehicle is similar to that of a BEV, from power grid to battery back that drive the electric motor. Only the size of the battery capacity will be different.

- Electricity (as a direct current) from the fuel cell can either be sent to the power inverter to create alternating current to drive the vehicle's electric motor, or to the battery to charge it. Depending on whether the

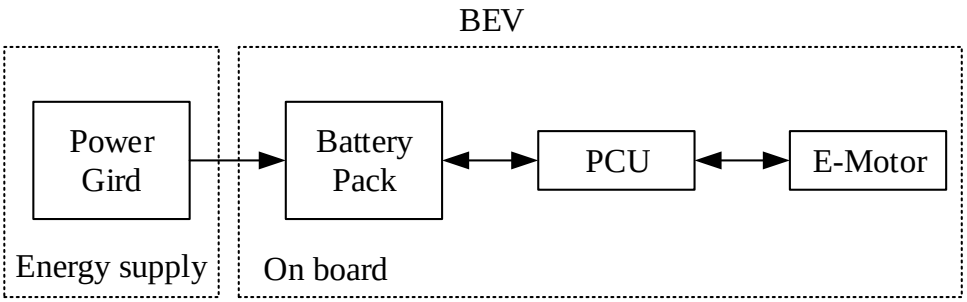

Figure 1.11: The energy flow direction of a battery electric vehicle [original]

battery is able to draw energy from the grid, fuel cell electric vehicle can be divided into hybrid and plug-in modes.

- Braking energy is recovered and stored in the battery pack.

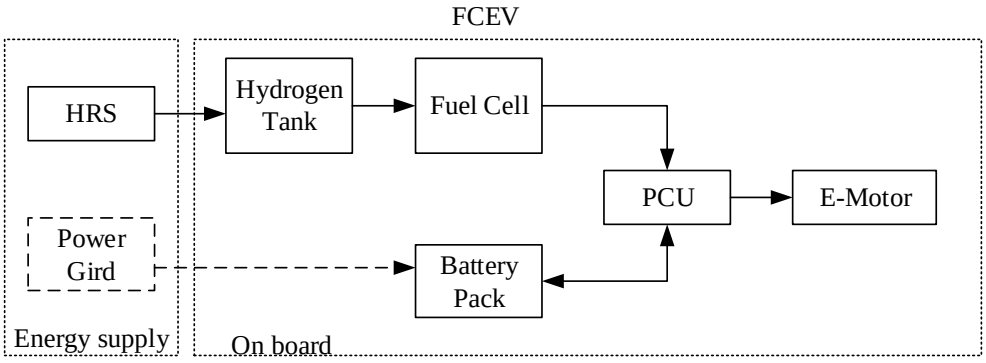

Figure 1.12: The energy flow direction of a fuel cell electric vehicle [original]

The key part of fuel cell vehicle is the powertrain, which indicates the style of the vehicle and has much more influences on vehicle performances, such as operation efficiency, fuel economy and so on. The simplest powertrain of fuel cell vehicle only uses the fuel cell power for the vehicle propulsion, but this powertrain has no regenerative energy recovery in braking. Due to the complexity of fuel cell and auxiliary system management, long start-up times and poor transient response, a fuel cell hybrid powertrain can be one of the solutions to overcome these drawbacks. In a typical powertrain with a fuel cell

system, a DC/DC converter and an energy storage device (battery packs or super capacitors) are necessary for the following reasons:

- Fuel cell stacks typically provide current at low voltage, which are not easy to exploit on electric vehicle powertrains. Additionally, fuel cells also exhibit a non-linear performance characteristic that can significantly influence vehicle drive system operation and component optimization and which has to be considered at the system design stage. Therefore, the control of fuel cell power necessitates power electronic conditioning via systems that consist mainly of DC/DC conversion, the design of which is crucial to the vehicle since the DC/DC converter performance directly influences the fuel cell lifetime.

- The operation of vehicles is not a steady state situation. Due to frequent start-up, acceleration, hill climbing and braking, the dynamic conditions of the vehicles are very complicated. For the high energy density, bad dynamic response, long starting time of fuel cell stack, the hybrid system becomes a solution with smaller fuel cell stack and high-power secondary sources. For this reason, in the powertrain of fuel cell vehicles energy storage must be connected in parallel to the fuel cell system. For example, FCX from Honda uses fuel cell stack and ultra capacitor, TUCSON FCEV from HYUNDAI uses fuel cell and LiPb or NiMH battery pack.

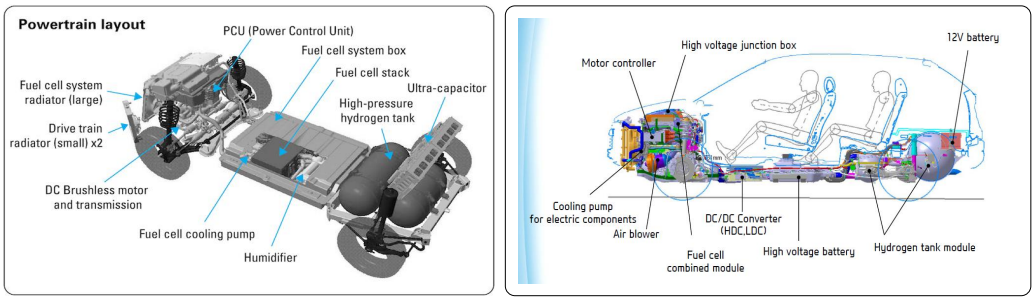

Figure 1.13: Powertrain of FCX from Honda (left) [35] and TUCSON from HYUNDAI (right) [36]

In powertrain of fuel cell electric vehicle, the fuel cell system and energy storage are generally interconnected via DC/DC converter. Depending on the location of the DC/DC converter in powertrain, the fuel cell hybrid powertrain has the following two typical configurations.

As shown in Figure 1.14, in configuration I, a bi-directional DC/DC converter is inserted between the DC bus and the battery. The fuel cell system is

directly connected to the electrical machine via the DC bus. This bidirectional DC/DC converter should have a fast dynamic response, because the energy transmission direction of the battery or double-layer capacitor is controlled by it, according to the requirements of the actual situation The DC/DC converter transfers energy to the DC bus, or charge the energy storage in braking recovery phase [32]. The advantage of this powertrain is that the bi-directional converter is only responsible for converting the energy flowing into or out of the battery pack, which is usually relatively small and of variable duration, such as the peak power required from the battery pack for acceleration of the electric motor, or the braking recovery energy stored in the battery pack. In this way, the energy loss in the DC/DC converter is relatively low. For example, this is the powertrain used in Hyundai's NEXO fuel cell electric vehicle.

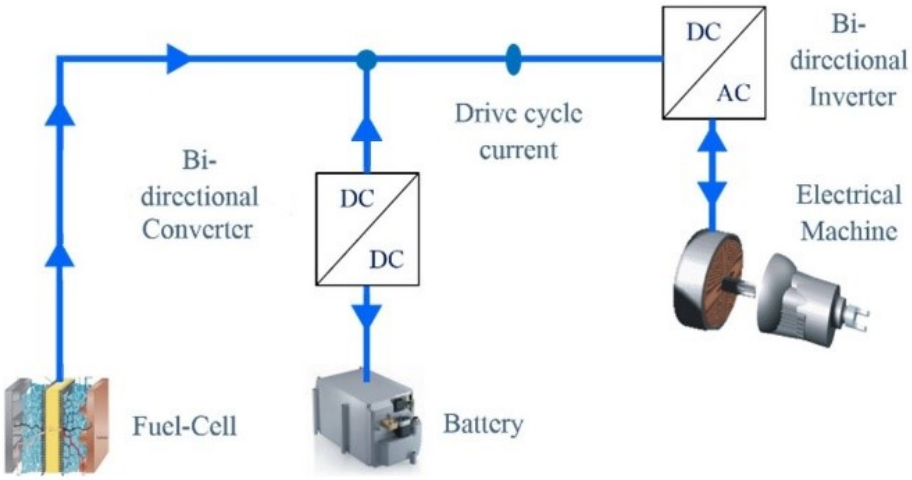

Figure 1.14: Configuration I of hybrid powertrain in fuel cell vehicle [32]

As shown in Figure 1.15, in configuration II, a unidirectional DC/DC converter is inserted between the fuel cell system and the DC bus. The battery is connected to the DC bus directly. This unidirectional DC/DC converter directly controls the energy output of the fuel cell systems, thus the control strategy of this converter needs to match the poor dynamic response of the fuel cell system [32]. The advantage of this powertrain is that the unidirectional DC/DC converter can boost the voltage of the fuel cell, and the high voltage of the bus means less current at the same power, which can reduce the cross-sectional area of the wiring harness and also reduce the power loss. However, because of the continuous operation of the DC/DC converter, the

energy loss caused by it will be higher. For example, the FCEV of Toyota's Mirai and Honda's Clarity are using this configuration.

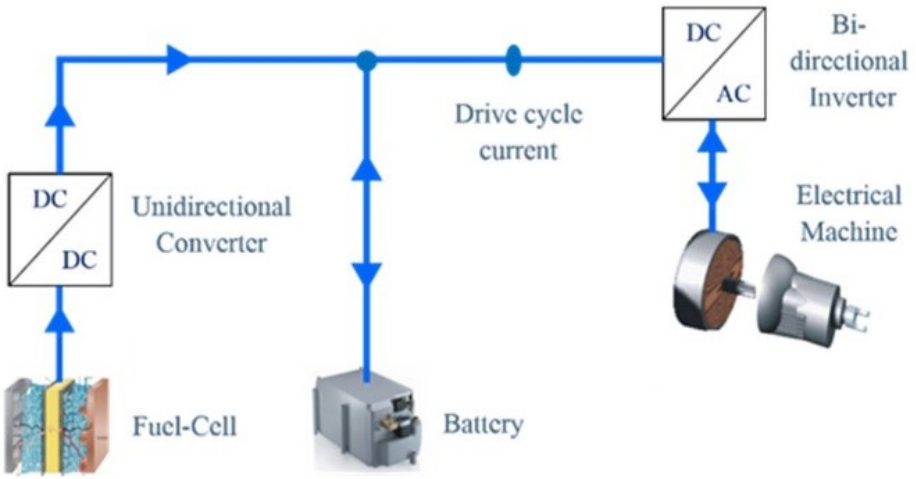

Figure 1.15: Configuration II of hybrid powertrain in fuel cell vehicle [32]

In addition, there is another structure of fuel cell electric vehicle that combines the above two configurations, where there is a unidirectional DC/DC between the fuel cell system and the DC bus, while a bidirectional DC/DC converter is placed between the battery pack and the DC bus, but this structure is rarely used in practice because of its overly complex controls [37].

As of 2021, there are three main types of fuel cell electric vehicles on the market, namely NEXO by HYUNDAI, Mirai by TOYOTA and Clarity by Honda. Table 1.3 compares the main features of 3 type FCEVs.

Table 1.3: Comparison of the features of the newest fuel cell passenger vehicles on the market (in 2021)

Parameters	**Unit**	**NEXO**	**Mirai II**	**Clarity**
Driving range	km	800	650	580
H_2 storage capacity	kg	6.33	5.6	5.0
Power of fuel cell stack	kW	95	128	103
Power of E-motor	kW	120	135	130
Battery capacity	kWh	1.56	1.24	N/A
Converters used	N/A	buck-boost converter	4 phases boost converter	N/A

1.3 Conclusions

This chapter describes the road map about "from hydrogen energy to fuel cell electric vehicle". According to the structure of this chapter, it can be summarized as follows:

- The importance of hydrogen energy for the global carbon reduction is first introduced. As a carrier of energy, hydrogen has many excellent characteristics such as cleanliness and high combustion calorific value, etc. Therefore, various countries and regions have formulated relevant policies and strategies to promote the development and use of hydrogen energy in the future.

- Although hydrogen has many advantages as an energy carrier, the cost of production, storage, transportation, and end-applications of hydrogen is higher than other similar products, so the main direction of future research is to optimize the efficiency of hydrogen energy and reduce the production cost in the industry chain.

- In terms of hydrogen energy conversion, fuel cells have unique advantages. They can efficiently convert hydrogen energy into electricity in various industries and applications without generating additional pollution. The construction and operating principles of individual PEMFC and PEMFC stacks used in practice are described in detail, and because of low-temperature operating environment of PEMFC, it is particularly suitable for use in the transportation, so that fuel cell electric vehicles

have been receiving attention as the application terminal of hydrogen energy.

- The development of fuel cell electric vehicles and hydrogen refueling stations around the world in recent years is presented, as well as the project SWARM, which is related to this thesis.

- The powertrains of fuel cell electric vehicle are introduced, when considering the output characteristics of the fuel cell and the characteristics of electric vehicle operation, energy storage units and a DC/DC converter are commonly used in powertrains.

Therefore, optimizing the DC/DC converters in fuel cell electric vehicle plays an important role in improving the overall efficiency of the fuel cell electric vehicle and prolonging the service life of the fuel cell.

Chapter 2.

Electronic Switch to Control the Powertrain of FCEV

2.1 Introduction

In Chapter 1, the powertrains of two commonly used fuel cell vehicles are described. In these two powertrains, a DC/DC converter is indispensable. The use of DC/DC converters allows active conversion of the voltage difference between the fuel cell and the DC bus voltage, but it also brings the following disadvantages:

- the DC/DC converter inevitably causes energy loss, which reduces the efficiency of the entire system.
- the control system of DC/DC converters in FCEV is more complicated.
- EMI problems due to high-frequency switching operation of DC/DC converter in FCEV.

This chapter presents a novel concept to control the powertrain in battery fuel cell hybrid vehicles. Instead of a DC/DC converter, a simple power electronic switch is connected between the battery and the fuel cell system. For this, the electronic switch has to work in linear operation for several seconds during the switch-on and switch-off process [31, 38, 39]. Because of the extreme switching loads, several semiconductors are connected in parallel and the individual currents are measured and balanced by a microprocessor control circuit.

After modification of Elano e-mobiles to elanoFC vehicles, the previous battery will continue to be used in the powertrain. In addition, the built-in battery charger in the vehicle should be kept so that the fuel cell system can be used as range extender. Instead of the DC/DC converter only a power electronic switch will be used, which can interconnect the battery and the fuel cell system together if necessary.

In this so-called "passive hybrid system" the switching process and the hydrogen supply must be coordinated with the electrical power change of the fuel cell system to prevent inadmissible operating conditions. This means that during switching operation the electronic power switch has to work in linear operation for several seconds. Furthermore, at the passive hybrid system, the voltages of the fuel cell system and the battery must be matched [31].

The selected fuel cell system Hydrogenics HYDM HD8-200 has a nominal power $P_N = 8.5\text{kW}$ and the open circuit voltage $U_O = 80\text{V}$. On the right in Figure 2.1 is shown the dependency between the principal fuel cell voltage and the output current. With increasing load, the voltage at the fuel cell system first drops very quickly and then the voltage only slightly decrease. At the nominal power which corresponds to a current of approx. $I_N = 170\text{A}$, only a fuel cell system voltage of $U_N = 50\text{V}$ is at the output. The battery voltage must be selected in such way that this voltage is reached when the battery is completely discharged.

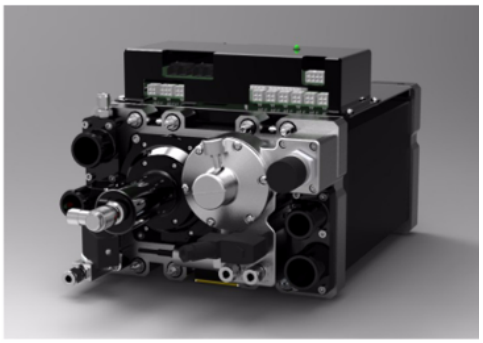

(a) Fuel cell stack system HYDM HD8-200

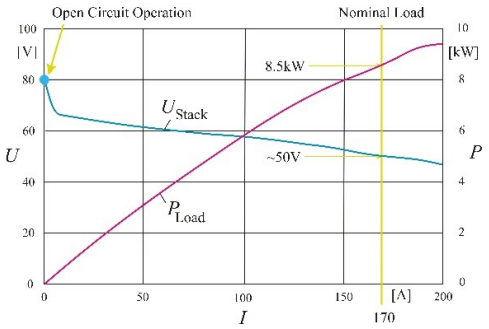

(b) Dependency between the output voltage and current of fuel cell stack

Figure 2.1: Selected fuel cell system of "passive hybrid system" [31]

The buffer battery in the fuel cell electric vehicle powertrain inherits the original battery pack. In the elano electric vehicle [31], the battery pack is divided into two parts and placed under the seat. It consists of 32 lithium iron phosphate batteries. The connection method is that two batteries are connected in parallel to form a unit, a total of 16 units are connected in series,

in Figure 2.2. In this way, the operating voltage range of this battery pack is between 40V and 58.4V. The main parameters of the fuel cell system and the battery pack are summarized in Tables 2.1 and 2.2 respectively.

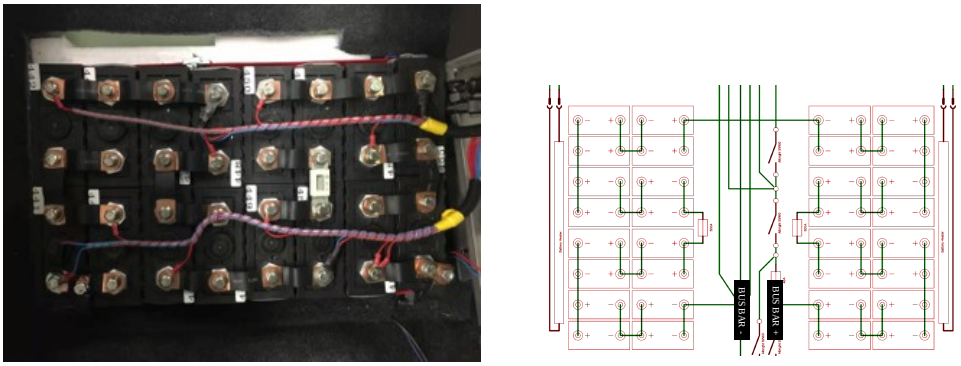

(a) One part of Battery pack (b) Schematic of battery pack

Figure 2.2: Selected battery pack of "passive hybrid system" [original]

Table 2.1: Characteristics of using fuel cell stack in powertrain

PROPERTY	UNIT	VALUE
Product Information		
Fuel Cell Model Number		HyPM HD8
Performance		
Rated Electrical Power	kW	8.5
Maximum Electrical Overload		None permitted
Operating Current	A_{dc}	0 *to* 200
Operating Voltage	V_{dc}	40 *to* 80
Time from Off to Rated Power	s	< 35

The powertrain of a battery-fuel cell hybrid vehicle is shown in Figure 2.3. The drive inverter with the electric machine is directly connected with the battery. At the output of the fuel cell, a diode is connected to prevent reverse energy flow and thus an inadmissible operation of the fuel cell system. In addition, an electronic switch is shown, which operates partly in linear operation mode, so that the fuel cell can be interconnected with the battery slowly over a defined period of time. When the electronic switch is fully switched on, an operating point sets itself automatically. Optionally, an additional mechanical

switch can be used, to reduce the losses in the switched-on state. In the realized concept the mechanical switch is not used because the switched-on state losses are very small [31].

Table 2.2: Characteristics of using battery pack in powertrain

PROPERTY	UNIT	VALUE
Product Information		
Model		A lithium iron phosphate battery pack
Performance		
Cell Number		32(2 Cells in parallel, 16 groups in series)
Nominal Capacity	A_h	3200
Nominal Voltage	V_{dc}	51.2
Operating Voltage	V_{dc}	40 *to* 58.4
SOC Usage Window		$10\% \sim 90\%$

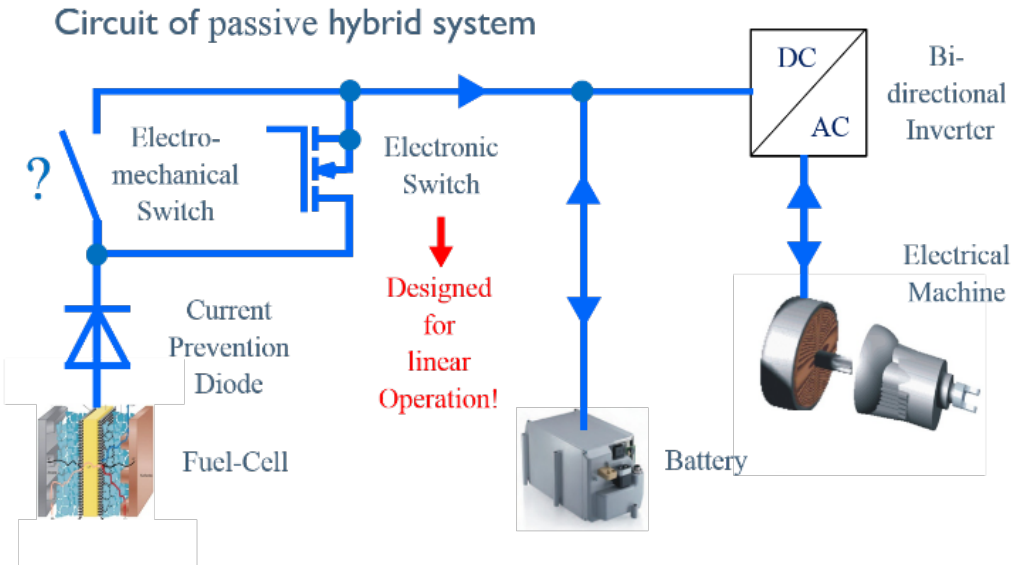

Figure 2.3: Powertrain diagram of passive hybrid system [31]

2.2 Design and implementation of electronic switch in FCEV

2.2.1 Hardware design and implementations of electronic switch

In the application of this chapter, in order to optimize the operation of the fuel cell, the following strategies are adopted. An electronic switch composed of power MOSFETs is connected in series between the fuel cell output anode and the DC bus. During startup and shutdown, the MOSFET is controlled to operate linearly in the saturation region, so that the fuel cell output current is slowly increased or decreased to the desired operating point, and then the fuel cell and the battery pack are directly connected or completely disconnected. During normal operation, the output power of the fuel cell is determined by the bus voltage. As shown in the Figure 2.4, in the developed circuit, the electronic switch is connected in parallel by six MOSFETs, and the current in a single MOSFET is measured and controlled by the microprocessor circuit during operation.

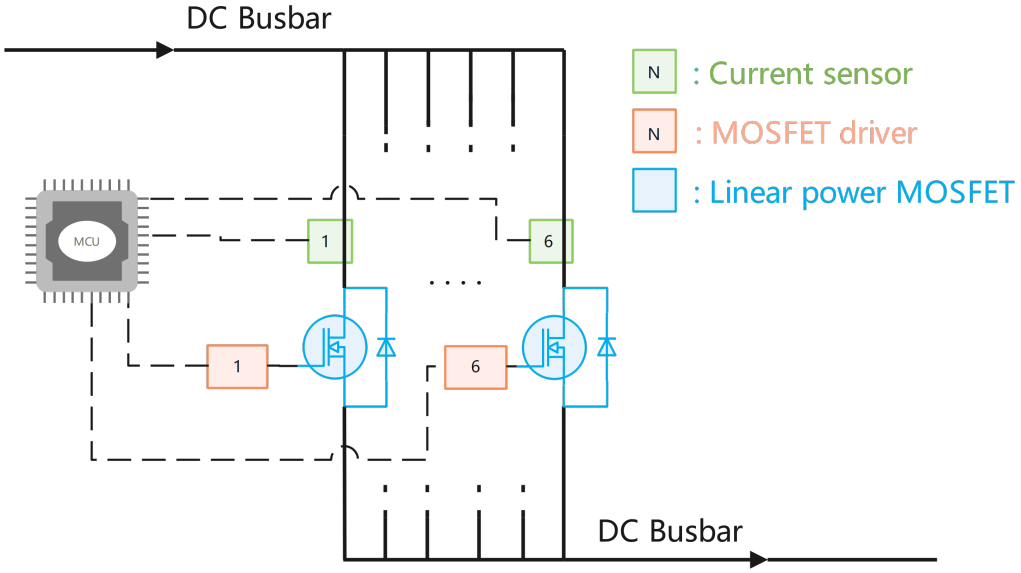

Figure 2.4: Design schematic of E-switch [original]

The Figure 2.5 shows the range of oo operating stages of the fuel cell. In the first stage, the operating point of the fuel cell is actively controlled by controlling the current of the electronic switch. At this time, the electronic

switch can be regarded as an adjustable resistor or current regulator. In the second stage, the electronic switch is fully turned on, and the fuel cell operating point is controlled by the DC bus voltage.

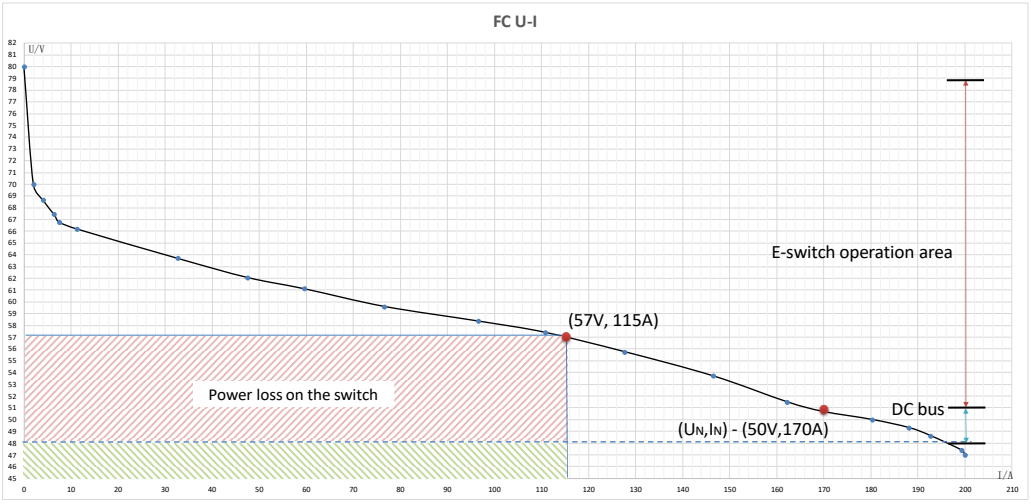

Figure 2.5: Curves of power loss, efficiency of hard switching and proposed converter [original]

When power MOSFETs are utilized in linear-mode operation, as opposed to their conventional switch-mode one, they are required to endure substantially high thermal and electrical stresses due to the simultaneous occurrence of high drain-source voltages and currents. These extreme stresses can cause typical devices to fail. In order to ensure that all semiconductors are functioning during the switching process in their Safe Operating Area (SOA), six power MOSFETs will be operated in parallel to reduce the current stress of a single MOSFET, and in this E-switch, linear MOSFETs (IXTN200N10L2) are used. Compared to the ordinary MOSFETs, the linear MOSFETs have the following differences and characteristics.

Characteristics of linear MOSFET

In order to reduce the conduction and switching losses of the power MOSFET, the traditional planar MOSFET is developed into a modern trench MOSFET. The trench technology makes the conduction loss of the same chip area smaller, and the transconductance characteristic is also steeper, which makes the switching speed faster. However, modern trench MOSFET also have limitations, one of the important features being the narrower SOA, so that modern trench MOSFETs are unsuitable for some applications, such as DC dynamic

loads for testing power supplies, batteries, fuel cells, etc. or high voltage, high current constant current sources [40, 41]. One solution to this is to use linear MOSFETs in these applications, and some linear MOSFETs offer the advantages of both the wide SOA of planar MOSFETs and the lowest drain-source on resistance ($R_{ds}(on)$) of modern trench MOSFETs compared with ordinary MOSFETs, linear MOSFETs can operate more robustly at high voltages and current, close to DC conditions, so that the linear MOSFETs are used generally in the following scenarios:

- E-fuses and hot-swap circuits
- Used as a variable power resistor (programmable loads)
- Soft start application (limit surge currents)
- Linear amplifier circuit

Figure 2.6 shows the SOA diagrams on an standard MOSFET [42] and linear MOSFET [43]. Both D^{2}pak7 pin devices come with the capability to block 100V and on-state resistance $R_{ds}(on) = 1.7m\Omega$. The standard MOSFET shows a much weaker behavior for longer power pulse. For example, in typical operating conditions with input voltage of 54V and in-rush period of 10ms, the standard MOSFET can allow only 0.5A of 10ms current, whereas linear MOSFET can withstand up to 11.5A which is more than 20 times higher [40].

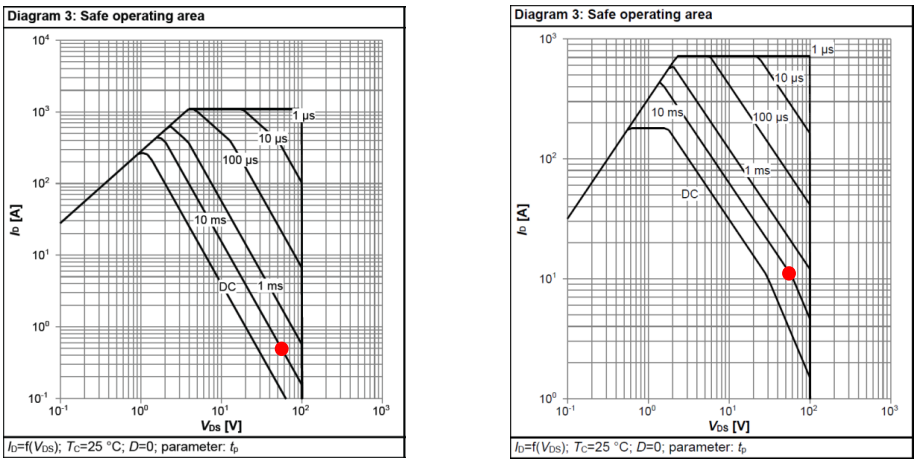

(a) standard MOSFET (b) linear MOSFET

Figure 2.6: SOA diagrams comparison [42] [43]

The output characteristic comparison between standard and linear MOSFET is shown in Figure 2.7. For linear MOSFET, the gate-source voltage (6V) must be significantly higher than standard device (<4.5V), so that the MOSFET switches on completely when the current is around 50A. This means that when using linear MOSFETs, a higher drive voltage V_{GS} is needed.

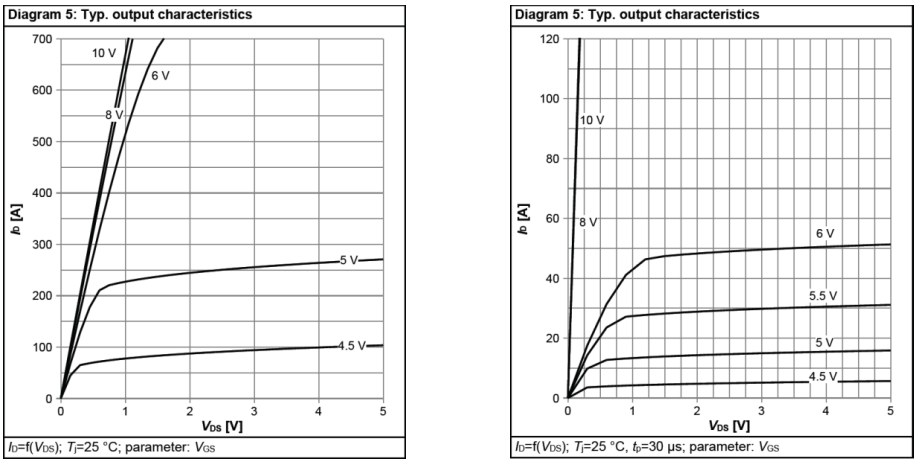

(a) standard MOSFET (b) linear MOSFET

Figure 2.7: The output characteristics comparison [42] [43]

In comparison to the standard MOSFET (Figure 2.8 left side), the characteristic curve of the linear MOSFET is less steep. Therefore,The gate-source voltage must be significantly increased to get the same current when compared to standard MOSFET.

It is of great interest to understand the importance of the intersection between the two transfer curves at different temperatures (respectively at 25°C and 150°/175°C). This intersection marks an important threshold and is called the zero temperature coefficient (ZTC) point. Operating below this point is unwanted due to the positive feedback coupling with negative temperature coefficient (NTC). It means with the same operating gate-source voltage and drain-source voltage, the hotter areas of the chip tend to conduct higher current than the colder areas. Due to higher power dissipation ($P_{loss} = i(t) \cdot v(t)$), the hotter areas get hotter and hotter, potentially leading to destruction due to thermal runaway. Above the ZTC point, the MOSFET stabilizes itself as warmer areas naturally get reduced current due to positive temperature coefficient (PTC). It can be seen as a clear advantage when the ZTC point occurs at a current as low as possible. For linear MOSFET, the intersection is

at around 30 A, which is much lower than the 400 A of the standard MOSFET. Linear MOSFET has much less chances to operate in the conditions which could run into thermal runaway. This is exactly the reason why the permitted SOA of the linear MOSFET is much larger and wider than that of the standard MOSFET [40, 44].

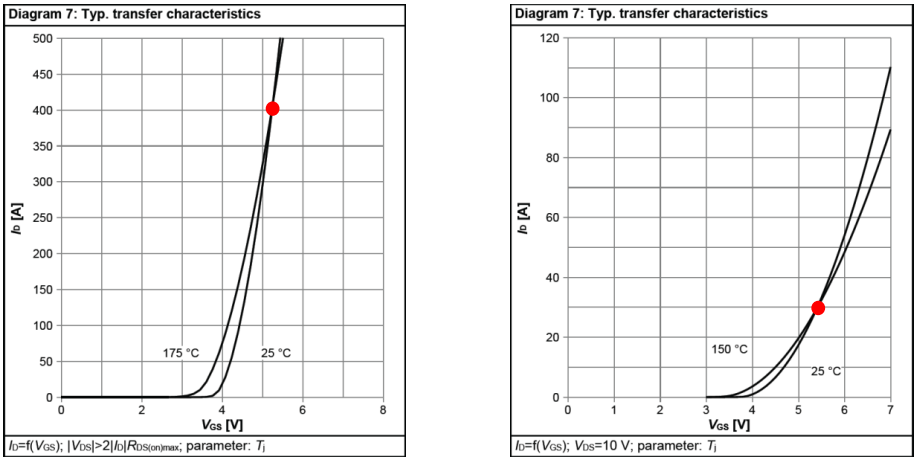

(a) standard MOSFET (b) linear MOSFET

Figure 2.8: The transfer characteristics comparison [42] [43]

In summary, in order to ensure the reliability of the E-switch, linear MOSFETs are selected to use. As shown in Figure 2.5, the voltage drop on the E-switch is equivalent to the difference between the output voltage of the fuel cell and the DC bus voltage. Because the fuel cell and the E-switch are connected in series, the current flowing through the E-switch equals the output current of the fuel cell stack. In the worst case, when the DC bus voltage is the lowest (here set to 48V) and stable, fuel cell operating at point (57V,115A), it can be calculated that U_{DS} is 9V and I_{FC} is 115A, which will be allocated to each linear MOSFET, for drain-source current I_D is 20A for individual MOSFET. Compared to the SOA diagram of the MOSFET manual, the MOSFET is still operating in the SOA interval and has a certain margin, as Figure 2.9 shows.

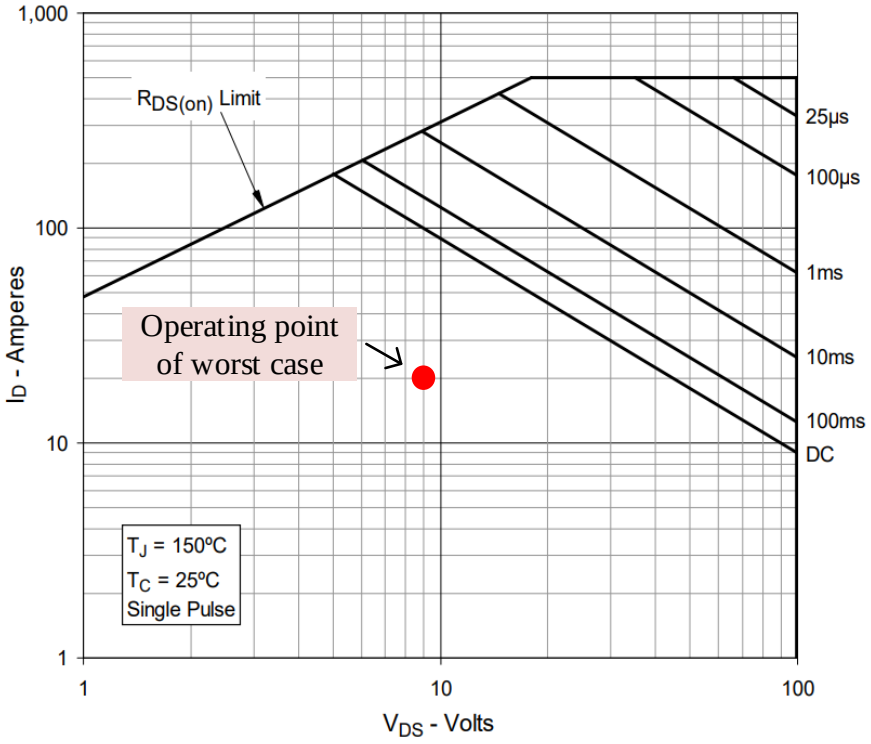

Figure 2.9: The worst case point in operating and SOA diagram of used linear MOSFET IXTN200N10L2 [original]

Current detection circuit

In the E-Switch circuit, another important part is the real-time and accurate tracking and measurement of the drain-source current I_D in a individual linear MOSFET. It is indispensable in the implementation of the following functions:

- As the return amount in the closed-loop control system.
- With measuring of I_D and U_{DS}, the power loss on a single MOSFET can be calculated, and formulate relevant strategies to ensure that the MOSFET is not damaged during operation.
- Monitor the actual total output current of the fuel cell, and cut off the connection between the fuel cell and the bus in time when an abnormality occurs.

In order to meet the above requirements, the closed-loop Hall current sensor type is used in the current tracking circuit with its high precision, high bandwidth, and electrical isolation characteristics. The used model is LA-55P. The operating principle of this sensor is shown in the Figure 2.10. The primary current being measured creates a magnetic flux in the core, the core is made up of thin pieces of steel stacked together to provide high frequency response, the hall effect sensor in gap measures the amount of flux in the core. The output of the Hall sensor is amplified in the compensation electronics. The current output of the compensation electronics (I_s) creates a second magnetic field in the coil. The magnitude of this secondary field is the product of current I_s times the number of turns in the coil (N_s). The magnetic flux from the secondary coil cancels out the flux from the primary to zero. The output of the closed-loop current sensor is the secondary current I_s. According to the feedback system of the current sensor,

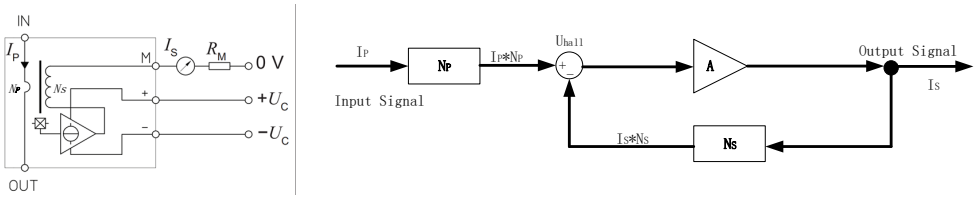

Figure 2.10: Construction and feed back system block diagram of closed-loop hall current sensor [original]

the current relationship between the primary side and the secondary side is as follows:

$$I_p \cdot N_p = I_s \cdot N_s \tag{2.1}$$

usually $N_p = 1$, then $I_s = I_p/N_s$ When the current I_s passes through a measuring or load resistor R_m, the output becomes a voltage U_m that is proportional to the primary current:

$$U_m = I_s \cdot R_m \tag{2.2}$$

Micro controller unit (MCU)

In the design of E-switch circuit, a high performance MCU of type STM32F4 is used to achieve the following main functions:

- Establish communication with the fuel cell stack management system, including sending and receiving commands.

- Establish a digital controller to regulate the drain-source current of the linear MOSFET. This includes the use of an Analog to Digital Converter (ADC) to measure the output signal of Hall sensor and converter it to digital values, then use a Pulse Width Modulation (PWM) generator to control the linear MOSFET.

- Monitoring the relevant parameters of the fuel cell stack and E-switch to ensure the normal operation of the system.

STM32F4 microprocessor provides a 12-bit ADC and a PWM generator. For the ADC, the following equation is established,

$$a = \frac{U_m}{U_{adc}} \cdot (2^{N_{adc}} - 1), \ with\ U_m \leq U_{adc} \tag{2.3}$$

where, U_m is the measured voltage, U_{adc} is the reference voltage of ADC, N_adc is the bit length of the ADC, and a is the converted digital value. Generally, the measured voltage should be less than or equal to the reference voltage to prevent the measured value from overflowing. Combining Equations 2.1-2.3, the following equation can be obtained:

$$a = I_p \cdot \frac{N_p}{N_s} \cdot \frac{R_m}{U_{adc}} \cdot (2^{N_{adc}} - 1) \tag{2.4}$$

When the linear MOSFET is operating in the saturation region, a stable gate-source voltage control V_{GS} is required, so it is necessary to connect the amplifying and filtering circuit after the PWM output signal to obtain a smooth DC signal (Digital to Analog Converter, DAC) [45]. In Figure 2.11 a PWM with duty cycle D and period T_P in seconds is presented, where $D = t_e/T_P$. It is know that the Fourier series representation of an even periodic function $f(t)$ is given by

$$f(t) = A_0 + \sum_{n=1}^{\infty} \left[A_n \cos\left(\frac{2n\pi t}{T}\right) + B_n \sin\left(\frac{2n\pi t}{T}\right) \right] \tag{2.5}$$

where

$$\begin{cases} A_0 = \dfrac{1}{2T} \displaystyle\int_{-T}^{T} f(t)dt \\ A_n = \dfrac{1}{2T} \displaystyle\int_{-T}^{T} f(t) \cos\left(\dfrac{2n\pi t}{T}\right) dt \\ B_n = \dfrac{1}{2T} \displaystyle\int_{-T}^{T} f(t) \sin\left(\dfrac{2n\pi t}{T}\right) dt \end{cases}$$

For the PWM signal $g(t)$ with amplitude U_{pwm} substituted into equation 2.5, the expansion coefficients are as follows:

$$\begin{cases} A_0 = U_{pwm} \cdot D \\ A_n = U_{pwm} \cdot \dfrac{1}{n\pi}[\sin(n\pi D) - \sin(2n\pi(1 - D/2))] \\ B_n = 0 \end{cases}$$

It can be seen from the expansion coefficients, the DC component A_0 term is equal to the PWM waveform amplitude multiplied by the duty cycle, which is the desired D/A conversion output result. By choosing the appropriate duty cycle, any D/A conversion output voltage between 0 and U_{pwm} can be obtained. The AC component A_n term is a series of high-frequency sinusoidal harmonics with a frequency that is an integer multiple of the PWM signal carrier frequency, and is not a required component for D/A conversion, it will be filtered out by a low pass filter.

As shown in Figure2.11, there are two major sources of errors in the desired D/A output. First, the PWM duty cycle can only be specified with limited resolution. The second source of error is the peak-to-peak ripple produced by unfiltered harmonics. The two error sources sum together to yield the total uncertainty, in the harmonic components. The fundamental wave has the lowest frequency and the maximum amplitude when the duty cycle is 50%, and therefore, the following conditions need to be met when designing the filter:

$$A_{(n=1),(D=0.5)} \cdot A_{filter} \leq \frac{1}{2} \cdot \frac{U_{pwm}}{2^{N_{pwm}}} \tag{2.6}$$

where N_{pwm} is the bit width of the PWM generator, U_{pwm} is the amplitude of PWM signal, A_{filter} is the gain of low-pass filter. For example, for a 12 bit PWM signal with 10kHz frequency and 50% duty cycle, the filter is required to attenuate the 10kHz component by more than 74dB.

In this circuit, a 1^{st}-order RC low-pass filter is placed (middle of Figure 2.11). The continuous-time domain transfer function, the 1^{st}-order RC low-pass filter is given by the equation:

$$Y(s) = \frac{U_{out}(s)}{U_{in}(s)} = \frac{1}{RC \cdot s + 1} \tag{2.7}$$

It can be seen from the transfer function of the 1^{st}-order RC low-pass filter is a typical inertial element, hence the design should consider the impact of the inertial element on the whole system.

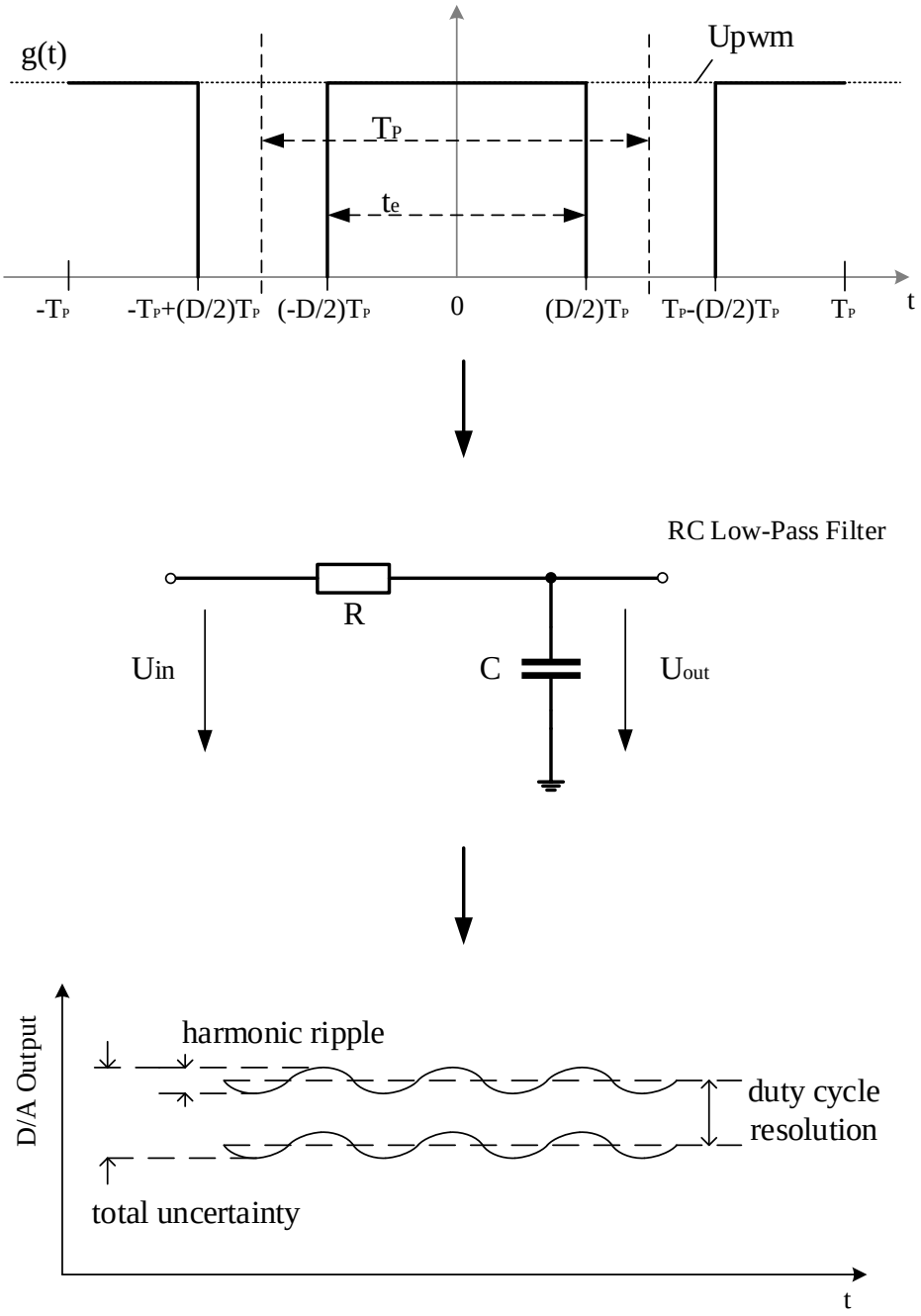

Figure 2.11: PWM signal even symmetry and uncertainty in the D/A output [original]

Figure 2.12: Image of the experimental E-Switch Prototype version I and II [original]

Figure 2.12 shows the technical realization of two prototypes in the development process. Version I is an early version for testing and verifying functionality, while version II is more finished, mounted on a test bench and able to communicate with other modules such as fuel cells for system testing.

2.2.2 Software and controller design of electronic switch

For individual MOSFETs of E-switch applications, the controller senses the drain-source current I_D and regulates this current value by varying the gate-source V_{GS} voltage of MOSFET. In doing so the MOSFET briefly operates in linear mode, and the V_{GS} voltage is being increased only slowly until the full current flows and finally the MOSFET is being operated in the triode region. Figure 2.13 illustrates the three operation states of the MOSFET in the output characteristics diagram. First the MOSFET is off and the entire voltage drops on it. Then the voltage V_{GS} is being increased continuously and the drain-source current starts to flow. At this point the MOSFET operates in the linear mode which is shown as second operational state in the diagram. Here the SOA becomes relevant. Finally, the MOSFET is fully enhanced (turned on) and operating in the ohmic region. The same three operational states occur when the MOSFET is used as a load of E-switch. Critical for the MOSFET is the dwell time in linear mode which depends on the controller timing.

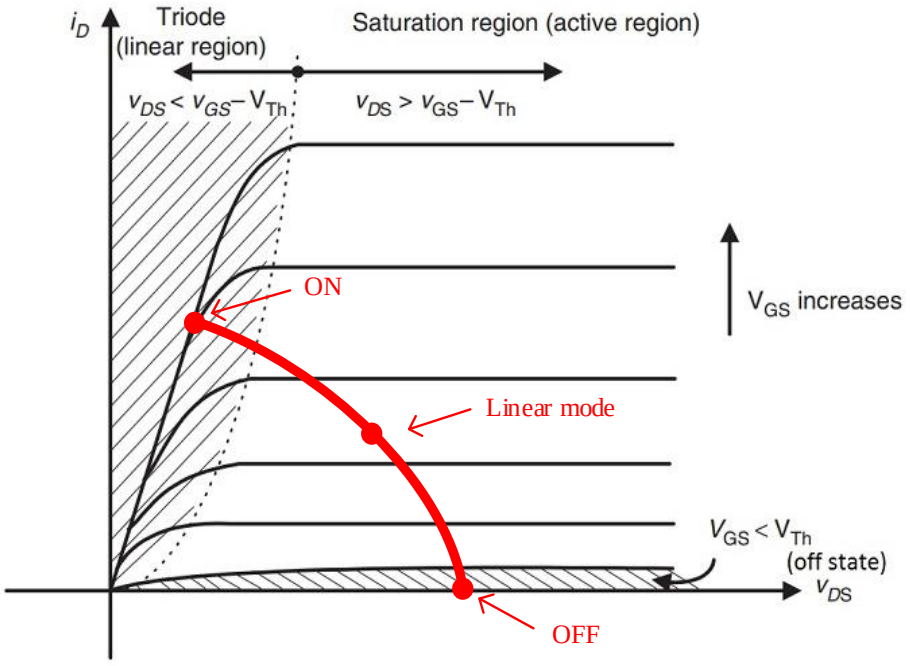

Figure 2.13: The operating states of individual linear MOSFET in E-switch [original]

It can be seen from the above Figure 2.13, the linear MOSFET will stay in the saturation region most of the time, but within this area, the gate voltage V_{gs} and drain-source current I_D of MOSFETs are not simply linear. So in order to accurately control the drain-source current of the MOSFET in real time, closed-loop control needs to be put into use. To facilitate the design of the controller, the continuous domain model will be studied first, then the controller is discretized using the digital redesign approach (DRA) to obtain the parameters of the controller. Figure 2.14 shows a block diagram of an individual linear MOSFET operating in closed-loop in the continuous domain.

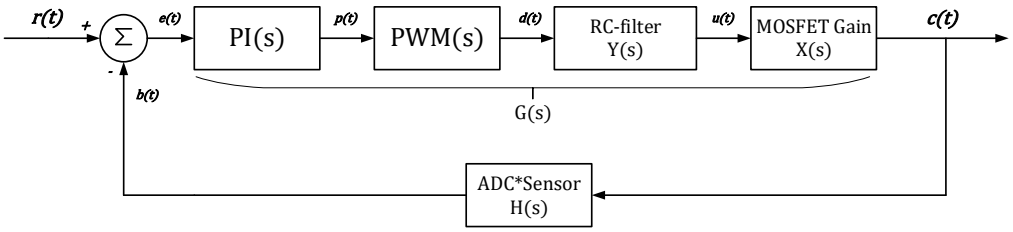

Figure 2.14: Block diagram of control system by continuous domain [original]

In the hardware design description in the previous section, it was specified that the power part of E-switch consists of six linear MOSFETs connected in parallel. According to the system requirements, the output current of the fuel cell is required to increase slowly at a constant slope during the turn-on phase. Due to individual and environmental differences between MOSFETs, the use of identical gate control signals V_{GS} for all MOSFETs does not guarantee the same current flowing through the MOSFETs. This means that a current sharing strategy needs to be set for the drain-source current balancing for all MOSFETs. In order to simplify the control strategy, the flow current regulator method is used for software design. First, the current I_{D1} of MOSFET1 is regulated slowly to rise to the first stage setting value (e.g. 5A) at constant slope, then keeping the gate voltage V_{GS1} of MOSFET1 constant, current I_{D1} will remain unchanged. Then the current I_{D2} of the MOSFET2 is controlled to increase to stage setting value. In this way, until all MOSFETs (MOSFET 1-6) have completed their first stage of current rise, the current I_{D1} of MOSFET1 increases continuously to the next stage (e.g. 10A). After the current $I_{sum}(t)$ reaches the desired value, or other corresponding control signals are received, such as complete turn on-off all MOSFETs, the control strategy will be stopped .The I_D of the individual MOSFET and the total E-switch current I_{sum} as a function of time, $I_D(t)$ and $I_{sum}(t)$ are shown in Figure 2.15. It can be seen

that the total E-switch current rises linearly and by changing the rate of change of the individual MOSFET current rise, the slope of I_{sum} can be adjusted.

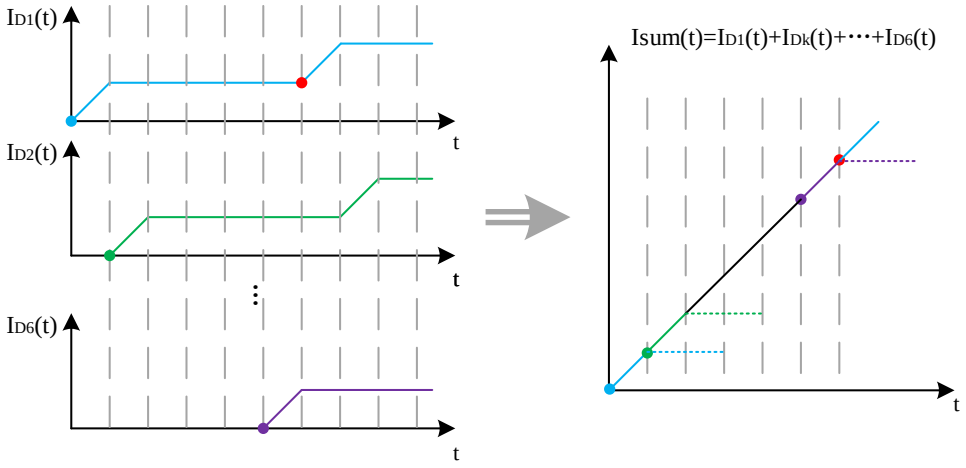

Figure 2.15: Desired drain-source current curves of individual MOSFETs (left) and E-switch current (right) [original]

When this strategy is applied, the input signal of the control system is a ramp-up, i.e. $r(t) = I_{Dk}(t)$, so static errors need to be considered when designing the closed-loop and controller. In the control block diagram, the transfer functions of PWM and ADC measurement block are given by:

$$PWM(s) = \frac{1}{2^{N_{pwm}} - 1} \cdot U_{pwm} \tag{2.8}$$

$$H(s) = \frac{2^{N_{adc}} - 1}{U_{adc}} \cdot \frac{N_p \cdot R_m}{N_s} \tag{2.9}$$

and the transfer function of the 1^{st}-order RC low-pass filter is given by equation 2.7. This is a closed-loop type-0 system without the use of a controller. When the system input is a ramp signal, the system static error is ∞,therefore, a controller is needed in the loop. In that control system, a PI-type controller is used, which has a transfer function in the continuous domain of:

$$PI(s) = K_P + K_I \cdot \frac{1}{s} \tag{2.10}$$

By adding an integration link K_I/s, the system can be transformed into a type 1. The type 1 systems still have static errors when following a ramp

input signal, however, this static error can be set within a specified range by adjusting the proportional parameter K_P.

When the MOSFETs operate in the saturation region, the relationship between V_{GS} and I_D can be obtained from the small signal analysis of its DC operating point as (without channel length modulation, using the MOSFET as a voltage-controlled current source):

$$g_m = \frac{i_d}{v_{gs}}|v_{ds=cons.} \tag{2.11}$$

where g_m is defined as the transconductance. The Figure 2.16 shows the g_m definition view on the transfer characteristic curve and the $g_m = f(I_D)$ curve of a linear MOSFET.

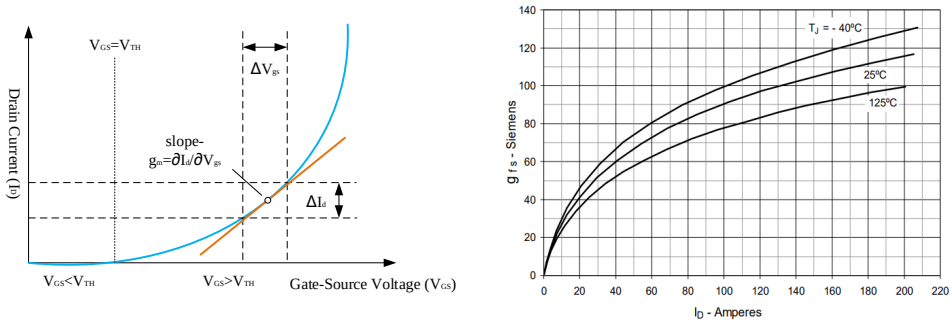

(a) Definition of transconductance g_m (b) g_m vs I_D

Figure 2.16: Definition of g_m and the curve of $g_m = f(I_D)$ [original]

According to equation 2.11 it can be derived that $X_s = g_m$. Integrating equations 2.8-2.11, the open-loop transfer function of the block diagram is:

$$\begin{aligned} G(s) \cdot H(s) &= [PI(s) \cdot PWM(s) \cdot Y(s) \cdot X(s)] \cdot H(s) \\ &= \left[\frac{K_P \cdot s + K_I}{s} \cdot \frac{U_{pwm}}{2^{N_{pwm}} - 1} \cdot \frac{1}{RCs + 1} \cdot g_m\right] \cdot \frac{(2^{N_{adc}} - 1) \cdot N_p \cdot R_m}{U_{adc} \cdot N_s} \\ &= g_m \cdot K_I \cdot \frac{(2^{N_{adc}} - 1) \cdot U_{pwm} \cdot N_p \cdot R_m}{(2^{N_{pwm}} - 1) \cdot U_{adc} \cdot N_s} \cdot \frac{(K_P/K_I) \cdot s + 1}{s(RCs + 1)} \end{aligned} \tag{2.12}$$

This formula can be rewritten in the following form:

$$\begin{cases} G(s) \cdot H(s) = K_{open-loop} \cdot \dfrac{\frac{K_P}{K_I} s + 1}{s(RC \cdot s + 1)} \\ K_{open-loop} = g_m \cdot K_I \cdot \dfrac{(2^{N_{adc}} - 1) \cdot U_{pwm} \cdot N_p \cdot R_m}{(2^{N_{pwm}} - 1) \cdot U_{adc} \cdot N_s} \end{cases} \tag{2.13}$$

Among them, K_P and K_I are adjustable parameters of controller, $K_{open-loop}$ is the open-loop gain for the system, as can be seen from Figure 2.16, the I_D operating range in the application is [0-40A], which corresponds to a g_m range of [0-60 Siemens] at 25°C. When using the root locus principle to analyze this system, the root locus plot is shown in Figure2.17. The real components of all poles are negative, this meaning that the system is stable when $K_{open-loop}$ is in the range of (0,+∞). It can be determined that parameters K_P, K_I and g_m have no effect on the stability of the system.

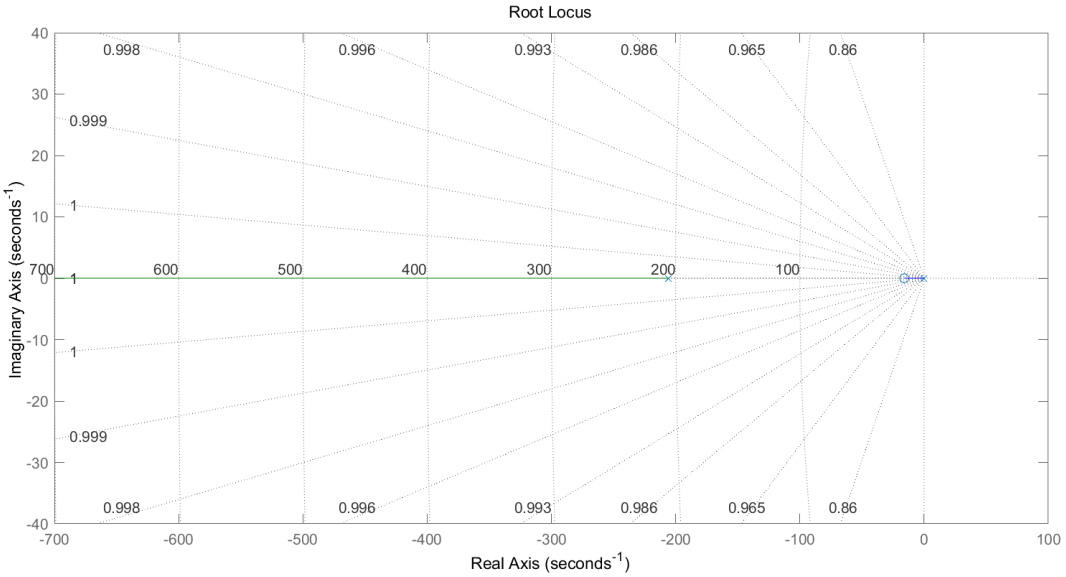

Figure 2.17: Root Locus for closed-loop transfer function with different values of $K_{open-loop}$ [original]

In summary, this system will eventually reach steady state. However, when the input signal of a type 1 system is a ramp, steady state errors exist in the control signal and response, with final value theorem it is represented as e_{ss}:

$$e_{ss} = \lim_{t\to\infty} e(t) = \lim_{s\to 0} s \cdot E(s) = \lim_{s\to 0} s \cdot \frac{1}{1 + G(s)H(s)} R(s) \tag{2.14}$$

where $E(s)$ and $R(s)$ are the Laplace transforms of the error signal $e(t)$ and reference signal $r(t)$ respectively. The transfer function in the continuous domain of the ramp signal is known to be A/s^2, where A is slope, and substitution into the above equation 2.14 eventually yields:

$$e_{ss} = \frac{A}{K_{open-loop}} \tag{2.15}$$

By analyzing the above equations, it can be seen that the static error depends on the values of g_m, A, and K_I. In practice, the static error is reduced by adjusting the value of K_I.

In the controller design, the value of g_m is first set to 1 Siemens and slope of storm ramp set to 40A/s. The parameters K_P and K_I are designed with the help of **MATLAB2021 PID Tuner Tool**, such that to find out the most suitable control parameters for the system. The values of the main parameters of the control loop in the application are listed in the Table 2.3 below:

Table 2.3: Parameters of the control loop in application

Parameters	**Description**	**Value**
N_{pwm} *and* N_{ad}	Bit-width of ADC and PWM generator	12 bit
$N_p : N_s$	Turns of Hall sensors	1:1000
R_m	Measuring resistance	100Ω
R *and* C	Parameters of 1^{st}-order RC filter	2.2KΩ, 2.2μF
g_m	Transconductance	[1,60] Siemens
U_{ad} *and* U_{pwm}	ADC reference voltage and PWM output voltage	3.3V and 15V
A	Slope of ramp signal	[5,40] A/s

Substituting the above parameters into equations 2.12-2.15 and with the help of MATLAB2021 PID Tuner Tool to tune the controller parameters, the final result is $K_P = 2$ and $K_I = 400$. In Figures 2.18- 2.21, the comparison of the output signal and desired response of the control system is shown for different slopes and for different g_m cases. It is concluded that the error between the desired value and the given value does not exceed 0.1A in the operating interval of the loop, which meets the application requirements.

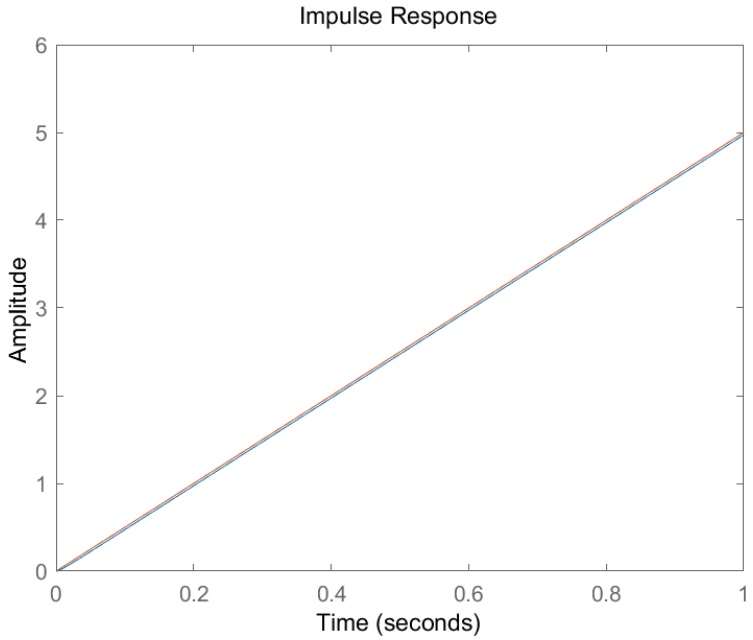

Figure 2.18: Output signal vs desired response of control system with slope=5, gm=1. [original]

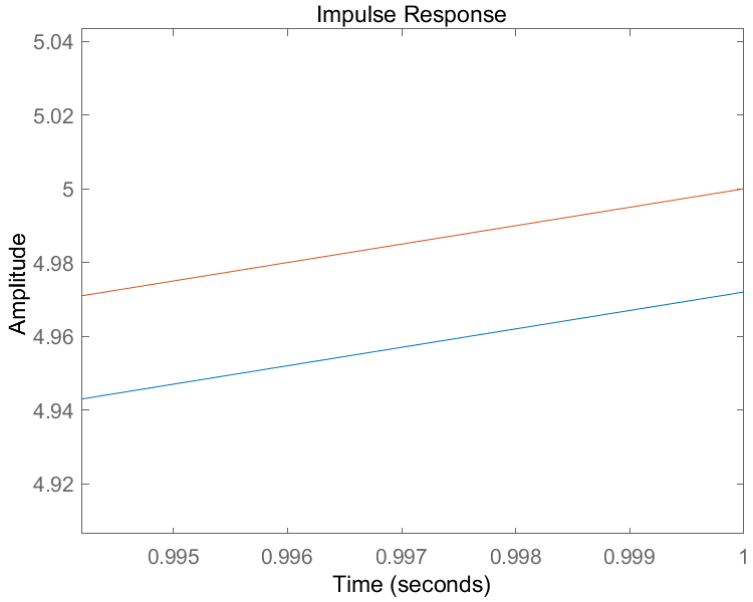

Figure 2.19: Steady state error of control system with slope=5, gm=1. [original]

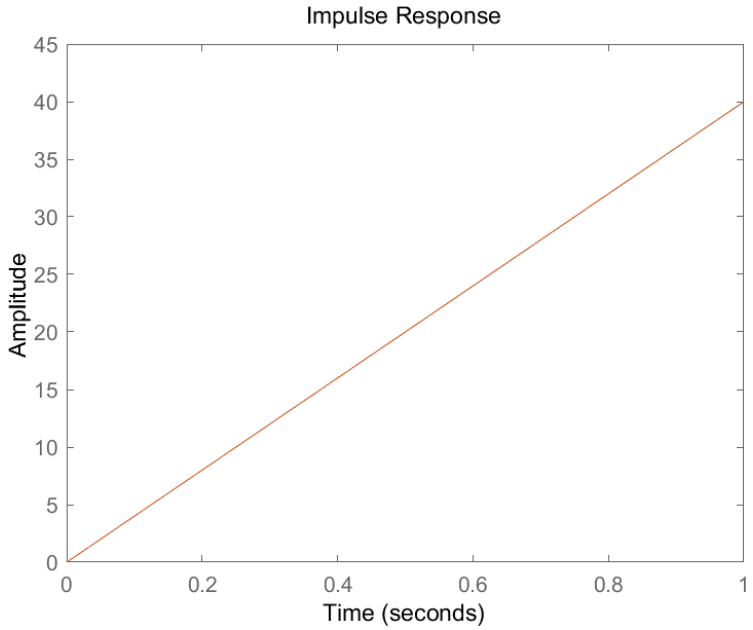

Figure 2.20: Output signal vs desired response of control system with slope=40, gm=60. [original]

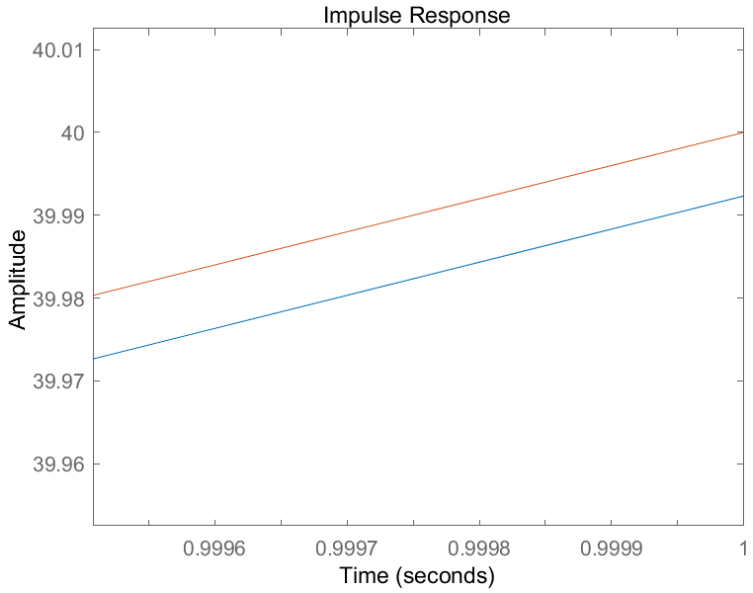

Figure 2.21: Steady state error of control system with slope=40, gm=60. [original]

The PI controller of the E-switch in continuous domain was analyzed and designed above. The digital control of MCU is a sampling control, which can only calculate the control quantity based on the deviation of the sampling moment. Therefore, the DRA method is used here to design digital controller, that is, the PI controller in the continuous domain is discretized and converted into the form of a difference equation, which can be programmed in MCU. Transforming equation 2.10 to the time-discrete domain with using backward difference $s = (z-1)/(zT_s)$, the results are as follows:

$$PI(z) = \frac{P_{(z)}}{E_{(z)}} = \frac{K_P(1-z^{-1}) + K_I \cdot T_s}{1-z^{-1}} \tag{2.16}$$

where T_s is the system sampling time. Further, for use in microprocessor programming, it can be rewritten as the following PI incremental equation:

$$p_{(k)} = p_{(k-1)} + K_P(e_{(k)} - e_{(k-1)}) + K_I \cdot T_s \cdot e_{(k)} \tag{2.17}$$

where p is output of the PI controller, k is sampling serial number, k=0,1,2...

Simulation of E-switch

In order to verify the feasibility of the above parameter design, a software simulation based on **MATLAB Simulink** was developed. The block diagram of control system is shown in Figure 2.22. The control system consists of a digital controller, the plant signal, the input signal, and the sampling frequency of the digital PWM module must be higher than 2 times for the E-switch control system.

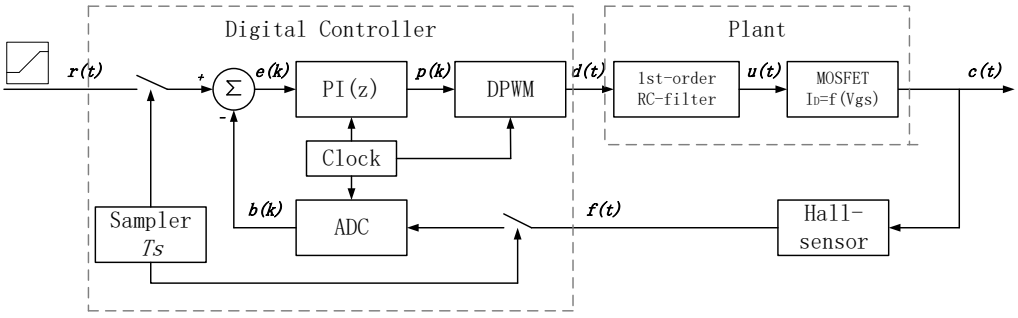

Figure 2.22: Simulation block diagram for control system [original]

Because the relationship between V_{GS} and I_D of MOSFET is not linear. The table look-up module of the linear interpolation method is used to describe

the relationship, that approximates the curve $I_D = f(V_{GS})$ instead and the simulated curve is shown in Figure 2.23.

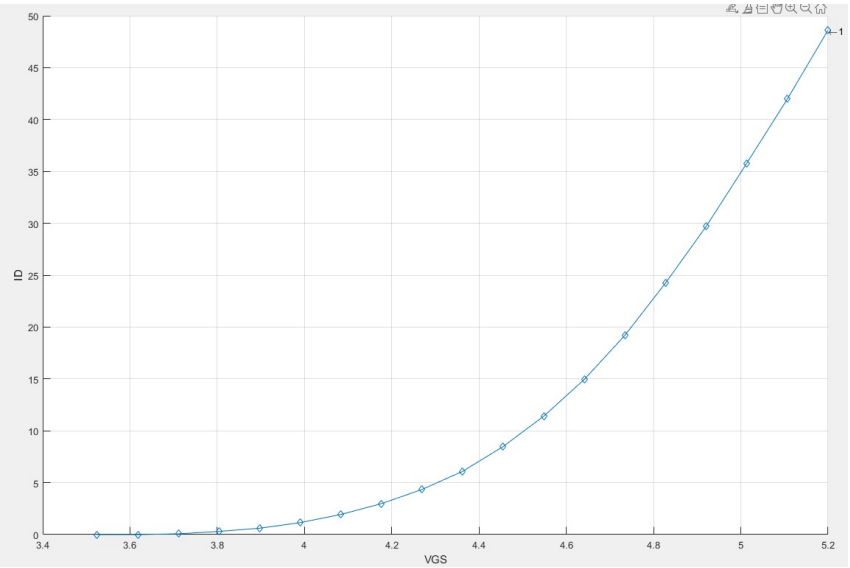

Figure 2.23: The simulated curve $I_D = f(V_{GS})$ using linear interpolation method [original]

The E-switch is simulated in MATLAB Simulink and the block diagram is shown in Figure 2.24.

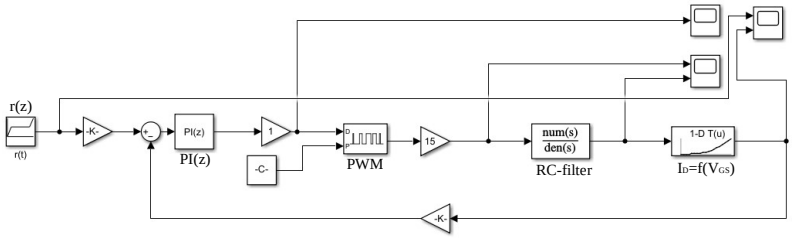

Figure 2.24: Simulation block diagram for control system [original]

Figure 2.25 and 2.26 show the final simulation results for an individual linear MOSFET with input signal $r(t)$ (green solid line) and output signal $c(t)$ (purple dotted line). In practice, it can be remarked that the current flow through the linear MOSFET follows the desired value precisely and in time.

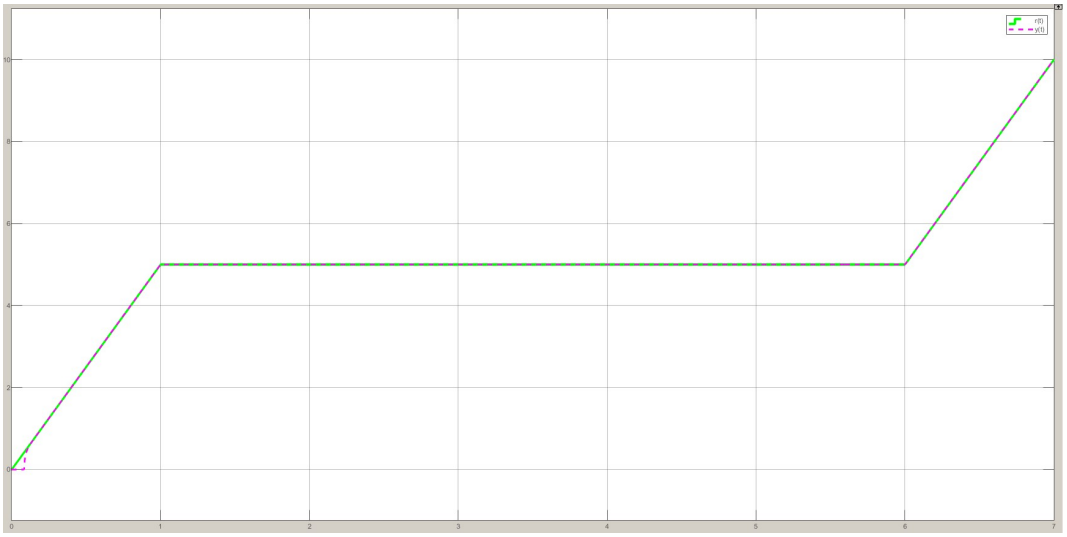

Figure 2.25: Simulation results of input signal (green solid line) and output signal (purple dotted line) with current ramp slope 5A/S and from 0s-6s [original]

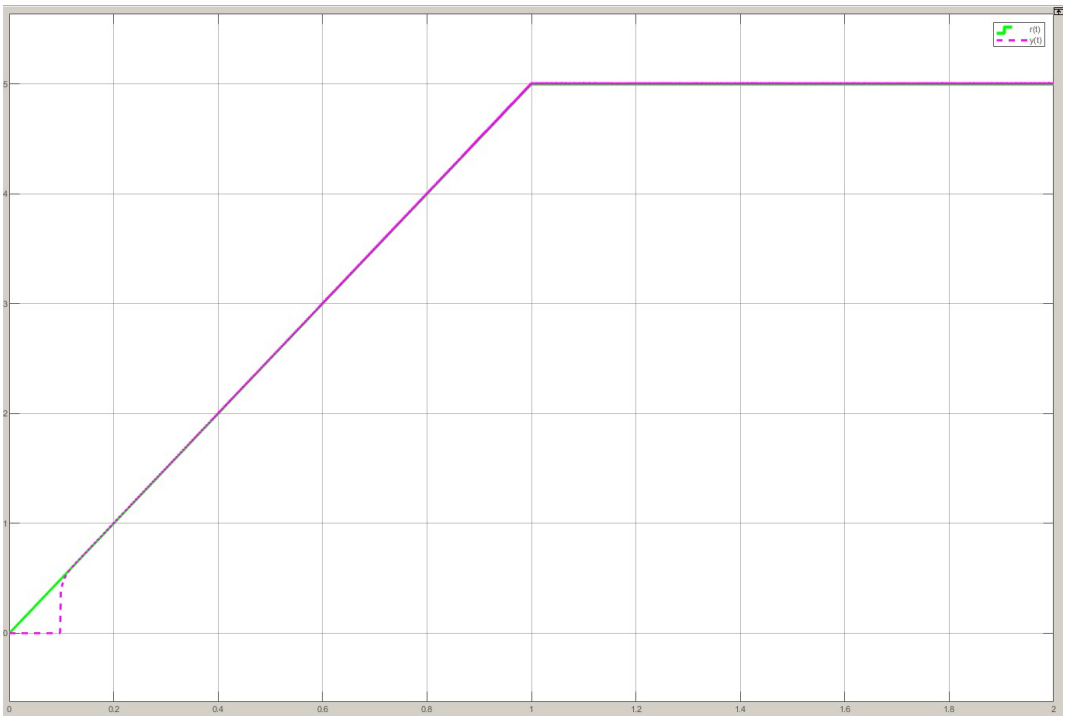

Figure 2.26: Simulation results of input-output signal with current ramp slope 5A/S and from 0s-2s [original]

From the results of the simulation, it can be seen that the output signal does not follow the input signal in the starting interval 0s-0.1s. This is caused by the MOSFET threshold voltage V_{th}, which can be avoided in practice by adding an offset voltage on V_{gs}. In addition, Figure 2.27 also shows the ripple of the output signal, from the above analysis. It can be concluded that the ripple is caused by the uncertainty of the PWM signal through the 1^{st}-order RC low-pass filter, with the provided design, the ripple can be controlled within the required range.

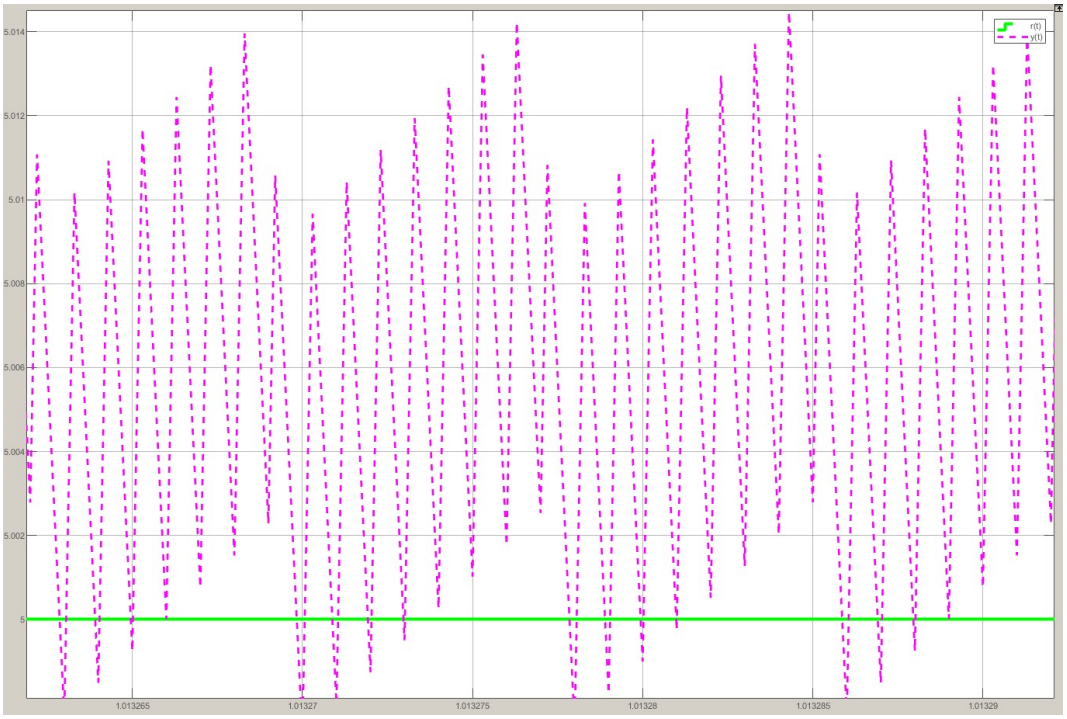

Figure 2.27: Ripple of the output signal in the simulation results [original]

2.3 Experimental results for E-switch in FC vehicles

After the corresponding hardware and software design was completed, the prototype was tested and verified. In Figure 2.28, the measurements for the switch-on operation of the electronic switch are presented. The switching duration in this example is t_{Switch} = 30s and the switch voltage before the switching process starts at U_{Switch} = 22V. After completion of the switch-on process, the measurements are stopped.

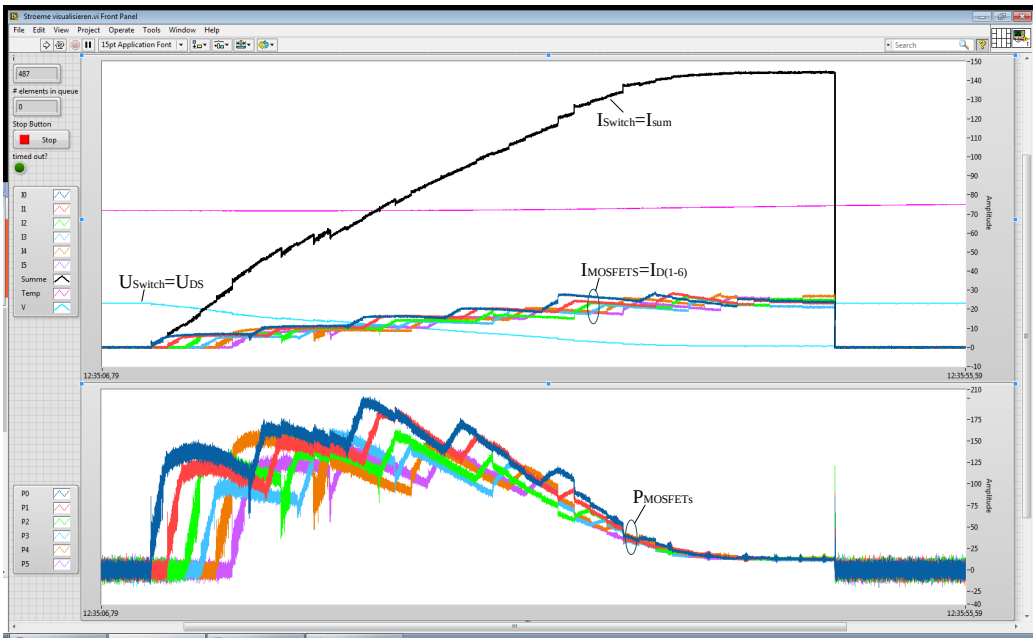

Figure 2.28: Current (above) and power losses (below) in the MOSFETs during a switching operation [31]

In the figure above the current waveforms in the MOSFETs during switch-on operation are presented. The currents in the six MOSFETs are successively increased step by step with 5A. The total current (black) in the switching element I_{Switch} with slope 5 A/s can be calculated by the sum of the six MOSFETs current $I_{D(1-6)}$. The voltage at the electronic switch, which is also the voltage across the individual MOSFETs, is slowly reduced during the switching operation to the value of the switched-on forward voltage.

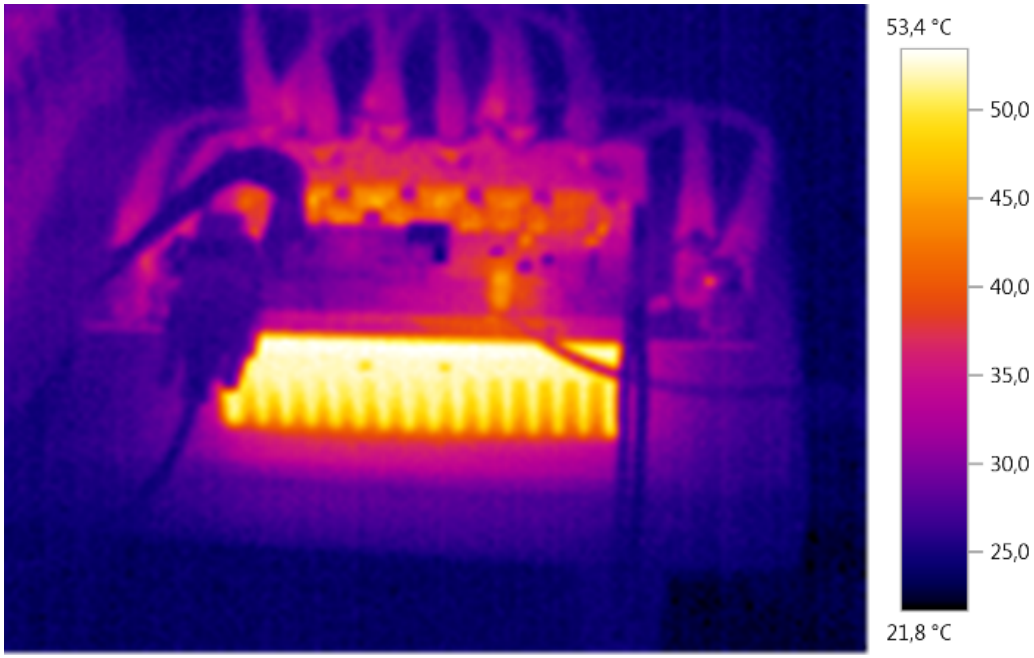

Figure 2.29: A temperature profile after switching operations [31]

In Figure 2.28, the power losses curves of the individual MOSFETs, which are calculated from the current waveforms and the applied voltage are shown. In the illustrated switching process, maximum losses of up to almost 200W occur in individual MOSFETs. With help of the step by step switching the total power losses of the electronic switch can be divided quite well between the different MOSFETs, Figure 2.29 shows the thermal characteristics of the electronic switch during operation, in the actual measurement. The maximum temperature of the heat sink rises to about 55 °C during the switch-on process.

The desired current gradient and thus indirectly the switching time can be transferred to the microprocessor by CAN communication. The current level, which depends on the state of charge of the battery, is set automatically after the switch-on process.

Figure 2.30 shows a switching on operation of the power electronic switch. In this example, the current increases during the switched-on time $t_{on} = 8.4$s to a current $I_{on} = 115$A. This means the output current of the fuel cell stack rises from 0 to 115A at a slope with 13.5A/s.

In an additional example, Figure 2.31 shows a fuel cell current of $I_{on} = 210$A adjusts itself in the switch-on and -off state, and the time duration of states is $t_{on} = t_{off} = 5$s. At this time, the rising and falling slopes of the fuel cell output current are 42A/s.

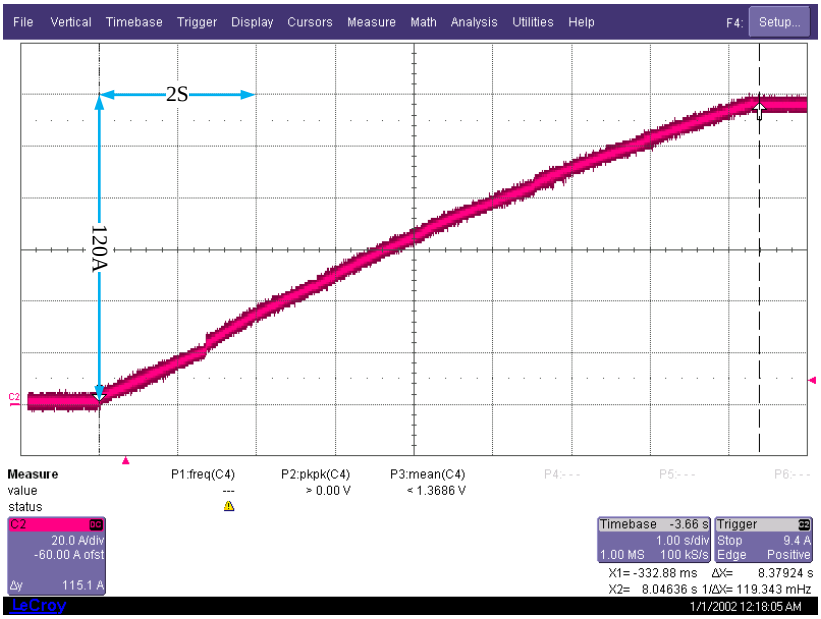

Figure 2.30: Current waveforms during switch-on operations of the E-switch [31]

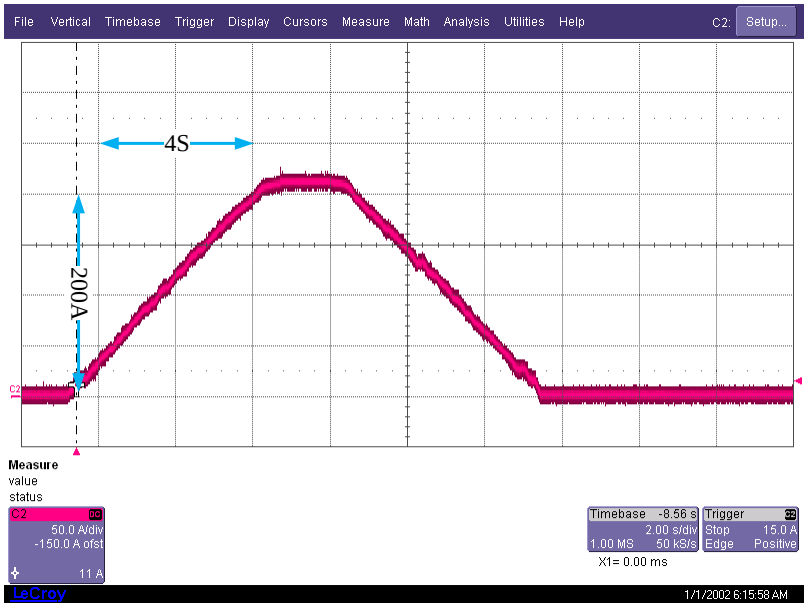

Figure 2.31: Current waveforms during switch-on and -off operations of the E-switch [31]

2.4 Conclusions and contributions

In this chapter, a novel concept to control the powertrain in battery fuel cell hybrid vehicles is presented. In this concept, simply an electronic switch between the DC bus and the fuel cells system is used. Thus, the effort for the powertrain construction can be significantly reduced. However, in this concept, the battery and fuel cell voltage must be matched to each other. These two voltages ultimately determine the power output of the fuel cell in switched-on state.

In the illustrated development of the electronic power switch six MOSFET modules are connected in parallel. In contrast to converters, the MOSFETs on the power electronic switch are operated in the linear region for several seconds during the switching process. The currents in the MOSFETs are thereby balanced by the use of a microprocessor. As a result, the losses that occur in the switching process in the kilowatt range, can be evenly distributed to the individual MOSFETs. The content of this chapter can be summarized as follows:

- The operating principle and limitations of this new concept are presented.

- The hardware circuit design implementation and software control strategy of E-switch are described in detail. Regarding hardware, the design requirements for linear MOSFETs, current measurement, DAC filter circuit, and MOSFET control circuits are explained. About the software design, the stability of the closed-loop control, the static error, and the digital controller are studied accordingly.

- In the process of verifying the feasibility of the application, a discrete control system based on MATLAB Simulink is first established. From the simulation results, it can be seen that the error and delay of the output signal and the desired value can be neglected, which verifies the feasibility of the system. Then, the prototype of the E-switch is implemented, and it can be seen from the actual measurement results that it can control the fuel cell current to rise at the set slope. The operating temperature of the prototype is less than about 60 °C.

During the start-up phase, gentle operation of the fuel cell can be achieved by controlling the E-switch. After the E-switch has completed connecting the fuel cell to the battery pack, the operating point of the fuel cell will be passively determined by the DC bus voltage i.e. battery voltage. If the DC bus voltage changes with a large amplitude, it also means that the fuel cell output voltage will frequently switch between high and low potentials, which will cause the

flaking of the platinum surface oxide layer (eventually leading to the dissolution of platinum) and the fuel cell life will be reduced as a result. Therefore, in this proposed powertrain, a large capacity battery pack is necessary to be placed to stabilize the DC bus voltage.

Adding a DC/DC converter to the powertrain is the option if the fuel cell output is to be controlled to remain smooth over the full operating range. DC/DC converters in fuel cell powertrain are discussed in the next chapter.

Chapter 3.

DC/DC converter for Powertrain in FCEV

3.1 Introduction

In Chapter 1, three different powertrain systems are described depending on the position of the DC/DC converter in the FCEV powertrain. Essentially, the voltage difference between different units of FCEV reflects the direction and magnitude of the energy flow. To match the voltage difference between the fuel cell stack, the energy storage unit, and the bus voltage, the output of these converters is a regulated DC voltage having a magnitude differing from the input voltage in operation. Numerous topologies having available to meet the corresponding requirements [37, 46–50]. These topologies can divided into two categories, isolated and non-isolated.

3.1.1 Non-isolated DC/DC converter

Non-isolated DC/DC converters are represented by classical converters such as buck, boost (shown in Figure 3.1 left) and buck-boost converter, etc. The advantages of these converters are fast dynamic response, high peak efficiency and low cost, but also with obvious disadvantages. For example, low voltage gain, high device stress (by high power), low efficiency for high conversion ratio, etc. Generally, the output voltage divided by the input voltage of the converters is defined as the conversion ratio:

$$M_{(D)} = f(D, f_s, \phi) \tag{3.1}$$

where D is duty cycle, f_s is frequency and ϕ is the phase difference of PWMs. Conversion ratio of non-isolated DC/DC converters is only related to the parameters of the PWM signals.

3.1.2 Isolated DC/DC converter

The difference between isolated and non-isolated DC/DC converters is that a high frequency (HF) transformer is used in isolated DC/DC converters to achieve DC isolation between the input and output. On the other hand, when a large step-up or step-down conversion ratio is required, this can be achieved by changing the turns ratio of the transformer. By an appropriate choice of the transformer, the current or voltage stresses can be improved on the semiconductors, leading to a higher efficiency and lower cost. The non-isolated converters are represented by flyback converter, forward converter, push-pull converter and half or full bridge converter (shown in Figure 3.1 right), etc. The conversion ratio of an isolated DC/DC converter is given by:

$$M_{(D)} = f(D, fs, \phi, n) \tag{3.2}$$

Comparing with Equation 3.2, the transformer turns ratio is also an important parameter affecting the conversion ratio of an isolated DC/DC converter.

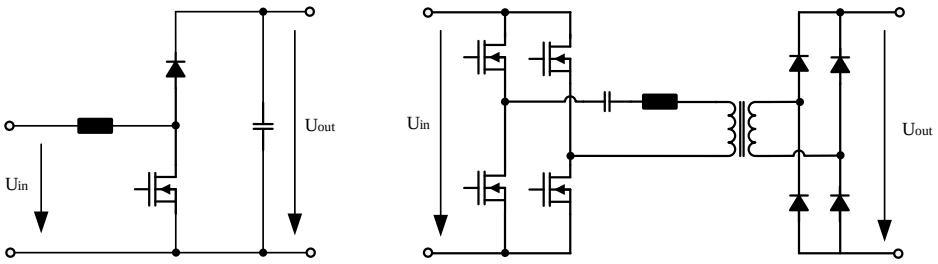

Figure 3.1: Non-isolated Boost converter and isolated LLC converter [original]

The isolated topology is worse than the non-isolated topology in terms of power density due to the presence of transformers, while the input and output range are subject to constraints, requiring redesign of parameters for different power levels. However, in multi fuel cell stack system applications, the isolated converter is more flexible because it can be directly connected in parallel. Contrary to that, the non-isolated topology is more adaptable, it can be designed to meet different power requirements through a single design.

In practical applications, cascade, series, parallel, multiphase, soft-switching and magnetic integration technologies of converters have been widely expanded and studied to meet the requirements of complex circuits such as high power and high conversion ratios [51–54]. In general, these studies are focused on the following properties of the DC/DC converter:

- Complete the conversion tasks at the corresponding power level.
- High efficiency, high power density, small size and low weight.
- Low EMI, electric isolation to prevent electric leakage and/or electric shock.
- Low cost.

In Chapter 2, the principle of using an electronic switch is explained. The electronic switch is used as an adjustable load resistor to match the fuel cell output voltage with the bus voltage, but it can only be operated actively for short periods of time, e.g. During the turn-on phase. However, if the rated output voltage of the selected fuel cell and the bus voltage cannot be passively matched, or if the control system of the fuel cell electric vehicle requires the ability to actively control the output power of the fuel cell in real time, then the control of the fuel cell power supply needs to be regulated by the power electronics of the system. The design of the DC/DC converter, which mainly includes DC/DC conversion, is critical to the vehicle, as the performance of the converter directly affects the fuel cell. In fact, the ripple and harmonic content of the current extracted from the fuel cell is an important component of the fuel cell. The current drawn from the fuel cell is one of the various phenomena that affect the fuel cell lifetime [55, 56]. Another aspect of current ripple is that it not only affects the lifespan, but also its capacity and fuel consumption . It has been suggested that the current ripple should be limited to less than 10% of the nominal FC current [57, 58]. Obviously, a major design goal is to minimize this ripple and harmonic content [46]. Another important point in designing a fuel cell DC/DC converter is the dynamic responsiveness of the converter. Using DC/DC converters to control operating point stability of fuel cell is also beneficial to the fuel cell lifetime.

Since the powertrain inherits the fuel cell stack and battery pack described in Chapter 2, only the electronic switches will be replaced. To ensure a better understanding, the multiphase parallel buck converter is selected for integration into the powertrain system. In this chapter, the ripple current and dynamic response of single and multiphase parallel buck converter will be in detail analyzed, and system will be evaluated from their advantages and disadvantages in FCEV powertrain system from the results.

3.2 Analysis of a multiphase buck Converter in FCEV

3.2.1 Single phase buck converter

Figure 3.2 shows a single phase synchronous buck converter. It consists of a bridge-leg, a filter circuit and a dc-link capacitor. By use of a pulse control method the semiconductors of the bridge-leg produce a sequence of rectangular pulses, which is filtered at the output so that a smooth DC-voltage is generated [34] [59].

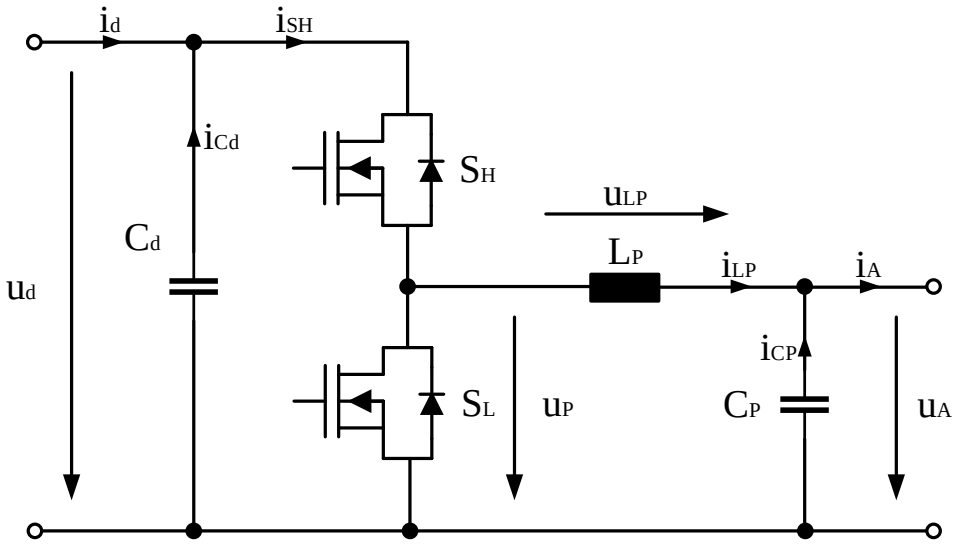

Figure 3.2: Schematic of a single phase buck DC/DC converter [59]

For the filter circuit design it is assumed that all elements of the converter are lossless and the voltage and currents at the input and output are ideally smoothed. The voltage and current waveforms are shown in Figure 3.3, where:

- u_d: input voltage, u_A: output voltage, u_{LP}: voltage on inductor L_P, u_P:voltage on lower MOSFET.

- i_d: input current, i_A: output current, i_{Cd}: current on input capacitor, i_{CP}:current on output capacitor, i_{LP}: current on inductor

- t_e: on time of MOSFET SH, T_P: operating period, duty cycle: $D = t_e/T_P$.

It is well known that in a single phase buck circuit the following equations hold:

$$\begin{cases} U_A = D \cdot U_d \\ I_d = D \cdot I_A \end{cases} \tag{3.3}$$

The inductance is determined from the maximum voltage-time-area at the inductance in the pulse periods and the defined permissible current change,Δi_{LP} the following Equation is given:

$$L_P = \frac{u_d \cdot T_P}{\Delta i_{LP}} \cdot (1 - D) \cdot D \tag{3.4}$$

With consideration of the full control range, the voltage-time-area in the pulse period reaches their maximum with a duty cycle of 50%. For this duty cycle the maximum permissible current change is specified for the inductance design between 10% - 30% from the nominal output current I_{AN}.

$$L_P = \frac{u_d \cdot T_P}{4 \cdot \Delta i_{LP\,\max}}, \text{with } \Delta i_{LP}\max = (0.1 - 0.3) I_{AN} \tag{3.5}$$

The rms-value of a triangular ripple current is calculated by division with the square root from twelve. With consideration of this fact the rms-value of the capacitor current can be determined as a function of the duty cycle with:

$$I_{Cp,rms} = \frac{\Delta i_{Lp}}{\sqrt{12}} = \frac{2 \cdot \Delta i_{Lp}\max}{\sqrt{3}} \cdot (1 - D) \cdot D \tag{3.6}$$

In the Figure 3.4, the rms-value of filter capacitor current I_{CP} is presented with different partially extremely large permissible current changes. In each case the current has its maximum value with 50% duty cycle.

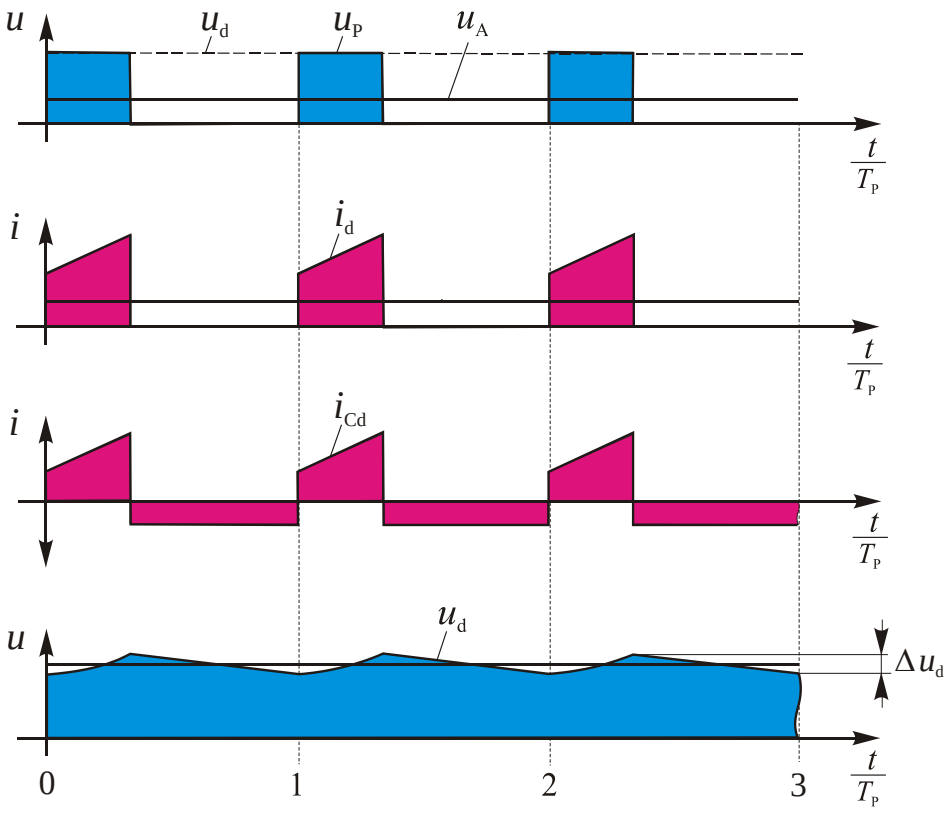

(a) Intput waveforms

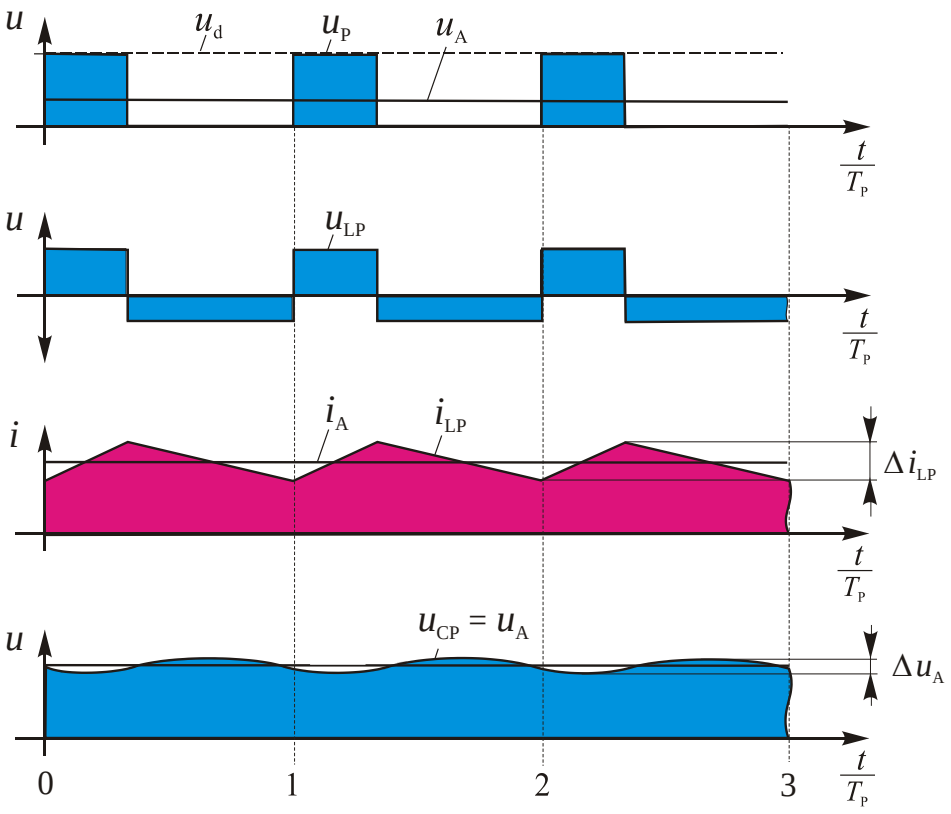

(b) Output waveforms

Figure 3.3: Current and voltage waveforms at the in-output of a single phase buck converter [59]

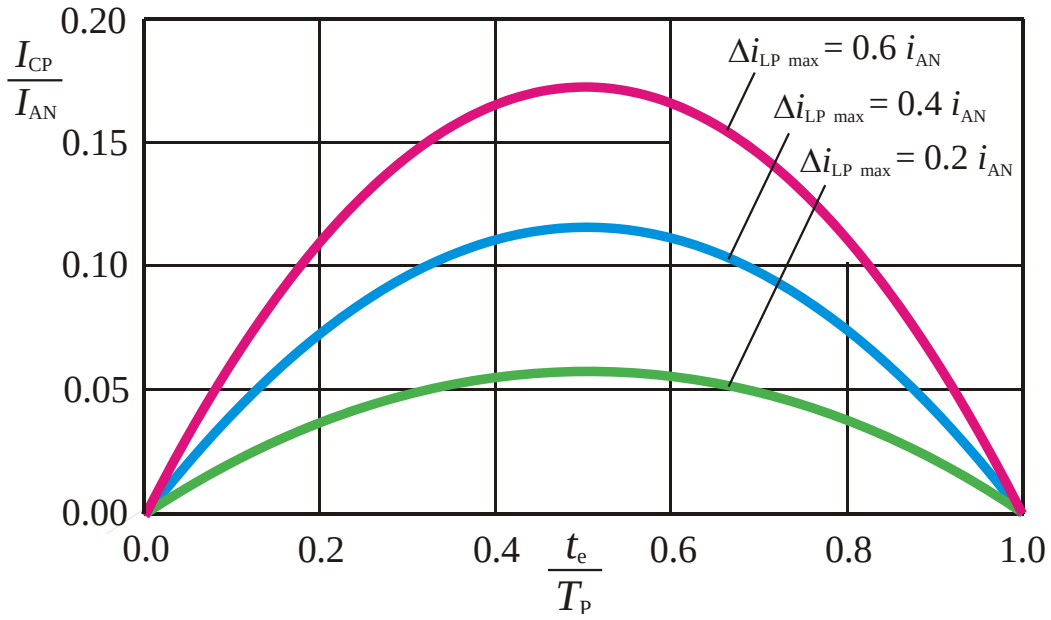

Figure 3.4: Rms-current in the output capacitor i_{CP} with different Δi_{Lp} max, $(i_A = I_{AN})$ [59]

When the duty cycle is 50%, in the time interval $0 - T_P$:

$$u_A = \frac{1}{C_P} \cdot \int_0^{0.5 \cdot T_P} i_{LP}\ dt \tag{3.7}$$

In practice the permissible static voltage ripple is selected smaller than 1% of the nominal output voltage u_{AN} so that in approximation an ideally smoothed output voltage is produced, and The value of the output filter capacitor can be calculated from the Equation 3.8.

$$C_P = \frac{T_P \cdot \Delta i_{LP\,\max}}{8 \cdot \Delta u_{A\,\max}}, \text{with } \Delta u_{A\,\max} \leq 0.01 \cdot u_{AN} \tag{3.8}$$

The rms-value of the inductance current consists of the squared addition of capacitor and output current, so the $I_{LP,rms}$ is given by:

$$I_{LP,\ rms} = \sqrt{I_A^2 + \left[\frac{2 \cdot \Delta i_{LP\,\max}}{\sqrt{3}} \cdot D \cdot (1 - D)\right]^2} \tag{3.9}$$

With help of the current waveforms in Figure 3.3(b), the current in the input capacitor can be calculated. By worst case, the current is ideally smoothed

in the input, and the input filter capacitor is loaded with the entire alternating current, so the current $I_{Cd,rms}$ is given by:

$$I_{Cd,rms} = \sqrt{I_{SH}^2 - I_d^2} \quad = \sqrt{I_{LP}^2 \cdot D - (I_A \cdot D)^2} \tag{3.10}$$

Therefor, the rms-current of input capacitor can be writes as function $f(D, \Delta i_{LP})$ and $f(D, \Delta i_{LP\,\max})$.

$$\begin{aligned} I_{Cd,rms} &= \sqrt{D \cdot \left[I_A^2 \cdot (1-D) + \frac{\Delta i_{LP}^2}{12} \right]} \\ &= \sqrt{I_A^2 \cdot D \cdot (1-D) + \frac{4 \cdot \Delta i_{LP\,\max}^2}{3} \cdot D^3 \cdot (1-D)^2} \end{aligned} \tag{3.11}$$

The following Figure 3.5 shows the current load of the input capacitor C_d with half nominal and nominal load without current ripple ($\Delta i_{LP\,\max} = 0$) and with a very large triangular ripple current of $\Delta\, i_{LP\,\max} = 0.6 \cdot I_{AN}$ in each case.

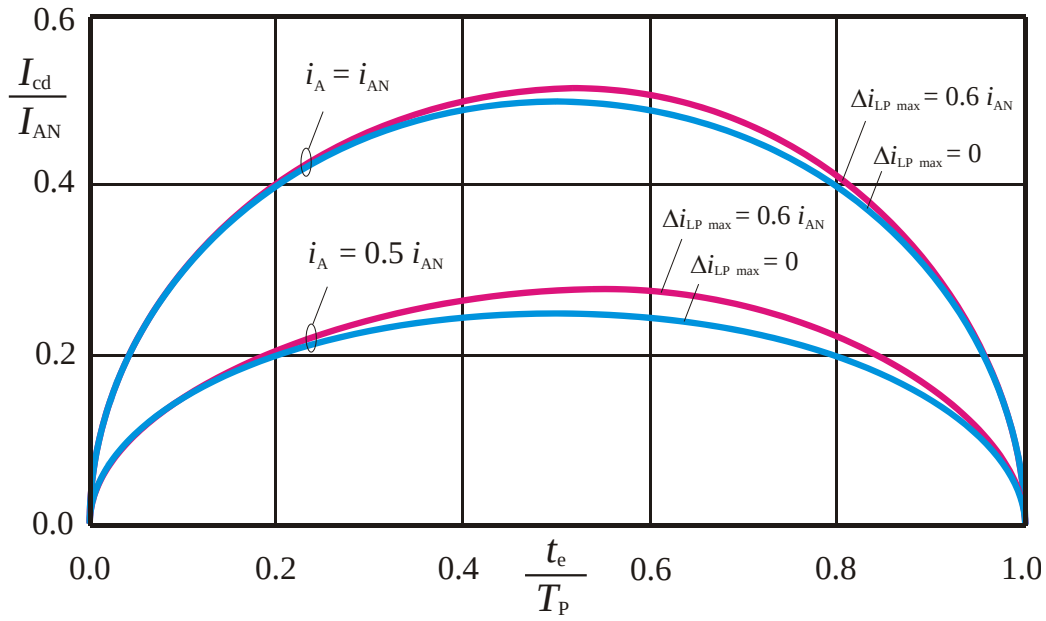

Figure 3.5: Rms-current in the input capacitor with half nominal and nominal load ($i_A = I_{AN}$) [59]

By neglecting the ripple current part ($i_{LP\,\max} = 0$) the current in the capacitor reaches its maximum with 50% duty cycle. During nominal load this maximum value is $I_{Cd} = 0.5 \cdot I_{AN}$. Beyond that it is clearly recognizable that

the influence of the triangular current becomes smaller with increasing current load at the output. During the extremely large current change in the inductance of $\Delta i_{LP}\,\max = 0.6 \cdot I_{AN}$ at nominal load, even only an additional current of approximate 3 % is caused by the triangular current in the capacitor C_d.

At last the necessary capacity in the input of the converter will be calculated. In a single phase buck converter the output current flows in the input of the bridge-leg $i_d = i_A$ during the time periods in that which the high side switch is activated. The difference between this current and the dc-component flows in the capacitor and produce a voltage ripple. This voltage ripple is imposed compared to the dc-voltage in the input.

$$\Delta u_d = \frac{(i_A - i_d) \cdot T_P}{C_d} \cdot \frac{t_e}{T_P} \tag{3.12}$$

So the input capacitor is selected to meet the following conditions:

$$C_d = \frac{T_P \cdot I_{AN}}{4 \cdot \Delta u_{d\,\max}}, \text{with } \Delta u_{d\,\max} \leq 0.01 \cdot u_{dN} \tag{3.13}$$

During the design of the capacitor the permissible static voltage ripple is selected smaller than 1% of the nominal voltage u_{dN}.

The analysis in this section shows that in a single phase buck DC/DC converter, the design of the output filter capacitor depends on the maximum value and the frequency of the ripple current (equivalent to the switching frequency) on inductor, while the factors affecting the capacity of the input filter capacitor are the output current and the operating frequency of the converter. In the case of constant power level, choosing a higher operating frequency allows the use small of inductors and capacitors, and also improves the performance of the converter when encountering step load. However, a high frequency also means higher switching losses, and also extends the frequency range of EMI radiated signals. In high-power applications, the coil design of single phase DCDC converters can become difficult, and the current or voltage stress on the semiconductor can become higher. One effective solution is the multiphase interleaved technology.

3.2.2 Multiphase buck converter

Single phase buck converter can also be built in multiphase interleaved design. For this purpose, the converter circuit is extended by several phases [34, 59–63]. All phases are connected to a common input C_{dN} and output C_{PN} capacitor. The current in these converters is divided in the different phases. The power part of a multiphase buck converter is shown in Figure 3.6.

The subdivision of a converter in several subunits of lower power has several advantages. One of them is the reduction in the current load of the components such as semiconductors, inductor coils or capacitors that is achieved by modularization. This simplifies the construction technique of the subunits. Under this situation, design concepts, such as printed circuit boards can be achieved, which would otherwise be unsuitable for a high current load. Due to the lower current load, the losses per individual component decrease, which is advantageous for the design of the cooling device. On the other hand, redundancy is created. With a suitable design and control, the converter can continue to operate at reduced power if one subunit fails. For vehicles with electric drive such as fuel cell vehicles or series hybrids, the vehicle may still be moved to the nearest station [64].

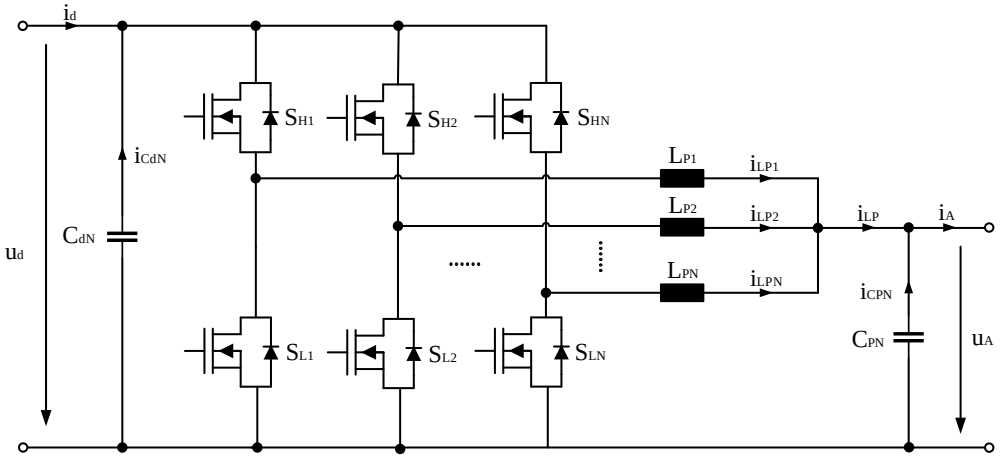

Figure 3.6: Power part of a multiphase DC/DC converter [34]

The different phases are controlled with PWM signals as illustrated in Figure 3.7. All PWMs are identical but with time offset T_P/N or phase shift equals to $2\pi/N$ (N is the number of phases) between two adjacent phases. By interleaved switching of the phases, also a corresponding time shift in the ripple currents in the inductors is achieved.

For a multiphase phase buck converter as example, the voltage and current waveforms in Continuous Conduction Mode (CCM) at the output phase is presented in Figure 3.8. The phases-legs are switched with a time shift of a third pulse period ($T_P/3$) to each other. This has the consequence that the dc-current, superimposed triangular current Δi_{LPN}, is also shifted in the inductor coils. The sum of the alternating currents Δi_{LP} in the three inductor coils results in a triangular current with clearly smaller amplitude and triple frequency. This sum current produces a small AC-voltage at the output capacitor, which consists out of parabolic sections superimposed on the output DC voltage.

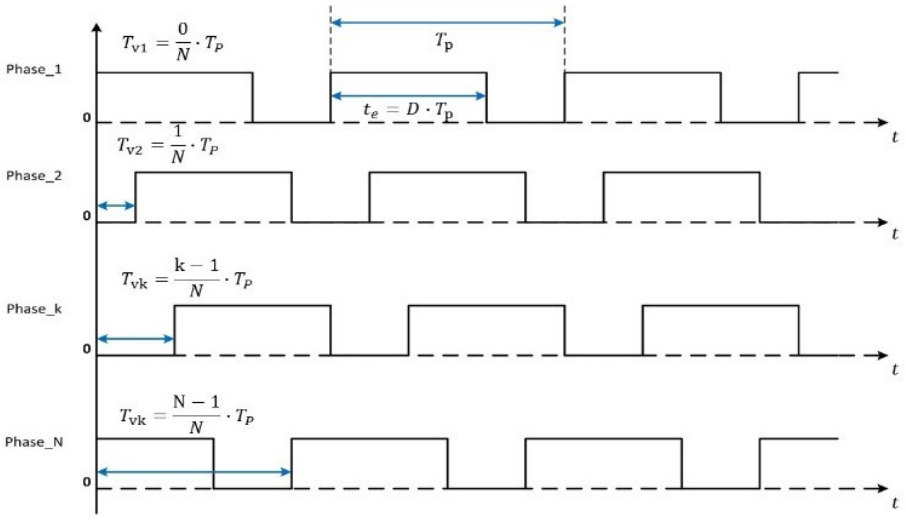

Figure 3.7: PWM signals of the different converter phases [34]

The calculation of the filter circuit inductances for N-phase design can be accomplished exactly in the same way as by single phase circuits. However, it must be considered that the output current is divided across all bridge-legs. That means the maximum current change in the inductances must be referred to the maximum dc-current in the individual bridge-legs. So, the direct current at nominal output current must be divided by the number of bridge-legs. Usually with the design of inductances the maximum current change is between 10% - 30% of the direct current per phase at nominal load.

$$L_{PN} = \frac{u_d \cdot T_P}{4 \cdot \Delta i_{LPN\,\max}} \quad \text{with } \Delta i_{LPN\,\max} = (0.1 - 0.3) \cdot \frac{i_{AN}}{N} \tag{3.14}$$

The inductance efforts of all these converters were always the same. That means each inductance of a N-phase DC/DC converter is around the factor of N larger than the inductance of a single phase converter. As at the same time the current is in each case in the inductances around the factor 1/N smaller, in sum the same inductance effort is needed as with a single phase design.

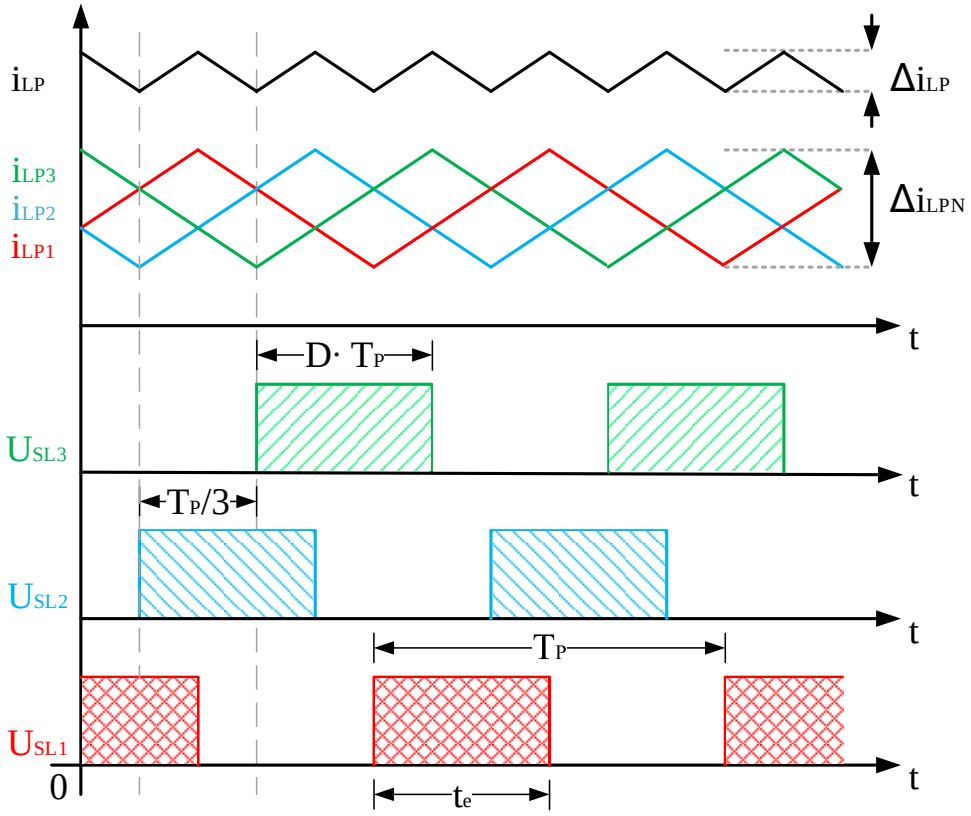

Figure 3.8: PWM signals of the different converter phases [original]

To calculate the total inductor current ripple in CCM, the following equation expresses the total inductor current, $i_{LP}(t)$

$$i_{LP}(t) = i_{LP1}(t) + i_{LP2}(t) + \cdots + i_{LPN}(t) \tag{3.15}$$

Equation 3.15 can be written as a function:

$$i_{LP}(t) = i_{LP1} + i_{LP1}(t - (T_P/N)) + \cdots + i_{LP1}(t - [(N-1) \cdot T_P/N]) \tag{3.16}$$

The inductor current waveform (M_+ and M_-) of one phase are identical to single phase buck converter, is triangular, therefore:

$$M_+ = (u_d - u_A)/L_{PN} = u_d(1-D)/(\cdot L_{PN}),\ 0 < t < D \cdot T_P \tag{3.17}$$

$$M_- = -u_d \cdot D/L_{PN},\ D \cdot T_P < t < T_P \tag{3.18}$$

In the time interval between $m \cdot T_P/N$ and $(m+1) \cdot T_P/N$, where $m = Floor(N \cdot D)$ and returns the maximum integer values less than the argument, the following Equations can be obtained:

$$C_1 = m \cdot M_+ + (N-m-1) \cdot M_- + M_+,\ m \cdot T_P/N < t < D \cdot T_P \tag{3.19}$$

$$C_2 = m \cdot M_+ + (N-m-1) \cdot M_- + M_-,\ m \cdot D \cdot T_P < t < (m+1) \cdot T_P/N \tag{3.20}$$

C_1 and C_2 are constant in related time intervals, and resulted that $C_1 > C_2$, such that the peck current can be given by:

$$\Delta i_{LP} = C_1 \cdot T_P \cdot (D - m/N) \tag{3.21}$$

Finally, according Equations 3.17, 3.18, 3.19 and 3.21, the total inductor current can be obtained:

$$\Delta i_{LP} = u_d \cdot N \cdot T_P[D - (m/N)][(m+1)/N - D]/L_{PN} \tag{3.22}$$

It can be seen that, if duty cycle D equals to k/N ($k = 0, \cdots, N-1$), the sum of ripple current will be absolutely zero.

Similar to single phase buck converter, the inductance of each phase is determined from the maximum voltage-time-area at the inductance in the pulse periods and the defined permissible current change. The following Equation holds:

$$L_{PN} = \frac{u_d \cdot T_P}{\Delta i_{LPN}} \cdot (1-D) \cdot D \tag{3.23}$$

Form Equations 3.22 and 3.23, the ratio between the sum of output ripple current Δi_{LP} and the ripple current Δi_{LPN} in any phase can be described by the following Equation 3.24.

$$\zeta = \frac{\Delta i_{LP}}{\Delta i_{LPN}} = \frac{\Delta i_{CPN}}{\Delta i_{LPN}} = N \cdot \frac{\left(D - \frac{m}{N}\right) \cdot \left(\frac{m+1}{N} - D\right)}{D \cdot (1-D)} \tag{3.24}$$

Figure 3.9 illustrates the ratio of $\Delta i_{LP}/\Delta i_{LPN}$ for different phases (N=2-6). It can be seen that as the number of phases increases, the total inductor ripple current will have a smaller amplitude over a wider duty cycle, and more zero-amplitude of the ripple current will appear.

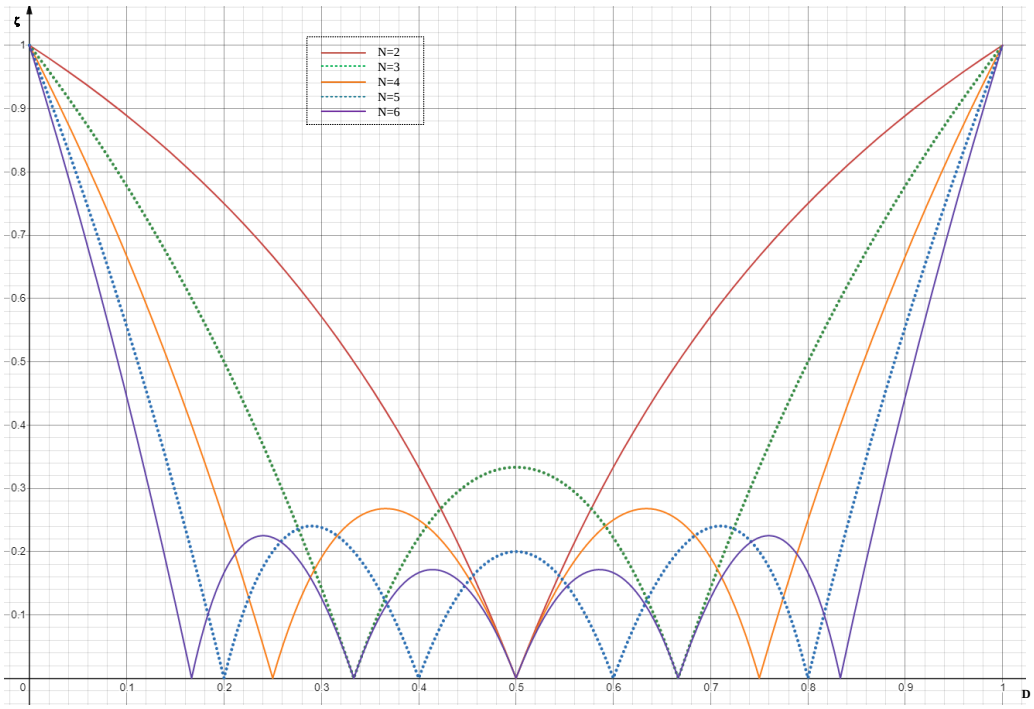

Figure 3.9: Ratio of $\Delta i_{LP}/\Delta i_{LPN}$ for different converter phases (N=2-6) [original]

As it is the case for the single phase converter, the amplitude of the triangular current depends on the duty cycle of the DC/DC converter. Because the duty cycle is in all bridge-legs the same,the current changes are equivalent large during the switch-on duration of all high side MOSFETs.

$$\Delta i_{LPN} = 4 \cdot D \cdot (1 - D) \cdot \Delta i_{LPN\,\max} \tag{3.25}$$

According to Equations 3.24 and 3.25, the current Δi_{CPN} of the output capacitor can be given as:

$$\Delta i_{CPN} = 4 \cdot N \cdot \left(D - \frac{m}{N}\right) \cdot \left(\frac{m+1}{N} - D\right) \cdot \Delta i_{LPN\,\max} \tag{3.26}$$

The rms-value of a triangular current can be calculated by division with square root of twelve. With consideration of this fact the maximum rms-value of the capacitor current can be determined with Equation 3.26 as a function of the duty cycle.

$$I_{CPN,\,rms} = \frac{\Delta i_{CPN}}{\sqrt{12}} \tag{3.27}$$

The current Δi_{CPN} can be rewritten in the following form:

$$\Delta i_{CPN} = \begin{cases} 4 \cdot \left(D - \frac{0}{N}\right) \cdot \left[1 - N \cdot \left(D - \frac{0}{N}\right)\right] \cdot \Delta i_{LPN\,\max} & \text{if } 0 \le D \le \frac{1}{N} \\ 4 \cdot \left(D - \frac{1}{N}\right) \cdot \left[1 - N \cdot \left(D - \frac{1}{N}\right)\right] \cdot \Delta i_{LPN\,\max} & \text{if } \frac{1}{N} \le D \le \frac{2}{N} \\ 4 \cdot \left(D - \frac{2}{N}\right) \cdot \left[1 - N \cdot \left(D - \frac{2}{N}\right)\right] \cdot \Delta i_{LPN\,\max} & \text{if } \frac{2}{N} \le D \le \frac{3}{N} \\ 4 \cdot \left(D - \frac{3}{N}\right) \cdot \left[1 - N \cdot \left(D - \frac{3}{N}\right)\right] \cdot \Delta i_{LPN\,\max} & \text{if } \frac{3}{N} \le D \le \frac{4}{N} \\ \quad \bullet \\ \quad \bullet \\ \quad \bullet \\ 4 \cdot \left(D - \frac{N-1}{N}\right) \cdot \left[1 - N \cdot \left(D - \frac{N-1}{N}\right)\right] \cdot \Delta i_{LPN\,\max} & \text{if } \frac{N-1}{N} \le D \le 1 \end{cases} \tag{3.28}$$

The first and second derivative of this equation shows the maximum values of the capacitor current. The maximum current changes on the points are smaller than the maximum triangular current changes in the inductances by the factor of 1/N.

$$\Delta i_{CPN\,\max} = \frac{1}{N} \cdot \Delta i_{LPN\,\max} \qquad \text{on the points } D = \sum_{n=0}^{n=N-1} \frac{1 + 2 \cdot n}{2 \cdot N} \tag{3.29}$$

After combining Equations 3.14 and 3.29, the Ratio range of sum of ripple currents Δi_{CPN} of all phases N and the max inductor current $\Delta i_{LPN\,\max}$ of one phase, $N = 1$ is illustrated in Figure 3.10.

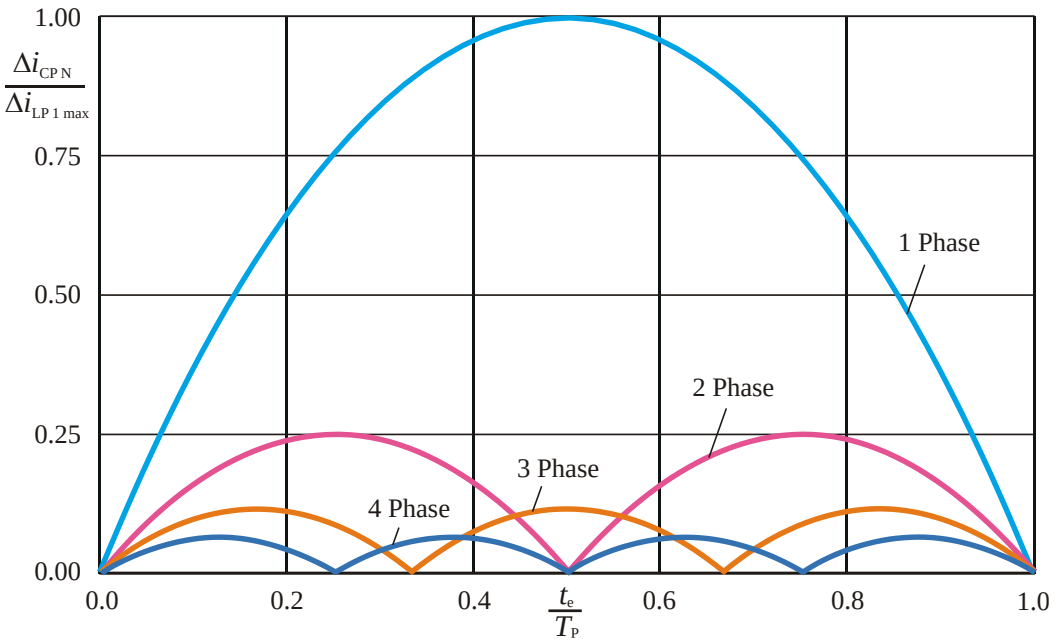

Figure 3.10: Ratio Current of $\Delta i_{CPN}/\Delta i_{LPN\,\max}$ of different phases (N=1-4)it must be considered that the output current is divided across all bridge-legs [34]

The triangular current sum of all inductor coils flows over the capacitor and produce an AC-voltage at the output. In principle from the resulting maximum current-time-area of one phase and the maximum permissible voltage change, the capacity can be calculated. But, by the number of phases, the current sum in the capacitor is reduced by factor of 1/N, and the pulse frequency of the capacitor current is increased by factor of N. This must be considered for the capacitor calculation. For the design of the capacitor, the permissible static voltage ripple is selected usually smaller than 1% of the nominal output voltage u_{AN}.

$$C_{PN} = \frac{T_P \cdot \Delta i_{LPN\,\max}}{8 \cdot N^2 \cdot \Delta u_{A\,\max}}, \text{with } \Delta u_{A\,\max} \leq 0.01 \cdot u_{AN} \tag{3.30}$$

Using the same analysis method as for single phase buck converter, the input capacitor current $I_{Cd\ N}$ of multiphase buck converter can be calculated. The result is divided into tow parts, The first part $I_{Cd\ N\ \Pi}$ depends on the output current and the second part $I_{Cd\ N\ \Delta}$ depends on the triangular inductance current, and they are expressed in the following Equations:

$$
I^2_{Cd\ N\ \Pi} =
\begin{cases}
\dfrac{I_A^2}{N}\cdot\left(D-\dfrac{0}{N}\right)\cdot\left[1-N\cdot\left(D-\dfrac{0}{N}\right)\right]\cdot\Delta i_{LPN\max} & \text{if } 0\le D\le\dfrac{1}{N}\\
\dfrac{I_A^2}{N}\cdot\left(D-\dfrac{1}{N}\right)\cdot\left[1-N\cdot\left(D-\dfrac{1}{N}\right)\right]\cdot\Delta i_{LPN\max} & \text{if } \dfrac{1}{N}\le D\le\dfrac{2}{N}\\
\dfrac{I_A^2}{N}\cdot\left(D-\dfrac{2}{N}\right)\cdot\left[1-N\cdot\left(D-\dfrac{2}{N}\right)\right]\cdot\Delta i_{LPN\max} & \text{if } \dfrac{2}{N}\le D\le\dfrac{3}{N}\\
\dfrac{I_A^2}{N}\cdot\left(D-\dfrac{3}{N}\right)\cdot\left[1-N\cdot\left(D-\dfrac{3}{N}\right)\right]\cdot\Delta i_{LPN\max} & \text{if } \dfrac{3}{N}\le D\le\dfrac{4}{N}\\
\bullet\\
\bullet\\
\bullet\\
\dfrac{I_A^2}{N}\cdot\left(D-\dfrac{N-1}{N}\right)\cdot\left[1-N\cdot\left(D-\dfrac{N-1}{N}\right)\right]\cdot\Delta i_{LPN\max} & \text{if } \dfrac{N-1}{N}\le D\le 1
\end{cases}
\tag{3.31}
$$

$$
I^2_{Cd\ N\ \Delta} =
\begin{cases}
\gamma\cdot(D-1)^2\cdot\left[1^2\cdot\left(D-\dfrac{0}{N}\right)^3-0^2\cdot\left(D-\dfrac{1}{N}\right)^3\right] & \text{if } 0\le D\le\dfrac{1}{N}\\
\gamma\cdot(D-1)^2\cdot\left[2^2\cdot\left(D-\dfrac{1}{N}\right)^3-1^2\cdot\left(D-\dfrac{2}{N}\right)^3\right] & \text{if } \dfrac{1}{N}\le D\le\dfrac{2}{N}\\
\gamma\cdot(D-1)^2\cdot\left[3^2\cdot\left(D-\dfrac{2}{N}\right)^3-2^2\cdot\left(D-\dfrac{3}{N}\right)^3\right] & \text{if } \dfrac{2}{N}\le D\le\dfrac{3}{N}\\
\gamma\cdot(D-1)^2\cdot\left[4^2\cdot\left(D-\dfrac{3}{N}\right)^3-3^2\cdot\left(D-\dfrac{4}{N}\right)^3\right] & \text{if } \dfrac{3}{N}\le D\le\dfrac{4}{N}\\
\bullet\\
\bullet\\
\bullet\\
\gamma\cdot(D-1)^2\cdot\left[N^2\cdot\left(D-\dfrac{N-1}{N}\right)^3-(N-1)^2\cdot\left(D-\dfrac{N}{N}\right)^3\right] & \text{if } \dfrac{N-1}{N}\le D\le 1
\end{cases}
$$

$$
\gamma=\frac{4\cdot N\cdot\Delta i^2_{LPN\max}}{3}
\tag{3.32}
$$

The geometric summation of these two components $I_{Cd\ N}$, results in the total capacitance current value of the N phase DC/DC converter at any duty cycle.

$$I_{Cd\ N,\ rms} = \sqrt{I^2_{Cd\ N\ \Pi} + I^2_{Cd\ N\ \Delta}} \tag{3.33}$$

It can be rewritten in the following form:

$$I_{Cd\ N,\ rms} = \sqrt{I_A^2 \left(D - \frac{m}{N}\right) \cdot \left(\frac{m+1}{N} - D\right) + \frac{4 \cdot N \cdot \Delta i^2_{LPN\,\max}}{3} \cdot (D-1)^2 \cdot \left[(m+1)^2 (D - \frac{m}{N}^3) - m^2 (D - \frac{m+1}{N})^3\right]} \tag{3.34}$$

Figure 3.11 shows the rms-current in the input capacitor for multiphase converters for rated output power. The current load of the capacitor decreases with the increasing number of phases. The capacitor current can be split in two different components: a rectangular part and a triangular part. The influence of the rectangle rms-component dominate clearly (dotted lines, $\Delta i_{LPN\,\max} = 0$). The maximum current from the rectangle part is smaller by a factor of 1/N for a N-phase converter. The triangular current is independent of the output power of the converter. In case of rated power the additional load from the triangular current in the capacitors is very small. For an extreme high current change $\Delta i_{LPN\,\max} = 0.6 \cdot I_{AN}/N$, the additional current is only approx. 3% from the maximum current value.

Now the necessary capacity in the input of the DC/DC converter will be calculated. If in single phase converters the high side switch is activated, the output current flows also in the input of the bridge-leg id = iA. The difference between this current and the dc-component flows into the capacitor and produces a voltage ripple. For multiphase converters it must be considered that the current per phase leg is smaller by a factor of 1/N, and the pulse frequency of the capacitor current is increased by a factor of N. With these conditions the input capacity of multiphase converters can easily be calculated for nominal output current.

$$C_{dN} = \frac{T_P \cdot I_{AN}}{4 \cdot N^2 \cdot \Delta u_{d\,\max}}, \text{with } \Delta u_{d\,\max} \leq 0.01 \cdot u_{dN} \tag{3.35}$$

Comparing the characteristics of single phase and multiphase buck converter by analysis, they can be summarized as follows:

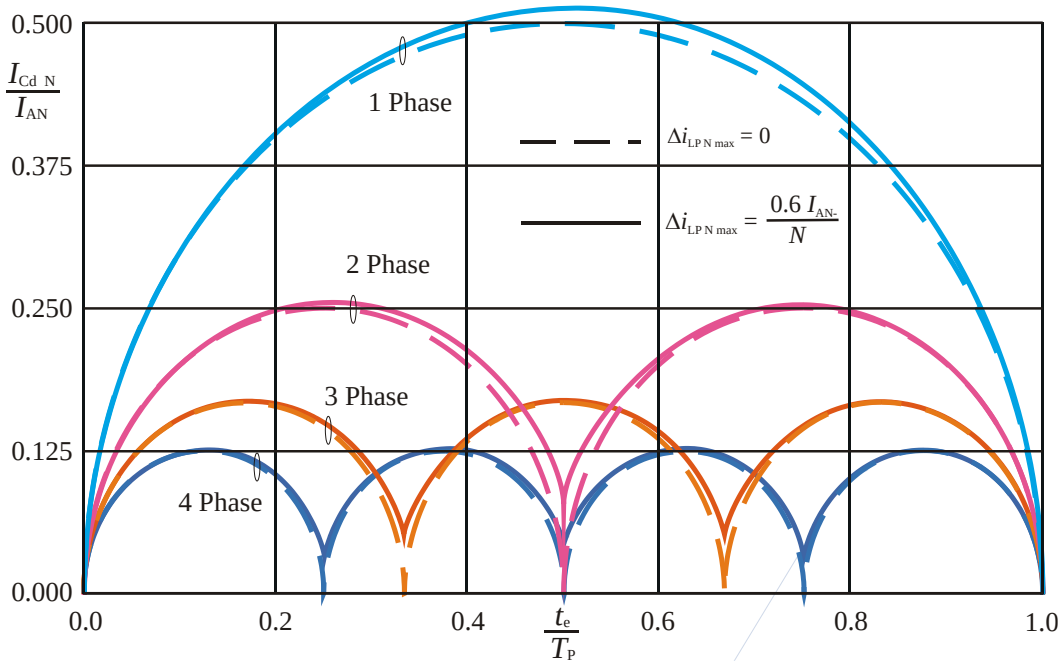

Figure 3.11: Ratio curve of the input capacitor current $I_{Cd}\ N/I_{AN}$ for multiphase DC/DC converter (N=1-4), $I_{AN} = i_{AN}$ it must to be considered that the output current is divided across all bridge-legs [34]

- In multiphase parallel system, the power of individual module is only 1/N of the total power, semiconductor device current stress is reduced, but the number is increased by a factor of N. This construction allows for even distribution of power and heat.

- With the same switching frequency, multiphase drive control reduces output and input current ripple, but increases its frequency. The size of the input-output filter capacitors can thus be reduced, facilitating input-output filtering networks and EMI design. For example, metal film capacitors can be used instead of electrolytic capacitors.

- Redundant design improves system reliability.

In general, multiphase parallel technology can bring many benefits to the overall system, cost reduction, size reduction and reliability increase. As the current RMS value of the capacitor is significantly reduced, the power loss on the capacitor is reduced and the temperature rise is effectively limited, which will extend the life of the capacitor. These advantages, especially the reduction of ripple current, demonstrate the suitability of a multiphase parallel DC/DC converter for use in the powertrain of a fuel cell electric vehicle.

The input current spectra of single and multiphase buck converter (4 phase) with different duty cycles are presented separately in Figure 3.12 and Figure 3.13, and the switching frequency is 50kHz. Therefore, the fundamental frequency of single phase buck converter is 50kHz, and for the 4 phase buck converter is 200kHz.

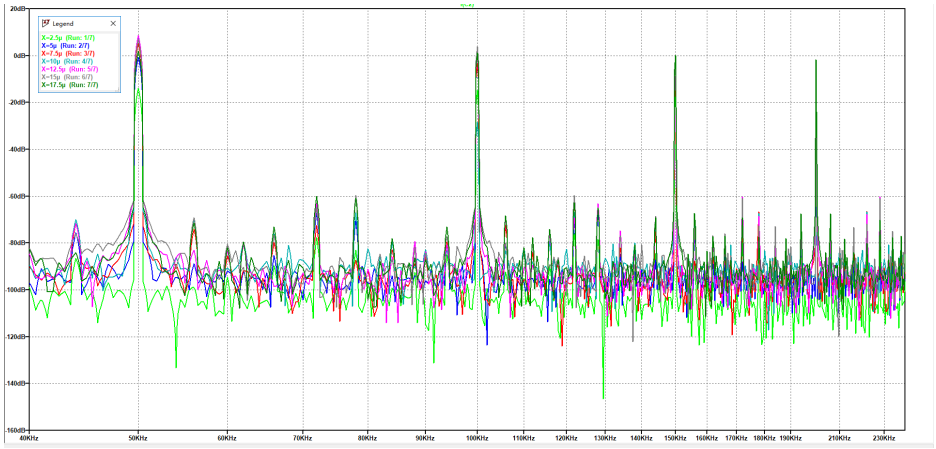

Figure 3.12: Input current spectra of a single phase buck converter with different duty cycles (using LT-spice FFT analyze) [original]

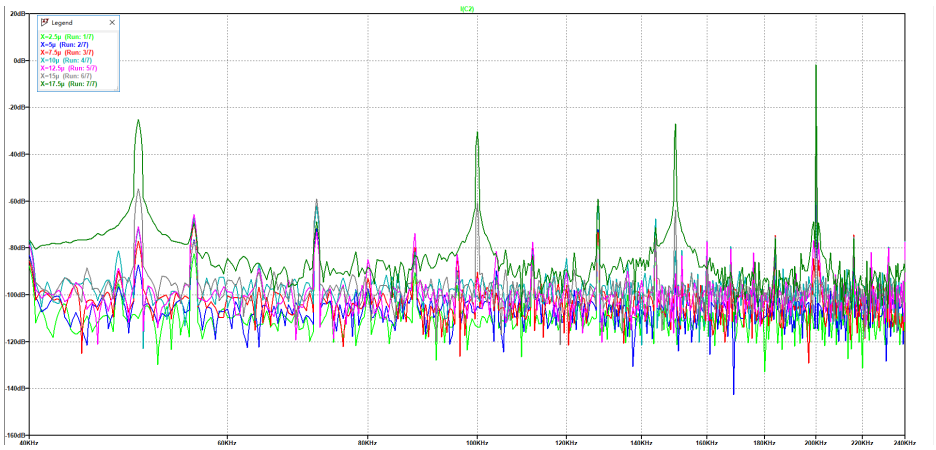

Figure 3.13: Input current spectra of a 4 phase buck converter with different duty cycles (using LT-spice FFT analyze) [original]

Comparing the above figures, it can be seen that in the multiphase buck converter, some harmonic currents are attenuated.

3.3 Control design of multiphase converter in FCEV

Usually switching power supplies have high order, nonlinear, and time-varying characteristics that make difficult to control them using classical control theory. The AC small signal model method is based on the state space averaging model method to linearize a switching cycle segment, which can establish a more accurate model [65–69].

3.3.1 Small signal model of single and multiphase buck converter

Single phase buck converter

When analyzing single phase and multiphase buck converters, the following parameters need to be considered:

- Equivalent series resistance of the inductor is R_{LP}.
- Output capacitor equivalent series resistance is R_{CP}.
- Buck converter is operating CCM.
- Switching frequency f_s is larger than the frequency of the AC small signal disturbance component.

In a single phase buck converter, the equivalent circuit diagrams of the switch in the on state and off state are shown in Figure 3.14.

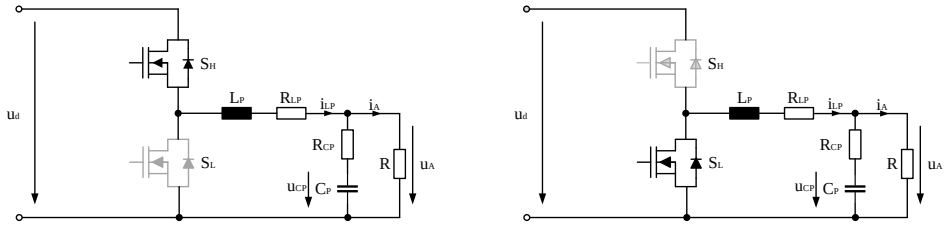

(a) ON State:0-te (b) OFF State:te-Tp

Figure 3.14: Equivalent circuit of CCM Buck converter in one period [original]

For the buck converter, a linearized model can be expressed in state space form:

$$\begin{aligned} \frac{dx}{dt} &= A \cdot x + B \cdot u \\ y &= E \cdot x + F \cdot u \end{aligned} \tag{3.36}$$

where the state variables are the inductor current, the voltage of output capacitor and the input variable is input DC voltage. The output variables are the output voltage and the input current.

$$x = \begin{bmatrix} i_{LP} \\ u_{CP} \end{bmatrix} \qquad u = \begin{bmatrix} u_d \\ 0 \end{bmatrix} \qquad y = \begin{bmatrix} i_d \\ u_A \end{bmatrix}$$

According to the Equation 3.36, The state space averaging equation for the two states in one period of the buck converter can be expressed as:

$$\frac{d}{dt}\begin{bmatrix} \bar{i}_{LP}(t) \\ \overline{u}_{CP}(t) \end{bmatrix} = \begin{bmatrix} -\frac{RR_{CP}+(R+R_{CP})R_{LP}}{(R+R_{CP})L} & -\frac{R}{(R+R_{CP})L} \\ \frac{R}{(R+R_{CP})C} & -\frac{1}{(R+R_{CP})C} \end{bmatrix} \begin{bmatrix} \bar{i}_{LP}(t) \\ \overline{u}_{CP}(t) \end{bmatrix} + \begin{bmatrix} \frac{d}{L} \\ 0 \end{bmatrix} \overline{u}_d(t) \tag{3.37}$$

$$\begin{bmatrix} \bar{i}_A(t) \\ \overline{u}_A(t) \end{bmatrix} = \begin{bmatrix} d & 0 \\ \frac{RR_C}{R+R_C} & \frac{R}{R+R_C} \end{bmatrix} \begin{bmatrix} \bar{i}_{LP}(t) \\ \overline{u}_{CP}(t) \end{bmatrix} \tag{3.38}$$

The output voltage and the voltage across output capacitor satisfy the following relationship:

$$\overline{u}_{CP} = -R_{CP} \cdot \bar{i}_{LP} + \frac{R + R_{CP}}{R} \cdot \overline{u}_A \tag{3.39}$$

Substituting the Equation 3.39 into Equations 3.37 and 3.38 provides:

$$\frac{d}{dt}\begin{bmatrix} \bar{i}_{LP}(t) \\ \overline{u}_{CP}(t) \end{bmatrix} = \begin{bmatrix} -\frac{R_{LP}}{L} & -\frac{1}{L} \\ \frac{1}{C_P} & -\frac{1}{RC_P} \end{bmatrix} \begin{bmatrix} \bar{i}_{LP} \\ \overline{u}_{CP} \end{bmatrix} + \begin{bmatrix} \frac{d}{L} \\ 0 \end{bmatrix} \overline{u}_d \tag{3.40}$$

$$\begin{bmatrix} \bar{i}_d \\ \overline{u}_A \end{bmatrix} = \begin{bmatrix} d & 0 \\ 0 & 1 \end{bmatrix} \begin{bmatrix} \bar{i}_{LP} \\ \overline{u}_A \end{bmatrix} \tag{3.41}$$

from Equation 3.40 and 3.41, the schematic diagram of state space model for the buck converter is shown in Figure 3.15.

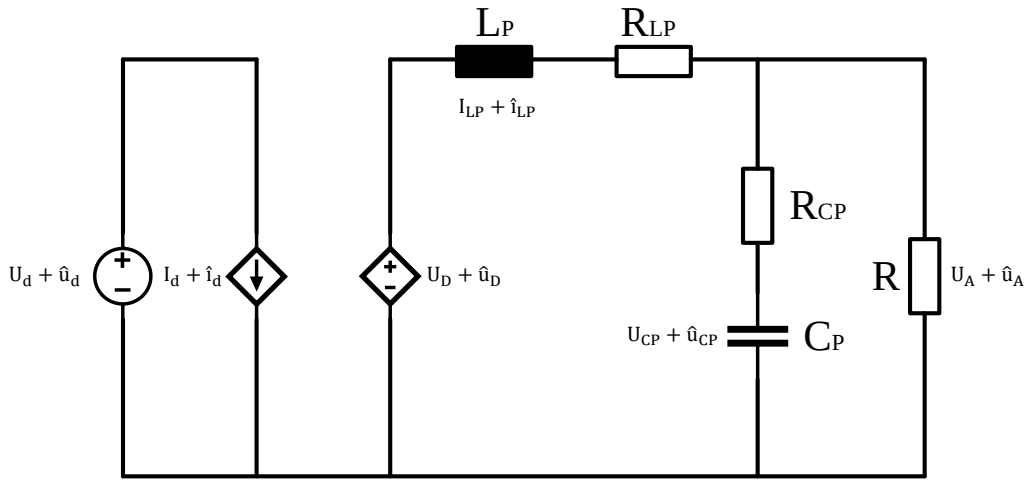

Figure 3.15: The schematic diagram of state space model for the buck converter operating in the CCM [original]

Where the controlled current source and the controlled voltage source are denoted as:

$$\begin{cases} \bar{i}_d = d \cdot \bar{i}_{LP} \\ \overline{u}_D = d \cdot \overline{u}_d \end{cases} \tag{3.42}$$

Each signal in the formula can be regarded as a superposition of a DC signal and an AC signal

$$\begin{cases} \overline{u}_d = U_d + \hat{u}_d \\ \bar{i}_d = I_d + \hat{i}_d \\ \overline{u}_D = U_D + \hat{u}_D \\ \bar{i}_{LP} = I_{LP} + \hat{i}_{LP} \\ \overline{u}_{CP} = U_{CP} + \hat{u}_{CP} \\ \overline{u}_A = U_A + \hat{u}_A \\ d = D + \hat{d} \end{cases} \tag{3.43}$$

Among them, $\overline{u}_d$, $\bar{i}_d$, $\overline{u}_D$, $\bar{i}_{LP}$, $\overline{u}_{CP}$, $\overline{u}_A$ and d are the signal in time domain, U_d, I_d, U_D, I_{LP}, U_{CP}, U_A and D refer to the DC component of the signals, $\hat{u}_d$, $\hat{i}_d$, $\hat{u}_D$, $\hat{i}_{LP}$, $\hat{u}_{CP}$, $\hat{u}_A$ and $\hat{d}$ refer to the AC component of signals. Substituting Equation 3.43 into Equations 3.37 and 3.38. The higher order quantities of the AC component can be neglected during the calculation because the DC

component is much larger than the AC component. Eventually, the DC component of state equation for buck converter in CCM is described by Equation 3.44, and the AC component of state equation for buck converter in CCM is given by Equations 3.45 and 3.46.

$$\begin{bmatrix}0\\0\end{bmatrix} = \begin{bmatrix} -\frac{RR_{CP}+(R+R_{CP})R_{LP}}{(R+R_{CP})L} & -\frac{R}{(R+R_{CP})L} \\ \frac{R}{(R+R_{CP})C} & -\frac{1}{(R+R_{CP})C} \end{bmatrix} \begin{bmatrix} I_{LP} \\ U_{CP} \end{bmatrix} + \begin{bmatrix} \frac{D}{L} \\ 0 \end{bmatrix} U_d \tag{3.44}$$

$$\hat{i}_d(t) = D \cdot \hat{i}_{LP}(t) + I_{LP} \cdot \hat{d}(t) \tag{3.45}$$

$$\begin{aligned} \frac{d}{dt}\begin{bmatrix}\bar{i}_{LP}(t)\\ \bar{u}_{CP}(t)\end{bmatrix} = &\begin{bmatrix} -\frac{RR_{CP}+(R+R_{CP})R_{LP}}{(R+R_{CP})L} & -\frac{R}{(R+R_{CP})L} \\ \frac{R}{(R+R_{CP})C} & -\frac{1}{(R+R_{CP})C} \end{bmatrix} \begin{bmatrix}\hat{i}_{LP}(t)\\ \hat{u}_{CP}(t)\end{bmatrix} + \\ &\begin{bmatrix}\frac{D}{L}\\ 0\end{bmatrix} \hat{u}_d(t) + \begin{bmatrix}\frac{1}{L}\\ 0\end{bmatrix} u_d \cdot \hat{d}(t) \end{aligned} \tag{3.46}$$

According to Equations 3.45 and 3.46, an equivalent transformer model circuit can be established in Figure 3.16

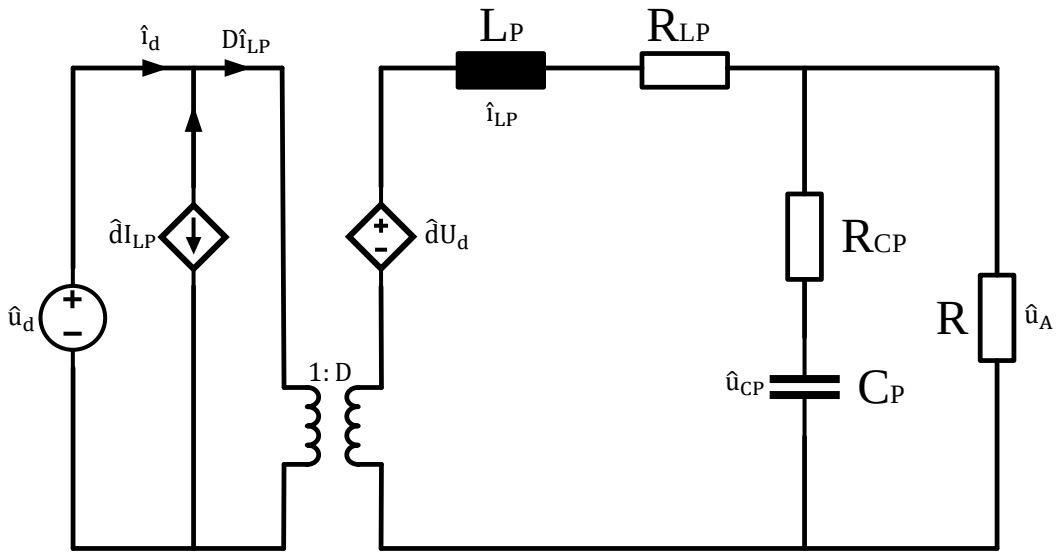

Figure 3.16: Small signal equivalent AC circuit of the single phase buck converter [original]

The analysis of the small signal model is usually performed in the complex frequency domain, and after the Laplace transformation, the following equation

can be obtained:

$$\begin{cases} \hat{i}_{LP}(s) = \hat{u}_A(s)(\dfrac{sC_P}{1+sC_PR_{CP}} + \dfrac{1}{R}) \\ \hat{u}_D = \hat{d}(s)U_d + \hat{u}_d(s)D = (sL_P + R_{LP})\hat{i}_{LP}(s) + \hat{u}_A(s) \end{cases} \tag{3.47}$$

The transfer functions of "The output voltage to input voltage" and "The output voltage to duty cycle" can be derived for Equation 3.47 and characterized by:

$$\begin{cases} \left.\dfrac{\hat{u}_A(s)}{\hat{u}_d(s)}\right|_{\hat{d}(s)=0} = \dfrac{(R+sC_PRR_{CP})D}{s^2(R+R_{CP})L_PC_P + s(C_PRR_{LP} + C_PR_{CP}R_{LP} + C_PRR_{CP} + L_P) + (R+R_{LP})} \\ \left.\dfrac{\hat{u}_A(s)}{\hat{d}(s)}\right|_{\hat{u}_d(s)=0} = \dfrac{(R+sC_PRR_{CP})U_d}{s^2(R+R_{CP})L_PC_P + s(C_PRR_{LP} + C_PR_{CP}R_{LP} + C_PRR_{CP} + L_P) + (R+R_{LP})} \end{cases} \tag{3.48}$$

Small signal model of the multiphase buck converter

The AC small signal model of the multiphase converter can be described similarly to that of a single phase converter, and the equivalent AC circuit is shown in Figure 3.17.

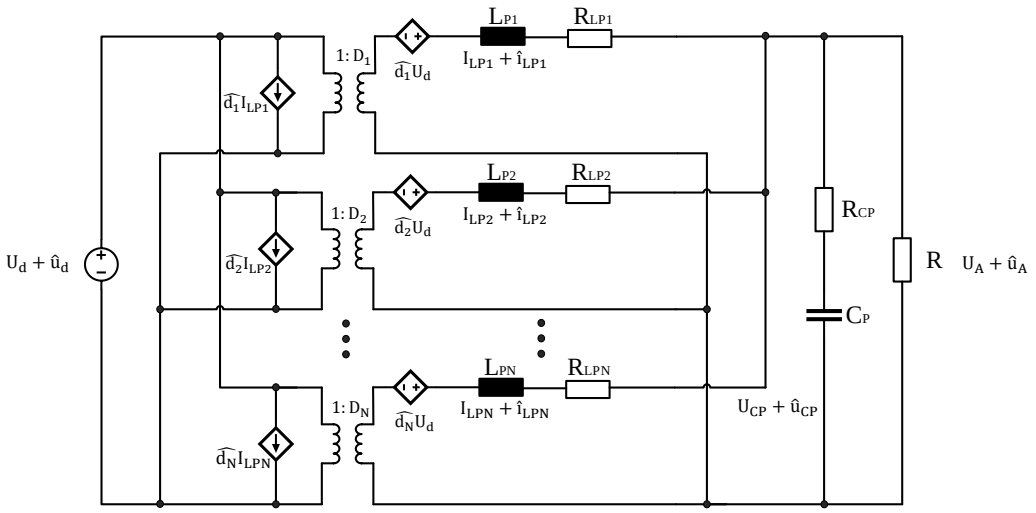

Figure 3.17: Small signal equivalent AC circuit of multiphase buck converter [original]

Kirchhoff's laws can be used to solve the transfer function of any two variables in the complex frequency domain. To simplify the calculations, first define the parameters:

$$\begin{cases} \alpha = sL_{Pk} + R_{LPk}, \text{ where } k = 1.2.3 \cdots N \\ \beta = \left(\dfrac{1}{sC_P} + R_{CP}\right) // R = \dfrac{R(1 + sC_P R_{CP})}{1 + sC_P(R + R_{CP})} \end{cases} \tag{3.49}$$

In the multiphase buck converter, because the parameters of all phases are the same, i.e. all α are identical, the transform functions of duty cycle to output voltage and duty cycle to inductor current are:

$$G_{u_a,\ d}(s) = \frac{U_d \beta}{\alpha + N\beta} \tag{3.50}$$

$$G_{i_{LPk},\ d}(s) = \frac{U_d[\alpha + (N-1)\beta]}{\alpha^2 + N\alpha\beta} \tag{3.51}$$

According to Equation 3.50, the equivalent inductance L_{eq} of a multiphase buck converter is equal to the value of the inductance of the branch phase divided by the number of phases N. Figure 3.18 shows the bode diagrams of the 1 to 6 phase buck converter of transfer function $G_{u_a,\ d}(s)$. It can be seen that with increasing phase number, the bandwidth of multiphase buck converters is getting wider. Similarly, the closed-loop step response of the multiphase buck converter in Figure 3.19 verifies this. Obviously, a wider bandwidth provides a faster response of the system.

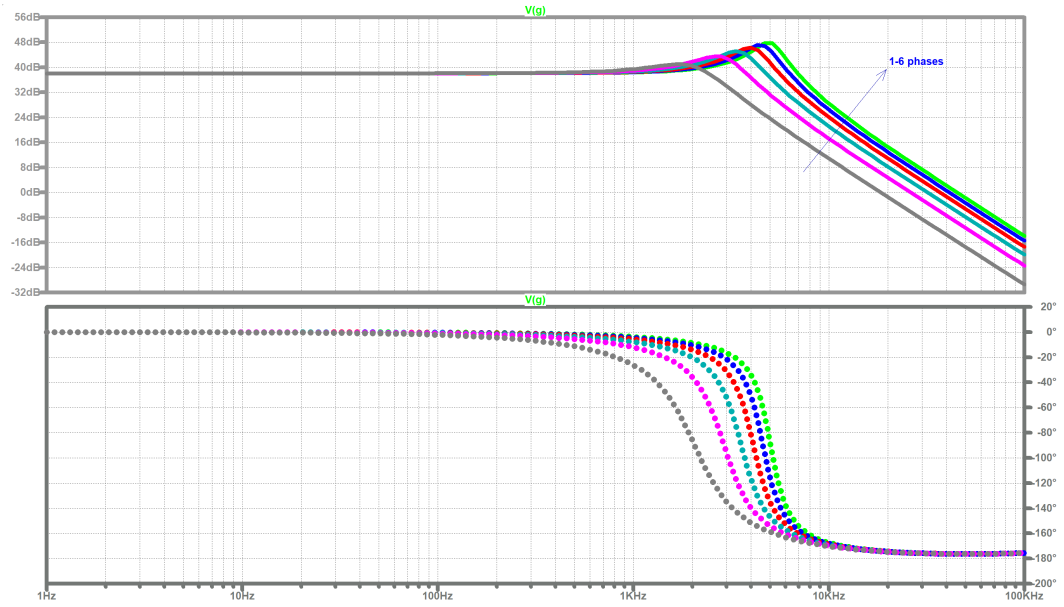

Figure 3.18: Plots for 1-6 phases buck converter: Bode diagram of $G_{u_a,\ d}(s)$ [original]

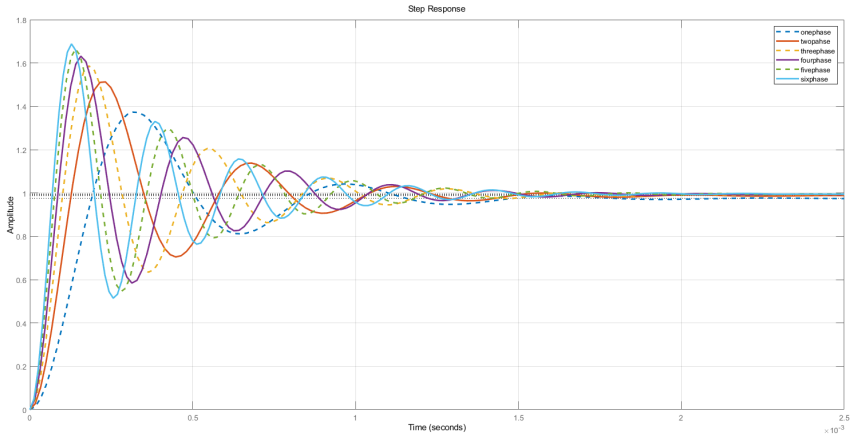

Figure 3.19: Plots for 1-6 phases buck converter: closed loop step response of $G_{u_a,\ d}(s)$ [original]

3.3.2 Current sharing controller of multiphase buck converter

In a multiphase parallel converter, the current sharing of all phases does also need attention [70]. In the multiphase converter, the current of each phase branch will be uneven due to the difference of component parameters or PWM control signal. Figure 3.20 shows the current imbalance caused by the difference of inductor series resistance. If the converter is operated for a long time under high power, it will cause the heat generation of one branch is much larger than the other branches, which will reduce the service life of the components and the reliability of the system. In order to quantify the unbalanced phenomenon, a coefficient CS_error denoting current sharing error is introduced, which can be expressed as:

$$CS_{error} = \frac{\max|I_x - I_y|}{\sum_1^N I_k/N} \tag{3.52}$$

where $\max|I_x - I_y|$ is the maximum current difference of all branches and the denominator is the average of all branch output currents. When the coefficient is less than 10%, this means the current sharing performance is qualified. Figure 3.21 shows the currents of inductors through the current sharing method. It can be seen that the current equalization effect reaches the requirement. Presently, there are many current-sharing methods, such as: master-slave current with dedicated master [71], average current with democratic control [72] and maximum current with automatic master control [73].

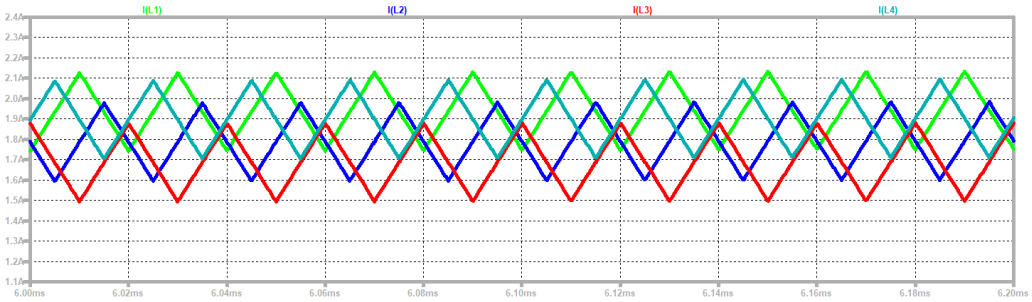

Figure 3.20: Inductor currents without current sharing control [original]

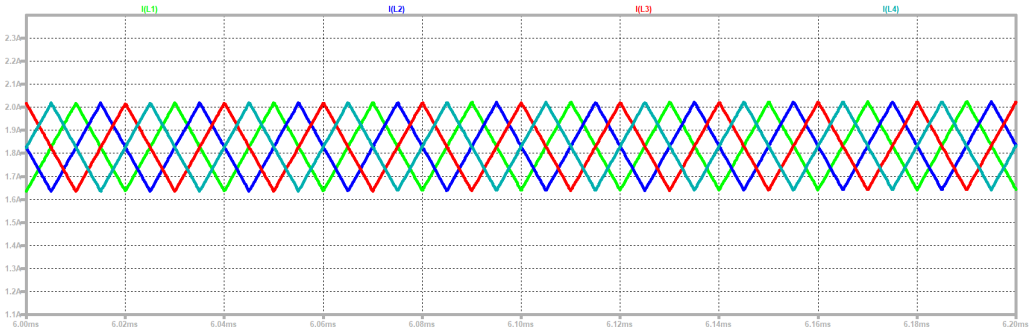

Figure 3.21: Inductor currents with current sharing control [original]

- **Master-slave current averaging method**
  In this mode, one phase of the converter is selected as the master module, and the rest of the phases are all slave modules. Figure 3.22 shows the schematic diagram of a master-slave module with voltage and current loop control. U_r is the reference voltage of the converter, U_m is the feedback signal of the output voltage. After the voltage error amplifier, the voltage error U_e is obtained, which is used as the current reference of the master module, and after comparing with the actual measured current value U_{I_LPK}, it generates the control voltage U_{ck} to modulate the PWM output. Each slave module uses the same voltage follower output U_e as the reference module, so the current of all slave modules remains basically the same as the master module, thus realizing the current equalization.

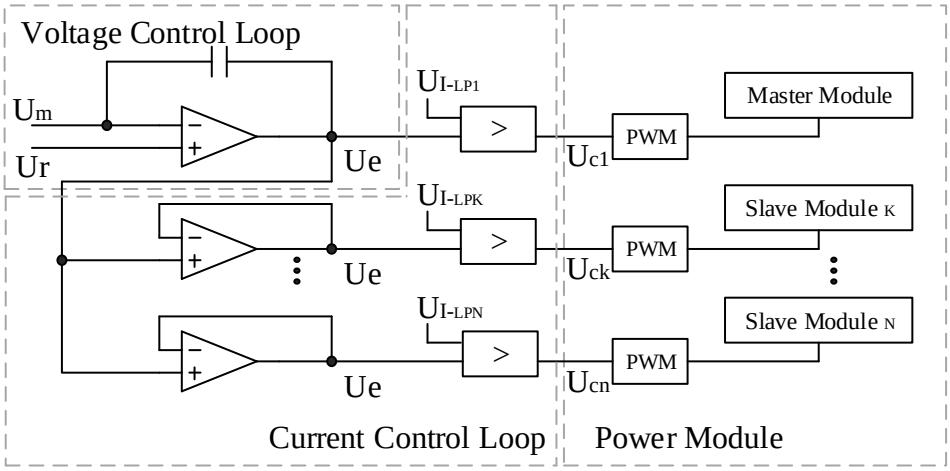

Figure 3.22: Schematic of master-slave current sharing control [original]

- **Average current sharing control**
  In the average and maximum current sharing control mode, current sharing bus (CS_bus) is used in control circuit, and all phases use the same bus voltage as current control reference, so that the current in all phases will be balanced. The difference is that the reference value used in the average current sharing method is the average of the current sum of all phases, i.e.

$$CS\_bus = (U_{I_{LP1}} + \cdots + U_{I_{LPN}})/N \tag{3.53}$$

  The left part of Figure 3.23 illustrates the schematic of average current sharing control.

- **Maximum current sharing control**
  With maximum current sharing mode, the reference value is the maximum current of all phases, and during operation, the maximum current value in all phases automatically becomes the master. i.e.

$$CS\_bus = \max(U_{I_{LP1}}, U_{I_{LP2}}, \cdots U_{I_{LPN}}) \tag{3.54}$$

  The right part of Figure 3.23 illustrates the schematic of maximum current sharing control.

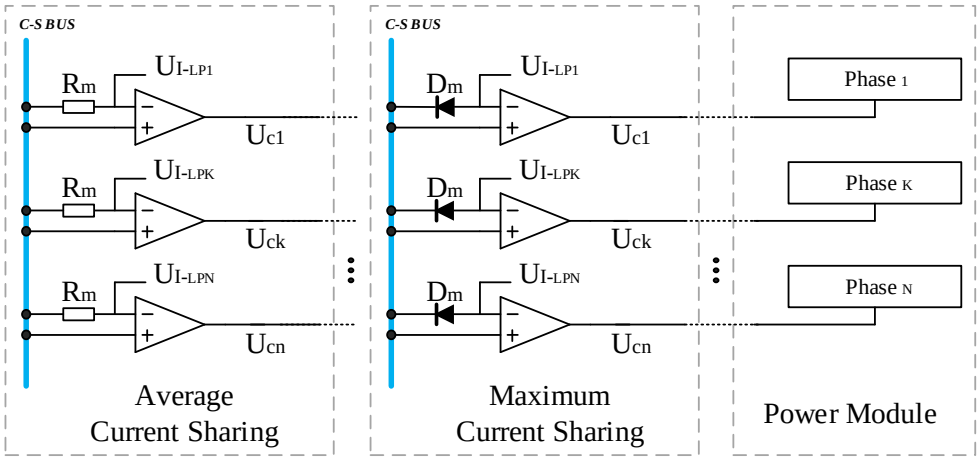

Figure 3.23: Schematic of average and maximum current sharing control [original]

- **Current sharing via MCU**
  Nowadays, high performance microprocessors are widely used in digital converters to generate PWM drive signals, measure voltage and current values, and complete the digital controller at the same time. Obviously, it is also possible to digitize and implement the various methods of current sharing mentioned above, but the disadvantage is a more complex control algorithms. The following diagram illustrates a digital implementation of the average current sharing control using a MCU. Figure 3.24 shows the schematic of current sharing of multiphase buck converter via MCU. The detected currents and voltages are processed by external circuitry and converted to digital values by the ADC. After digital processing in MCU, it becomes the parameter that controls the PWM wave. The advantage of using this approach is that complex external hardware circuits for current sharing calculation can be omitted.

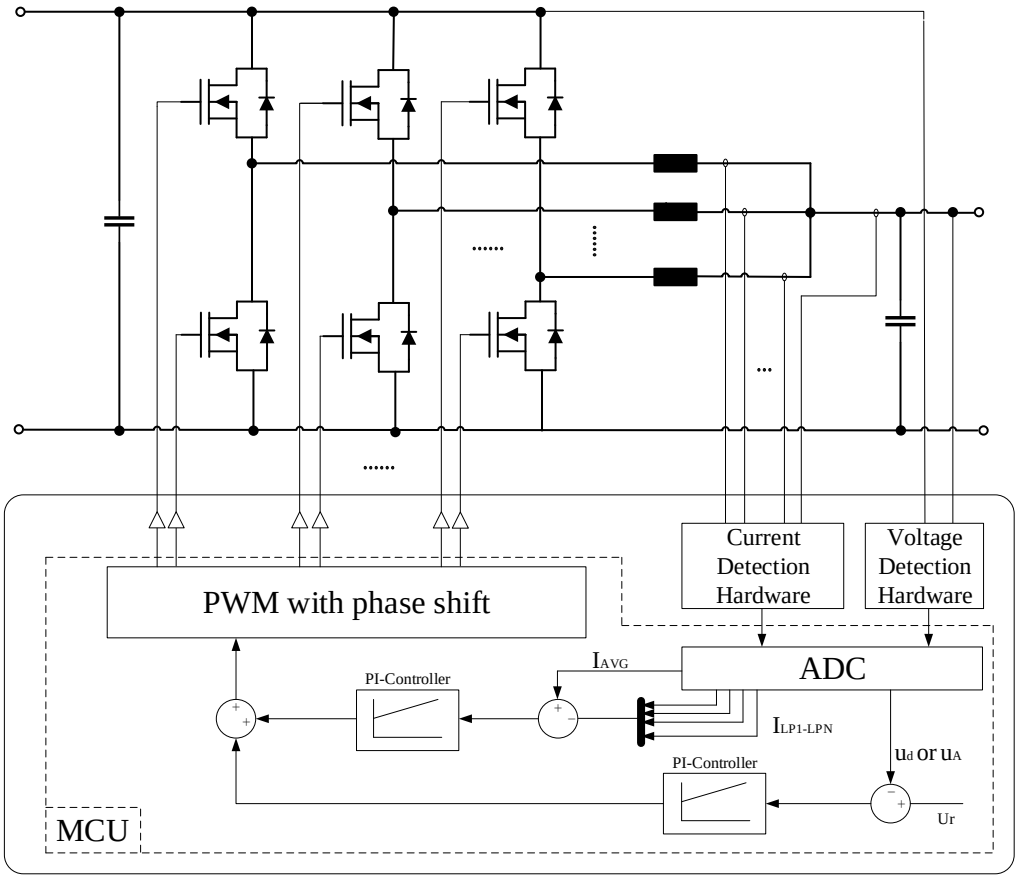

Figure 3.24: Current sharing of multiphase buck converter via MCU [original]

3.4 Implementation and experimental results of a Six-phase buck converter

The practical realization of the power part with the half bridges and the gate driver circuits is shown in Figure 3.25. The size of the board is 30cm x 20cm and the height including heat sink is 12cm. Under the board, copper bars are attached to carry the current of up to 180A. In the Figure one power board side with the gate driver circuits of three half bridges can be seen. The other three half-bridges with gate driver circuits are placed on the opposite side (Not visible!). To each gate driver circuit a cable for power supply and a coaxial cable, that transmits the PWM-signals, is connected.

Figure 3.25: Power part of the converter with gate-driver circuits [34]

The filter circuit board of the converter, shown in Figure 3.26, has the same size and can be screwed under the power semiconductor board. The inductor coils at the output of each half bridge are connected on this board. The coil former and the covers of the coils (yellow) are made in 3D-printing process. After that, the coil bodies were provided with copper windings.

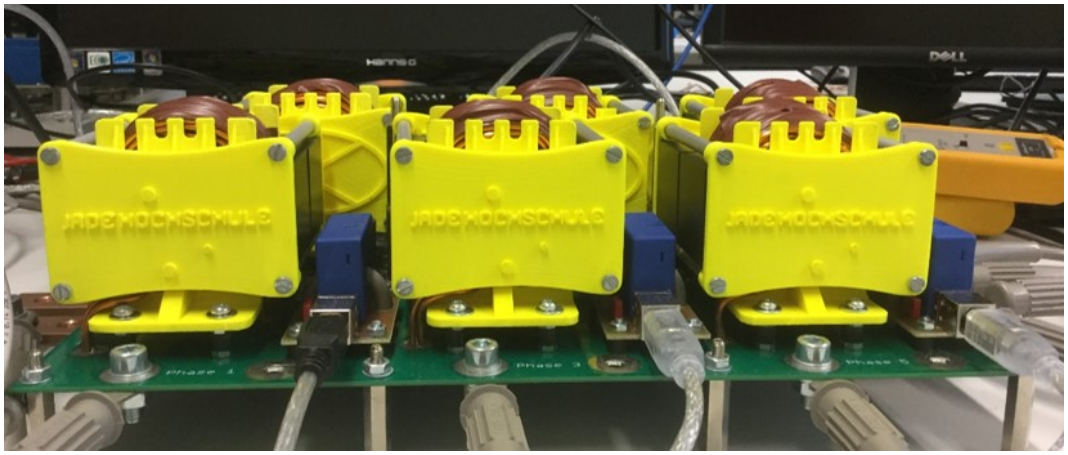

Figure 3.26: Filter circuit of the converter with inductor coils [34]

In addition, the current in each inductor coil is measured with a current sensor of LA-55P. In this way, the current load of the individual phases can be balanced by use of a control circuit. Furthermore, the output capacitors of which the phases are connected are also placed on the circuit board. Under this board, there are also copper bars attached to carry the output current up to 200A.

In the power part, the six phases of the converter are operating in parallel. For this reason, the current in the individual phases must be balanced. To do this, the current in all inductor coils at the output of the bridge-legs are measured. Then the measured values are supplied to a balancing controller. This controller modifies the PWM-signals from the processor such that the DC-components of the inductor currents are equal.

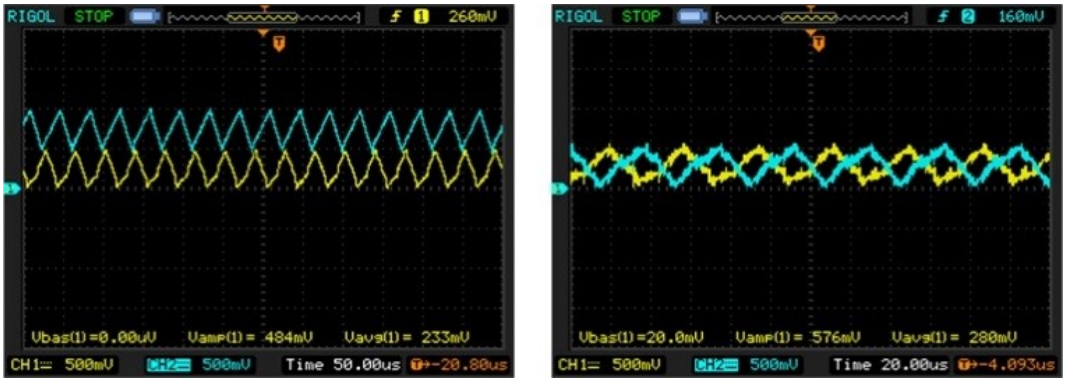

Figure 3.27: Inductor currents without (left) and with control circuit (right) [34]

Figure 3.27 shows the inductor currents of phase 1 and phase 4. On the left, the currents are unbalanced due to the tolerances of the components and deviations in the PWM-signals. The difference is already very large, so some components are in danger to being overloaded. With the control circuit on the right, the dc-current values of the inductors are equal.

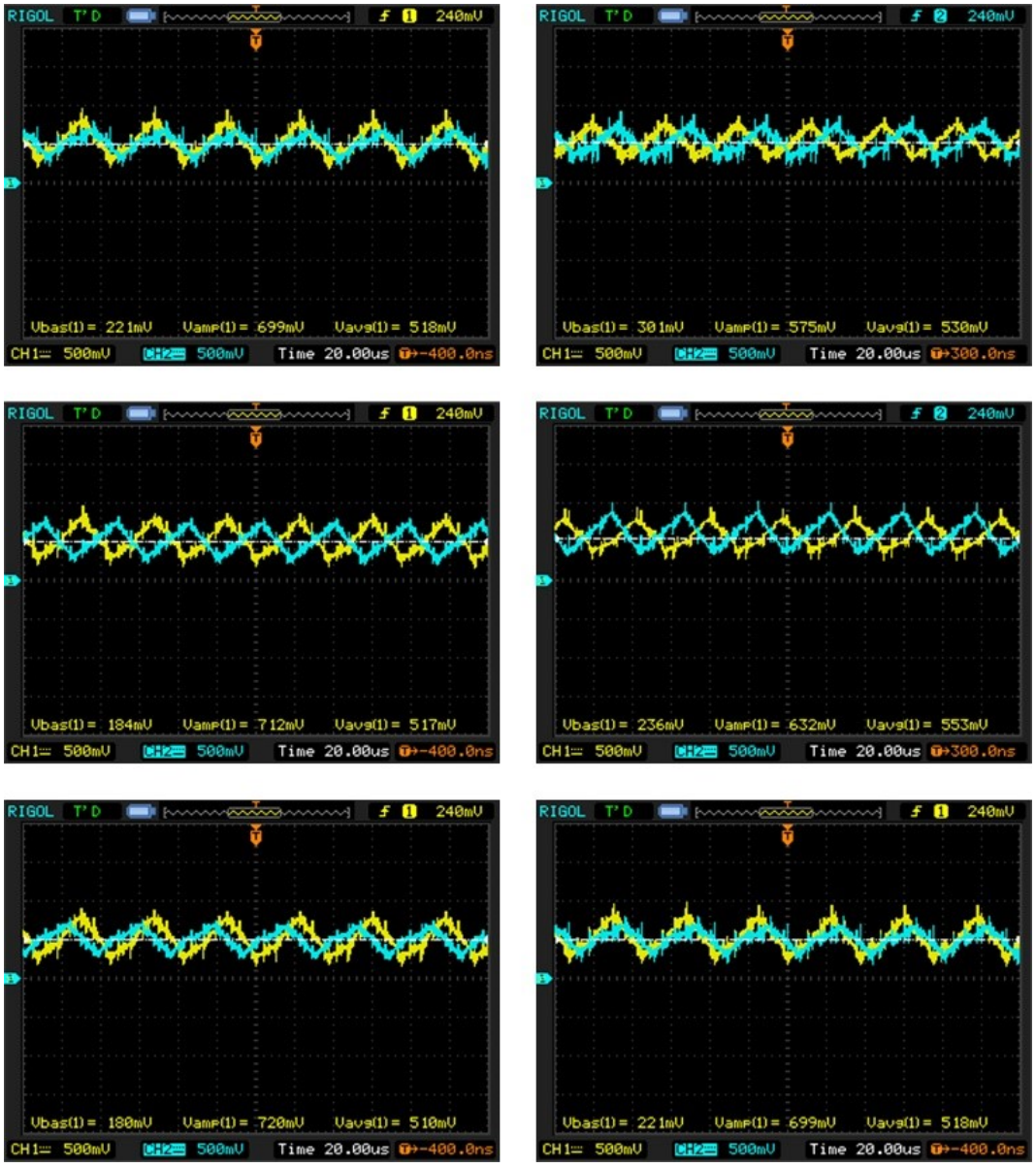

Figure 3.28: Inductor currents in the different phases with balancing circuit [34]

All current waveforms in Figure 3.27 and 3.28 have a current scale 1div ¡=¿ 500mV ¡=¿ 10A, and the scale in the time axis 1div=20μs. Figure 3.28 shows the controlled inductor currents of the different phases. At the shown operating point, the input voltage U_{in} = 80V and the approx. output voltage U_{out} = 50V. At a converted power of P_{Out} = 3kW the output current I_{Out} = 60A. This results in a DC-current component of approx. 10A per inductor. To this DC-component, the typical triangular inductor current is added.

All six representations in the Figure 3.28 show the inductor current of phase 1 in yellow color. In the illustration above left, in addition to phase 1 the current of phase 2 with the phase shift of 1/6 pulse period is shown in blue. Related to phase 1 the position of the other phases have multiple of this phase shift. Thus, above on the right, next to phase 1, phase 3 is shown with the double phase shift. In the middle, also in blue, on the left phase 4 with a 3-fold phase shift, and on the right phase 5 with a 4-fold phase shift to phase 1 can be seen. Below is shown on the left in addition phase 6 with the 5-fold phase shift also related to phase 1. In the illustration below right are depicted phase 1 and phase 2.

For the efficiency calculation of the multiphase converter, the output and input power are measured in 1kW load steps. Subsequently, the quotient of output and input power is calculated for each load step.

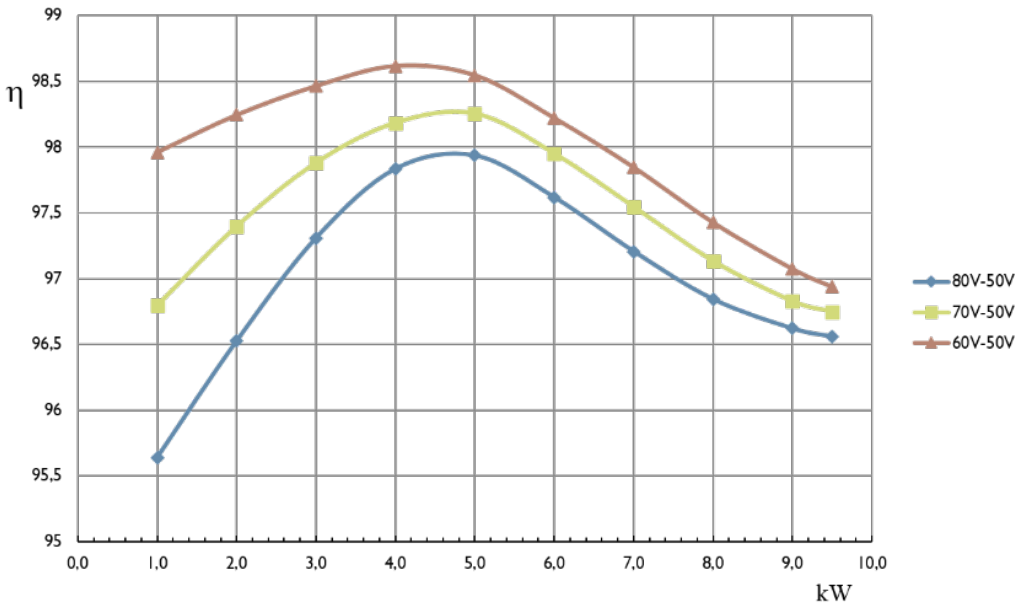

Figure 3.29: Efficiency diagram of the multiphase DC/DC converter [34]

The results show an excellent efficiency, especially when stepping down from U_{In} = 60V to U_{Out} = 50V. This converter operation will occur especially at higher output power in fuel cell applications. For this reason, a good efficiency is very important during this operation. But also at lower output power when stepping down from U_{In} = 80V to U_{Out} = 50V good efficiencies are achieved, which are between 95% and 98%.

Control strategy for the DC/DC converter in powertrain of FCEV

In [32], the author presents the control strategy for the DC/DC converter in powertrain of FCEV. The control principles of different converters in fuel cell electric vehicles are explained and analyzed. Taking a single phase buck converter as an example, the control method and results in a fuel cell power system are given below. The configuration II of the fuel cell powertrain system is used here. During the start-up process, the output current is controlled to rise slowly until the duty cycle achieve 100%, the fuel cell system is directly connected to the DC bus and operate under the "passive hybrid" condition. This process is the same as using the electronic switch in powertrain in FCEV. During the shutdown process, let the output current drop slowly until it achieves 0A. In order to implement control strategy of the fuel cell system proposed above, the test platform shown in Figure 3.30 was built.

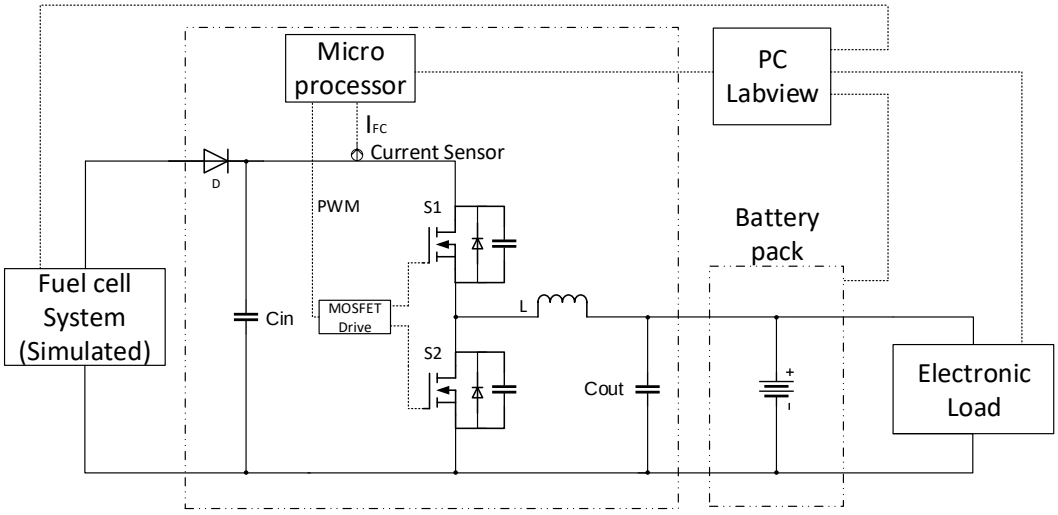

Figure 3.30: The schematic of DC/DC converter in powertrain of FCEV test platform [32]

This test platform contains the following components:

- A power supply that can simulate the output characteristics of a fuel cell system
- A 2kW synchronous buck converter and driving circuit, back flow prevention diode and output current sensor
- A lithium iron phosphate battery pack with a rated voltage of 50V and a capacity of 300AH

- An electronic load with a maximum power of 2.4kw can be used to simulate load changes
- A microprocessor used to implement control strategies, PI controllers, and generate PWM signals
- The LabVIEW program on the PC is used to simulate the control signals interacting with the microprocessor and to measure the circuit data in real-time

Because of the limitation in the rated power of the selected DC/DC converter, the simulated fuel cell system limits the output power. In order to match the operating range of the battery pack, the output characteristic curve is modulated as shown in Figure 3.31 below, where the open circuit voltage U_O = 80V, nominal power P_N = 2.3kW with U_N=50V, I_N=47A.

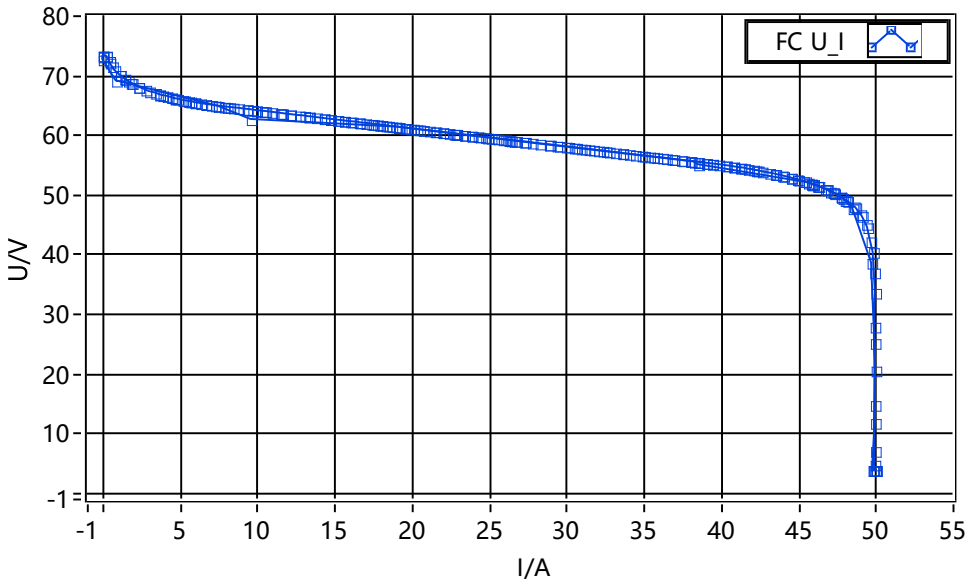

Figure 3.31: The output behavior U-I curve of the simulated fuel cell system [32]

The experimental results on the test platform for proposed control strategy are shown in Figures 3.32-3.34. They show the output current (the red line) of the fuel cell system at the rate of 4A/s, 2A/s and 1A/s separately, the current ramp up from 0A to about 40A, after a while a ramp down from about 40A to 0A again. The load current (The blue line) is set to vary randomly between 0 and 40A, and the battery current (the green line) shows the charge

and discharge of the battery pack. The value on the horizontal axis is time unit, the measurement interval is 200ms, here 50 ≒10s. According to the experimental results, through the proposed control method for buck converter the output power of the fuel cell can be regulated slowly, and quickly respond to the sudden change of load. Therefore, in the process of output current rising or falling, the fluctuation of the load does not affect the rate of current. Because "passive hybrid" is used in normal operation, during this time, the output current of the fuel cell will change with the voltage of the DC bus, although the output power of the fuel cell fluctuates in a small range, but the loss of the DC/DC converter can be avoided.

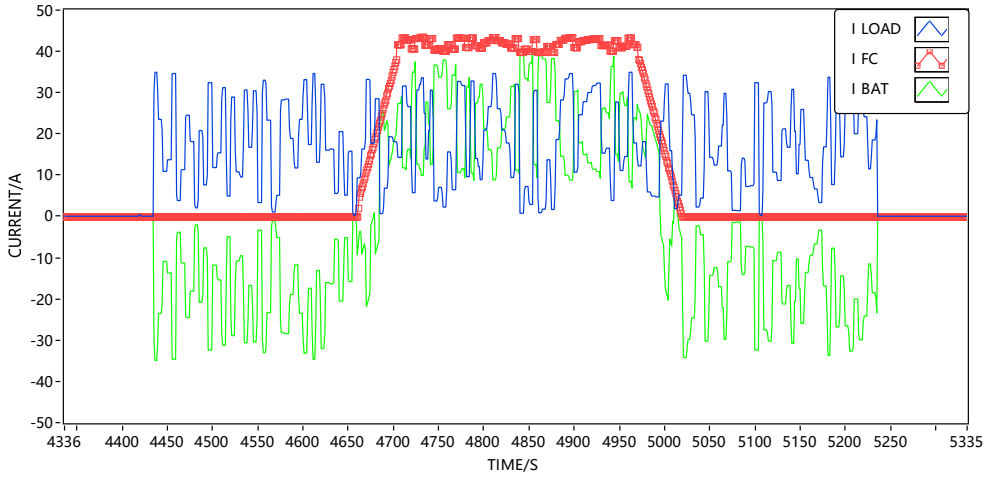

Figure 3.32: The fuel cell system current ramp up and down with 4A/s rate [32]

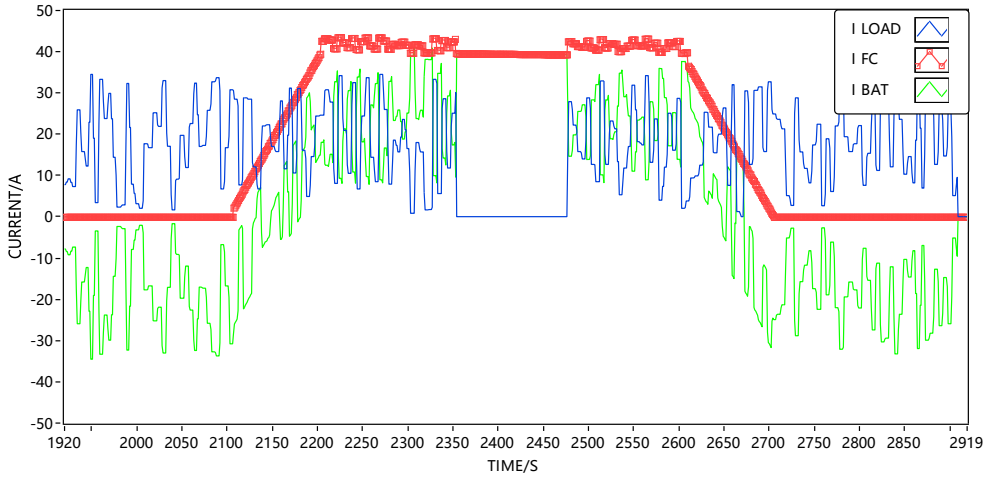

Figure 3.33: The fuel cell system current ramp up and down with 2A/s rate [32]

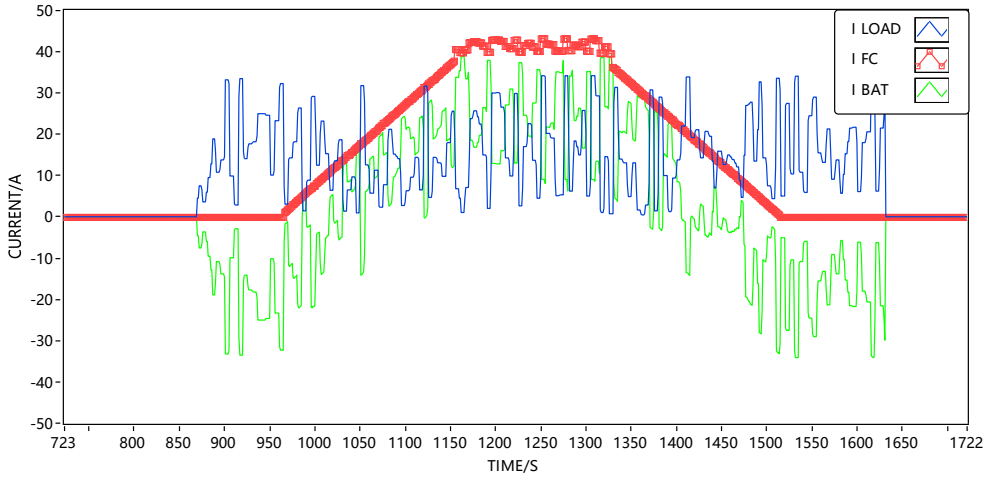

Figure 3.34: The fuel cell system current ramp up and down with 1A/s rate [32]

In addition, these pictures show that when the duty cycle of the synchronous buck converter changes to 100%, a small abrupt change appears in the current curve. The reason is that a certain dead time exists in the PWM signals of MOSFETs in the buck converter half-bridge circuit, from the point of actual results. It does not affect the stability of the whole system.

3.5 Conclusions and contributions

This chapter describes the use of DC/DC converters for powertrain of FCEV. In general, the voltage difference between the fuel cell and the DC bus makes the converter indispensable in the powertrain. Nowadays, there are many types of DC/DC converters, which can be divided into two categories: isolated and non-isolated. Since the operation of fuel cells is a chemical reaction, the power output of fuel cells needs to be as smooth as possible in order to prolong the life of the fuel cells. In this regard, the converter needs to have a low input current ripple as well as a fast dynamic response. Multiphase buck converter was chosen to study its advantages and disadvantages in powertrain of FCEV.

From a single phase buck converter, the input ripple current, output ripple current, and the corresponding filter capacitor design requirements are investigated, and then extended to a multiphase buck converter. Due to the phase shift between the control signals of multiphase buck converter, the AC portion of the inductor currents appear superimposed. As the number of phases increases, this phenomenon of superimposed phase extinction becomes more obvious, and at the same time, the number of points of zero ripple appearances increases. Further, the superposition of inductive currents affects the ripple currents at the inlet and outlet, but of course, this effect is positive. The reduced peak-to-peak value of the ripple current, as well as the exponential increase in frequency, both make the filtering requirements of the input and output significantly lower. From a hardware design point of view, the multiphase buck converter brings a lot of excellent features. They can be summarized as follows:

- The parallel structure provides low current stress requirements for semiconductor and other devices and contributes to heat dissipation.

- Compared to single phase converters, multiphase converters require less capacitance for input and output filtering. More possibly, metal film capacitors are used instead of electrolytic capacitors to reduce the impact of ESR on the circuit. More significantly, the reduced ripple of the input current will benefit the fuel cell.

- The modular and redundant design increases the reliability of the multiphase DC/DC converter.

Of course, there are disadvantages such as the need for exponentially larger drive modules and detection circuits for semiconductors. In terms of control, the multiphase buck converter is studied from two perspectives. First, in

order to complete the closed-loop control of the multiphase converter, the small-signal model of the single phase buck converter is extended to the small-signal model of the multiphase buck converter. After comparing the small signal model of single- and multiphase buck converter, it can be found that the multiphase buck converters have wider bandwidth and faster response, which is beneficial to the application of fuel cell electric vehicle powertrain. The second point is that the current sharing problem of multiphase buck conversion needs to be solved by additional hardware circuits or software algorithms, among them, the master-slave method, the average current method, the maximum current method, and the use of a high-performance microprocessor for sharing the current are described in detail.

Finally, the feasibility of hardware design and software control is verified by a 12KW multiphase buck converter and a 2kW single phase buck converter.

Chapter 4.

Soft-Switching Converters for Fuel Cell Vehicles

4.1 Introduction

In Chapter 3, the operating principle of the multiphase buck converter, the advantages and disadvantages of this converter in fuel cell powertrain were analyzed in detail. Under PWM control, the semiconductor switches (MOSFET) are all operating in hard-switched state. In actual operation, the drain source current I_D and voltage V_{DS} do not immediately drop or rise to the desired value when the MOSFET is turned on or off. During this time, the current and voltage will have a crossover region, generating losses, known as turn-on or turn-off losses, or collectively referred to as switching losses. Assuming certain conditions, the switching losses are constant in each cycle, hence the switching losses of the converter are proportional to the switching frequency, the higher the switching frequency cause the higher the total switching losses and the lower the efficiency of the converter. The presence of switching losses limits the increase in the switching frequency of the converter, thus limiting the miniaturization and light weighting of the converter. Figure 4.1(a) shows the voltage and current waveform for turn-on and -off of hard-switching. Other significant drawbacks of hard switching operation used in converters are the high levels of dv/dt and di/dt. They are a major source of conducted and radiated EMI. Figure 4.2 gives the trajectory of the MOSFET operating under hard switching, the short dashed line in the figure is the safe operating area of MOSFET. It can be seen that the MOSFET may operate out of the safe

operating area, resulting in damage to the MOSFET.

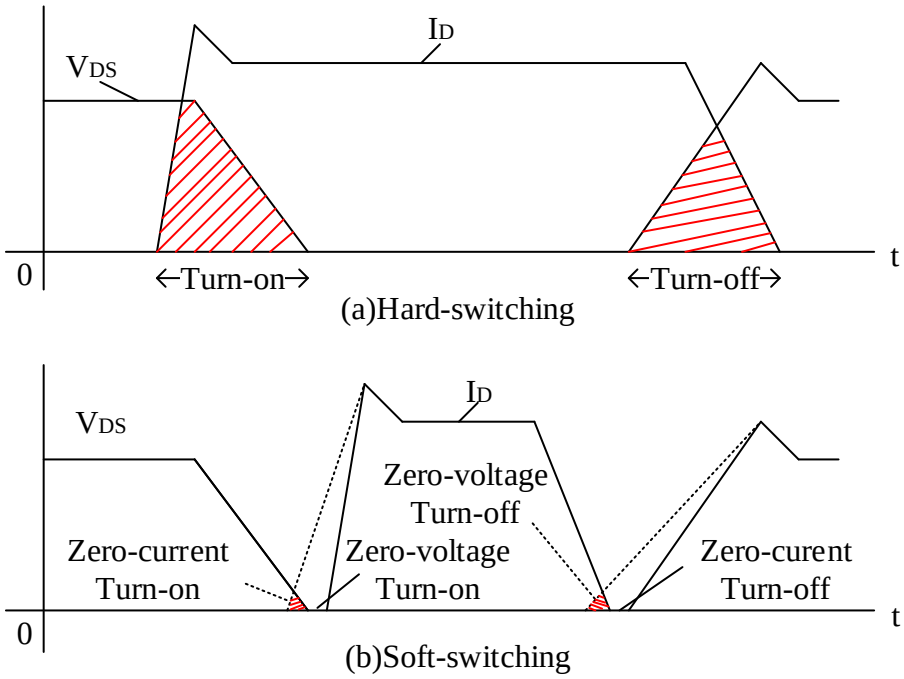

Figure 4.1: The voltage and current waveform of MOSFET turn-on and -off process of hard- and soft-switching [original]

Generally, increasing the operating frequency of the converter can reduce the size and weight. However, the increased operating frequency brings excessive switching losses, and an effective method to solve this problem is to implement soft-switching of the switches [74,75]. Figure 4.1(b) shows the voltage and current waveform for turn-on and -off of soft-switching. In order to reduce the switching losses, there are usually several methods:

- Zero voltage turn-on: Before the switch is turned on, the voltage across the switch is already dropped to zero. The turn-on loss at this point is essentially zero.

- Zero current turn-on: When the switch is open, keep the current flowing through the switch at zero , or reduce the current rise rate to reduce the current and voltage crossover zone.

- Zero current turn-off: Before the switch is turned off, the current through

the switch is already dropped to zero. The turn-off loss at this point is essentially zero.

- Zero voltage turn-off: When the switch is closed keep the voltage at the switch at zero , or reduce the voltage rise rate to reduce the current and voltage crossover zone.

The trajectory of the soft-switching is shown in the Figure 4.2, with soft-switching technology. The MOSFETs operate under better conditions and not out of the SOA region during the switch process.

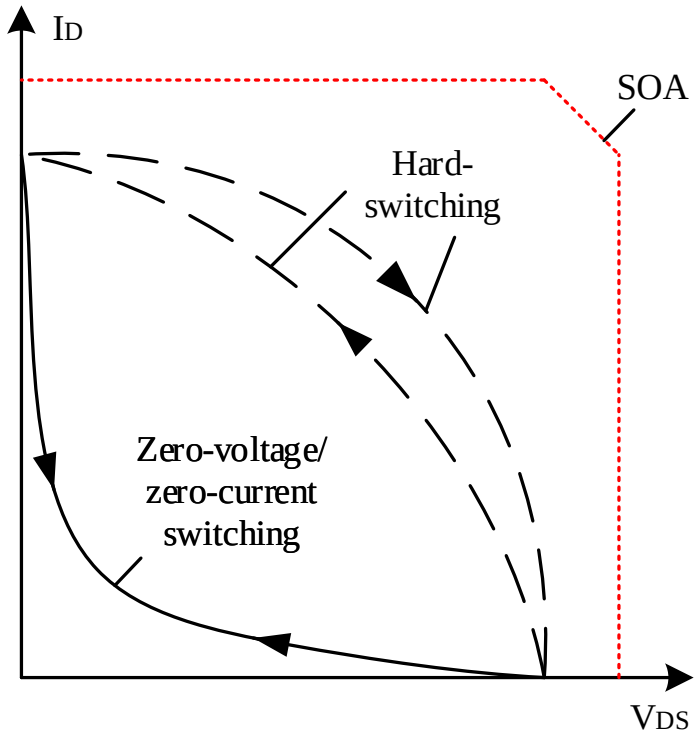

Figure 4.2: Trajectory of the MOSFET operating under hard- and soft-switching [original]

The soft-switching technology can be divided into the three major groups:

- Snubber: Dissipative snubber [76], lossless passive snubber [77], active clamp circuits [78]

- Driver based soft transition control: Passive gate driver control, active gate driver, multi stage gate driver [79]

- soft-switching: Traditional Series and Parallel Resonant Converters (SRC and PRC), Quasi-Resonant Converters (QRC), Zero-Switching-PWM converters (Zero-Voltage-Switching, ZVS and Zero-Current-Switching, ZCS), Zero-Transition-Converters (Zero-Voltage- Transition, ZVT and Zero-Current-Transition, ZCT) [65, 80–82].

Soft-switching topologies possess a number of advantages over hard-switching topologies, and many of the approaches proposed so far achieve these advantages to varying degrees. They include:

- Reduction of switching losses down to virtual elimination
- Increased switching frequencies allowing small filter components
- Reduced device cooling requirements
- Reduced size/cost
- Low dv/dt and di/dt, less EMI

To further optimize multiphase converters in fuel cell electric vehicle powertrains, soft-switching technology is considered for integration into these converters, but the snubber circuit and driver based soft transition control are not suitable for use in multiphase converters, because the additional components and control complexity required will be N times that of a single phase circuit [83]. In soft-switching, the resonant converters and QRCs are controlled by pulse frequency modulation (PFM) method, therefore, zero switching PWM and zero transition converters are more suitable for use in multiphase converters. The circuit structure is characterized by its resonant network connected in parallel with the main switch, during the switching transition. The resonant network generates resonance and obtains a zero-switching condition. After the switching transition is over, the circuit returns to normal PWM operation.

In this chapter, two soft-switching multiphase buck converters will be studied, and their feasibility is analyzed mainly from operation principles and simulations, and finally an experimental prototype is constructed to verify the theoretical and simulated results.

4.2 Theoretical analyses of multiphase ZVT-PWM synchronous buck converter

In this section, a new multiphase ZVT-PWM synchronous buck converter is presented, which uses the soft-switching implementation method, to improve and extends to multiphase synchronous buck converter [84]. In [85,86], a ZVT-PWM converter family is studied, The typical ZVT-PWM buck converter is shown in Figure 4.3(a). On the basis of the ordinary buck converter, a resonant network composed of an auxiliary switch S, a resonant inductor Lr, a resonant capacitor C_r, and an auxiliary diode D_r is added. Figure 4.3(b) shows a typical hard switching multiphase PWM synchronous buck converter. It consists of multiple buck converters connected in parallel and controlled by phase shift PWM signals.

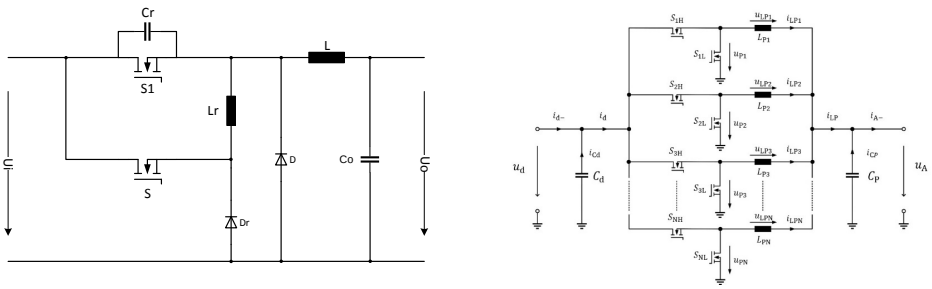

(a) (b)

Figure 4.3: Typical ZVT-PWM buck converter and the hard switching multiphase PWM synchronous buck converter [84]

The characteristics of this ZVT-PWM buck converter are:

- Adopt PWM control method, realize constant frequency, variable duty cycle control.
- The auxiliary circuit only works during the MOSFET opening or closing process, and does not work in other time periods to reduce the loss of the auxiliary circuit.
- The auxiliary circuit is not connected in series in the main power circuit, but in parallel with the main circuit, so that the losses in the auxiliary circuit can also be reduced.
- The auxiliary circuit operates without increasing the voltage and current stress on the MOSFETs in the main power circuit.

These features of the ZVT converter make it widely used in high-power applications.

An implementation of the proposed multiphase ZVT-PWM buck synchronous converter is depicted in Figure 4.4. The auxiliary circuit is composed of the main switch S_0, freewheeling diode $D1$, resonant inductor L_r, while the resonant capacitor is distributed to each phase circuit, that is, the capacitors parallel to the switches. Due to the phase shift $360°/N$ (N is the number of phases) between the control signals of multiphase converter, the additional switches ($S_{1\cdots N}$) should be placed in series between the auxiliary circuit and the buck converter, thereby separating the soft-switching process of each phase.

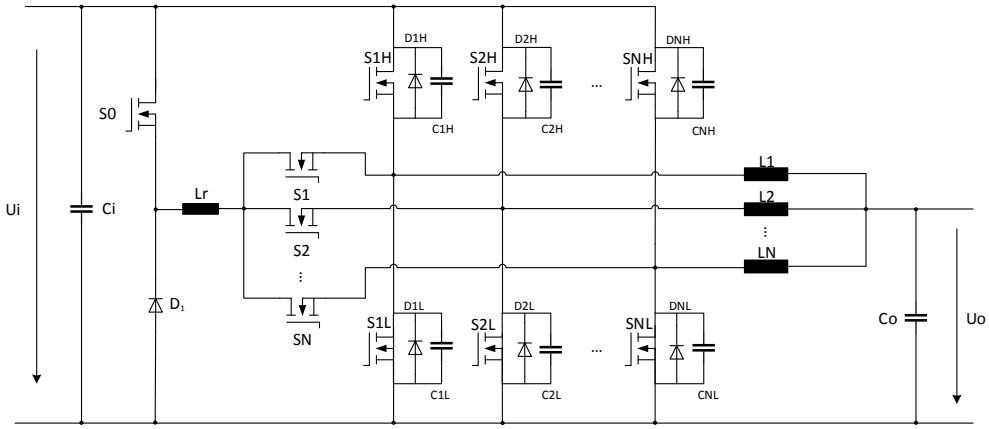

Figure 4.4: The proposed multiphase ZVT-PWM synchronous buck converter [84]

In the proposed circuit, each phase operates identical except the phase shift, so the phase 1 is selected for analysis. As shown in Figure 4.5, the key waveforms of the multiphase ZVT-PWM buck converter can be divided into seven operation stages in one switching cycle, S_{1H} is the PWM control signal of MOSFET SH1 of phase 1, S_{1L} is the PWM control signal of MOSFET SL1 of phase1, T_{D1} and T_{D2} are the dead times between S1H and S2H, and the duration of dead time muss be controlled. S_0 and S_1 are control signals for MOSFET S0 and S1 in auxiliary circuit, I_{Lr} is the current in inductor Lr of auxiliary circuit, I_o is the load current, U_{S1H} and U_{S2H} are drain-source voltage of main MOSFETs, I_{S1H} and I_{S2H} are drain-source current of main MOSFETs.

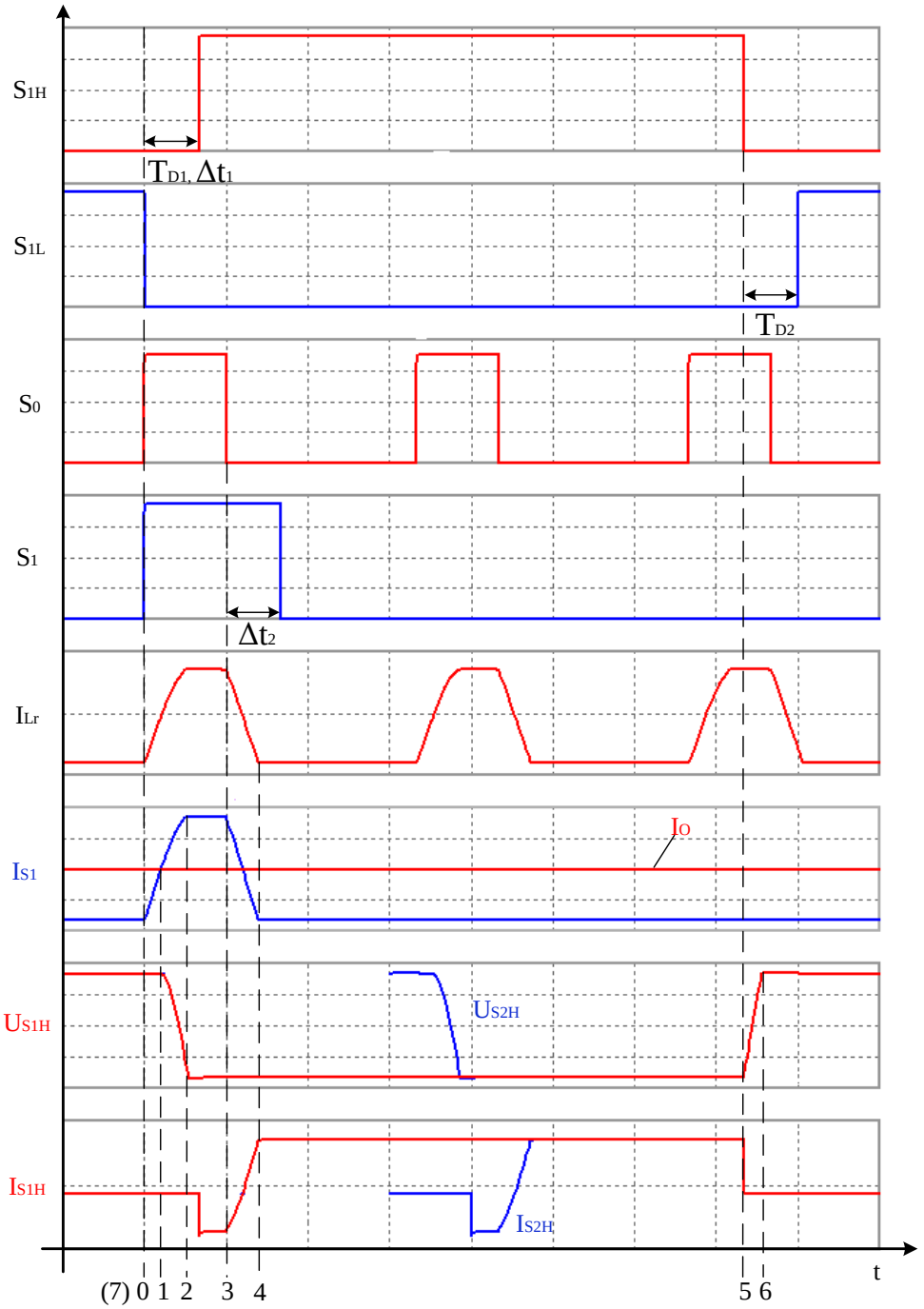

Figure 4.5: The key waveforms of the multiphase ZVT-PWM buck converter. $S_{1H} - S_1$: control signals of switches, I_{Lr}: resonant inductor current I_o: load current, I_{S1}, I_{S1H}, I_{S2H}: switch currents, U_{S1H}, U_{S2H}: switch voltages [84]

To simplify the analysis, the following assumptions are made:

- The load inductor L is much larger than resonant inductor L_r so that the load current can be seen as constant I_o.
- All the components are ideal.

The following variables are defined:

- The snubber capacitors $C_{1H},\ C_{1L} \cdots C_{NH},\ C_{NL}$ are identical, and $C_r = 2C_{1H}$.
- Angular resonant frequency $\omega_r = 1/\sqrt{L_r C_r}$ and characteristic impedance $Z_r = \sqrt{L_r/C_r}$.
- The peak-to-peak current of load inductor (I_{Lmax}—I_{Lmin}) is ΔI.
- Switching period is T and duty cycle is D.

The equivalent circuits for different operation stages are shown in the following pictures.

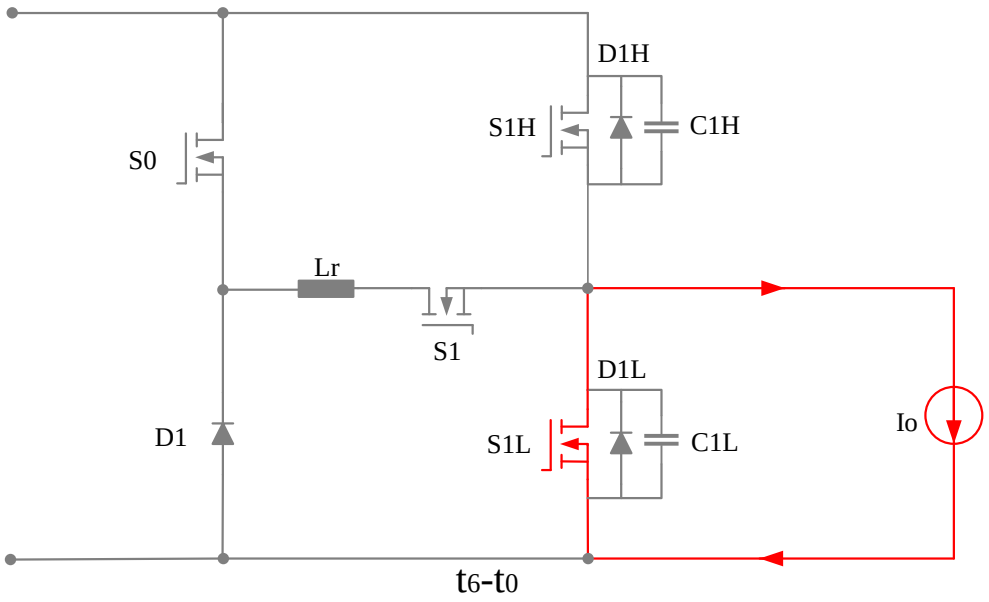

Figure 4.6: Equivalent circuit diagram operating in stage 1 [84]

Stage 1, see Figure4.6, prior t_0: The auxiliary switches S_0, S_1 and phase one main switch S_{1H} are turned off, the switch S_{1L} is conducting. Using MOSFETs instead of Diodes can reduce losses during the current freewheeling phase.

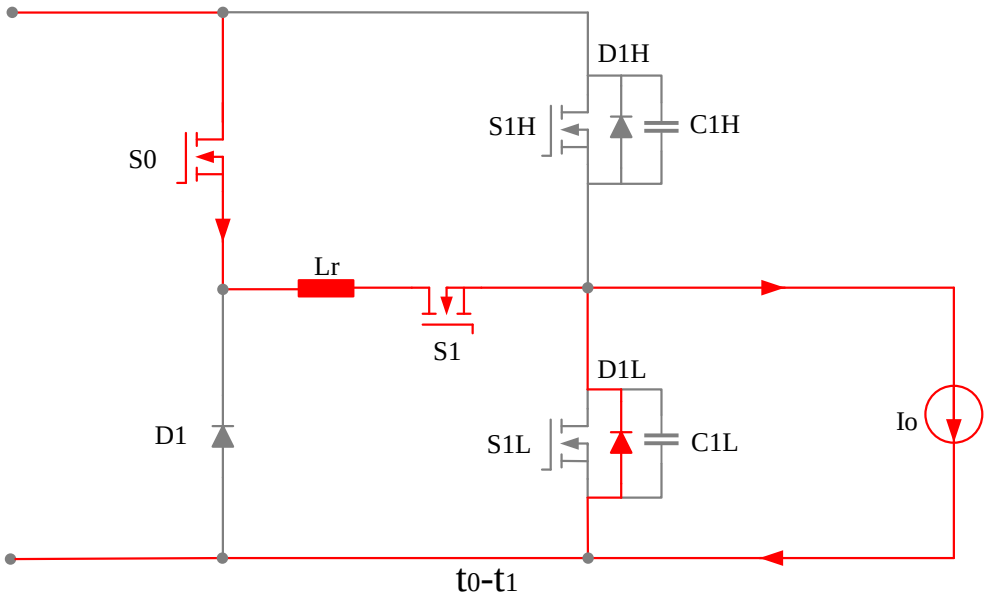

Figure 4.7: Equivalent circuit diagram operating in stage 2 [84]

Stage 2, see Figure4.7, interval $t_0 - t_1$: At t_0, S_0, S_1 are turned on with zero current transition (ZCT) owing to inductor L_r, S_{1L} can be closed at the same time or a short time in advance, and the current continues to flow through the body diode D_{1L}. As the current I_{Lr} increases linearly, the current in body diode decreases accordingly. When $t = t_1$, I_{Lr} reaches I_o, then the body diode turns off naturally. The stage duration is:

$$T_{01} = \frac{L_r I_o}{U_i} \tag{4.1}$$

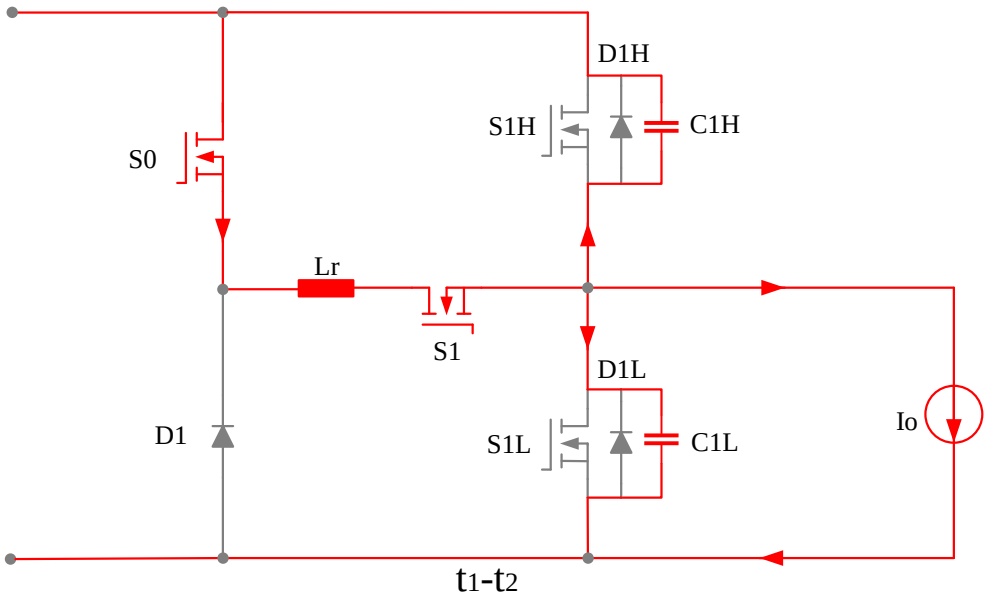

Figure 4.8: Equivalent circuit diagram operating in stage 3 [84]

Stage 3, see Figure4.8, interval $t_1 - t_2$: At t_1, S_{1L} is turned off with ZCT. After that, the capacitors C_{1H} and C_{1L} start to resonate with the inductor L_r, the capacitor voltage U_{C1H} drops to 0, U_{C1L} rises to the input voltage U_i, and the resonant inductor current I_{Lr} satisfies the following equation.

$$I_{Lr} = I_o + \frac{U_i}{Z_r} \sin \omega_r (t - t_1) \tag{4.2}$$

When $t = t_2$, I_{Lr}=$I_{Lr\ max}$. The stage duration is:

$$T_{12} = \frac{\pi}{2} \sqrt{L_r C_r} \tag{4.3}$$

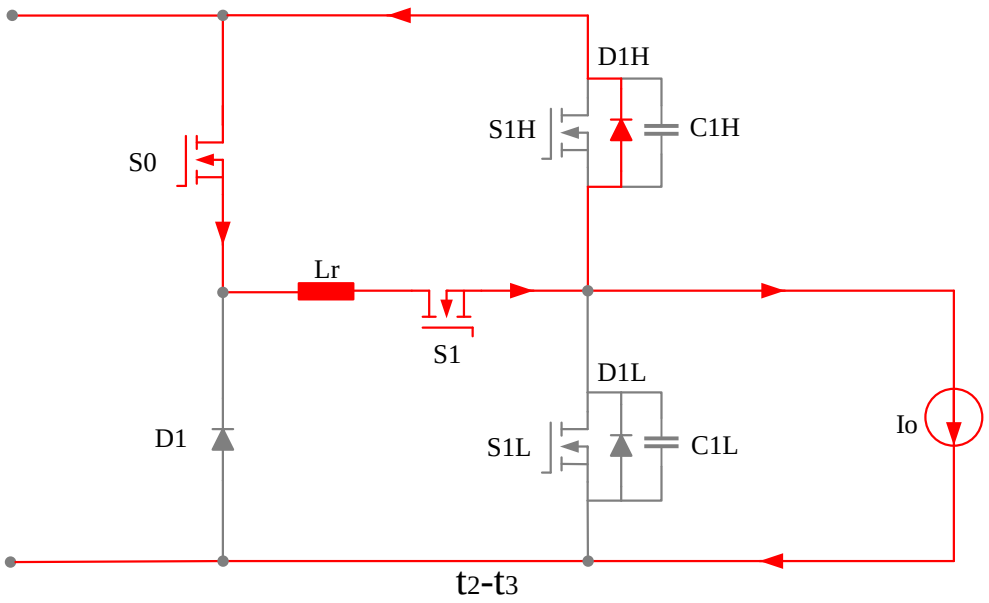

Figure 4.9: Equivalent circuit diagram operating in stage 4 [84]

Stage 4, see Figure4.9, interval $t_2 - t_3$: The anti-parallel diode of S_{1H} is on, U_{C1H} and voltage of inductor U_{Lr} are clamped to zero, so the current i_{Lr} on L_r remains constant. During this interval, S_{1H} can turn on with ZVT. The duration of this stage is controlled by the closing time of switch S_0.

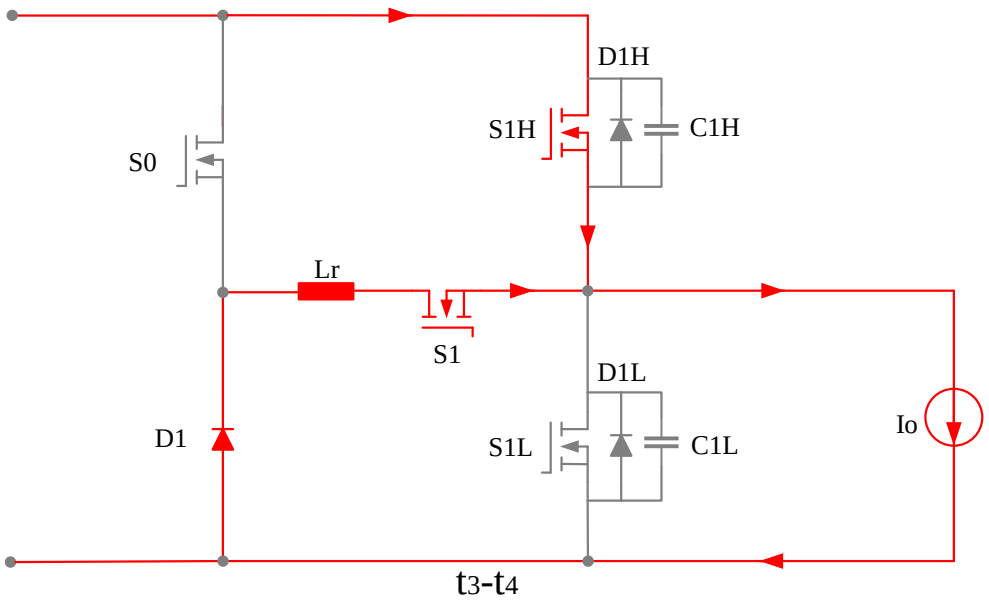

Figure 4.10: Equivalent circuit diagram operating in stage 5 [84]

Stage 5, see Figure4.10, interval $t_3 - t_4$: At t_3, the auxiliary switch S_0 turns off hard, resonant inductor voltage $U_{Lr} = -Ui$, then the energy stored in L_r is transferred to the load. Auxiliary diode D is turned on, resonant inductor current I_{Lr} starts to decrease, and drops to 0 at t_4. Switch S_1 can be opened at this time and the current I_{S1H} rises linearly. The stage duration is:

$$T_{34} = \frac{I_{Lr\,\max} L_r}{U_i} = \frac{L_r I_o}{U_i} + \frac{L_r}{Z_r} \tag{4.4}$$

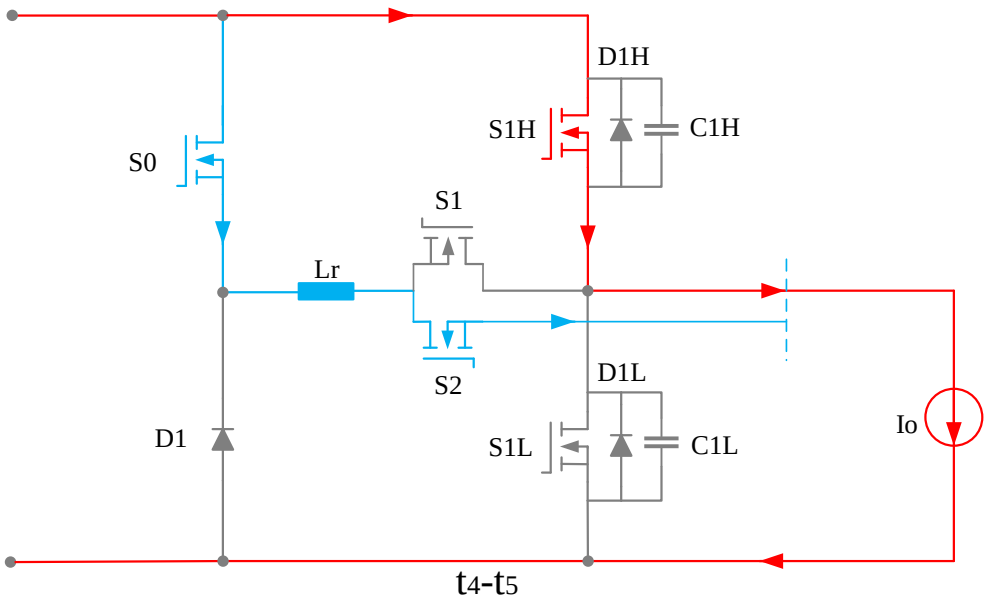

Figure 4.11: Equivalent circuit diagram operating in stage 6 [84]

Stage 6, see Figure4.11, interval $t_4 - t_5$: The operation in this interval is identical to that of the PWM buck converter, the half-bridge and auxiliary circuit are completely separated, after t_4, next phase of multiphase buck converter is allowed to operate that resonant process, for example, the second phase circuit marked in blue. The duration of this stage is controlled by PWM.

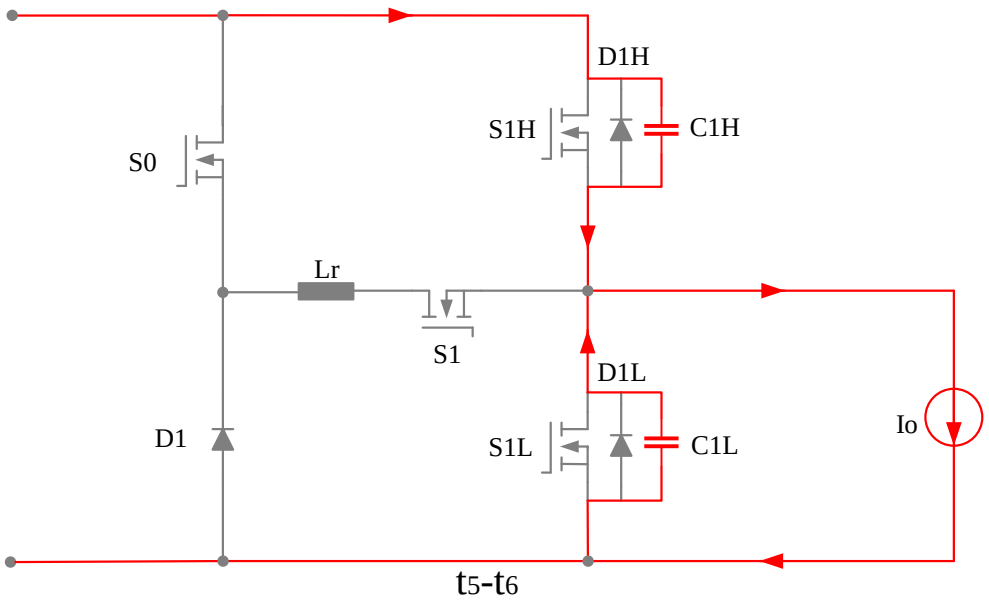

Figure 4.12: Equivalent circuit diagram operating in stage 7 [84]

Stage 7, see Figure4.12, interval $t_5 - t_6$: At $t = t_5$, S_{1H} is turned off and the capacitor C_{1H} is charged while C_{1L} is discharged with load inductor current I_{Lmax}. Since this period lasts for a short time, it can be considered as a constant current source to charge and discharge the capacitors. The voltage U_{C1L} is linearly decreased until it drops to 0. Due to the snubber capacitors, the turn-off process of S_{1H} and conduction of body diode D_{1L} operate approximately with ZVT. The stage duration is:

$$T_{56} = \frac{U_i C_r}{I_{Lmax}} = \frac{U_i C_r}{I_o + 0.5\Delta I} \tag{4.5}$$

In this stage, soft switching will depend on many different factors: input voltage U_i, buffer capacitance value C_r and maximum value of inductive current I_{Lmax}.

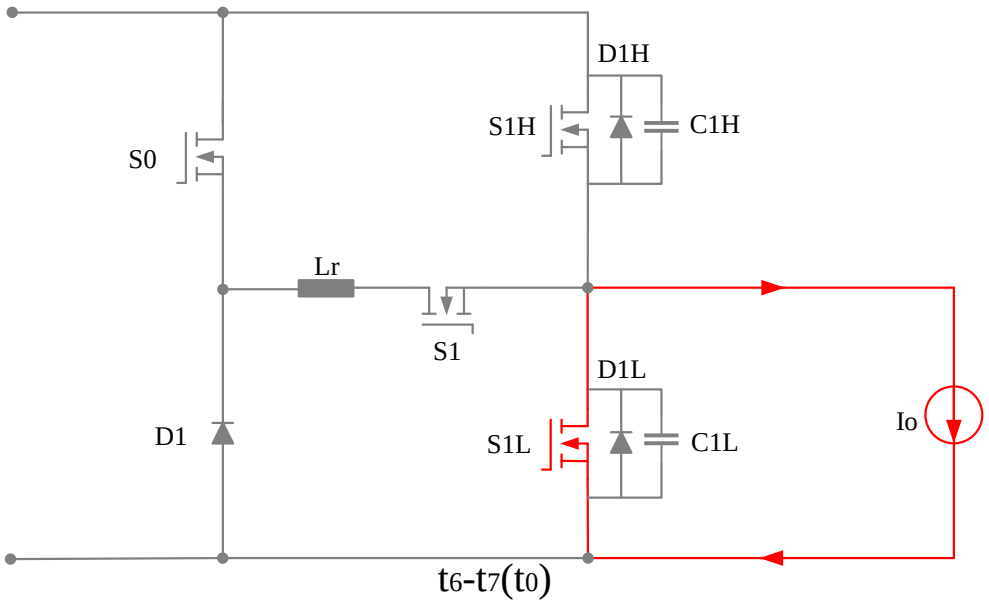

Figure 4.13: Equivalent circuit diagram operating in stage 1 [84]

Stage 1, see Figure4.13, interval $t_6 - t_7$: At this stage, S_{1L} is turned on at t_6 and current flows through the switch. At t_7, S_{1L} is turned off and next switch cycle begins. The duration of this stage is also controlled by PWM.

The basic concept of this converter is the following: to achieve zero-voltage turn-off of the main MOSFET, a buffer capacitor will be connected in parallel with this MOSFET, which is used to limit the rise rate of the drain-source voltage of MOSFET. However, before the main MOSFET turns on, the charge on the buffer capacitor has to be released to zero to achieve zero-voltage-switching of the MOSFET, and this function requires an auxiliary circuit to achieve. When this process is finished, the auxiliary circuit will stop operating as well. In this way, the auxiliary circuit operates for a shorter period of time and only close the turn-on of the main MOSFET. In the case of multiphase buck converters, the function of the auxiliary circuit is multiplexed to zero-voltage-switching of main MOSFETs in each phase, to ensure that the soft-switching processes of each phase are independent and not disturbed. Additional MOSFETs S1-SN are used to separate each phase.

In this design, the number of phases, the duration of the dead time and the timing of the control signals of the MOSFETs in the auxiliary circuit are subject to the following design rules.

The following conclusions can be drawn from the above stage analysis. The

dead time T_{D1}, the time delay Δt_1 between S_0 and S_{1H}, has to satisfy

$$T_{D1} \geq \Delta t_1 \geq T_{01} + T_{12} = \frac{L_r I_o}{U_i} + \frac{\pi}{2}\sqrt{L_r C_r}. \tag{4.6}$$

When the diode $D1$ in auxiliary circuit is on, the corresponding switch $S_{1\cdots N}$ must remain closed with the minimum delay time

$$\Delta t_2 \geq T_{34} = \frac{L_r I_o}{U_i} + \frac{L_r}{Z_r}. \tag{4.7}$$

The resonance process of the auxiliary circuit occurs within the time interval $t_0 - t_4$. In order to ensure that the multiphase buck converter operates independently, the resonance process is not allowed for interleaving, so the number of phases N is respected as below,

$$2 \leq N \leq \lfloor \frac{T}{T_{04}} \rfloor, \tag{4.8}$$

where $[\cdots]$ is the floor function and

$$T_{04} = 2\frac{L_r I_o}{U_i} + \frac{\pi}{2}\sqrt{L_r C_r} + \frac{L_r}{Z_r} + T_{23}. \tag{4.9}$$

In addition, the soft-switching process realized by the snubber capacitors in the $t_5 - t_6$ interval is also affected by factors such as input voltage, snubber capacitor size, etc. The condition for completing soft-switching in the dead time T_{D2} is:

$$T_{D2} \geq \frac{U_i C_r}{I_o + 0.5\Delta I} \tag{4.10}$$

where

$$\Delta I = \frac{(U_i - U_o)DT}{L} \tag{4.11}$$

In order to calculate the hardware parameters of the auxiliary circuit, the time duration T_{04} and T_{D2} need to be confirmed first. Typically, set the duration of $T_{D2} = (2 \sim 3)t_f$, where t_f is the turn-off time of MOSFET in power part, which is used to limit the rate of change of voltage on MOSFET. Then according to Equation 4.10, the value of C_r can be obtained. The operating time of the auxiliary circuit cannot be too long, in order not to affect the circuit of other phases. T_{04} needs to be less than the phase difference T_P/N, and the value of L_r can be calculated according to Equation 4.9. From the above analysis, it can be seen that the conditions of the soft switch are influenced by many factors. In the actual design process, it is generally necessary to adopt a compromise or iterative calculation method to obtain the most suitable parameters.

4.3 Experimental Verification

A 2kW, two phase ZVT-PWM synchronous buck converter has been implemented to demonstrate the operation. The power part of the converter is shown in Figure 4.14 and the key parameters are presented in Table 4.1.

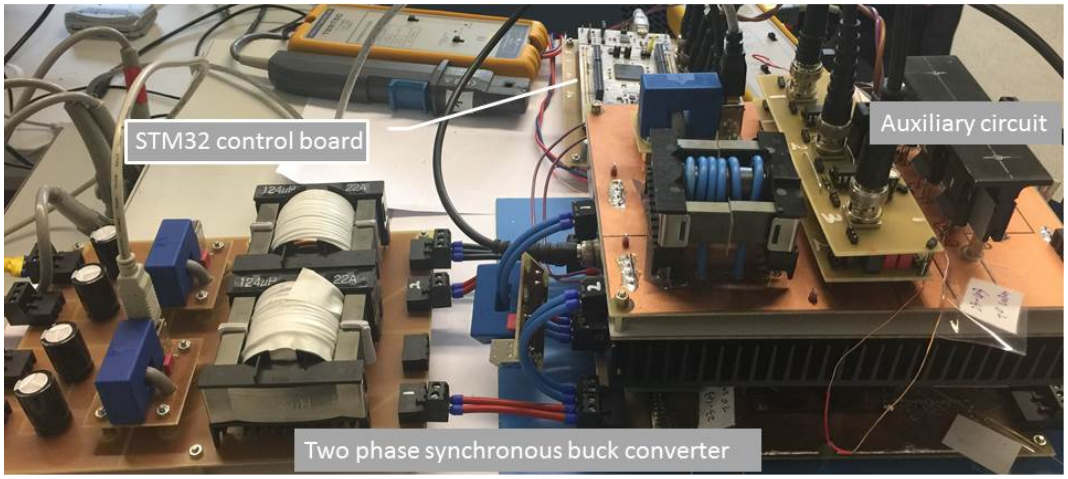

Figure 4.14: Realization of two phase ZVT-PWM synchronous buck converter [84]

Table 4.1: Experiment parameters of the two phase ZVT-PWM synchronous buck converter

Parameter	Description	Value
N	number of phases	2
U_i	input voltage	$50-80V$
U_o	output voltage	$10-70V$
L_1, L_2	load inductor	$124\mu H$
L_r	resonant inductor	$2\mu H$
C_r	resonant capacitor	$20nF$
f_{S0}	switch frequency of MOSFET $S0$	$50kHz$
$f_{S1,2}$	switch frequency of MOSFETs $S1$ and $S2$	$25kHz$
P	maximum operating power	$2kW$

In order to meet the requirements like high number of parallel output PWMs, finely controlled dead time, and accurate phase shift, the high performance STM32 Micro Controller is used to generate the PWM waveforms and the associated timing control.

Figure 4.15 shows the oscillograms of the circuit operating at 80V input, 40V output and 500W power load. The curves from top to bottom are: switch current I_{S1H} (green) of phase1, I_{S2H} (red) of phase 2, auxiliary inductor current I_{Lr} (yellow), and load inductor current I_{L1} (blue) of phase 1. It can be seen that, phase 1 and 2 run with a phase shift of 180° and ZVT process was successfully achieved when the upper switches of the half-bridge were opened, showing negative current portion, this is consistent with the results of time interval $t_2 - t_3$ analysis in Figure 4.9. The operating frequency of the I_{Lr} is twice that of the buck converter and load inductor current I_{L1} is the same as the ordinary buck converter.

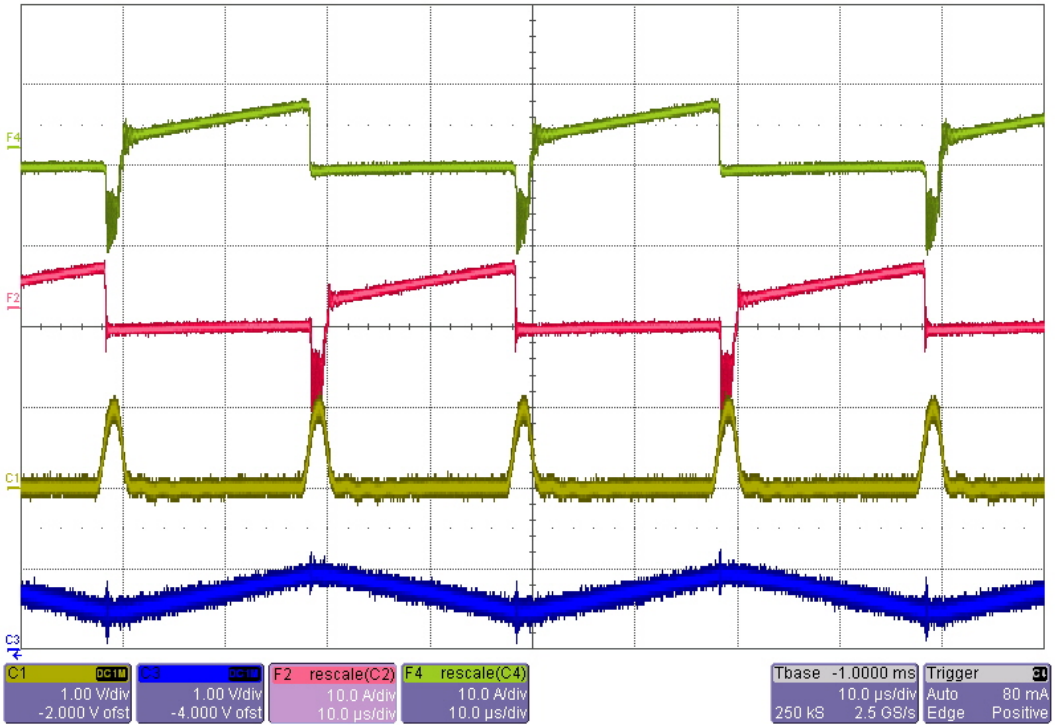

Figure 4.15: Operating oscillograms of two phase ZVT-PWM synchronous buck converter, 10A/div [84]

In order to show the soft-switching process more detail, the voltage and current waveforms of switches S_{1H}, S_{1L} of the phase 1 circuit are measured and depicted in Figure 4.32. It can be seen that the soft-switching process formed by the auxiliary circuit is very obvious, a clear separation exists between the current and voltage curves. But soft-switching process formed by the snubber capacitor is relatively weak, because the output current is high at this time and the value of the buffer capacitor in parallel with the MOSFET is small

and according to Equation 4.5, T_{56} is small. In other words, the voltage on snubber capacitor changes rapidly.

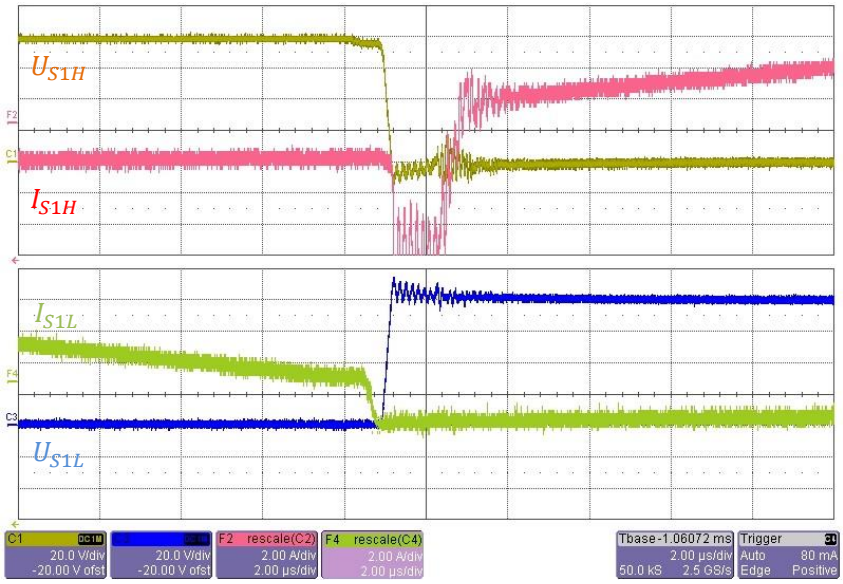

Figure 4.16: Oscillograms of soft-switching process formed by auxiliary circuit (S_{1H} switch on and S_{1L} switch off) [84]

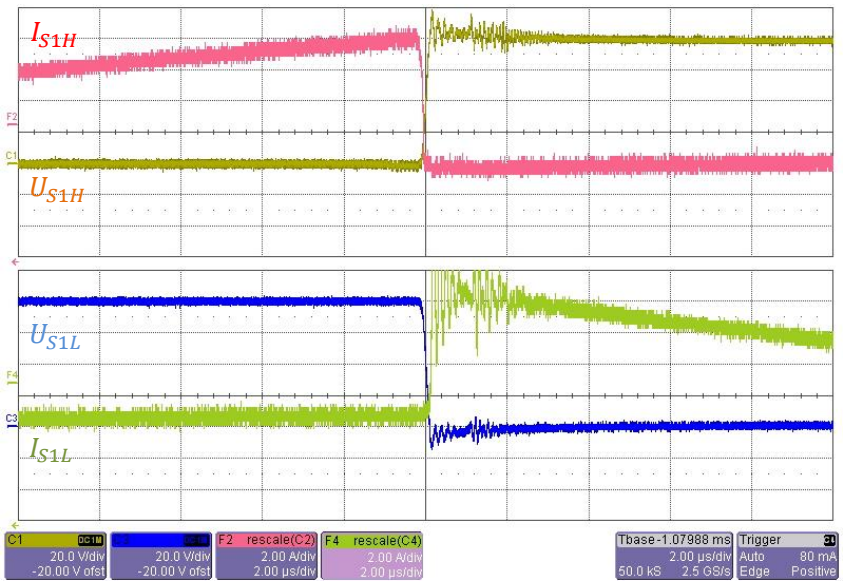

Figure 4.17: Oscillograms of soft-switching process formed by snubber capacitor (S_{1H} switch off and S_{1L} switch on) [84]

The efficiency and power loss curve (red curves) are measured and depicted in Figure 4.18 under the following conditions: input voltage 80V, output voltage 40V, power load range from 200W to 1600W, and the hard switching two-phase buck converter is used as a reference (blue curves).

It can be seen when the output power is less than 400W, the efficiency of the two-phase ZVT-PWM buck converter have no superiority compared to hard switching buck converter, this is because the conduction losses are dominant at this point, and in the circuit of 2 phase ZVT-PWM buck converter, the operation of the auxiliary circuit leads to additional losses. With the increase of the output power, the auxiliary circuit comes into action to reduce the switching losses of the main power circuit. So that the total loss of the ZVT-PWM buck converter is less than that of the ordinary converter, and this difference tends to increase.

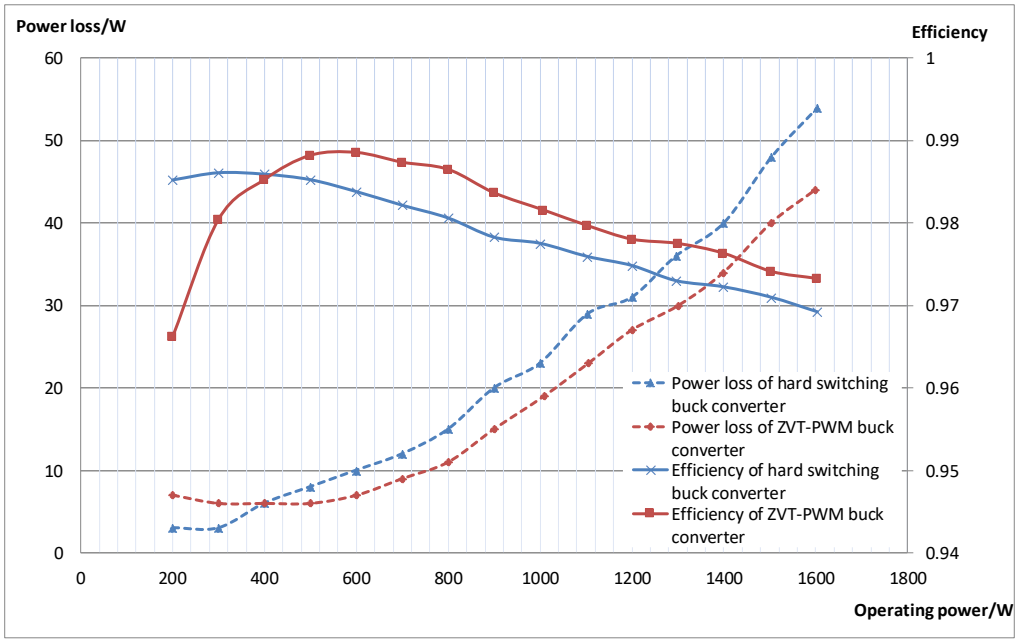

Figure 4.18: Curves of power loss, efficiency of hard switching and 2-phase ZVT-PWM buck converter [84]

4.4 Summary of ZVT-PWM multiphase buck converter

A multiphase ZVT-PWM synchronous buck converter is presented above. The feasibility is verified through theoretical analysis and experiments. This method allows all phases of the buck converter to use the same auxiliary circuit, which separates the soft-switching process of each phase through auxiliary switches $S_{1\cdots N}$ and reduces the switching losses in the dead time T_{D2} through the snubber capacitor, so that soft-switching is basically realized for all switches of buck converter. The disadvantage is that the main switch S_0 in the auxiliary circuit still turns off with hard switching. For the entire converter, the following points are summarized:

- In this multiphase ZVT-PWM synchronous buck converter, only one auxiliary circuit is used to realize soft-switching of all MOSFETs in main power circuits. Thus the complexity of the converter is significantly reduced and the reliability is improved.

- The switching frequency of the power part is constant, and the operating frequency of the auxiliary circuit is N times that of the main power circuit. The main losses are concentrated in the auxiliary circuit, which facilitates the thermal design of the circuit. Extra devices or circuits can be added, such that the MOSFETs in the auxiliary circuit can also achieve the soft-switching turn-off.

- Based on the soft-switching operation principle, the conversion ratio of the multiphase buck converter is the same as the normal buck converter. Soft-switching operation can be easily maintained for wide line range and load rage. Considering that the auxiliary circuit needs to operate on ahead of main power circuit , the converter cannot be operated with too large or too small a duty cycle.

- The PWM control signals and timing of this converter are more complex and require a high performance MCU to handle the related tasks.

Finally, the laboratory prototype was built and the above analysis and conclusions were verified.

4.5 Soft-switching multiphase buck converter with parallel resonant DC-Link circuit

To provide for either a zero voltage or zero current condition (or both), soft-switching inverters apply some form of resonant LC network between input and output sides of a converter circuit and are therefore broadly classified as "resonant converters". This LC network is used to resonate either the current in the devices or the voltage across the devices to zero for long enough to allow soft turn-off and turn-on of all devices that require a status change [87] [88]. The dv/dt and di/dt in the devices is therefore limited by the resonant tank components and can be greatly reduced compared with the hard-switched case.

This section presents a soft-switching multiphase DC/DC converter with parallel resonant dc-link circuit for high frequency power conversion [89]. This well-known soft-switching converter provides variable link pulse position as well as variable link pulse width and thus a good control capability (Figure 4.19). Moderate combination of two soft-switching operations enables the conventional pulse-width modulation technique to be used. Due to distinctive advantages including true PWM capability, minimum device voltage stresses and reasonable additional device count (3 devices), the proposed converter can be operated for a wide power range.

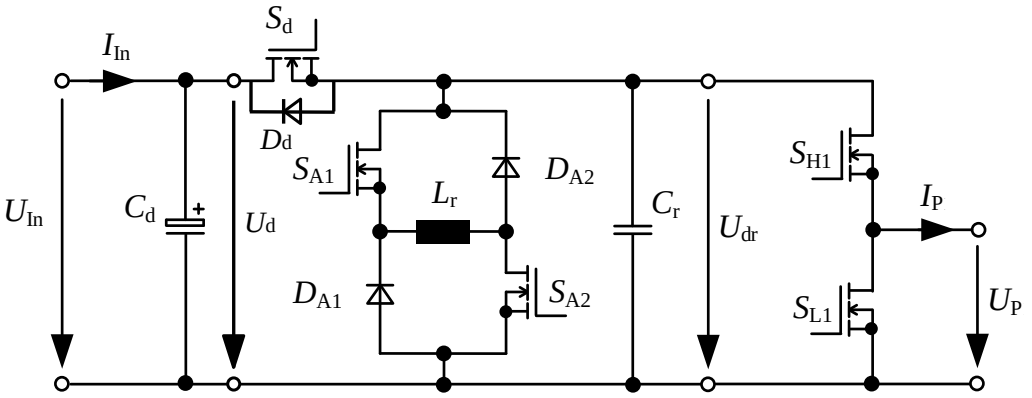

Figure 4.19: Circuit of the parallel resonant dc-link converter [89]

The maximum voltage at the resonant circuit capacitor is limited in this circuit to the dc input voltage. Thus, the voltage stress of the switching elements is significantly reduced. A disadvantage is the required high current in the resonant circuit inductance, which must be greater than the output current of the converter in order to fully charge the resonant circuit capacitor again and thus to guarantee zero voltage switching in the phase leg. The

additional on-state losses occur at the switching elements in the DC voltage input of the converter. These losses must at least be compensated by the soft-switching operations. The high expenditure on semiconductor elements makes the converter profitable only operating with larger power.

In principle, the duty cycle can be changed as required with this converter version, with the exception of restrictions for very large and very small duty cycles caused by the resonant oscillation process. These duty cycle range limitations can be prevented by a scheduler shown in. This multiphase converters will also be analyzed. The advantages of multiphase converters include small ripple current, redundant structure, easy heat dissipation, etc. In general, multiphase converters are controlled by PWM signals with phase-shift, thus they require multiple identical auxiliary circuits to allow each phase to operate soft-switching conditions, but this thesis proposes a method of using one resonant dc-link circuit to control the soft-switching operation of multiple phases. First the operational principles, analyzes and the realization of PWM control are presented using a single phase converter, and then the circuit analysis is extended to interleaved multiphase converter in the simulation. Eventually the feasibility of the circuit is verified through a tow-phase buck converter with PRDCL prototype.

4.6 Theoretical Analyses of the Parallel Resonant DC-Link Converter

Referring to Figure 4.19, in this parallel resonant dc-link converter (PRDCL), individual phase legs are separated from the DC input by a switching element S_d. In the converter, a capacitor C_r and an inductance L_r are arranged, which from a resonant circuit. With the help of auxiliary switching elements and diodes S_{A1}, S_{A2}, D_{A1} and D_{A2}, the resonant circuit inductance can be magnetized, switched into freewheeling and demagnetized again.

The switch S_d in the input of the converter is initially closed, and both switching elements S_{A1} and S_{A2} in the auxiliary circuit are opened. The converter is located in one of the areas of operation (working, free-wheeling or back-working area). Before a switching process in the converter is started, S_{A1} and S_{A2} are switched on (unloaded switching operation) and a current is impressed into the resonant circuit inductance, the switches are turned on with zero current conditions. The switching element S_d in the DC voltage input is now opened with zero voltage conditions, and the inductor current continues to flow through the resonant circuit capacitor C_r. The voltage U_{dr} at the input of the converter is decreased resonantly until it becomes zero. A possible input

current of the bridge - positive or negative - accelerates or delays the discharging process of the capacitor. After the resonant circuit capacitor is completely discharged, the inductor current continues to flow freewheel through the diodes and switching elements in the auxiliary circuit. During this time, the switching elements of the converter can be turned on or off with zero voltage conditions.

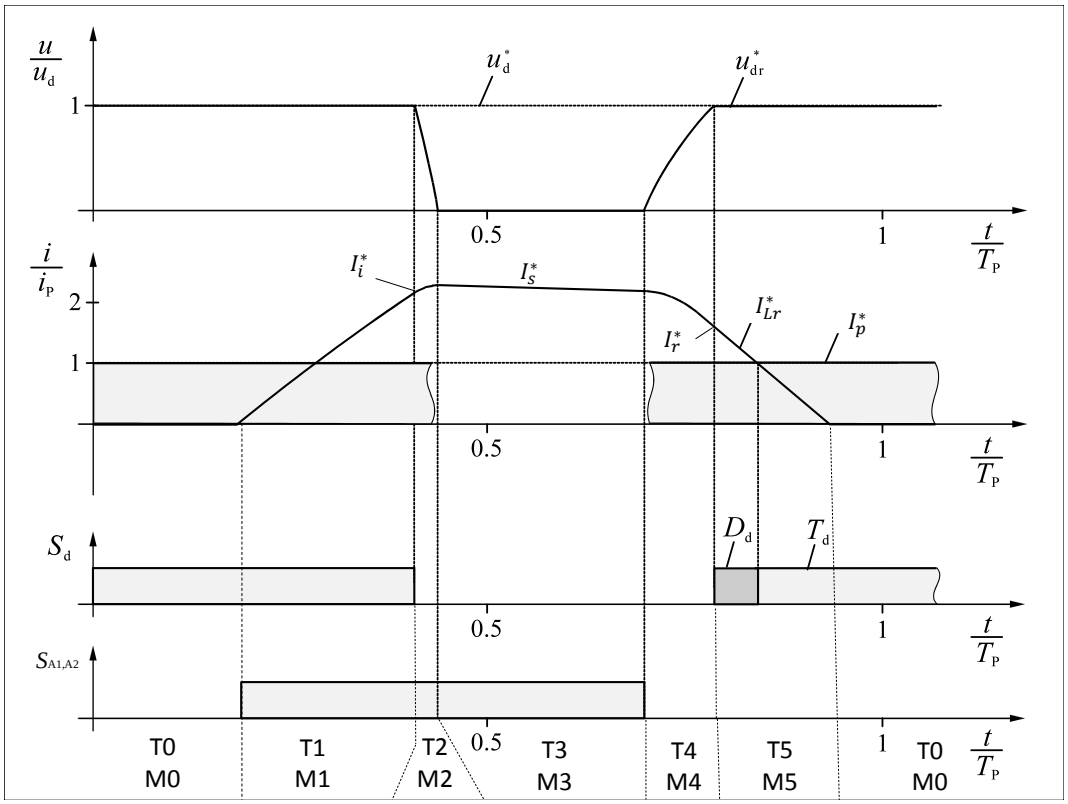

Figure 4.20: Current and voltage curves during a switching process of a parallel resonant dc-link converter with nominal value [89]

If the switching operations in the converter have been completed, the switching elements of the auxiliary circuit are opened again with zero voltage conditions, and the current of the resonant inductor continues to flow via the diodes D_{A1} and D_{A2} of the auxiliary circuit and the resonant circuit capacitor C_r parallel to the individual phases. The voltage U_{dr} increases to U_d. A possible current of the converter legs- positive or negative-delays or accelerates the charging process of the capacitor. After the resonant circuit capacitor is charged, the antiparallel diode of the switching element S_d takes over the current. Now the switching element S_d can be switched on again with zero voltage conditions, and a new operating area of the converter begins. For bet-

ter representation the current flow in the anti-parallel diode of the switching element S_d is indicated in the last waveform of Figure4.20.

To understand the requirements of multiphase converter with PRDCL control, the PRDCL operation should be first performed on a single phase converter. Since the resonant inductor is sufficiently smaller than the load inductance, the multiphase converter load can be replaced by a current source (I_p) during the switching periods. The current paths for all PRDCL modes and the required time for each mode to successfully achieve the PRDCL operation are illustrated in Figure 4.20, where $\omega_r = 1/\sqrt{L_r C_r}$, $Z_r = \sqrt{L_r/C_r}$, $I_{Lr}(T1) = I_i$, $I_{Lr}(T2) = I_s$, $I_{Lr}(T4) = I_r$.

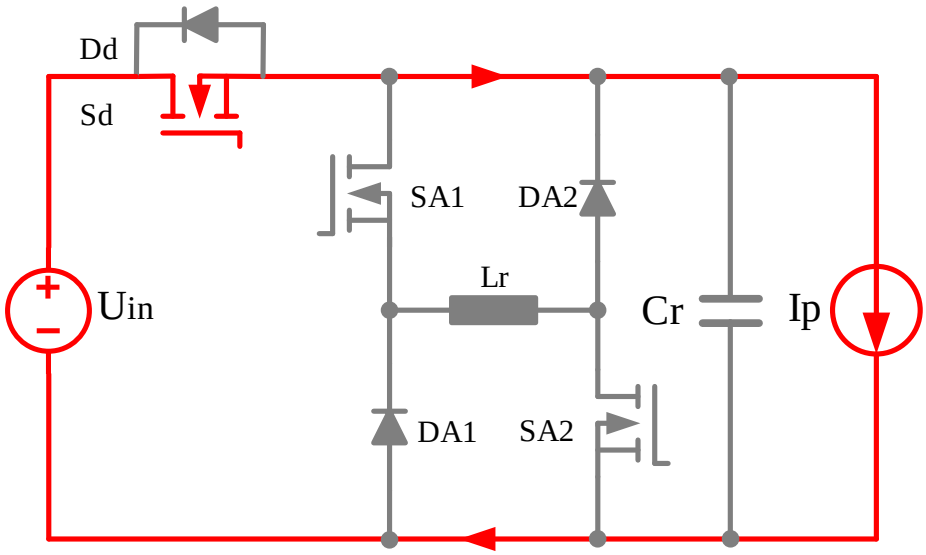

Figure 4.21: Mode 0 diagram of the PRDCL operation [original]

Mode 0 (Time interval 0, S_d: on, S_{A1} and S_{A2}: off): the switch S_d flows the load current, the duration is controlled by the pulse time T0. The parameters on the resonant circuit are as follows:

$$\begin{aligned} I_{Lr}(t) &= 0 \\ U_{Cr}(t) &= U_{dr}(t) = U_{in} \end{aligned} \tag{4.12}$$

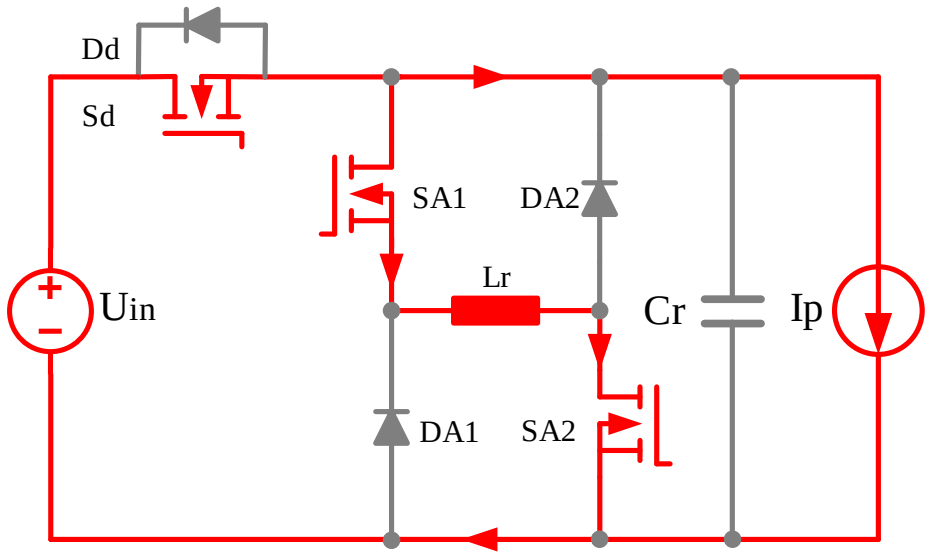

Figure 4.22: Mode 1 diagram of the PRDCL operation [original]

Mode 1 (Time interval 1, S_d: on, S_{A1} and S_{A2}: on): When the resonant process begin, the switches S_{A1} and S_{A2} are turned on with zero current conditions, the inductor current will be increased linearly, and the capacitor voltage is kept with U_{in}, until the inductor current rises to the desired reference value I_i.

$$I_{Lr}(t) = \frac{U_{in}}{L_r}t \tag{4.13}$$

$$U_{Cr}(t) = U_{in} \tag{4.14}$$

The duration of this mode 1 $T_1$is calculated form the condition of $I_{Lr} = I_i$

$$T_1 = \frac{L_r I_i}{U_{in}} \tag{4.15}$$

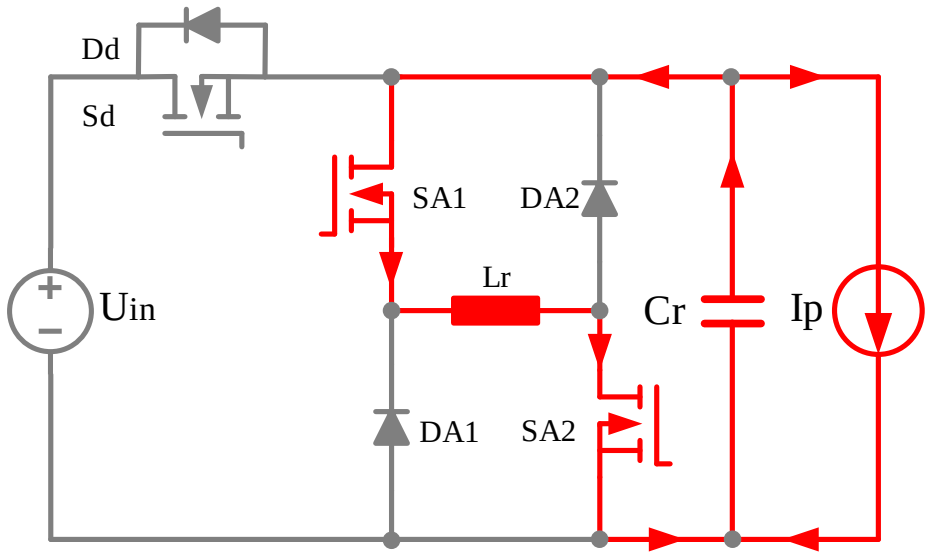

Figure 4.23: Mode 2 diagram of the PRDCL operation [original]

Mode 2 (Time interval 2, S_d: off, S_{A1} and S_{A2}: on): The switch S_d is turned off with zero voltage condition and then, the LC resonant circuit starts to resonate with offset current I_p as follows:

$$I_{Lr}(t) = \frac{U_{in}}{Z_r}\sin(\omega_r t) + (I_i + I_p)\cos(\omega_r t) - I_p \tag{4.16}$$

$$U_{Cr}(t) = U_{in}\cos(\omega_r t) - (I_i + I_p)\sin(\omega_r t) \tag{4.17}$$

The capacitor voltage U_{Cr} is decreased resonantly until it becomes zero. Thus, the duration of this mode T_2 can be obtained:

$$T_2 = \frac{1}{\omega_r}\arctan\left(\frac{U_{in}}{Z_r(I_i + I_p)}\right) \tag{4.18}$$

The peak resonant inductor current I_s is also obtained by

$$I_s = \sqrt{(I_i + I_p)^2 + \left(\frac{U_{in}}{Z_r}\right)^2} - I_p \tag{4.19}$$

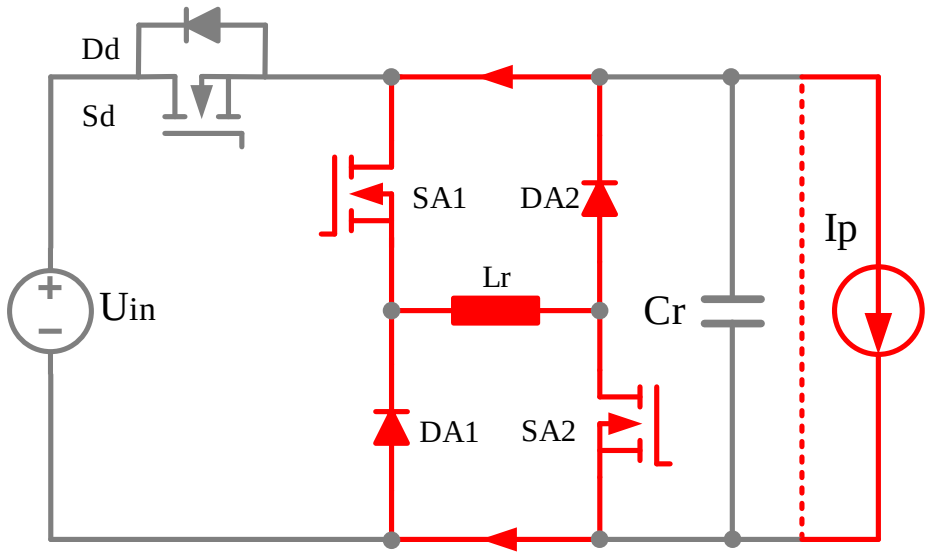

Figure 4.24: Mode 3 diagram of the PRDCL operation [original]

Mode 3 (Time interval 3, S_d: off, S_{A1} and S_{A2}: on): The resonant capacitor voltage U_{Cr} is kept zero while the inductor current I_{Lr} freewheels through paths $S_{A1} \rightarrow D_{A1}$ and $S_{A2} \rightarrow D_{A2}$.

$$\begin{aligned} I_{Lr}(t) &= I_s \\ U_{Cr}(t) &= 0 \end{aligned} \tag{4.20}$$

In practice, due to the losses in the freewheel circuit, the value of I_s is slightly reduced. This zero dc-link voltage period, T_3, provides zero voltage switching condition for converter devices. And the duration of this mode is controllable, the zero pulse position can be located at any position by PWM controller. If the S_{H1} switch in Figure 4.19 is switched at this time, the ZVT and ZCT conditions will be met at the same time. The load current is supplied by the inductor in the power circuit.

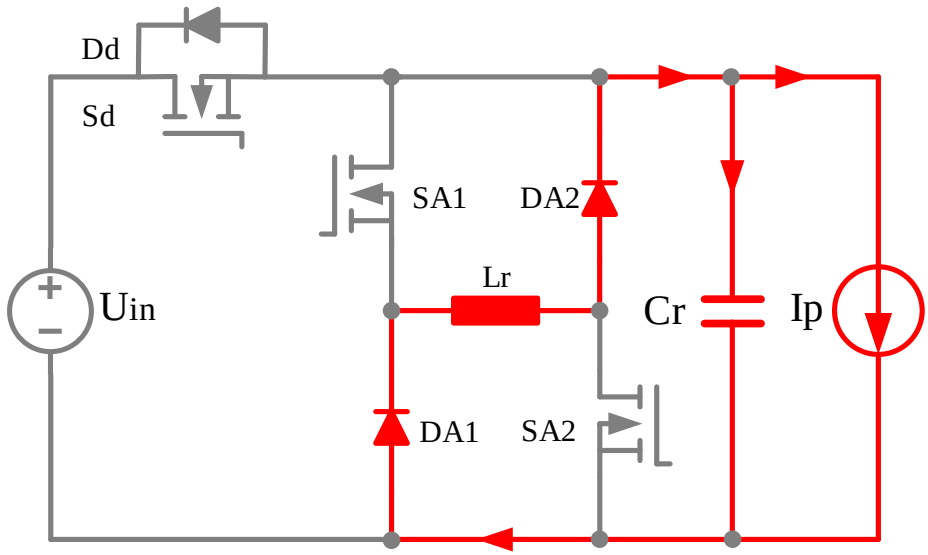

Figure 4.25: Mode 4 diagram of the PRDCL operation [original]

Mode 4 (Time interval 4, S_d: off, S_{A1} and S_{A2}: off): When the switching of converter devices is completed, the switches S_{A1} and S_{A2} are turned off with zero voltage condition, and the flowing path of inductor current is $D_{A1} \rightarrow Lr \rightarrow D_{A2} \rightarrow Cr$. Thus, the capacitor voltage U_{Cr} returns to U_{in}. Assuming that the load remains the same, i.e., the I_p is constant, the parameters on the resonant circuit are given by:

$$I_{Lr}(t) = (I_s - I_p)\cos(\omega_r t) + I_p \tag{4.21}$$

$$U_{Cr}(t) = Z_r(I_s - I_p)\sin(\omega_r t) \tag{4.22}$$

The duration of this mode is calculated when $U_{Cr} = U_{in}$ as follows:

$$T_4 = \frac{1}{\omega_r}\arcsin\left(\frac{U_{in}}{Z_r(I_s - I_p)}\right) \tag{4.23}$$

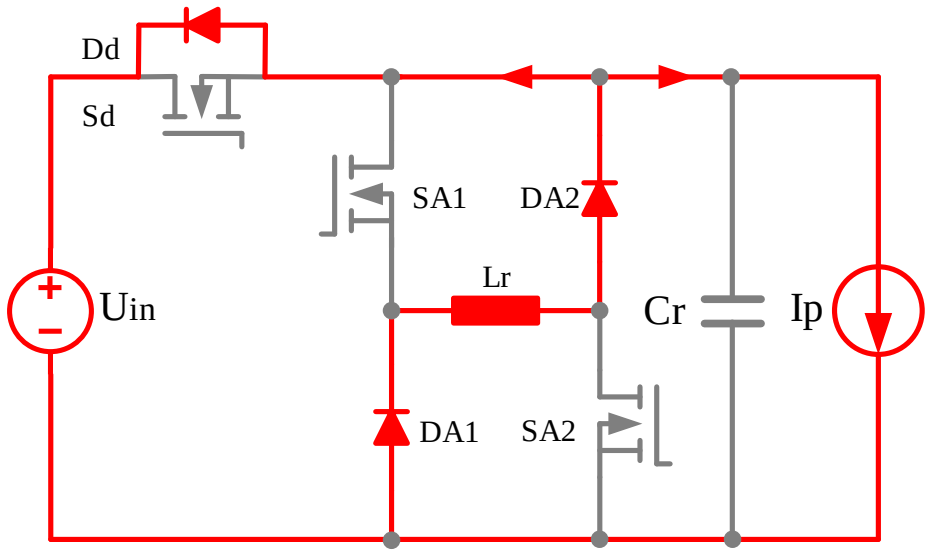

Figure 4.26: Mode 5 diagram of the PRDCL operation [original]

Mode 5 (Time interval 5, S_d: on, S_{A1} and S_{A2}: off): When the capacitor voltage U_{Cr} is increase slightly over U_{in}, the anti-parallel diode D_d is turned on with zero voltage condition. Then, the capacitor voltage U_{Cr} is clamped by input voltage U_{in} and the remained energy of inductor L_r is returned to voltage source. S_d can now be turned on again with zero voltage. The equations for this mode are:

$$I_{Lr}(t) = -\frac{U_{in}}{L_r}t + I_r \tag{4.24}$$

$$U_{Cr}(t) = U_{in} \tag{4.25}$$

The duration of this mode is:

$$T_5 = \frac{L_r I_r}{U_{in}} \tag{4.26}$$

One switching cycle of the PRDCL is completed at the end of mode 5. Now this well-known method will be used in soft-switching of multiphase converters. In order to limit the effort only one auxiliary circuit should to be used to switch the individual interleaved phases of the converter. The challenge is that the switching operations in the individual phases to overlap. This will be examined by numerous simulations.

4.7 Simulations of the Parallel Resonant DC-Link Converter

The circuit of a multiphase converter used for simulations is shown in Figure 4.27. The capacitor C_r is distributed to the individual switch elements in the main power circuit. The capacitor $C_{r1\cdots 2N}$ connected with individual devices are chosen as $C_{rk} = (2/N) \cdot C_r$, where $k = 1, 2, \cdots 2N$, so that the equivalent resonant capacitance is still C_r, and the soft-switching process can be achieved in the same manner as in the circuit shown in Figure 4.19. The load of different phases is simulated by a constant current source in each case. Besides, all components of the circuit are under ideal conditions. For circuit simulation, the program LT-Spice is used.

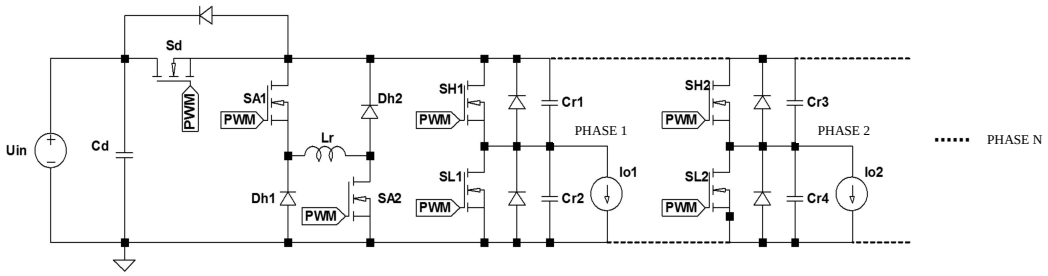

Figure 4.27: The simulated multiphase circuit of the parallel resonant dc-link converter [89]

First, simulations were performed on a single phase converter. In this case, only phase 1 is switched in the illustrated circuit. The auxiliary circuit of oscillating processes is excited at each switching operation in the phase. The simulation results are shown in Figure 4.28 with two duty cycles: 37.5% (a) and 62.5% (b). The first pane indicates the control signals of switches in the half-bridge, for the high side switch S_{H1} (purple) and the low side switch S_{L1} (green). In the middle, the dc-link voltage U_{dr} (blue) and the current in resonant inductor I_{Lr} (red) are presented. When the auxiliary circuit is operating and S_{H1} is still closed, that part of the current flows to the load, so there is a difference between the adjacent current peaks of I_{Lr}. The voltage curve (blue) and the current curve (red) of the high side switch are shown in the last two panes respectively. When the auxiliary circuit resonates, C_{r2} will be discharged during T_2 and charged during T_4. Therefore, a current spike will be generated on the load current.

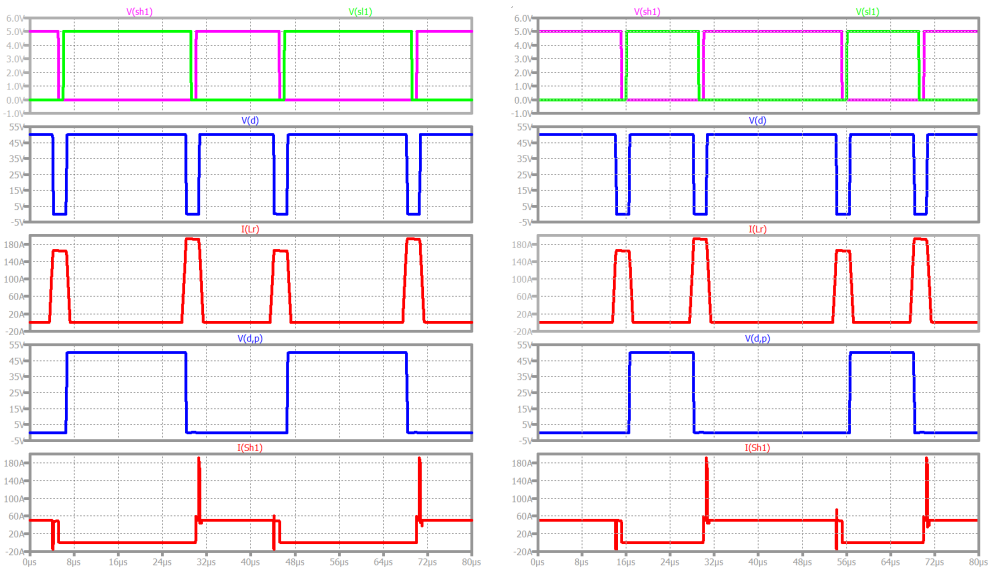

(a) 37.5% duty cycle (b) 67.5% duty cycle

Figure 4.28: Current and voltage curves of single phase PRDCL converter [89]

In this method, the auxiliary switches are employed to each switching operation, and thus the switches in the half-bridge are all operating under soft-switching conditions. For multiphase converters, this concept is not feasible since the individual phases are overlapping. In a multiphase converter with PRDCL, the following control strategy are used. The oscillating processes are initiated by the auxiliary circuit only when the high side switch is turned on. The resonance frequency in the auxiliary circuit must be N times the operating frequency of the switch in the half-bridge circuit, where N is the number of phases. If the high side switch is switched off, the switching process is relieved switched by the parallel capacitor. This operation was already presented in section 4.2.

The current and voltage waveforms for a two-phase converter are shown in Figure 4.29, with two duty cycles: 37.5% (a) and 62.5% (b). The first and second panes are the control signals for switches in the half-bridge, the second phase is switched interleaved to the first phase by half a period. If the high side switch of this phase is turned on, the auxiliary circuit must also be activated. The dc-link voltage U_{dr} (blue) and the resonant inductor current I_{Lr} (red) in the middle of an additional oscillating processes can be seen. Last two panes describe the voltage (blue) and current (red) of half-bridge high side switch in different phases. It can be seen from the figure that during the opening process, the high-side switch realizes zero voltage and current turn on with the

help of auxiliary circuit. During the closing process, the existence of parallel capacitance reduces the switching losses.

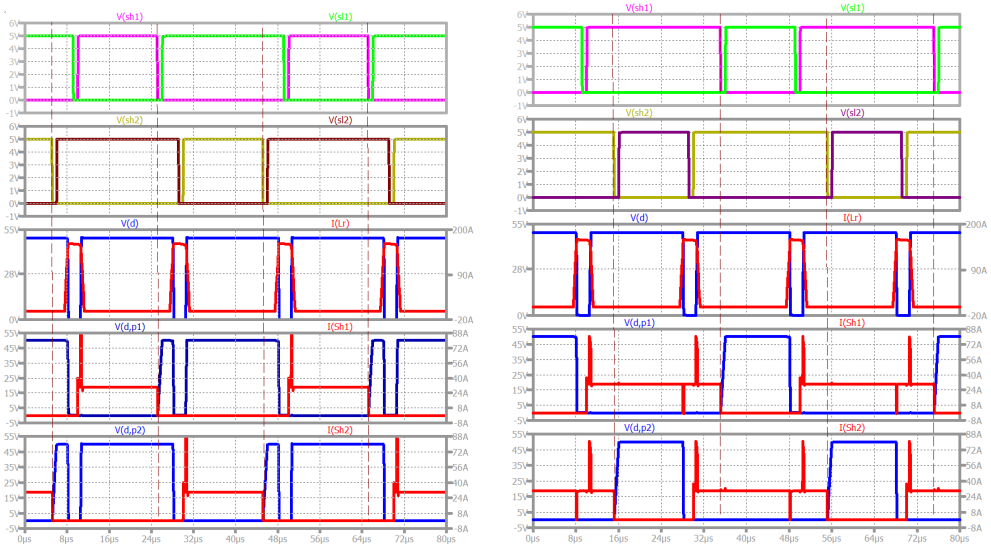

(a) 37.5% duty cycle (b) 67.5% duty cycle

Figure 4.29: Current and voltage curves of two-phase PRDCL converter [89]

In this control strategy, the problem is a lower conversion ratio when compared with the normal multiphase buck converter. As shown in Figure 4.30, the voltage drop and rise during resonance process can be approximated as linear in time interval T2 and T4. In a multiphase converter, when the duty cycle is greater than the phase shift difference (1/N), the conversion ratio will be affected. In Figure 4.20, the duration of resonance process depends on 3 time interval, T2, T3 and T4. The period of T3 is controllable, and the switch needs to complete the state switching in this period. When the N phase buck converter operates with f_s as the switching frequency, the auxiliary circuit operates at a frequency of $N \cdot f_s$. Similarly, a voltage gap with frequency $N \cdot f_s$ occurs on U_{dr}. When the D is 100%, here D is the duty cycle for half-bridge to control, the conversion ratio of an N phase buck converter with switching period T_P is:

$$M_{(D=1)} = \frac{U_{in}}{U_{out}} = 1 - \frac{N \cdot (2 \cdot T_3 + T_2 + T_4)}{2 \cdot T_P} \tag{4.27}$$

From the above equation, it can be seen that the multiphase expansion of this converter is limited by more elements, including the switching frequency of the converter, and the time of the resonance process. When the operating

frequency and resonance parameters are determined, the appropriate number of phases is then selected to ensure that the conversion ratio of the converter meets the design requirements.

Figure 4.31 shows the voltage at phase output with different duty cycles for a two-phase converter. When duty cycle is 37.5%, the conversion ratio is given by:

$$M_{(D=0.375)} = D - \frac{T_3 + T_4}{2 \cdot T_P} \tag{4.28}$$

When duty cycles is 50% or 62.5%:

$$M_{(D=0.5,0.625)} = D - \frac{T_2 + 3 \cdot T_3 + 2 \cdot T_4}{2 \cdot T_P} \tag{4.29}$$

When duty cycle is 100%:

$$M_{(D=1)} = D - \frac{T_2 + 2T_3 + T_4}{T_P} \tag{4.30}$$

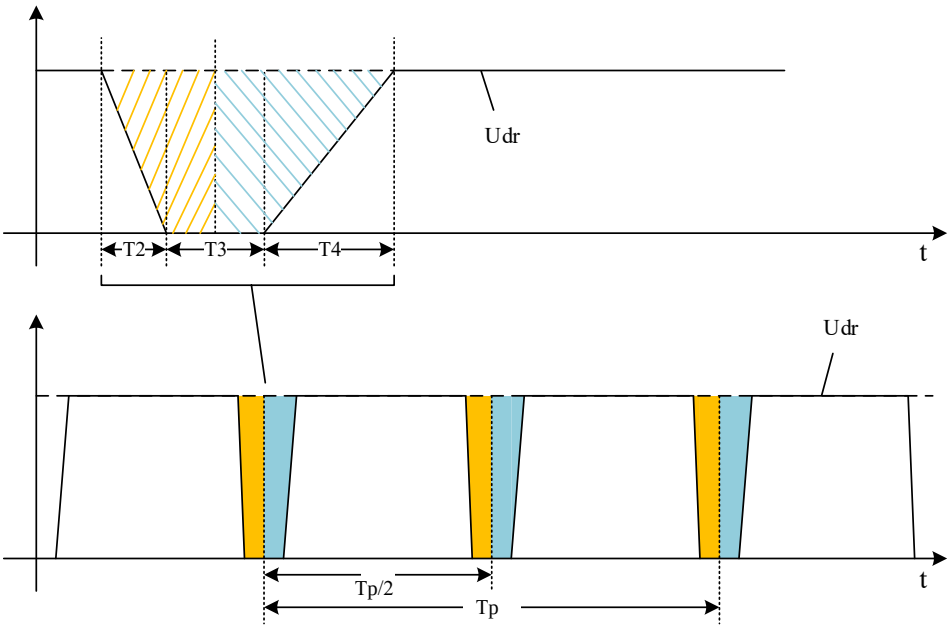

Figure 4.30: Timing of resonant processes in multiphase buck converter [original]

From equations 4.28 to 4.30, it can be seen that resonance process has an influence on the average value of the output voltage. For this reason,

the auxiliary circuit switching operation should be completed in the shortest possible time. A converter with more phases has an even greater influence on the phase output voltage.

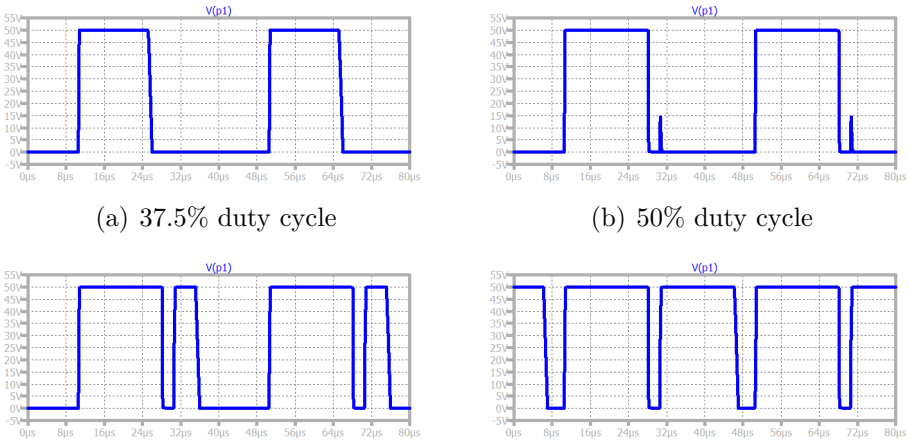

(a) 37.5% duty cycle

(b) 50% duty cycle

(c) 62.5% duty cycle

(d) 100% duty cycle

Figure 4.31: Phase output voltage of a two-phase converter with different duty cycles [89]

4.8 Practical results of the parallel resonant dc-Link converter

The practical realization of a two-phase buck converter with PRDCL is shown in Figure 4.32.

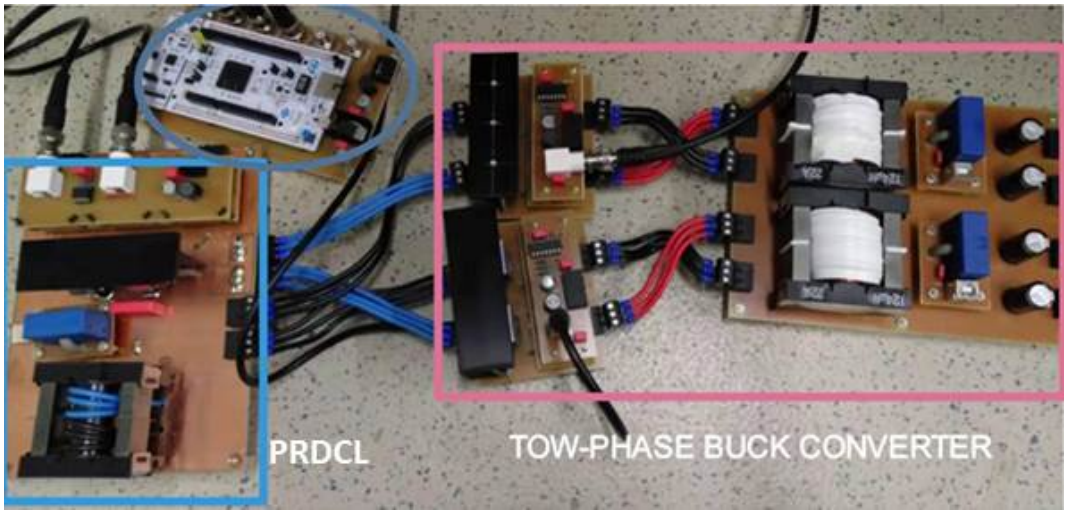

Figure 4.32: Realization of a two-phase buck converter with PRDCL [89]

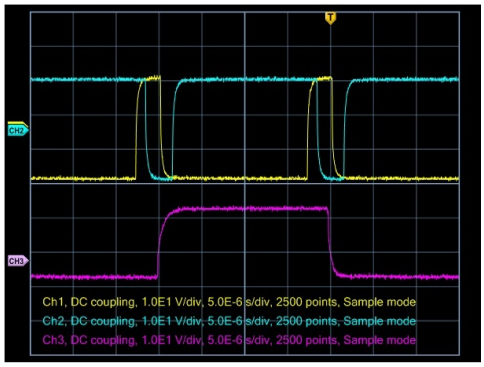

(a) Control signals of PRDCL. Yellow: $S_{A1,A2}$, Blue: S_d, Pink: S_{H1}

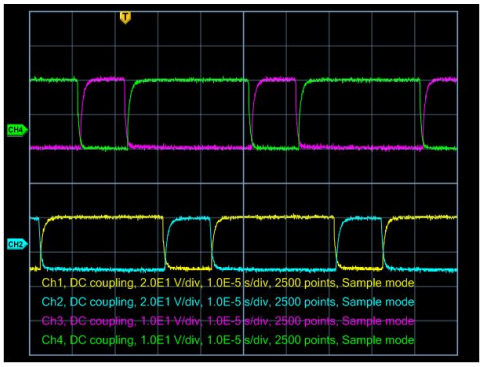

(b) Control signals of two phase buck converter with 180° phase angle

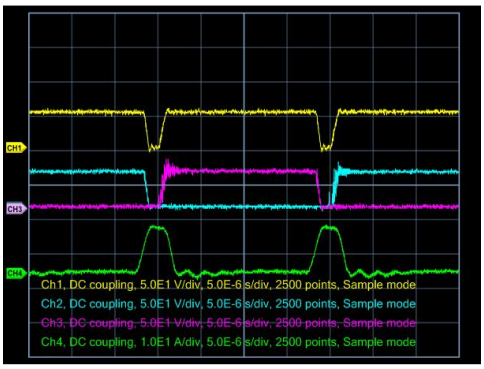

(c) Yellow: U_{dr}, Blue: U_{SH1}, Pink: U_{SH2}, Green: I_{Lr}, D: 50%

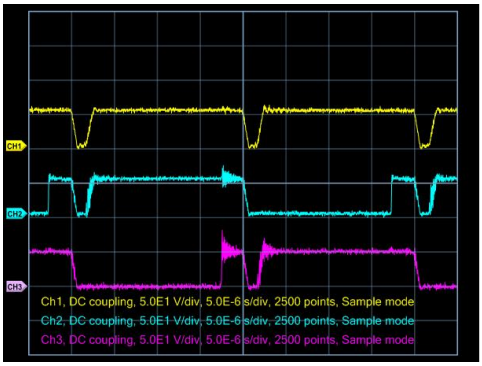

(d) Yellow: U_{dr}, Blue: U_{SH1}, Pink: U_{SH2}, D: 37.5%

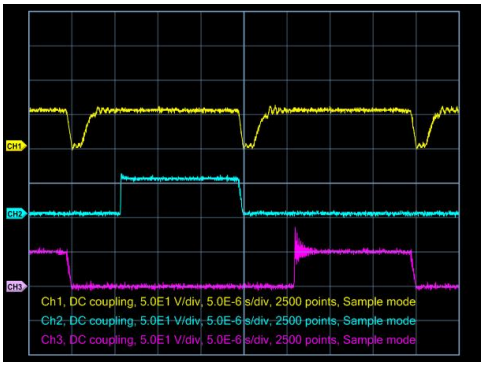

(e) Yellow: U_{dr}, Blue: U_{SH1}, Pink: U_{SH2}, D: 67.5%

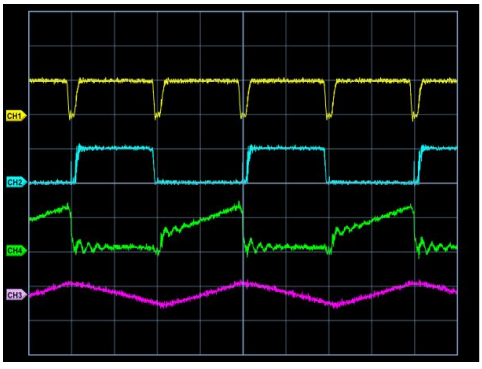

(f) Yellow: U_{dr}, Blue: U_{SH1}, Green: I_{SH1}, Pink: I_L, D: 50%

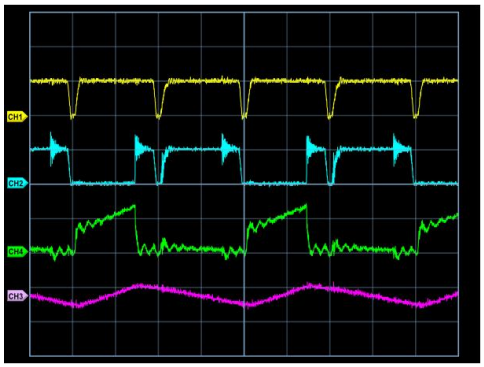

(g) Yellow: U_{dr}, Blue: U_{SH1}, Green: I_{SH1}, Pink: I_L D: 37.5%

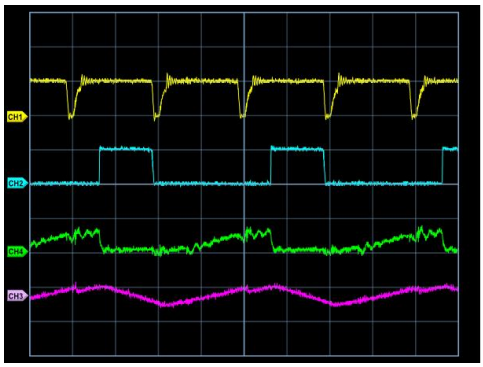

(h) Yellow: U_{dr}, Blue: U_{SH1}, Green: I_{SH1}, Pink: I_L D: 67.5%

Figure 4.33: The key waveforms of two-phase buck converter with PRDCL [89]

It can be seen in Figures 4.33(a)-(h), the key waveforms of two-phase buck converter with PRDCL are presented. First, Figure 4.33(a) and (b) show the control signals of MOSFETs in the auxiliary circuit (50kHz) and the connected two-phase buck converter (25kHz). Under open-circuit condition, the dc-link circuit voltage U_{dr}, the voltage of MOSFET U_{SH1} in phase 1, U_{SH2} in phase 2 are presented with different duty cycles in Figure 4.33(c)-(e). In addition, the resonant inductor current I_{Lr} is shown by 50% duty cycle. At last, Figure 4.33(f)-(h) show the U_{dr}, U_{SH1}, MOSFET current I_{SH1} and the current I_L of the main inductor in buck converter phase 1. The above data are measured with 2kW and 50V input voltage. It can be seen that the measured data is consistent with the simulation results, and the zero voltage transition of the two-phase buck converter for the main MOSFETs S_{H1} and S_{H2} is realized. During the shutdown process, the parallel capacitors of MOSFETs reduce the loss.

The efficiency and power loss curve (red curves) are measured and depicted in Figure 4.34 under the following conditions: input voltage 80V, output voltage 40V, power load range from 200W to 1600W, and the hard switching two-phase buck converter is used as a reference (blue curves).

It can be seen when the output power is less than 1300W, the efficiency of the two-phase PRDCL buck converter have no superiority compared to hard switching buck converter. When the load is light, the switching losses are not obvious, while additional auxiliary circuit operation will also generate losses, so the overall efficiency of the buck converter with PRDCL is rather lower than the ordinary buck converter at this time. But when the power of the load is greater than 1300W, the role of the soft-switching process provided by the PRDCL auxiliary circuit is demonstrated, because as the load increases, the operating current increases and the switching losses become a major part of the total losses. The soft-switching process reduce switching losses. This trend becomes obvious when the operating power increases further.

When comparing the efficiency curves of ZVT-PWM (in Figure 4.18) and PRDCL (in Figure 4.34) buck converter, the characteristics of these two topologies can be seen. In practice, the ZVT-PWM has an auxiliary switch turn-off hard, therefore the switching losses still rise at heavy loads. In PRDCL operation 2 diodes are involved, this part of the loss will be more obvious at light load, and the total efficiency will be affected.

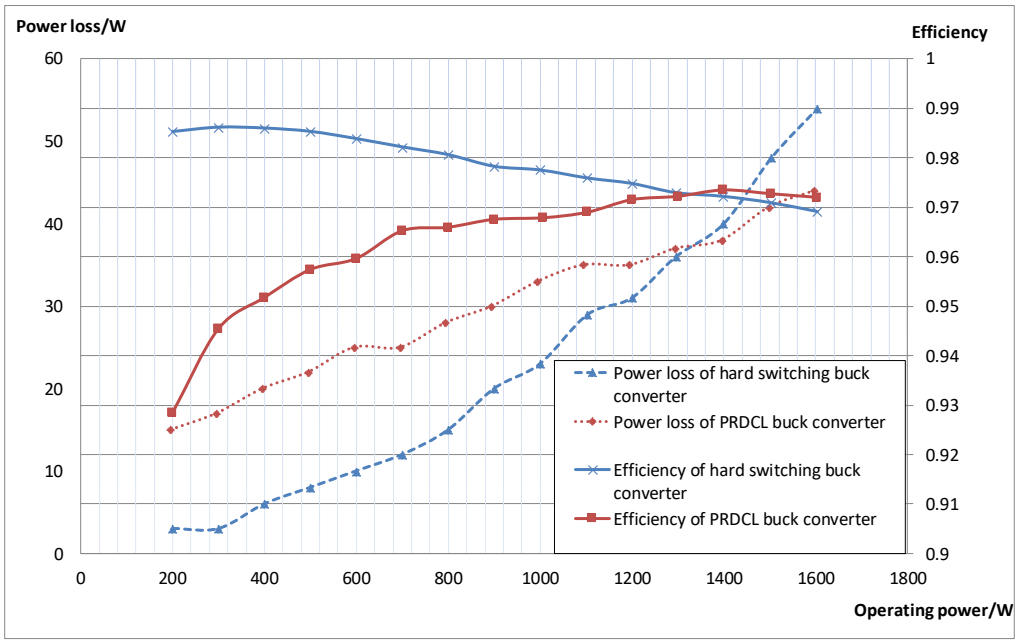

Figure 4.34: Curves of power loss, efficiency of hard switching and 2-phase buck converter with PRDCL [original]

4.9 Summary of multiphase buck converter with PRDCL

A soft-switching multiphase DC/DC converter with a PRDCL circuit is presented. The feasibility of this circuit is proved by simulation and experiment. In this method, one PRDCL circuit can provide zero voltage transition conditions for all main switches of multiphase converter. As the number of circuit phases increases, the conversion ratio of the output and input voltages will actually be less than the duty cycle. Therefore, this circuit is more suitable for the requirement of large difference between in-output voltage. For this converter, the following points are summarized:

- In the multiphase buck converter with PRDCL, no additional voltage stress for the auxiliary as well as the power part of converter, and a resonant cycle requires less switching action by the auxiliary devices.

- An additional circuit can realize the soft-switching process of all switches in the main power circuit, but the operating frequency of the auxiliary

circuit is N times that of the multiphase buck converter, and the zero-voltage turn-off process of the switch is still achieved by the capacitor connected in parallel.

- When the main power circuit is multiphase, zero pulses will appear on the power inductor, which will cause the conversion ratio of the multiphase converter to be small than that of the normal converter. With the increase in the number of phases, the duty cycle is larger. This phenomenon is more obvious, so the auxiliary circuit should operate for as short a time as possible.

- In practice, converters require multiple PWM control signals and have strict timing requirements, which generally need to be implemented by a high-performance MCU.

4.10 Conclusions and contributions

This chapter describes two types of soft-switching multiphase buck converters proposed by author. First, the types of soft-switching circuits, their operating principles and advantages are described in detail. However, in a multiphase converter, there is a superposed effect between the phases, and the number of devices used increases exponentially if an auxiliary circuit is added separately for each phase to achieve soft-switching. Therefore, how to use an auxiliary switch to achieve soft-switching process for all phases is the difficult part of the circuit design. In both types of converters presented in this chapter, only one auxiliary circuit is used, and this circuit requires fewer additional devices.

Multiphase ZVT-PWM synchronous buck converter consists of typical ZVT-PWM resonant circuit and hard switching multiphase PWM synchronous buck converter. All phases share the same auxiliary circuit. The drawback is that each phase still requires an additional switch to separate the soft-switching process. Figure 4.6- 4.13 illustrate the 7 stages of the process of soft-switching, according to the operation principle of the auxiliary circuit. The timing relationship between the PWM control signals and the maximum number of phases in the circuit can be derived. Afterwards, the parameters of the resonant element are designed in this way. Experimental waveforms form hardware measurements are presented at the end and they validated theoretical analyses. The characteristics of this converter are also discussed.

Soft-switched multiphase buck converter with PRDCL circuit consists of the PRDCL resonant circuit and a multiphase buck synchronous converter.

Similarly, all phases in a multiphase buck circuit share a single auxiliary resonant circuit, which is built with three switches and two diodes. Unlike the multiphase ZVT-PWM synchronous buck converter, this converter does not require additional switches to separate the different phases, and all devices implement a soft-switching process. However, the consequence is that there is an interaction between the phases. The conversion rate of the converter is lower than that of a normal converter, Therefore, this converter is more suitable for cases where the input and output differentials are significant. Figure 4.21- 4.26 illustrate the 7 stages of the process of soft-switching, the operation of single-phase and multiphase buck converters with PRDCL. Auxiliary circuits have been simulated using LT-spice. Finally, the analysis and simulation results are verified by constructing the corresponding prototype.

From the study of multiphase soft-switching buck converters, it can be concluded that the advantages of soft-switching are obvious, but they also bring many challenges. The most suitable solution should be selected by considering all aspects in the practical application.

Chapter 5.

Application of Small Fuel Cell Vehicle

5.1 Test bench of FCEV

To optimize the powertrain of fuel cell vehicles, the load of powertrain under real driving conditions need to be reproduced. A test bench for fuel cell powertrain has to built before implementing a fuel cell electric vehicle [33]. With help of the test bench, the following goals can be easily achieved.

- The test bench is more flexible and allows easy implementation of different powertrains (described in Chapter 1) of fuel cell system. In practice, only the wiring location of the converter in the powertrain needs to be changed.
- Distribute or combine the testing of individual modules in powertrain. For example, measuring the performance of a fuel cell system separately or testing the powertrain performance of a pure electric vehicle.
- Testing the characteristics of the electronic switch in the powertrain.
- To find the optimal control strategy for the drive to ensure that the components of the powertrain are operated as gently as possible, in order to increase their lifetime.

The implementation of a test bench for powertrain will be described in detail below. In addition, the test results of the "passive hybrid system" and the multiphase buck converters, described in Chapter 2, are also presented.

5.1.1 Powertrain with fuel cell systems in practice

In practice, a powertrain with integrated fuel cell system is complex. It consists of the following important modules:

1. Electrical machine with the inverter
2. Fuel cell power module (FCPM)
3. Thermal management system
4. Oxygen supply system, hydrogen supply and storage system
5. Battery pack and battery management system (BMS)
6. Electronic switch or DC/DC converters

In addition, the test platform requires a host computer to send, receive and store data as well as to display the operating status of the system.

Powertrain type, E-machine, and inverter

For convenience of understanding, the configuration II of a fuel cell powertrain is selected and the powertrain of these vehicles consists of an electric machine which is controlled by an inverter. On the DC-side of the inverter a battery is generally connected. In addition, the fuel cell is coupled to the battery via an electronic switch (described in Chapter 2) or with DC/DC-converters (described in Chapter 3 and 4). If the electrical machine is operating in motor mode, energy for the drive is taken from the onboard powertrain. In braking and deceleration phases the machine operates in the generator mode and supply energy back into the powertrain battery.

In the test bench, the electrical machine with the inverter to be replaced by power supplies and electronic loads (Figure 5.1). For acceleration phases can be simulated by electronic loads and the braking and deceleration phases can be reproduced by power supply units. In the current state for accelerations, in motor mode, currents of up to 420A and for deceleration, in generator mode, currents of up to 260A can be simulated with the test bench. A power extension is easily possible by the parallel connection of equipment units. For this test bench, power supply units and electronic loads from the Company Elektro-Automatik GmbH are used. The special feature of the power supply units is that they can be combined as "modules" to enlarge the system. Because of the master-slave function, these "blocks" behave like a power supply that can be manually controlled or via an external controller. The power supplies are

designed to have both the function of a constant controlled current control and a regulated voltage.

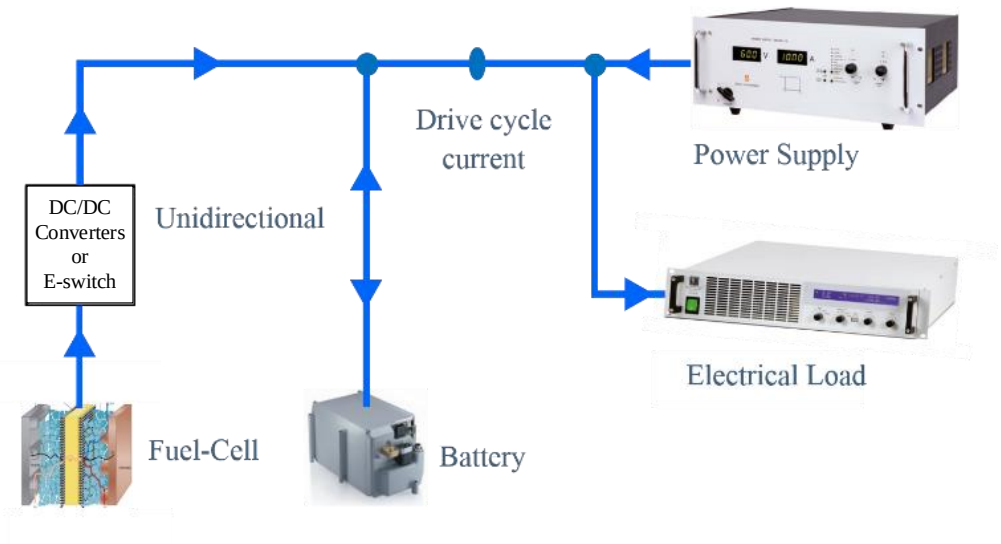

Figure 5.1: Reproduction of the powertrain for fuel cell vehicles [33]

Fuel cell power module

The electrical output characteristics of the HyPM HD8 fuel cell power module are described in Chapter 2, but in practice, the fuel cell stack needs to be correctly configured first [90, 91]. Using HyPM HD8 FCPM as an example, the physical interfaces are shown in Figure 5.2. As can be seen, the blue boxes show the input interface of the FCPM, including the air flow to the anode, the hydrogen flow to the cathode, the coolant flow, the electrical input (power supply and control signals). The yellow boxes show the output interface of the FCPM, including emissions of anode and cathode, coolant flow and the electrical output (load power and control signals). The gases and liquids have to meet the relevant conditions in terms of flow rate, temperature, pressure, etc. The emissions from the cathode and anode of the fuel cell are mainly non-polluting water vapor and small amounts of other gases, which can be exhausted directly into the environment without additional treatment.

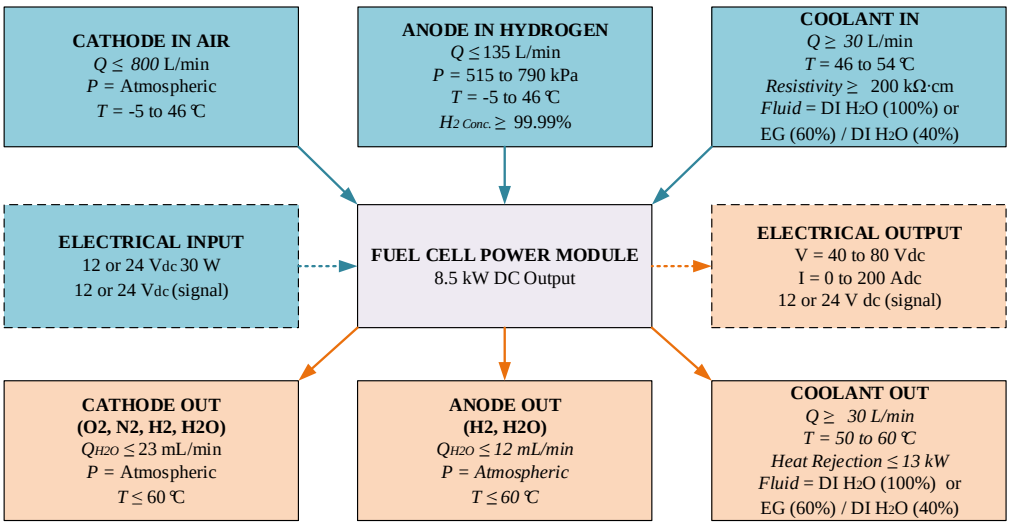

Figure 5.2: The physical interfaces of the FCPM (Q: Flow rate P: Pressure T: Temperature) [original]

Figure 5.3 shows the detailed electrical interface of the FCPM. In order for the FCPM to operate properly, it exports a number of signals to control external circuits. The most important of these is the power output enable signal, which drives an external contactor when the FCPM has passed its self-test.

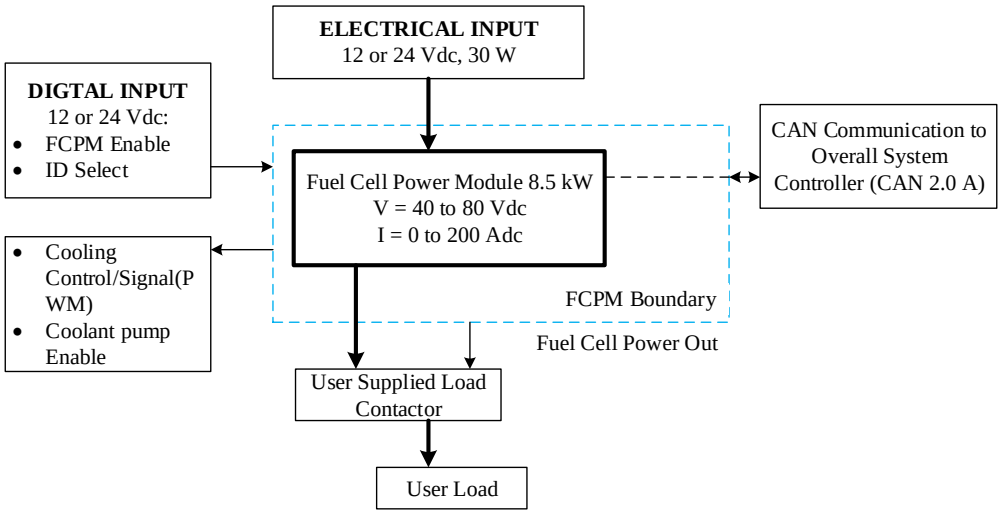

Figure 5.3: The electronic interfaces of the FCPM [original]

The other output signal is a PWM signal to control the temperature, which forms a negative feedback control loop with the external cooling system. The state of the FCPM can only be controlled by system operational commands via CAN bus, e.g. standby, stop, etc.

There are two operation modes of the FCPM for power output:

- Current Draw Allowed Mode: The FCPM controller sends out a Current Draw Allowed (CDA) value. The FCPM always attempts to satisfy the current demand and issue a CDA limit that is higher than the actual demand - subject to power availability. This model was selected to use in the test bench.

- Current Draw Request Mode: In Current Draw Request mode, the FCPM controller must continuously receive a Current Draw Request (CDR) value every 200 ms. The FCPM will attempt to deliver the requested current and issue a CDA limit higher than the CDR.

In both modes, the actual output power of the fuel cell is always controlled by the bus voltage. In CDR mode, the fuel cell output can over-respond to the demand of the load, but if the load does not change correspondingly, the efficiency and performance of the fuel cell will decrease, thus reducing the fuel cell life.

External Oxygen and Hydrogen supply system

The external oxygen supply system, the hydrogen supply and storage system for the FCPM are shown in the Figure 5.4.

The oxygen required for reaction in the FCPM will be captured from the air, However, harmful gases in the air, such as sulphur dioxide (SO_2), nitrogen oxides (NOx) and ammonia (NH3), can cause irreversible damage to the fuel cell catalyst, resulting in reduced FCPM performance. Air filters with harmful gas adsorption protect the catalyst and extend the life of the fuel cell. The air filter can also filter solid particles in the air to avoid system wear and channel blockage.

The air blower is responsible for delivering clean air at a specific pressure and flow rate to the reactor in the fuel cell system, providing the necessary oxygen for the reactor reaction. On the clean air side, an air flow sensor measures the air flow rate entering the FCPM. This information is used to calculate the exact ratio of oxygen to hydrogen to ensure optimum operation and the efficiency of the fuel cell stack. The power of the air blower is determined by the control unit of the FCPM. Finally, the clean air has to pass through

a humidifier to reach the required humidity level for the reaction, which is integrated into the FCPM side and therefore not discussed here.

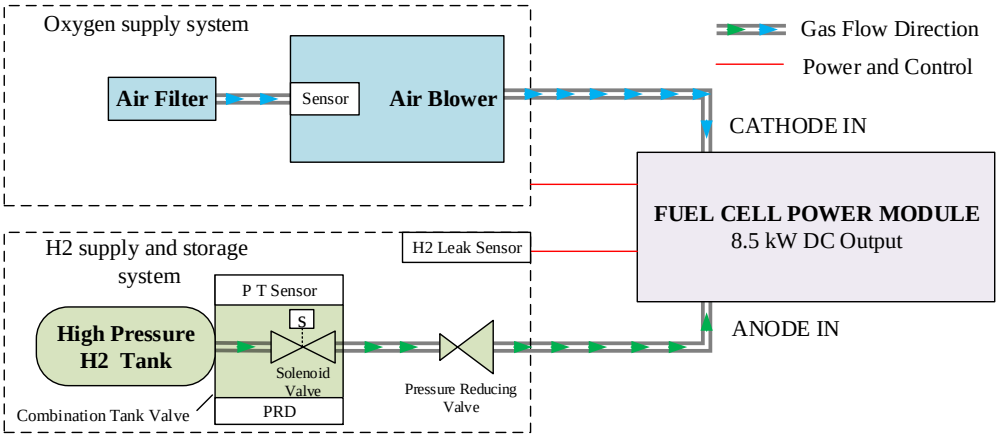

Figure 5.4: The external oxygen and hydrogen supply system [original]

High pressure hydrogen storage and supply systems are important components of the FCPM, It consists of a high pressure hydrogen storage tank, solenoid valve, pressure reducing valve, pressure reducing device (PRD), temperature sensor, pressure sensor and hydrogen leak sensor.

As a major part of the on-board hydrogen system, the high pressure hydrogen storage tank takes on the important task of storing hydrogen, but in order to increase the density of hydrogen storage per unit weight and to provide fuel cell vehicles with a higher range, the tank must be subjected to very high operating pressures. The industrial hydrogen tanks use steel cylinders with filling pressures between 20 and 35MPa, but these cylinders are heavy and suffer from metallic hydrogen embrittlement in long-term use. High performance ultra-thin metal-lined carbon fibre wound composite high-pressure cylinders exist. Compared to traditional metal high pressure cylinders, composite high-pressure cylinders have many advantages such as light weight, high pressure, filling pressure up to 70MPa, safe failure mode of leakage before bursting.

In order to ensure that the on-board hydrogen system and the fuel cell can operate in harmony, the high-pressure hydrogen storage tank must work with a series of valves. The most important of these is the main solenoid valve, which has to be sure to open during normal operation, including when the hydrogen is replenished at the hydrogen refueling station and supplied to the fuel cell, and to be able to close immediately during non-operational periods and when additional conditions occur, such as when the pressure and

temperature in the tank exceed the upper limit, or when the hydrogen in the vehicle is too concentrated due to leaks or other reasons. The pressure reducing valve regulates the pressure of the hydrogen in the high pressure storage tank to the required operating pressure of the FCPM (515 to 790kPa). The purpose of the pressure reducing device is that when the pressure in the tank exceeds the maximum value, the hydrogen is automatically released through the pressure reducing device to ensure that the pressure in the tank is within the normal operating range.

The temperature, pressure and hydrogen leak sensor need to be installed in the system. The operating status of the system can be monitored by the return value of the sensors. While ensuring the safe operation of the system, it can also estimate the amount of hydrogen remaining from the measured pressure.

In the fuel cell test bench, the common cylinder is used because it is easy to replace. In an experimental fuel cell vehicle, an ultra-light composite hydrogen tank produced by the company "ILJIN Composites", made of a nano-composite lining and carbon fibre composite, was put into use in the system.

Thermal management system

The typical external coolant flow system of FCPM is presented in Figure 5.5, and the characteristics of this cooling system can be summarized as follows:

- The coolant flow rate is based on the use of deionized water only. To ensure that the coolant has a resistivity $>200k\Omega \cdot cm$, an appropriate DI polisher in the coolant loop needs to be installed. This is used to remove conductive ions of the coolant. In fuel cell operation, high voltages are generated across the bipolar plates, but it is also required that this high voltage no to be transmitted through the coolant in the middle of the plates to the entire cooling circulation flow path, such that the coolant is not conductive.

- Install a particle filter, capable of filtering particles greater than 233 μm (a 60 mesh filter) without significantly impeding flows on the main coolant line, to avoid accidental clogging of the stack coolant channels.

- A thermostatic valve is required to maintain the system operating temperature. The radiator and fan are not involved in system cooling when the coolant temperature is less than 40 $°C$. When the temperature is between 41 $°C$ and 52 $°C$, the pump, radiator and fan together provide cooling for the system. The power of the pump and fan is controlled by the FCPM via feedback loop.

- The coolant can be either deionized water or 60% ethylene glycol/40% deionized water. The flow rate must be maintained above the heat dissipation requirement.

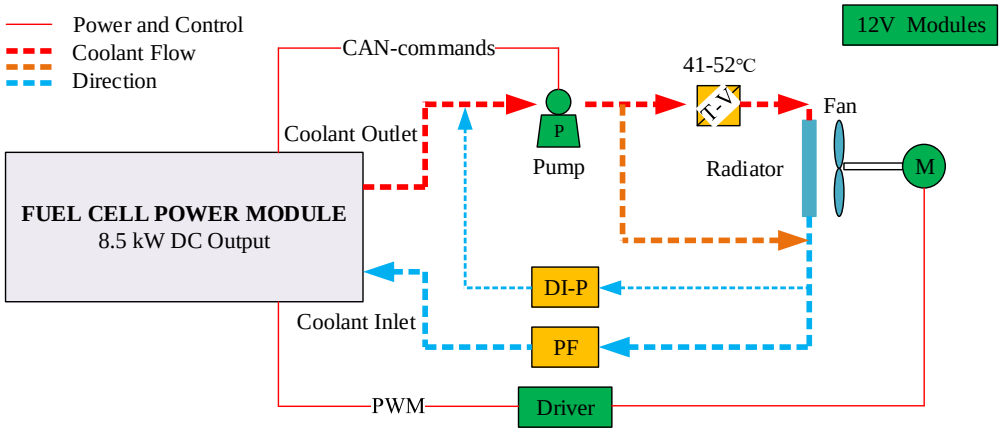

Figure 5.5: The typical external coolant flow system of FCPM (TV: Thermostatic Valve DI-P: Deionized Water Polisher, PF: Particulate Filter) [original]

Battery and battery management systems

The energy storage module in the fuel cell test bench inherits the lithium iron phosphate battery pack described in Chapter 2. The lithium iron batteries can be used only in specified conditions, and therefore BMS is necessary in order to monitor battery state and ensure safety of operation. The principles of BMS and utilization in electric vehicles are not discussed here. The typical function of a BMS is to estimate the state of charge (SoC) of the battery pack, the SoC is the level of charge of an electric battery relative to its capacity. The units of SoC are percentage points (0% = empty, 100% = full). An alternative form of the same measure is the depth of discharge (DoD), the inverse of SoC (100% = empty, 0% = full). Therefore, SoC is an important basis for energy distribution in the fuel cell powertrain

Host computer

To fully drive cycle simulation, the electronic loads and power supplies need to be controlled. For this purpose a LabVIEW program is used, it is possible to build a multi functional upper computer and include the following functions:

- Uniformly establish communication between different modules with interface board. Different modules have different communication methods, for example, the fuel cell system uses CAN bus interface, while the power supply and electronic load use USB interface.

- After establishing the system communication system. It is possible to send control commands to the corresponding modules and to receive the measured values back from the modules. In this way, the operation status of the system can be controlled and the operation process can be observed with image and recorded with table.

- Monitor the operation of each module and the operating environment, such as temperature, hydrogen concentration, etc. Disconnect the physical connection between modules in case of emergency.

A measured current in the powertrain of an electric vehicle can completely be reproduced on the test bench. In the shown test bench, only a battery is loaded with currents from the drive cycle. In addition, for reproducing the current in the powertrain of fuel cell vehicles (see Figure 5.6), the power distribution between the battery and fuel cell with E-switch or DC/DC converter still have to be controlled.

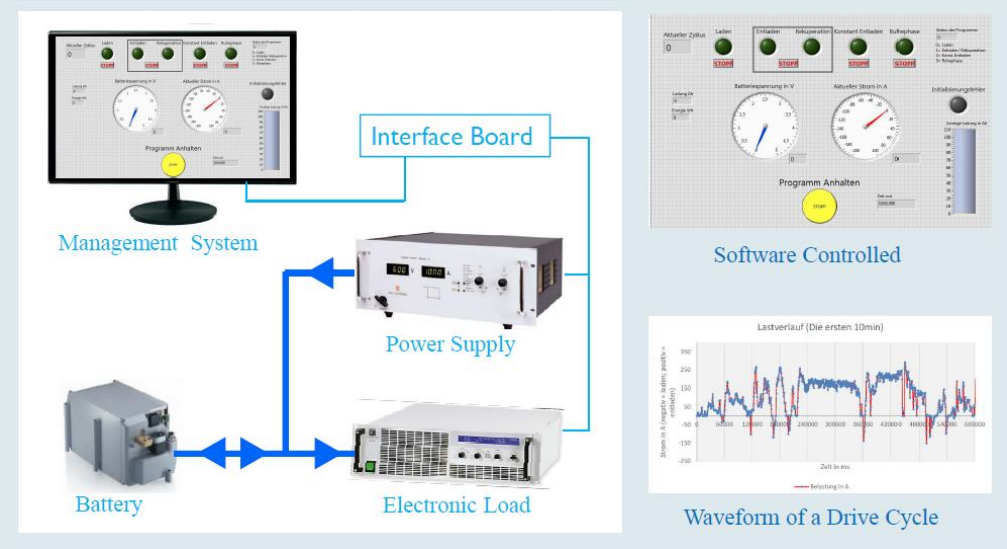

Figure 5.6: Software controlled test bench with power management system [33]

Implementation of a fuel cell powertrain test bench

Figure 5.7 presents the test bench for reproducing the powertrain of fuel cell vehicles. As can be seen from the figure, many components are necessary for construction of the fuel cell system. The hydrogen from the outside bottle to the fuel cell system is lead by thin gas pipes that need to work stable within the permissible operating ranges. In the fuel cell, the ambient air is supplied with a blower in compressed form. This allows the reaction of hydrogen with the oxygen of the air in the fuel cell system. In the background of the image a part of the cooling circuit can be seen. A motorbike cooler is connected outdoors for heat dissipation.

As battery storage, a lithium iron phosphate battery with an energy content of approx. 10kWh is used (Not visible in the figure!). With the constructed test bench with fuel cell system and lithium-iron-phosphate battery, the DC/DC converter or E-switch can be tested under real (driving) conditions. During these drive cycle it must be ensured that the fuel cell system is working within the permissible operating ranges.

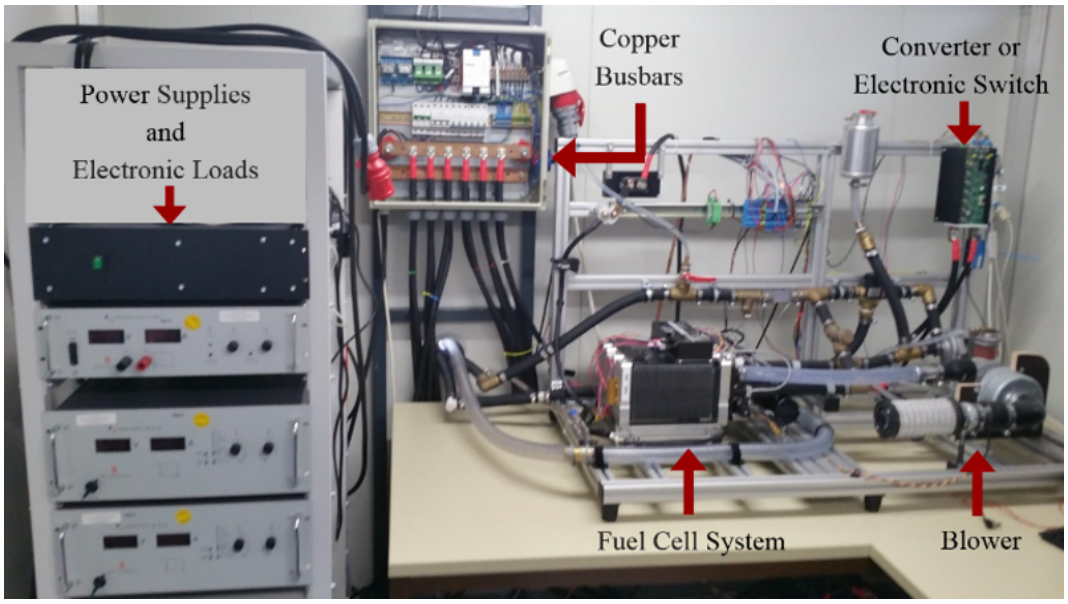

Figure 5.7: Test bench for reproducing the powertrain of fuel cell vehicles [33]

Figure 5.8 shows the schematic of test bench with load, cooling and hydrogen-oxygen supply systems of THE FCEV powertrain. All modules can be powered by the 12V supply, except for the air blower in the oxygen supply system which requires the 48V supply. In the test bench, the air blower is powered by an additional power supply (62V) in order to differentiate the current. But in

vehicles, blower will be powered by 48V battery pack and other modules supplied by 12V battery. In addition, two sets of CAN buses are used to link all modules to ensure communication, and the key information of the module will be uploaded to the host computer and displayed in real time by the LabVIEW program. In the main power circuit, two relays are placed, controlled by the FCPM and the BMS, to ensure that these two modules can be connected to the busbar or separated from it in case of a fault. Another Schottky diode is placed between the FCPM and the bus to prevent the current from flowing back into the FCPM.

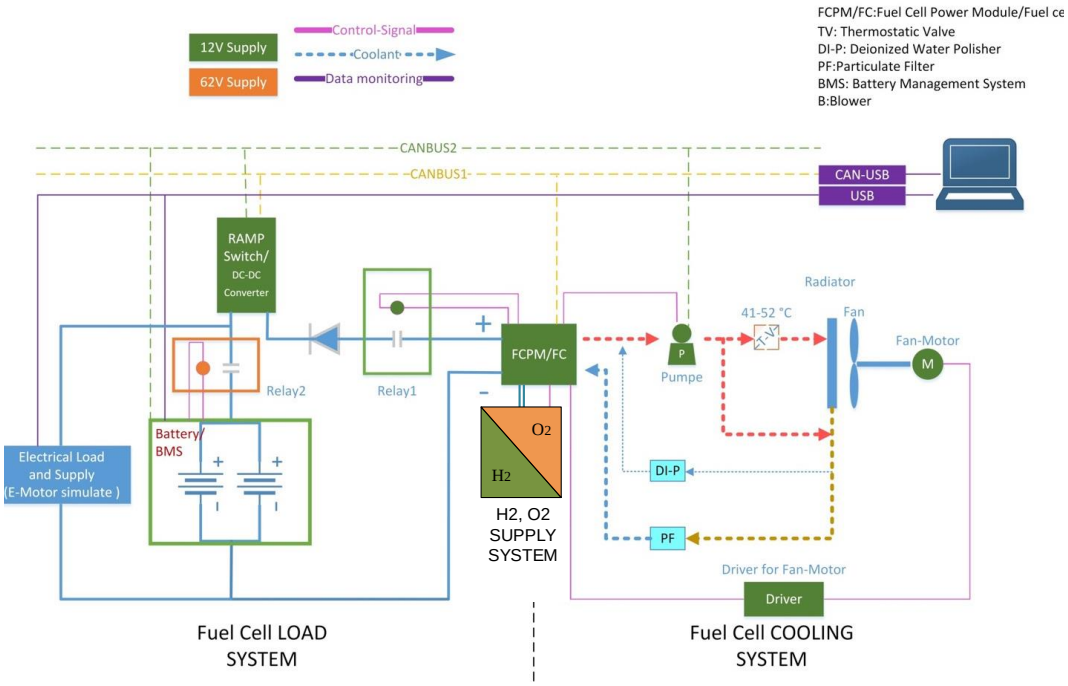

Figure 5.8: Schematic of test bench with load, cooling and hydrogen-oxygen supply systems of fuel cell vehicles [original]

5.2 Implementation of a small fuel cell vehicle

The implementation of a small fuel cell electric vehicle is shown in Figure 5.9. Essentially, a fuel cell power module, cooling system, hydrogen-oxygen supply system and converter are integrated into the original small electric vehicle. In the diagram, the modules marked in blue are the original devices of the EV (Elano e-mobile), while the modules marked in green were later integrated into the system. Due to the limited space inside the vehicle, the fuel cell, cooling system and oxygen supply system are placed at the head of

the vehicle, and because of the large size of the high-pressure hydrogen storage tank in the hydrogen supply system, it will be placed in the trunk of the vehicle. The E-switch or DC/DC converter is positioned close to the OBC, to ensure the safety of the fuel cell. A diode to prevent reverse currents and a relay are installed between the FCPM system and the busbar.

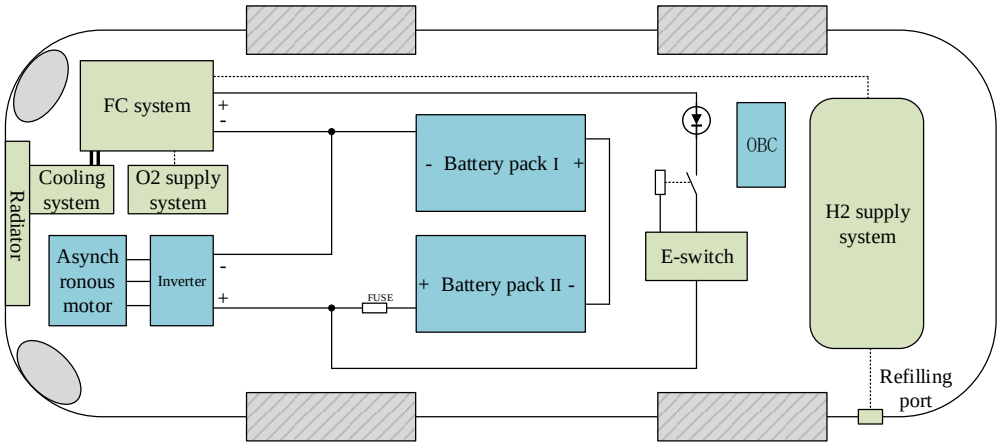

Figure 5.9: Implementation of a small fuel cell vehicle [original]

In order to prevent the safety risks associated with hydrogen leaks, several hydrogen leak detectors have to be installed in different locations at the highest point in the vehicle. If the hydrogen concentration in a confined space exceeds the safety limits, the system must be able to immediately shut down the hydrogen system and give an alarm signal.

Figure 5.10 illustrates the placement of the fuel cell system in BEV. It is important to note that the coolant fill point must be at the highest point of the entire cooling cycle, and the air entrained in the coolant to escape during priming.

Figure 5.10: The placement of the fuel cell system in BEV [original]

5.3 Test results of fuel cell powertrain

In Chapter 2, a novel concept to control the powertrain in FCEV is mentioned. The operating principle of the electronic switch is analyzed in detail and a prototype is implemented. This section will show the operation process and results of the passive hybrid system.

By use of an electronic switch in the powertrain of battery fuel cell hybrid vehicles, the voltage of the battery and the fuel cell system automatically sets an operating point in switched-on state. This is a problem, because during powertrain load cycles, the battery voltage varies a little and thus also the current and the power of the fuel cell system. For this reason, the first measurements are made in switched-on state with variable electronic loads. This means that only the vehicles engine drive cycle is replicated. The results are shown in the following figures. The duration of the recorded measured values is about 14 minutes. In Figure 5.11, the battery current (yellow), the fuel cell current (red) and the maximum allowed current curve of the fuel cell system (blue) are shown.

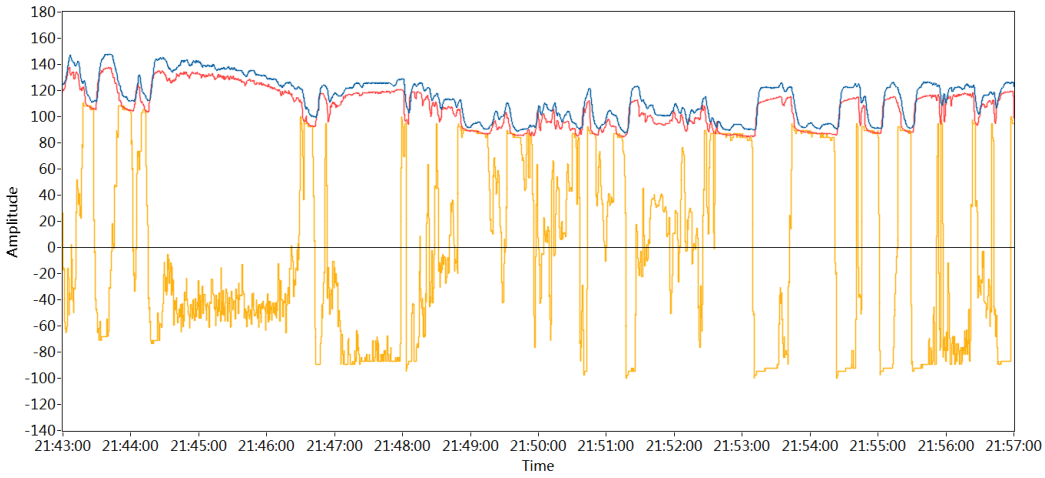

Figure 5.11: Battery (yellow), fuel cell (red) and allowed fuel cell current (blue) during a drive load [31]

In the measurements it can be seen that the drive cycle current mainly load the battery. In case of a negative current, the battery is discharged and the battery is charged when the battery current is positive. The fuel cell current consists predominantly of a DC component. These values vary a little with the cycle of the load. The load current can be calculated from difference between the fuel cell current and the battery current. In the fuel cell system, the electrical power must be coordinated with the hydrogen supply. Then, from the hydrogen supply a maximum allowed output current is calculated, and in the Figure, at each moment the allowed current in the fuel cell (blue) is higher than the real fuel cell system current (red).

Figure5.12 shows the battery voltage (purple) and the voltage of the fuel cell (green). Both voltages vary slightly during the measured power load cycle. Because of the positive fuel cell current in switched-on state, the voltage of the fuel cell is slightly higher than the battery voltage.

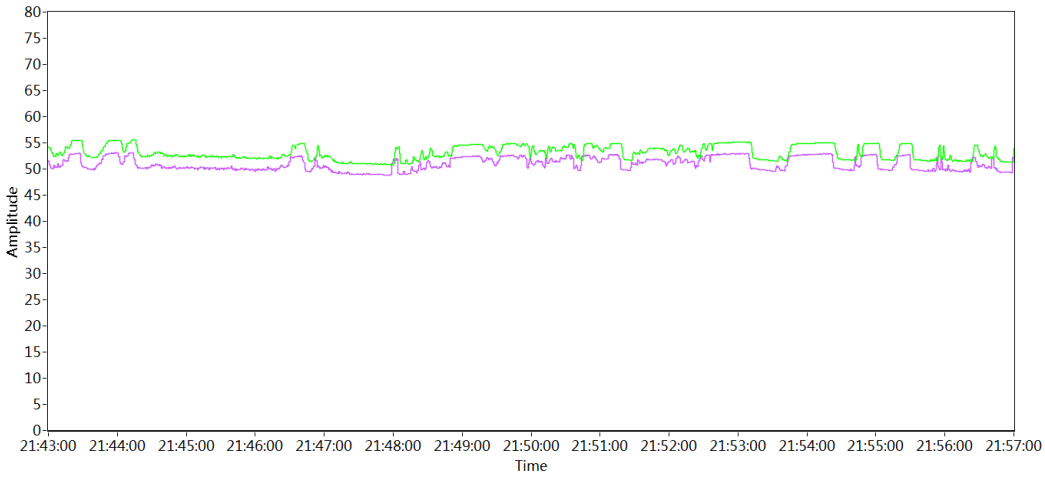

Figure 5.12: Battery voltage (purple) and the voltage of the fuel cell (green) during a drive load [31]

The measurements in Figure 5.13 and Figure 5.14 show the current and voltage waveforms when using the power electronic switch to connect the fuel cell system with the battery. The duration of the recorded measurements is 20 minutes. In this example, the fuel cells system starts operating at a battery state of charge of 15% and shutdown again at a state of charge of 16%.

Figure 5.13: Battery (yellow), fuel cell (red) and allowed fuel cell current (blue) during a drive load [31]

In Figure 5.13 first the fuel cell system is switched-off such that the battery is loaded with the complete drive cycle current. After a few seconds, at 15%

battery state of charge the fuel cell starts operating. Now the drive cycle current is split up into the fuel cell current and battery current. Thus, the battery is charged slowly. After a few minutes, the fuel cell is shut down and the process starts again. When the fuel cell system starts operating, the allowed fuel cell current has an overshoot that is also visible on the figure. This operating philosophy was checked by the fuel cell manufacturer and rated as fine.

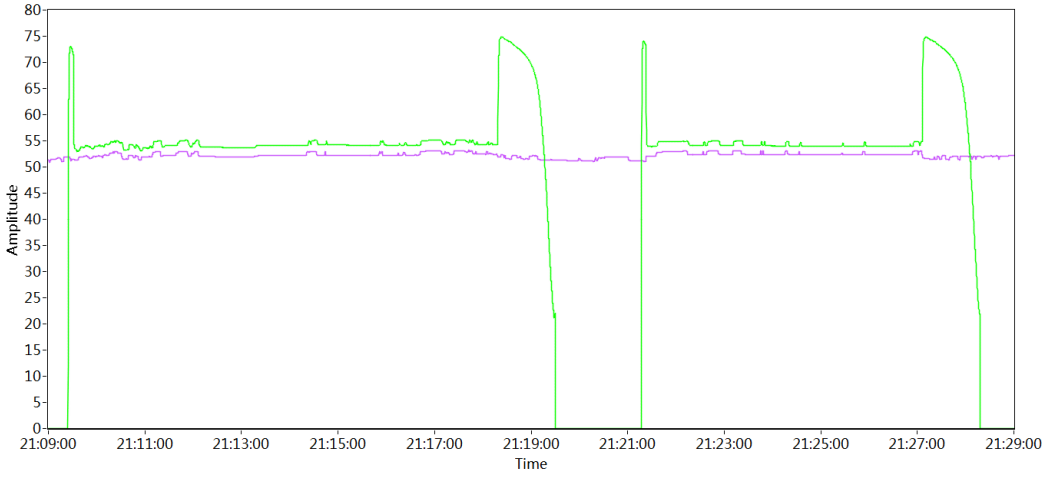

Figure 5.14: Battery voltage (purple) and the voltage of the fuel cell (green) during a drive load [31]

The voltage of the fuel cell system and the battery are shown in Figure 5.14. The battery voltage varies only slightly depends on with the measured load cycle. Initially, the fuel cell voltage is zero because the system is in shutdown state. After the fuel cell starts operating, the voltage rises close to the open circuit voltage. Then the developed power electronic switch is switched-on and operating point adjusts automatically. In this state, the fuel cell voltage is slightly above the battery voltage. This comes from the voltage drop in power lines, power electronic switch and current prevention diode. After the power electronic switch is turned off, the voltage of the fuel cell rises again nearly up to the open circuit voltage. Thereafter, the fuel cell is turned off, such that the voltage slowly drops back to zero and the process starts again.

5.4 Conclusions

This chapter describes the method and process of building a small fuel cell electric vehicle specifically. To facilitate test data and verification of individual

modules in the powertrain of fuel cell electric vehicles,a test bench was first built.

In the test bench, to simulate the real driving conditions of the FCEV, power supplies and electronic loads are composing the corresponding modules to simulate the dynamic conditions of motors and converters, such as acceleration or deceleration. In practice, fuel cell operating conditions are complex, in addition to the fuel cell power module, a hydrogen and oxygen supply system, a cooling system, and a load system are required. These modules need to operate together to ensure the proper operation of the fuel cell and the load. Using the HyPM HD8 fuel cell power module manufactured by HYDROGENICS as an example, the construction of the fuel cell system is described in detail. In addition to the fuel cell system, the lithium iron phosphate battery pack and BMS, the DC/DC converter (E-switch), and the simulated electric motor complete the load system.

Once the entire system of powertrain of the FCEV has been tested on the bench, the entire fuel cell system can be integrated into an electric vehicle.The space inside the passenger vehicle is limited, so the high pressure hydrogen storage tank needs to be placed in the trunk and other modules need to be placed in the correct position.

Finally, the concept described in Chapter 2 was tested on the completed test bench, after the fuel cell has been slowly interconnected to the battery for a specified period of time via an electronic switch. The voltages and currents of the fuel cell and battery pack are illustrated in Figures 5.11 to 5.14, and the results verify the feasibility of the “passive hybrid system”.

Chapter 6.

Conclusions and contributions

6.1 Conclusions

The focus of this thesis is on power electronics in the powertrain of a fuel cell electric vehicle.

- In Chapter 1, the basic principles of the technology route from hydrogen energy to fuel cells and then to fuel cell electric vehicles are introduced, such that the function and necessity of power electronics (converters) in the FCEV powertrain is explained. DC/DC converters have the role of distributing power in the powertrain.

- In Chapter 2, a new concept of FCEV powertrain is presented. Since in this strategy, the output energy of the fuel cell stack is passively controlled by the DC bus voltage of powertrain, voltage conversion is not required here. Instead, an electronic switch with a buffering effect is used in the fuel cell stack turn-on phase. The hardware and software design of the electronic switch is also described in detail. The operation results of the direct connection between the fuel cell and the busbar are demonstrated in Chapter 5. The advantage of this strategy is that no ordinary converters are used, such that losses on the converters are avoided, and the EMI problems caused by high frequency operation of the converter can be reduced. The disadvantage is that there are corresponding requirements for the rated output conditions of the fuel cell stack and the bus voltage of the powertrain, and a larger capacity power battery pack is required to provide peak power draw of electric motor.

- In Chapter 3, a multiphase buck converter is studied in the powertrain of FCEV, in terms of ripple current and dynamic response. Multiphase converters are more suitable for powertrain of FCEV. The fuel cell electric vehicles that exist in the market today (such as NEXO by HYUNDAI, Mirai by TOYOTA and Clarity by HONDA) all use multiphase boost converters in the powertrain, which also proves this point.

- In order to further optimize the efficiency and EMI issues of multiphase converters, two soft-switching multiphase buck converters are proposed and analyzed in Chapter 4. The actual efficiency of the converters is measured with prototypes and their advantages and drawbacks are compared and analyzed.

- In the end, a test bench for fuel cell powertrain was actually built and the conversion of a small fuel cell electric vehicle was realized.

This thesis introduces the powertrain of a fuel cell electric vehicle, the enhancement route of the converter in powertrain of FCEV is studied, and the analysis of the theory is verified by practice.

6.2 Contributions

The authors' contributions can be summarized as follows:

1. A novel concept (E-switch) to control the powertrain of FCEV is proposed and implemented.

2. Theoretical analysis of the use of non-isolated multiphase converters in fuel cells.

3. Two soft-switching multiphase buck converters are proposed and investigated, and their feasibility is verified by the prototypes.

4. The test bench construction for fuel cell powertrain and the concrete implementation of small fuel cell electric vehicle are introduced in detail.

4. "Passive hybrid system" of powertrain of FCEV is verified at test bench and the test results are given.

6.3 Publications list

- F. Renken, **W. Shen**, C. Wang, I. -M. Pop-Calimanu and A. Ciresan, "Multiphase hybrid buck-boost converter with wide conversion ratio," 2017 19th European Conference on Power Electronics and Applications (EPE'17 ECCE Europe), 2017, pp. P.1-P.9.

- F. Renken, **W. Shen**, U. Schürmann and I. -M. Pop-Calimanu, "Multiphase DC/DC Converter and its Use in the Powertrain of Fuel Cell Vehicles," 2018 IEEE 18th International Power Electronics and Motion Control Conference (PEMC), 2018, pp. 280-286.

- **W. Shen**, I. -M. Pop-Calimanu and F. Renken, "Test bench to optimize the Powertrain in Battery-Electric and Fuel-Cell Vehicles," 2018 International Symposium on Electronics and Telecommunications (ISETC), 2018, pp. 1-4.

- F. Renken, D. Piwczyk, **W. Shen**, I. -M. Pop-Calimanu and R. Steinberger-Wilckens, "A Novel Concept to Control the Powertrain in Battery Fuel Cell Hybrid Vehicles," 2018 20th European Conference on Power Electronics and Applications (EPE'18 ECCE Europe), 2018, pp. P.1-P.9.

- **W. Shen**, I. -M. Pop-Calimanu and F. Renken, "Control Strategy for DC/DC Converter in Drive Train of Fuel Cell Vehicles," 2021 IEEE 19th International Power Electronics and Motion Control Conference (PEMC), 2021, pp. 243-249.

- **W. Shen**, F. Renken and D. Lascu, "Soft Switched Multiphase Converter with Parallel Resonant DC-Link Circuit," 2020 International Symposium on Electronics and Telecommunications (ISETC), 2020, pp. 1-4.

- **W. Shen**, F. Renken and D. Lascu, "A New Multiphase ZVT-PWM Synchronous Buck Converter," 2020 International Symposium on Electronics and Telecommunications (ISETC), 2020, pp. 1-4.

6.4 Future works

In order to further optimize the converter in the powertrain of fuel cell electric vehicles, the following research directions are suggested:

- To investigate whether "passive hybrid systems" have an impact on fuel cell lifetime under real driving conditions.

- Improving and extending soft-switching multiphase converters and investigating their corresponding small-signal models to design the control loops.

- Study of isolated soft-switching converters. For example, the transformer-isolated LLC resonant converter, the feasibility of using them in fuel cell electric vehicle powertrain.

- Comparing the performance and efficiency of multiphase converters in different fuel cell powertrains.

References

[1] P. K. Rohith, Jayesh Priolkar, and G. R. Kunkolienkar. Hydrogen: An innovative and alternative energy for the future. In *2016 World Conference on Futuristic Trends in Research and Innovation for Social Welfare (Startup Conclave)*, pages 1–5, 2016. 1.1

[2] Derek Abbott. Keeping the energy debate clean: How do we supply the world's energy needs? *Proceedings of the IEEE*, 98(1):42–66, 2010. 1.1

[3] Mikhail Granovskii, Ibrahim Dincer, and Marc A. Rosen. Economic aspects of greenhouse gas emissions reduction by utilisation of wind and solar energies to produce electricity and hydrogen. In *2006 IEEE EIC Climate Change Conference*, pages 1–5, 2006. 1.1

[4] Yufeng Song, Xuan Zhang, Shuangqing Xu, Xinliang Guo, Lei Wang, Xin Zheng, Wenrui Huang, Yunhua He, Ronghai Liu, Xing Yan, and Junhua Ma. International hydrogen energy policy summary and chinese policy analysis. In *2020 IEEE 4th Conference on Energy Internet and Energy System Integration (EI2)*, pages 3552–3557, 2020. 1.1

[5] LiXin Wan, Wei Zhang, and ZhiPeng Xu. Overview of key technologies and applications of hydrogen energy storage in integrated energy systems. In *2020 12th IEEE PES Asia-Pacific Power and Energy Engineering Conference (APPEEC)*, pages 1–5, 2020. 1.1

[6] Daniel Santoso, Fransiscus Dalu Setiaji, and Deddy Susilo. Demonstration of renewable electrical energy generation based on solar-hydrogen fuel cell technology. In *2011 2nd International Conference on Instrumentation, Communications, Information Technology, and Biomedical Engineering*, pages 342–347, 2011. 1.1

[7] Christopher J. Greiner, M. Korpas, and T. Gjengedal. Value of combining hydrogen production with wind power in short-term electricity markets. In *2008 IEEE 2nd International Power and Energy Conference*, pages 1259–1264, 2008. 1.1

[8] Domenico Curto and Marco Trapanese. Experimental tests on hydrogen production from seawaves energy. In *OCEANS 2017 - Anchorage*, pages 1–5, 2017. 1.1

[9] Hiroki Kimura, Yuto Takeuchi, Yasushi Yamamoto, and Satoshi Konishi. Hydrogen production from biomass using nuclear fusion energy. In *21st IEEE/NPS Symposium on Fusion Engineering SOFE 05*, pages 1–4, 2005. 1.1

[10] LiXin Wan, Wei Zhang, and ZhiPeng Xu. Overview of key technologies and applications of hydrogen energy storage in integrated energy systems. In *2020 12th IEEE PES Asia-Pacific Power and Energy Engineering Conference (APPEEC)*, pages 1–5, 2020. 1.1

[11] BP p.l.c. Energy outlook 2020 edition, 2020. (document), 1.1, 1.1

[12] Chen-Chun Lin and Joseph Z. Shyu. Technology development and application of future hydrogen energy industry and taiwan hydrogen industry. In *PICMET 2010 TECHNOLOGY MANAGEMENT FOR GLOBAL ECONOMIC GROWTH*, pages 1–9, 2010. 1.1

[13] Ulf Bossel. Does a hydrogen economy make sense? *Proceedings of the IEEE*, 94(10):1826–1837, 2006. 1.1

[14] Zuo Jian, C Cadet, Zhongliang Li, Christophe Berenguer, and Rachid Outbib. Post-prognostics decision making for a two-stacks fuel cell system based on a load-dependent deterioration model. 08 2020. (document), 1.2.1, 1.5

[15] Henning Lohse-Busch, Kevin Stutenberg, Michael Duoba, and Simeon Iliev. Technology assessment of a fuel cell vehicle: 2017 toyota mirai. 1.2.1

[16] Department of energy hydrogen prrogram plan. https://www.hydrogen.energy.gov/pdfs/hydrogen-program-plan-2020.pdf. 1.2.1

[17] Janaki Balakrishnan. Fuel cells - configuration and operation. In *2007 IEEE Canada Electrical Power Conference*, pages 213–217, 2007. 1.2.1

[18] Paolo Di Sia. Hydrogen and the state of art of fuel cells. *Journal of Nanoscience with Advanced Technology*, 2:6–13, 04 2018. 1.2.1

[19] R. F. Shyu, H. Yang, and J.-H. Lee. Micro-electroforming metallic bipolar electrodes for mini-dmfc stacks. In *2008 Symposium on Design, Test, Integration and Packaging of MEMS/MOEMS*, pages 192–196, 2008. 1.2.1

[20] Phatiphat Thounthong, Bernard Davat, Stephane Rael, and Panarit Sethakul. Fuel cell high-power applications. *IEEE Industrial Electronics Magazine*, 3(1):32–46, 2009.

[21] Stefani Vanussi Melo Guaitolini, Imene Yahyaoui, Jussara Farias Fardin, Lucas Frizera Encarnação, and Fernando Tadeo. A review of fuel cell and energy cogeneration technologies. In *2018 9th International Renewable Energy Congress (IREC)*, pages 1–6, 2018. 1.2.1

[22] Waffler Stefan. *Hochkompakter bidirektionaler DC-DC-Wandler für Hybridfahrzeuge*. PhD thesis, ETH Zuerich, 2013. (document), 1.4

[23] M. Venkateshkumar, G. Sarathkumar, and S. Britto. Intelligent control based mppt method for fuel cell power system. In *2013 International Conference on Renewable Energy and Sustainable Energy (ICRESE)*, pages 253–257, 2013. 1.2.1

[24] Chen Yong, Enearu Louise, Montalvao Diogo, and Sutharssan Thamo. A review of computational fluid dynamics simulations on pefc performance. *Journal of Applied Mechanical Engineering*, 2016. (document), 1.6

[25] Nedstack Fuel Cell Technology BV. NEDSTACK FCS 7-XXL PEM FUEL CELL STACK. https://nedstack.com/, 2019. (document), 1.7

[26] M. Venturi, C. Mohrdieck, and J. Friedrich. Mercedes-benz b-class fuel cell: The world largest hydrogen vehicle fuel cell fleet experience. In *2013 World Electric Vehicle Symposium and Exhibition (EVS27)*, pages 1–11, 2013. 1.2.2

[27] Lu Xueqin, Huang Fuzhen, Liu Gang, and Qiu Rongfu. The challenges of technologies for fuel cell and its application on vehicles. In *2009 IEEE 6th International Power Electronics and Motion Control Conference*, pages 2328–2333, 2009. 1.2.2

[28] https://www.iea.org/data-and-statistics/charts/fuel-cell-electric-vehicles-stock-by-region-and-by-mode-2020. *Fuel cell electric vehicles stock by region and by mode, 2020, IEA,*, 2020. (document), 1.8, 1.9

[29] R. Steinberger-Wilckens. "presentation of the eu-project swarm", "swarm ("demonstration of small 4-wheel fuel cell passenger vehicle applications in regional and municipal transport" german-language "demonstration von kleinen 4-rädrigen brennstoffzellen-fahrzeugen für den regionalen und kommunalen verkehr")", 2016. (document), 1.10

[30] B. Madden and L. Ruf. "swarm-project presentation", "swarm ("demonstration of small 4-wheel fuel cell passenger vehicle applications in regional and municipal transport")" fuel cell and hydrogen joint undertaking (fch ju), 2016. http://www.fch.europa.eu/page/EVENT-programme-review-days-2016. 1.2.2

[31] Folker Renken, David Piwczyk, **Wensong Shen**, Ioana-Monica Pop-Calimanu, and Robert Steinberger-Wilckens. A novel concept to control the powertrain in battery fuel cell hybrid vehicles. In *2018 20th European Conference on Power Electronics and Applications (EPE'18 ECCE Europe)*, pages P.1–P.9, 2018. (document), 1.2.2, 2.1, 2.1, 2.1, 2.3, 2.28, 2.29, 2.30, 2.31, 5.11, 5.12, 5.13, 5.14

[32] **Wensong Shen**, Ioana-Monica Pop-Calimanu, and Folker Renken. Control strategy for dc/dc converter in drive train of fuel cell vehicles. In *2021 IEEE 19th International Power Electronics and Motion Control Conference (PEMC)*, pages 243–249, 2021. (document), 1.2.2, 1.2.3, 1.14, 1.2.3, 1.15, 3.4, 3.30, 3.31, 3.32, 3.33, 3.34

[33] **Wensong Shen**, Ioana-Monica Pop-Calimanu, and Folker Renken. Test bench to optimize the powertrain in battery-electric and fuel-cell vehicles. In *2018 International Symposium on Electronics and Telecommunications (ISETC)*, pages 1–4, 2018. (document), 1.2.2, 5.1, 5.1, 5.6, 5.7

[34] Folker Renken, **Wensong Shen**, Udo Schürmann, and Ioana-Monica Pop-Calimanu. Multiphase dc/dc converter and its use in the powertrain of fuel cell vehicles. In *2018 IEEE 18th International Power Electronics and Motion Control Conference (PEMC)*, pages 280–286, 2018. (document), 1.2.2, 3.2.1, 3.2.2, 3.6, 3.7, 3.10, 3.11, 3.25, 3.26, 3.27, 3.28, 3.29

[35] Powr train of fcx form honda. https://www.drivingthenation.com/2017-honda-clarity-fuel-cell-vehicle-fcx/. (document), 1.13

[36] Powr train of tucson form hyundai. Tucson Fuel Cell Emergency Response Guide. (document), 1.13

[37] Mohammad Kabalo, Benjamin Blunier, David Bouquain, and Abdellatif Miraoui. State-of-the-art of dc-dc converters for fuel cell vehicles. In *2010 IEEE Vehicle Power and Propulsion Conference*, pages 1–6, 2010. 1.2.3, 3.1

[38] Guido Chiappori, Ph. Le Moigne, Ph Delarue, and Michael Chemin. Low cost linear current limiter for stop-start vehicles. In *2014 IEEE 23rd International Symposium on Industrial Electronics (ISIE)*, pages 550–555, 2014. 2.1

[39] Guang Feng, Boris Deriy, and Ju Wang. A linear mosfet regulator for improving performance of the booster ramping power supplies at the aps. In *2007 IEEE Particle Accelerator Conference (PAC)*, pages 434–436, 2007. 2.1

[40] Infineon. AN201705PL11005,Linear FET combines advantages of planar and trench MOSFETs. www.infineon.com. 2.2.1, 2.2.1

[41] Giuseppe Consentino. Power mosfets working in linear zone: The dangerous effect of the k gain factor on thermal instability. In *International Symposium on Power Electronics Power Electronics, Electrical Drives, Automation and Motion*, pages 1515–1519, 2012. 2.2.1

[42] Infineon. IPB017N10N5.pdf,"optiMOS 5 Power-Transistor, 100V". www.infineon.com. (document), 2.2.1, 2.6, 2.7, 2.8

[43] Infineon. IPB017N10N5LF.pdf,"optiMOS 5 Linear FET, 100V". www.infineon.com. (document), 2.2.1, 2.6, 2.7, 2.8

[44] Donald Dibra, Matthias Stecher, Stefan Decker, Andreas Lindemann, Josef Lutz, and Christoph Kadow. On the origin of thermal runaway in a trench power mosfet. *IEEE Transactions on Electron Devices*, 58(10):3477–3484, 2011. 2.2.1

[45] Feng Zhou and Wei Xiong. Using pwm output as a digital-to-analog converter on dsp. In *2010 International Conference on System Science, Engineering Design and Manufacturing Informatization*, volume 2, pages 278–281, 2010. 2.2.1

[46] Monzer Al Sakka, Joeri Van Mierlo, Hamid Gualous, and Philippe Lataire. Comparison of 30kw dc/dc converter topologies interfaces for fuel cell in hybrid electric vehicle. In *2009 13th European Conference on Power Electronics and Applications*, pages 1–10, 2009. 3.1, 3.1.2

[47] Pop Ioana-Monica. *A new class of high efficiency multiphase DC-DC converters*. PhD thesis, University of Politehnica Timisoara, 2015. 3.1

[48] R. Sharma and Hongwei Gao. Low cost high efficiency dc-dc converter for fuel cell powered auxiliary power unit of a heavy vehicle. *IEEE Transactions on Power Electronics*, 21(3):587–591, 2006. 3.1

[49] A. Andreiciks, I. Steiks, and O. Krievs. Design of resonant dc/dc converter for fuel cell application. In *2012 13th Biennial Baltic Electronics Conference*, pages 219–222, 2012. 3.1

[50] Huang Yong, Zeng Fan, Zhou Qiang, and Chen QuanShi. Study on the characteristics of boost converter in hybrid fuel cell city bus. In *2005 IEEE International Conference on Industrial Technology*, pages 453–458, 2005. 3.1

[51] Phatiphat Thounthong, Bernard Davat, Stephane Rael, and Panarit Sethakul. Fuel cell high-power applications. *IEEE Industrial Electronics Magazine*, 3(1):32–46, 2009. 3.1.2

[52] Abdelfatah Kolli, Arnaud Gaillard, Alexandre De Bernardinis, Olivier Bethoux, Daniel Hissel, and Zoubir Khatir. A review on dc/dc converter architectures for power fuel cell applications. *Energy Conversion and Management*, 105:716–730, 2015. 3.1.2

[53] Nnlna Rasid, N A Rahim, and S R S Raihan. Comparative study of dc-dc converters for fuel cell vehicle. In *4th IET Clean Energy and Technology Conference (CEAT 2016)*, pages 1–4, 2016. 3.1.2

[54] Xiaoqiang Li, Jingyang Fang, Pengfeng Lin, and Yi Tang. A common magnetic integration method for single-phase lcl filters and llcl filters. In *2017 IEEE Energy Conversion Congress and Exposition (ECCE)*, pages 5595–5600, 2017. 3.1.2

[55] Wafa Ben Salem, Houssem Chaouali, Dhia Mzoughi, and Abdelkader Mami. Interactions between fuel cell and boost converter: Influence of current harmonics on a fuel cell. In *2017 International Conference on Engineering MIS (ICEMIS)*, pages 1–6, 2017. 3.1.2

[56] Guillaume Fontes, Christophe Turpin, Stphan Astier, and Thierry A. Meynard. Interactions between fuel cells and power converters: Influence of current harmonics on a fuel cell stack. *IEEE Transactions on Power Electronics*, 22(2):670–678, 2007. 3.1.2

[57] Jih-Sheng Lai, Changrong Liu, and Amy Ridenour. Multiphase soft switched dc/dc converter and active control technique for fuel cell ripple current elimination. 3.1.2

[58] Mohammad Kabalo, Damien Paire, Benjamin Blunier, David Bouquain, Marcelo Godoy Simões, and Abdellatif Miraoui. Experimental evaluation of four-phase floating interleaved boost converter design and control for fuel cell applications. *IET Power Electronics*, 6(2):215–226. 3.1.2

[59] Folker Renken. Multiphase dc/dc converters for hybrid electric vehicles. In *Proceedings of 14th International Power Electronics and Motion Control Conference EPE-PEMC 2010*, pages T9–98–T9–105, 2010. (document), 3.2.1, 3.2, 3.3, 3.4, 3.5, 3.2.2

[60] Afshin Keshtkar Teeula and Shahriyar Kaboli. A reliable and fast response buck converter based on interleaved converter. In *2019 27th Iranian Conference on Electrical Engineering (ICEE)*, pages 804–807, 2019. 3.2.2

[61] Xiaobo Yang, Sheng Zong, and Guoxing Fan. Analysis and validation of the output current ripple in interleaved buck converter. In *IECON 2017 - 43rd Annual Conference of the IEEE Industrial Electronics Society*, pages 846–851, 2017. 3.2.2

[62] Fernando Sobrino-Manzanares and Ausias Garrigos. Bidirectional, interleaved, multiphase, multidevice, soft-switching, fpga-controlled, buck–boost converter with pwm real-time reconfiguration. *IEEE Transactions on Power Electronics*, 33(11):9710–9721, 2018. 3.2.2

[63] Folker Renken, **Wensong Shen**, Chao Wang, Ioana-Monica Pop-Calimanu, and Aurel Ciresan. Multiphase hybrid buck-boost converter with wide conversion ratio. In *2017 19th European Conference on Power Electronics and Applications (EPE'17 ECCE Europe)*, pages P.1–P.9, 2017. 3.2.2

[64] Hegarty Tim. *Benefits of multiphasing buck converters*. EE Times, 2007. 3.2.2

[65] Robert W. Erickson and Dragan Maksimović. *Fundamentals of Power Electronics*. Springer, 2001. 3.3, 4.1

[66] A. Schittler, D. Pappis, C. Rech, A. Campos, and M. D. Dalla Costa. Generalized state-space model for the interleaved buck converter. *XI Brazilian Power Electronics Conference*, pages 451–457, 2011. 3.3

[67] Dorin O. Neacsu, William Bonnice, and Evgeny Holmansky. On the small-signal modeling of parallel/interleaved buck/boost converters. In *2010 IEEE International Symposium on Industrial Electronics*, pages 2708–2713, 2010. 3.3

[68] Veerachary Mummadi and Kamlesh Krishna Sawant. Control of multi-input integrated buck-boost converter. In *2008 IEEE Region 10 and the Third international Conference on Industrial and Information Systems*, pages 1–6, 2008. 3.3

[69] Haozhe Li, Rong Long, Liyan Zhang, and Qihong Chen. Analysis and design of four-phase interleaved parallel buck converter based on high-power charging system for electric vehicles. In *2020 16th International Conference on Control, Automation, Robotics and Vision (ICARCV)*, pages 38–43, 2020. 3.3

[70] Minrui Leng, Guohua Zhou, Qingxin Tian, Lunbo Deng, and Songrong Wu. Current sharing method of charge controlled interleaved buck converter. In *2019 IEEE Energy Conversion Congress and Exposition (ECCE)*, pages 681–685, 2019. 3.3.2

[71] J. Rajagopalan, K. Xing, Y. Guo, F.C. Lee, and B. Manners. Modeling and dynamic analysis of paralleled dc/dc converters with master-slave current sharing control. In *Proceedings of Applied Power Electronics Conference. APEC '96*, volume 2, pages 678–684 vol.2, 1996. 3.3.2

[72] Yuri Panov and Milan M. Jovanovic. Loop gain measurement of paralleled dc–dc converters with average-current-sharing control. *IEEE Transactions on Power Electronics*, 23(6):2942–2948, 2008. 3.3.2

[73] Qingqing Li, Shulin Liu, Huisan Xu, and Xiao Wang. Research on the maximum current automatic current-sharing control based on dsp. In *2017 IEEE International Conference on Information and Automation (ICIA)*, pages 1044–1049, 2017. 3.3.2

[74] T.W. Ching and K.U. Chan. Review of soft-switching techniques for high-frequency switched-mode power converters. In *2008 IEEE Vehicle Power and Propulsion Conference*, pages 1–6, 2008. 4.1

[75] Maria Teresa Outeiro, Giuseppe Buja, and Dariusz Czarkowski. Resonant power converters: An overview with multiple elements in the resonant tank network. *IEEE Industrial Electronics Magazine*, 10(2):21–45, 2016. 4.1

[76] Alexandre Rodrigues Vaz and Fernando Lessa Tofoli. Practical design of a dc-dc buck converter using an rcd snubber. In *2017 Brazilian Power Electronics Conference (COBEP)*, pages 1–6, 2017. 4.1

[77] Mehdi Mohammadi, Ehsan Adib, and Mohammad Rouhollah Yazdani. Family of soft-switching single-switch pwm converters with lossless passive snubber. *IEEE Transactions on Industrial Electronics*, 62(6):3473–3481, 2015. 4.1

[78] E. Firmansyah, S. Tomioka, S. Abe, M. Shoyama, and T. Ninomiya. Steady state characteristics of active-clamped full-wave zero-current-switched quasi-resonant boost converters. In *2009 IEEE 6th International Power Electronics and Motion Control Conference*, pages 556–560, 2009. 4.1

[79] Naim Suleyman Ting and Nihan Altintas. A soft switching single phase power factor correction ac-dc boost converter with passive snubber. In *2017 4th International Conference on Electrical and Electronic Engineering (ICEEE)*, pages 13–17, 2017. 4.1

[80] Ann Merine Tony and P Saritha. Voltage mode control of soft-switched single switch resonant converter. In *2015 International Conference on Circuits, Power and Computing Technologies [ICCPCT-2015]*, pages 1–6, 2015. 4.1

[81] Danis Farrakhov, Kirill Barabanov, Alexander Podguzov, Ilnar Yamalov, and Ruslan Urazbakhtin. Quasi-resonant buck converter for high power application. In *2020 International Conference on Electrotechnical Complexes and Systems (ICOECS)*, pages 1–4, 2020. 4.1

[82] Guichao Hua, Ching-Shan Leu, Yimin Jiang, and F.C.Y. Lee. Novel zero-voltage-transition pwm converters. *IEEE Transactions on Power Electronics*, 9(2):213–219, 1994. 4.1

[83] Hanqing Wang, Arnaud Gaillard, and Daniel Hissel. 6-phase soft-switching interleaved boost converter based on sic semiconductor for fuel cell vehicles. In *2016 IEEE Vehicle Power and Propulsion Conference (VPPC)*, pages 1–7, 2016. 4.1

[84] **Wensong Shen**, Folker Renken, and Dan Lascu. A new multiphase zvt-pwm synchronous buck converter. In *2020 International Symposium on Electronics and Telecommunications (ISETC)*, pages 1–4, 2020. (document), 4.2, 4.3, 4.4, 4.5, 4.6, 4.7, 4.8, 4.9, 4.10, 4.11, 4.12, 4.13, 4.14, 4.15, 4.16, 4.17, 4.18

[85] G. Hua, C.S. Leu, and F.C. Lee. Novel zero-voltage-transition pwm converters. In *PESC '92 Record. 23rd Annual IEEE Power Electronics Specialists Conference*, pages 55–61 vol.1, 1992. 4.2

[86] G. Hua and F.C. Lee. Soft-switching techniques in pwm converters. *IEEE Transactions on Industrial Electronics*, 42(6):595–603, 1995. 4.2

[87] Markus Krogemann. *The parallel resonant DC link inverter: a soft-switching inverter topology with PWM capability.* PhD thesis, University of Nottingham, 1997. 4.5

[88] J.G. Cho, H.S. Kim, and G.H. Cho. Novel soft switching pwm converter using a new parallel resonant dc-link. In *PESC '91 Record 22nd Annual IEEE Power Electronics Specialists Conference*, pages 241–247, 1991. 4.5

[89] **Wensong Shen**, Folker Renken, and Dan Lascu. Soft switched multiphase converter with parallel resonant dc-link circuit. In *2020 International Symposium on Electronics and Telecommunications (ISETC)*, pages 1–4, 2020. (document), 4.5, 4.19, 4.20, 4.27, 4.28, 4.29, 4.31, 4.32, 4.33

[90] Hydrogenics. Specification sheet of hypm hd 8. http://hydrogenics.eu/. 5.1.1

[91] Hydrogenics. Hypm hd 8 installation, operation and maintenance manual. http://hydrogenics.eu/. 5.1.1

Appendix

MATLAB code for E-switch control simulation

```
VPWM=15,VADC=3.3,NP=1,NS=1000,RM=100,GM=60,sloop=40;
%parameters of simulation
KP=4;KI=400;
% KP and KI set
R=2200;C=2.2E-6;
%filter parameters
K=VPWM*GM;Y=R*C;
DEN=[KP,KI],NUM=[Y,1,0];
SYS=K*tf(DEN,NUM);
HS=NP*RM/(VADC*NS);
GS=HS*SYS;
FS=feedback(SYS,HS);
% closed loop transferfunction of system
s=tf('s')
G1=FS/s^2*0.0303*sloop;
%output of system
G2=1/s^2*sloop;
%reference of system
impulse(G1,1);
hold on;
impulse(G2,1);
%capture pictures
```

Look up table module for linear MOSFET in E-switch

```
ID =[0,0,0.075572,0.302796,0.614215,1.150314,1.936165,2.98144,
     4.347621,6.093018,8.485639,11.413204,14.958891,19.213926,
     24.250391,29.696621,35.787148,42,48.6]

VGS=[3.524894,3.617935,3.710976,3.804017,3.897058,3.990099,
     4.08314,4.176181,4.269222,4.362263,4.455304,4.548345,
     4.641386,4.734426,4.827467,4.920508,5.013549,5.10659,
     5.1996]
```

MATLAB code for multiphase buck closed loop step response simulation

```
s=tf('s'),Lpk=50E-6,Rpk=0.026,Cp=200E-6,Rcp=0.001,R=1;
Ud=1,N=1;
a=s*Lpk+Rpk;
b=(R*(1+s*Cp*Rcp))/(1+s*Cp*(R+Rcp));
onephase=(Ud*b)/(a+N*b);
%bode(g);
%x=feedback(g,1);
step(onephase);hold on;
Ud=2;N=2;
twopahse=(Ud*b)/(a+N*b);
%bode(g);
%x=feedback(g,1);
step(twopahse);hold on;
Ud=3;N=3;
threephase=(Ud*b)/(a+N*b);
%x=feedback(g,1);
%bode(g);
step(threephase);hold on;
Ud=4;N=4;
fourphase=(Ud*b)/(a+N*b);
%x=feedback(g,1);
%bode(g);step(fourphase);hold on;
Ud=5;N=5;
fivephase=(Ud*b)/(a+N*b);
```

```
%x=feedback(g,1);
%bode(g);
step(fivephase);hold on;
Ud=6;N=6;
sixphase=(Ud*b)/(a+N*b);
%x=feedback(g,1);
%bode(g);
step(sixphase);hold on;
```

Key schematic and PCB layout of E-switch

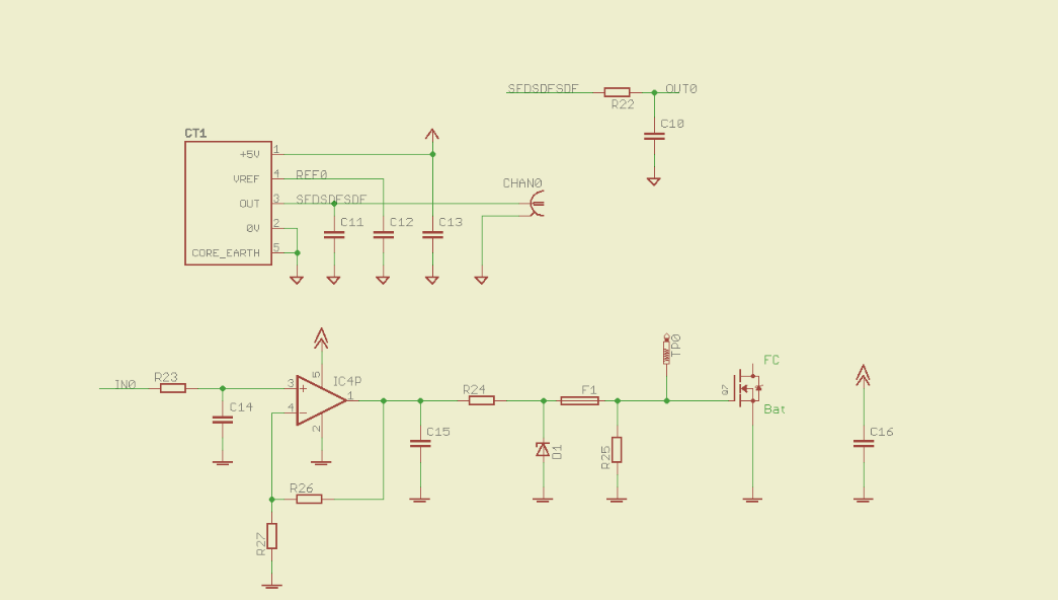

PWM filter and current sampling for E-switch

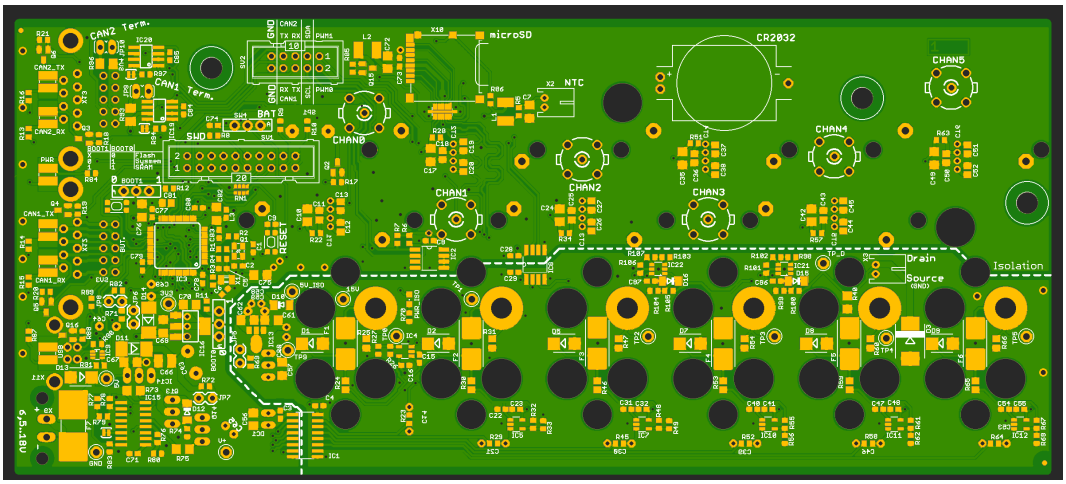

Overviwe of PCB layout for used E-switch

Key schematics of 6 phase buck converter

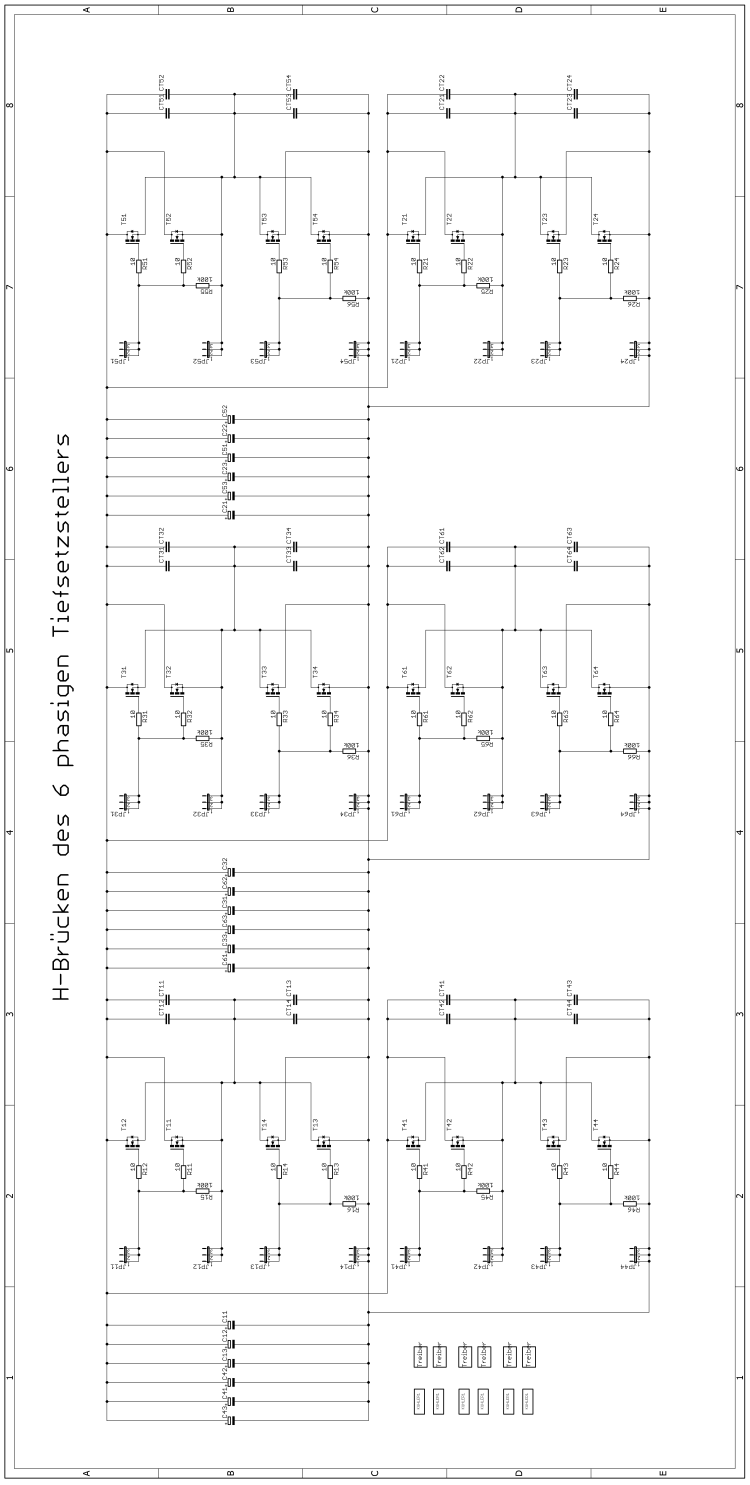

Power part of 6 phase buckconverter

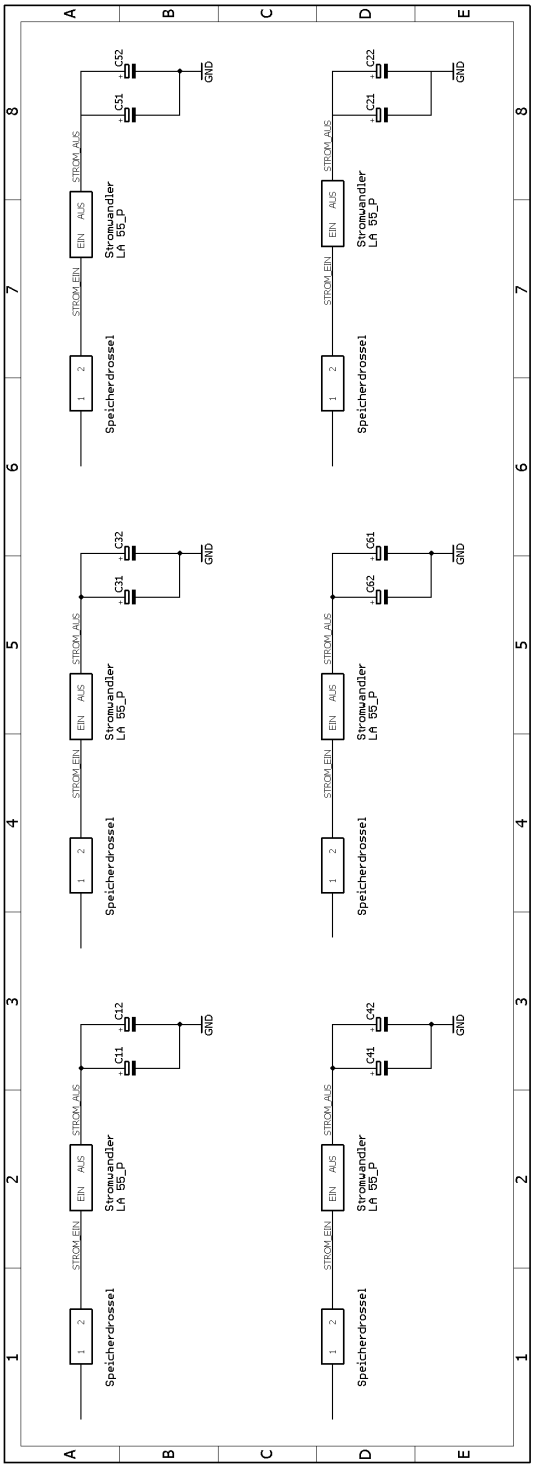

Filter part of 6 phase buck converter

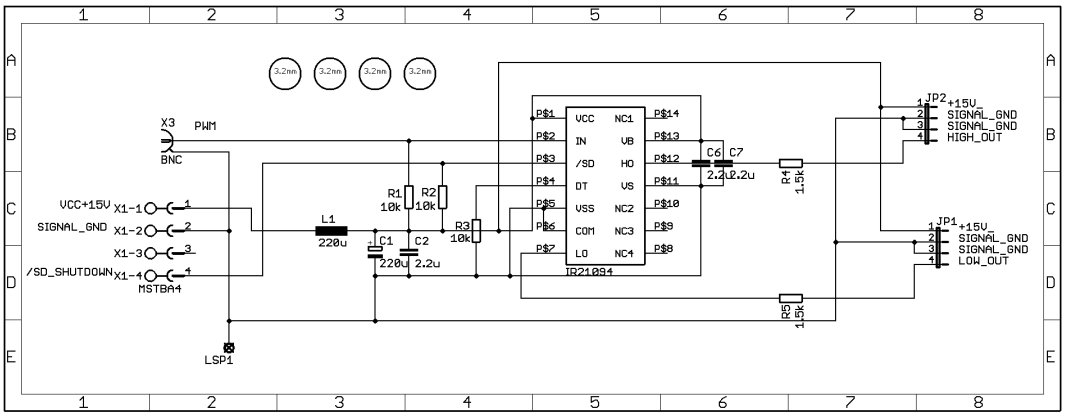

Driver circuit of 6 phase buck converter

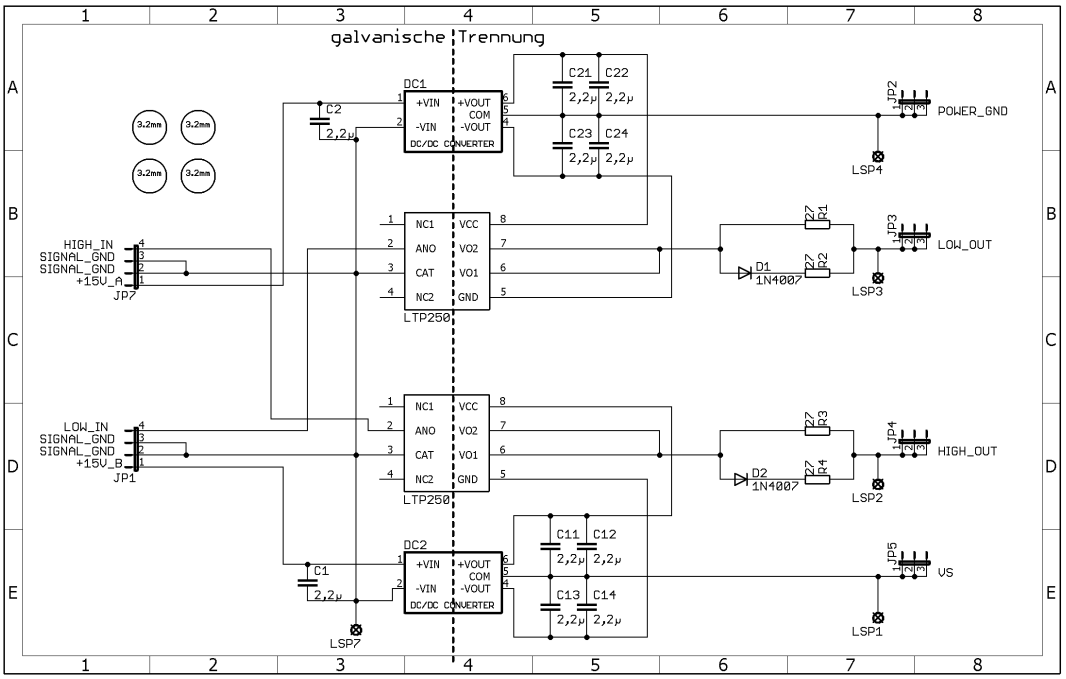

Isolated powersupply for driver circuit of 6 phase buck converter